A Thesis for the Degree of Ph.D. in Engineering

System Abstraction and Interactive Control Design Based on Element Description Method

August 2018

Graduate School of Science and Technology
Keio University

TAKEUCHI, Issei

Acknowledgments

This dissertation is the summary of my research from September 2014 to August 2018 as the member of Katsura Laboratory, the Faculty of Science and Technology, Keio University. In the four years since I entered the laboratory, I have had many valuable experiences and I was supported by a lot of people. Here, I would like to express my gratitude to all people who have given me the support and advice.

First of all, I would like to be deeply grateful from my heart for my supervisor Associate Professor Dr. Seiichiro Katsura, Department of System Design Engineering, Keio University. His dedicated teaching has grown me and provided a lot of precious things. Moreover, his passion for the academic research has inspired me to do research activity and to develop the novelty. Besides, he provided a lot of opportunities such as making the presentation of my research at domestic and international conferences, participating in exhibitions. I can never imagine that I could accomplish this work without this kind help.

I would like to offer my special thanks to the members of my Ph.D. dissertation committee, Professor Dr. Hiromitsu Ohmori, Department of System Design Engineering, Keio University, Professor Dr. Masayuki Kohiyama, Department of System Design Engineering, Keio University, Associate Professor Dr. Takahiro Yakoh Department of System Design Engineering, Keio University.

I would like to show my appreciation to Professors who gave precious comments at the research meetings. I would like to thank Professor Dr. Kouhei Ohnishi in Keio University, Professor Dr. Toshiyuki Murakami in Keio University, Professor Dr. Hiroaki Nishi in Keio University, and Assistant Professor Dr. Takahiro Nozaki in Keio University.

I am very grateful to everyone at Tokyo Automatic Machinery Works, Ltd., including President Haruo Yamamoto for giving me the chance to challenge the doctoral course while working, also thank you very much for your support for tuition. In particular, I would like to thank Mr. Makoto Kakiuchi, Mr. Masahiko Shimizu, and Mr. Tsuyoshi Moriyama for various support in getting permission to enroll at Keio University graduate school. Also, I would like to thank the members of the technology development department including Mr. Yoshikazu Sato, Mr. Kiyoshi Nobuta, and Mr. Shin Kuribayashi, who warmly supported the center of my school days. Thanks to your understanding, I was able to balance work and schoolwork.

Let me appreciate everyone who collaborated with and helped me in Katsura Laboratory. In particular, I would like to thank Dr. Hidetaka Morimitsu, Dr. Eiichi Saito, Dr. Yuki Nagatsu, Dr. Kazumasa Miura, and Dr. Satoshi Nishimura for giving various advice to the research. The things which I obtained at this laboratory are treasonable for me.

Finally, I would like to express my gratitude to my family who brought me up and helped me a lot. I especially appreciate my beloved wife Ran and three daughters Sakura, Ume, and Momo in particular. Your kind and warm-hearted assistance have enabled me to study without any inconvenience, and I would like to thank you from my heart. I was able to complete doctoral course research by a lot of people support. I will keep this gratitude in my heart, I cherish the connection between people and people I gained here lifelong, and I want to fulfill social contribution in the future.

August 2018
Issei Takeuchi

Table of Contents

List of Figures

List of Tables

Chapter 1

Introduction

1.1 Background of This Dissertation

1.1.1 Transition of Factory Automation and Historical Background

In 1913, in the production process of T-type Ford, mass production through the use of an assembly line was achieved. It achieved a substantial reduction of manufacturing cost by improving productivity, and it attracted worldwide attention. Since then, the importance of automation in production processes (i.e., factory automation) at the manufacturing site has been increased day by day [1]. The factory automation is achieved by automatic machinery [2]. The required functions of automatic machinery is diverse. For example, "Productivity," "Flexibility," "Adaptability," and "Intelligence" shown in Fig. 1-1 have been required. The importance of them requirements has gradually changed with the historical background. From the mid–20 th century when Japan entered the period of high economic growth, automatic machinery began to popularize. In this era, "Productivity" was the most important from the background of supply shortage society. Thereby, facilities that achieves mass production was required in the manufacturing site. In this era, the products were bought if these were made. It was the most important to achieve "Productivity" for the automatic machinery. However, as the product starts to saturate due to the collapse of the bubble, the age of oversupply society had come. In this era, customers gradually demanded quality and value for products, and it brought about diversification of products and shortening of the development period. Hence, the requirements of factory automation had shifted from mass production to high-mix low-volume production [3]. Due to this trend, automatic machinery was

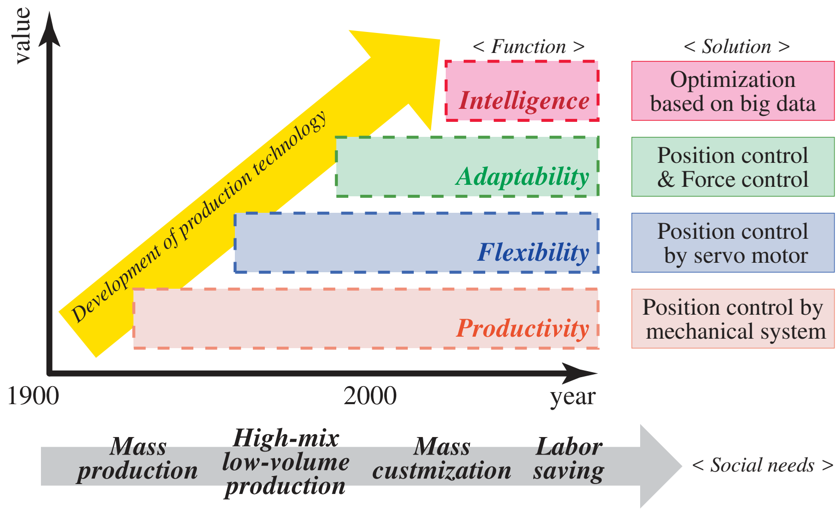

Fig. 1-1: Functions required for automatic machinery.

required to have "Flexibility" in addition to "Productivity." In recent years, mass-customization has been required with the advent of maturing society. Therefore, "Adaptability" like human's manual task has been required for automatic machinery in addition to "Productivity" and "Flexibility." In addition, with the development of information communication technology and data storage technology, the amount of data that can be handled by an automatic machinery has increased drastically. Moreover, due to the decrease in the number of workers, demands for labor-saving at the manufacturing site has been further increasing. From such backgrounds, "Intelligence" of automatic machinery that moves machines wisely has been needed. As an example of how automatic machinery has changed with the historical background, a case of packaging machinery are described.

1.1.2 Achievement of Productivity by Mechanical System

As mentioned above, "Productivity" was the most important to achieve mass production in supply shortage society. At the time, alternating current (AC) induction motors, large air cylinders, and direct acting solenoids were widely used as actuators in general. In other words, servo motors had not developed. Automatic machinery in this era had the multiple working ends, the power of each working end was covered by one AC induction motor. The trajectory of each working end could be designed arbitrarily using various mechanisms such as a cam and link [4, 5]. Namely, automatic machinery in this era was moved by a mechanical system (e.g., one AC induction motor and mechanism). Examples

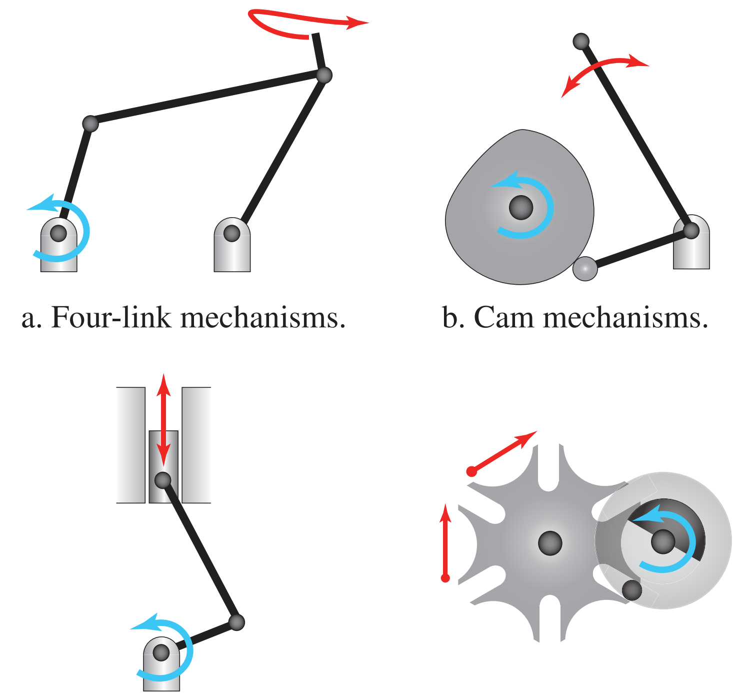

a. Four-link mechanisms. b. Cam mechanisms.

c. Crank piston mechanism. d. Geneva mechanism.

Fig. 1-2: Examples of motion-transformation mechanism.

of motion-transformation-mechanism are shown in Fig. 1-2. The four-link mechanisms makes reciprocating motion from circular motion The cam mechanisms can make arbitrary trajectory for the working end. The crank piston mechanism mechanism converts circular motion into linear motion. The geneva mechanism can generate index actions from circular motion. Here, the stiffness of a system is expressed as

$$\kappa = \frac{\partial F}{\partial x}, \tag{1.1}$$

where κ, x, and F stand for stiffness, position, and force, respectively. The control stiffness κ of a mechanical system is approximately ∞. Thereby, the position of each working end is determined uniquely by the mechanical angle of the main axis which directly connects to an AC induction motor. In an ideal mechanical system, the relationship of the angle of the main axis and each working end is expressed as

$$\begin{bmatrix} x_1 \\ x_2 \\ \vdots \\ x_n \end{bmatrix} = \begin{bmatrix} k_1(\theta_{\mathrm{m}}) \\ k_2(\theta_{\mathrm{m}}) \\ \vdots \\ k_n(\theta_{\mathrm{m}}) \end{bmatrix}, \tag{1.2}$$

where $x_i (i = 1, 2, \cdots, n)$, $k_i(\bullet)$, and θ_{m} refer to working end positions, coordinate conversion functions, and an angle of main axis, respectively. The subscript i denotes i–th working end. Since the mutual positional relationship is guaranteed in an ideal mechanical system, there is no fear of mechanical contact between the working ends. Therefore, the machinery will be possible to work faster according to increase the angular speed of the main axis. This era is supply shortage society, when productivity is more important than quality, and automatic machinery has also been required mass production of single kind of product. The mechanical system mentioned above matched this requirement and spread widely.

1.1.3 Achievement of Flexibility by Position Control Using Servo Motors

In oversupply society, "Flexibility" is also required in addition to "Productivity." Although the mechanical system has high speed property, it has no flexibility. For example, when changing the trajectory by switching the target product, it is necessary to change the length of the link or to replace parts, which takes time and labor. In this era, servo motors had been developed. In case of using servo motors, it is easy to change the operation pattern necessary for product type switching by rewriting the trajectory of position command value. Namely, the coordinate conversion functions $k_i(\bullet)$ in (1.2) can be arbitrarily changed. For this reason, the system using servo motors had high "Flexibility." Since it matched the market demand, it began to spread rapidly and widely. Servo motors was required to have positioning accuracy and multi-axis synchronous performance. This is because that productivity and flexibility can be achieved if servo motors that are easy to change trajectories can control like an infinite rigid mechanical system. Therefore, various researches have been conducted to improve the performance of positioning control. Ohnishi *et. al.* proposed a disturbance observer (DOB) [6, 7]. The DOB can eliminate the effect of disturbance, realizing to control position robustly. Tomizuka *et. al.* proposed zero phase error tracking (ZPET) control [8]. By using the ZPET control, high performance of position control can be achieved. Fujimoto *et. al.* expanded above methods to perfect tracking control [9]. By these methods, the position can be controlled nearly perfect by eliminating the effect of disturbance and implementing feed-forward controllers. Thanks to these researches, position control became possible with ultrahigh accuracy [10], "Productivity" and "Flexibility" were achieved simultaneously.

1.1.4 Achievement of Adaptability by Force Control Using Servo Motors

As mentioned above, high accurate position control by servo motors evolved the automatic machinery. However, there were problems in order to realizing mass customization. Since the ideal position control has infinite stiffness, it cannot adapt to changing in the position, size, and hardness of target products. In other words, automatic machinery based on position control system requires strict management to keep the quality of target products consistently constant. However, it is quite difficult to eliminate the fluctuation of the target products due to various factors such as subtle changes in raw materials and differences in producing areas, and differences in climate. Therefore, control technologies that adapts to the fluctuation of the target products are indispensable for achieving mass customization.

Addition of force control element [11–13] is one of the effective solutions in order to overcome above issues. The position control and the force control have duality relationships. The position control has infinite stiffness, whereas the force control has zero stiffness. In other words, while position control is a "position definite – force indefinite" system that moves to the desired location regardless of the target product, the force control can be said to be "force definite – position indefinite" which completely follows the target product. Therefore, force control can adapt to changing in the position, size, hardness of target products. In order to achieve mass customization, it is necessary to integrate the position control and the force control because both of tracking ability and adaptation ability are needed. Also, by expanding position control and the force control structure, various advanced control methods are achieved such as hybrid control [14], compliance (or impedance) control [15–18], and bilateral control [19–21]. All of these control methods can be achieved based on acceleration control using the DOB. A motion-copying system [22, 23] is one of effective integration methods of the position control and the force control because it can save and reconstruct the fusion of the position control and the force control that are unconsciously performed by human beings as motion data. Also, various methods of extending the theory of a motion-copying system to adapt wisely to environmental fluctuations have been extensively studied [24–31]. By using technologies such as the motion-copying system, work skills of experienced engineers in the factory can be preserved and reproduced by machinery and robots; therefore it can be an important fundamental technology for achieving mass customization.

1.2 Motivation of This Dissertation

1.2.1 Intelligentization of Automatic Machinery Toward Labor Saving

Currently, the demand for labor saving is increasing due to labor population shortage. In order to achieving labor saving, not only extraction of human skills but also abstraction of knowledge are necessary. By abstraction of human's knowledge and extraction of human's skills, it can be expected that

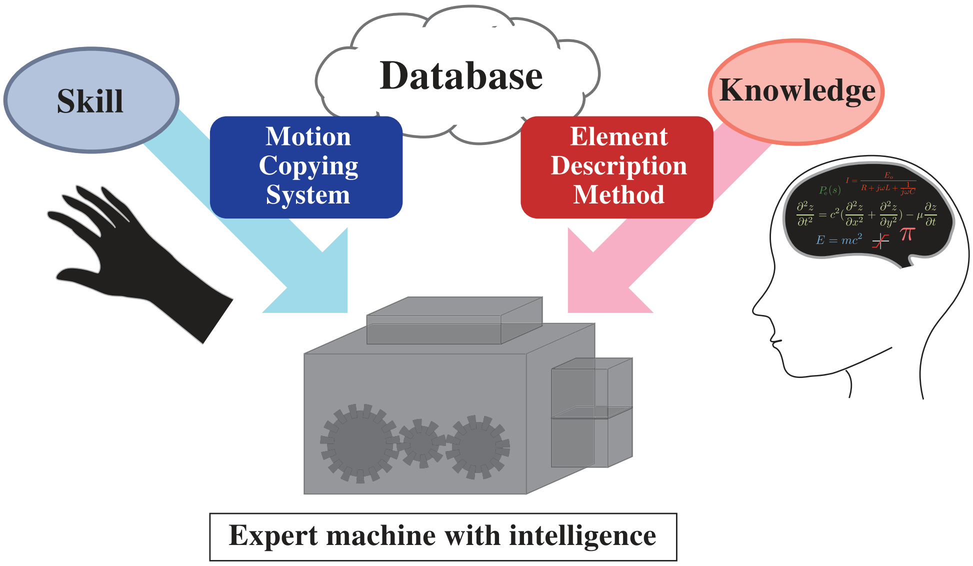

Fig. 1-3: A conceptual view of skill extraction and knowledge abstraction.

intelligentization of automatic machinery and labor saving in the manufacturing site. Fig. 1-3 is the conceptual view of skill extraction and knowledge abstraction of human. Experienced machine operators can recognize subtle changes in such target products and adjust machine parameters. However, the adjustment is often based on heuristics, which can be said to be tacit knowledge. Therefore, quantitative evaluation is difficult, and it is often not formalized. Furthermore, in recent years, such skilled workers retire often in the absence of technology succession. Therefore, knowledge accumulated over the years is lost. Against such a background, it is an important task to extract tacit knowledge of experienced workers.

Also, the amount of applicable time-series data have been increased according to the development of information and communication technology and evolution of sensing or storage devices. Thereby, it has been envisioned to realize smart factory utilizing big data [32] in various countries and organizations, such as industrie 4.0 [33], Society 5.0, Cyber Physical System (CPS) [34], Industrial Internet of Things (IIoT) [35, 36], and Industrial Internet Consortium (IIC). Automatic machinery so far can not make effective use of production data, been limited to detecting abnormality in each process and checking the validity of quality. Now that data collection technology has developed, effective utilization of production data is one of the innovative challenges for automatic machinery. By effectively using the big data, there is a possibility that it can substitute for the tacit knowledge of experienced engineers. This makes it possible to achieve the adaptability to the fluctuation of a target products and an environment, similar to the adjustment of experienced engineers.

One of the classical utilization methods of time-series data is system identification based on a regression equation [37–40]. This method can be called as model-based identification ones. In this method, a system model for identification is designed in advance. After that, parameters for the model are fitted based on a least-square method. The advantages of this method is obviously the system model and optimization process are simple. By using this method, the physical meaning of the identification result is clear because this method is based on a pre-specified model. Hence, it is relatively easy to handle the identification results, and it can be applied to design the controller of the target system by its synthesis. However, the method is difficult to use because the structure of the model is needed in advance. In this case, identification results cannot be declared optimally because they are based on a pre-specified model and there is a possibility that the model does not match the actual one.

On the contrary, a data-based identification method is effective for unknown systems containing uncertainty, nonlinearity, and time-varying elements because it does not need to design the model in advance [41–46]. Therefore, it can achieve better input-output characteristics than the model-based method. Particularly, machine learning based on a neural network [45, 46] is well known as an effective method to achieve input-output characteristic. Recently, it has been applied to various fields such as searching algorithm, voice recognition software, and image processing technology. However, it is difficult to understand the physical meaning of the calculation process of the identification result. This is a big problem in future society because it means that humans cannot understand a computer's thread. There is a risk that humans are used by machines. Human beings should always know the reason of an answer. Therefore, understandability about the inside of the optimization result is required for a sustainable application of big data. As mentioned above, there is a trade-off between adaptation against uncertain elements and understanding of the identification results. In order to overcome this problem, this dissertation attempts to establish both adaptation for uncertainty and understandability.

In this research, big data are used to achieve response to the target products and the environmental fluctuation which is the subject of the automatic machinery. Fig. 1-5 shows the concept image of intelligentization of automatic machinery. In order to achieve intelligentization of automatic machinery, it is necessary to recognize and design the system as a whole. In smart sensing process, technologies to sense more valuable information more efficiently are needed. Even if a lot of information are collected, if there are no values in that information, machine intelligence cannot be achieved. In the case of cooking, it means to collect more good ingredients. Hence, smart sensing can be said to be an important tech-

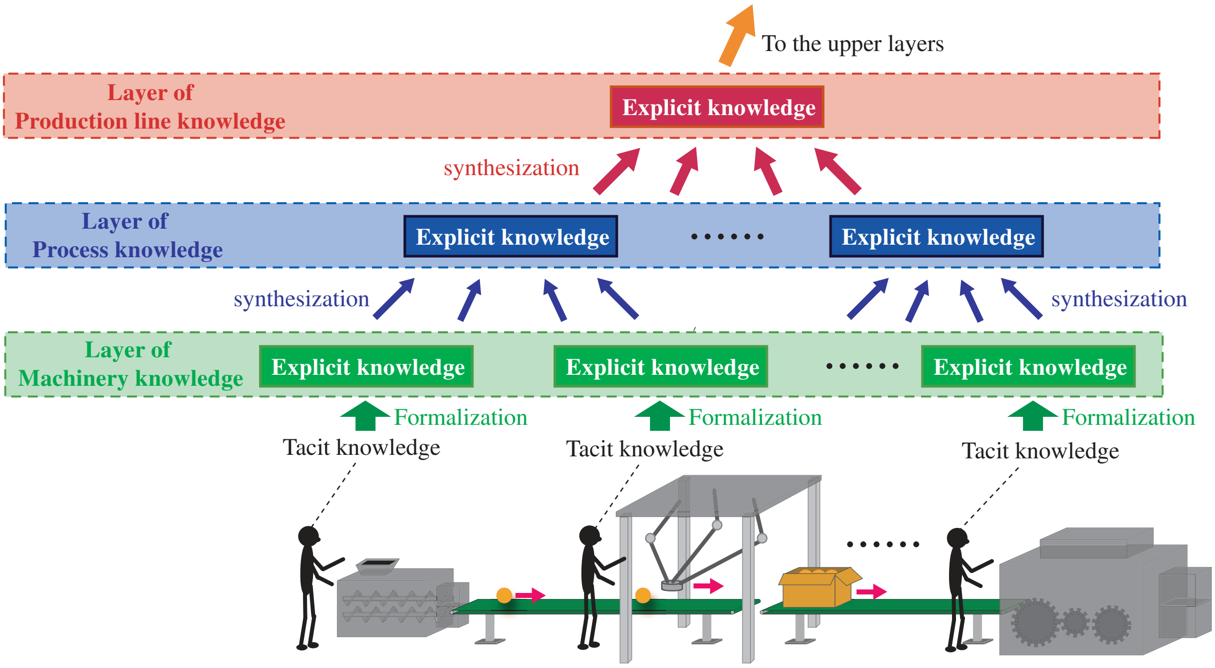

Fig. 1-4: Conceptual diagram of integration of formal knowledge.

nology responsible for the foundation of intelligent machines. Big data analysis process is the process of analyzing the collected information and creating more valuable information. The collected data are often simple time series data; however, it can generate more valuable data by performing information processing according to the purpose. In the case of cooking, it is an important process like pretreatment. Integrated modeling process means abstraction of the target system. It means extracting the dominant physical law of the system based on the big data. In the case of cooking, it corresponds to making a recipe. It is important to represent more essential parts more easily in integrated modeling process. In intelligent control process, adaptive control is conducted based on the abstracted model and current information of the target system. In the case of cooking, it means to cook. Through these series of processes, intelligence of machines based on big data can be achieved. A machine with such intelligence can be said to be a machine with skilled skills like an experienced technician. In this research, the process of abstraction is regarded as the most important part in this series of flows. The calculation process (i.e., model abstraction) is made visible so that it can be extracted as formal intelligence that is understandable by humans. Since formalized knowledge is immutable, even if a skilled technician retires, it will not be lost. Also, since it is in a form that human can understand, there is no risk of losing knowledge. As described above, transparency of thinking process is lost when using neural network based methods such as

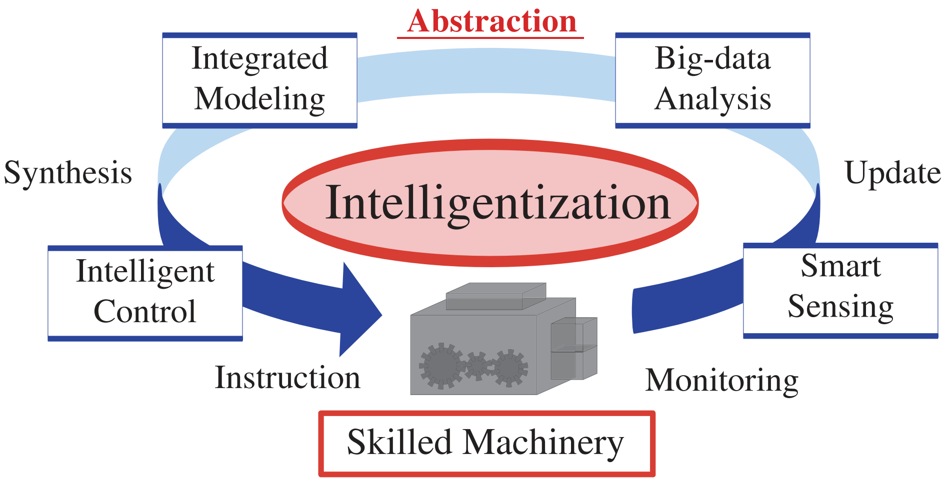

Fig. 1-5: Concept of intelligent machinery.

deep learning. Therefore, realization of abstraction is difficult. Conversely, model-based methods have high transparency in the thought process. However, it is completely restricted to a predetermined model, so abstraction with a high degree of freedom can not be performed. Also, modeling error increases for a system whose model is unknown.

As the method to overcome this trade-off, this research proposes an element description method (EDM) [47]. The EDM is one of optimization method. Because the EDM can estimate the system model and parameter simultaneously, it can be applied to unknown systems containing uncertainty, non-linearity, and time-varying elements. Moreover, since the identification result of the EDM is expressed as the combination of elements, the identification result is understandable. By using the EDM, the identification results can be used for the synthesis of the target system thanks to the understandability. In addition, the EDM can choose the kind of elements used for identification and size of an element matrix arbitrarily according to the required specification. When limited elements are prepared, an approximation can be conducted. Also, the resolution of the element matrix can be set arbitrarily. Moreover, identification results can be inherited in the next identification as initial population. The EDM is a optimization method based on genetic algorithm (GA) [48–50]. The GA has been widely researched in various field. Since the GA is a meta-heuristic method [51, 52], it is easy to apply it to various applications such as multi-objective optimization; on the contrary it is difficult to prove the validity analytically and optimality. Also, genetic programming (GP) [53–57] is researched as a meta-heuristic method. The GP had been applied to various fields such as classification of data [53], automated synthesis of analog electrical circuits [54], and synthesizing of a proportional-integral-differential (PID) controller [55]. The GP is one of the methods that does not need to determine the model in advance; however, it is inferior to the expressibility of the system and the readability of the result. As a method of solving the disadvantages, this dissertation proposes the EDM. Furthermore, it is possible to inherit, obtain and deepen the obtained formal knowledge. Therefore, sustained knowledge growth becomes possible. Moreover, the formal knowledge of the machine thus obtained can be obtained new knowledge by integrating with the machine adjacent to that opportunity. By repeating the integration upstream in this way, it is possible to extract aggregated formal knowledge for controlling the factory as a whole. Fig.1-4 shows the conceptual diagram of the integration of formal knowledge. This symbiosis of human and machine, the realization of human and machine are both revitalizing societies can be expected.

Here, explanations are given by taking packaging machinery [58] as an example about intelligentization of machinery and formalization of experienced engineers. Traditional packaging machinery was driven by a single AC induction motor; the movement of the working tips was produced by geometric conversion using mechanical components such as cams or links. The mechanical system using these components is shown in Fig. 1-2. In Fig. 1-2, the main axis is rotated at the angular velocity ω, and positions of working tips x_1, x_2, and x_3 are actuated by using cams and links. Since the system ensures the positional relationship between the working tips and other components, these machines were possible to produce with very fast speed. Moreover, the system matched the historical background in which the production speed was the most important. An example of machinery using mechanical systems is shown in Fig. 1-6. This machinery can wrap 1,200 sheets of plate gum per minute. This high-speed property is the advantage of mechanical systems. However, these types of machinery are designed on the premise that the target products are always supplied with constant quality. Therefore, the productivity may be remarkably deteriorated due to variations in products.

After that, the flexibility of the manufacturing machinery to achieve the high-mix low-volume production was required. A mechanical system can do fast motion; on the other hand, when the trajectory change of the tip is required, the system involves the replacement of mechanical parts. Consequently, it takes a long time for adapting to the change. By the development of the technologies, servo motors appeared next and it got attention as the means for overcoming the non-flexibility which was one of the problems of mechanical systems. Position-trajectory control by servo motors became popular since it can achieve an equivalent manner with the movement of mechanical systems. Nowadays, to achieve precise motion, motion control technologies has been developed more and more. In the case of the sys-

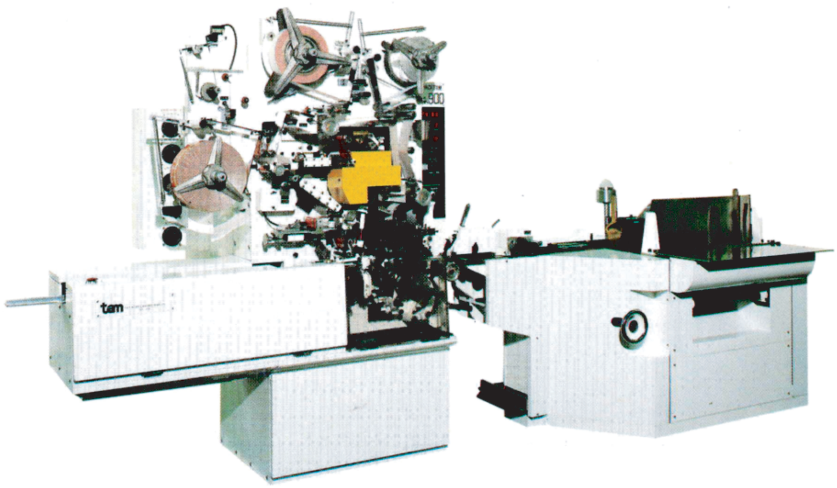

Fig. 1-6: Plate gum wrapping machinery (Tokyo automatic machinery works, Ltd.).

tem of position-trajectory control, the trajectory can be changed easily by only setting the value of data register; this control system has the flexibility which mechanical systems does not have. As an example of packaging machinery using servo motors, vertical fill form seal machine is introduced. Fig. 1-7 refers to the vertical fill form seal machine. This machinery consists of a film reel part, tension bar part, former part, vertical seal part, feed belt part, and horizontal seal part. A plurality of servo motors are used as the power of the machine. This machinery can unwind the sheet of film wound on the reel, and package the contents at the same time while molding the shape of the bag. This type of packaging machinery is called a pillow packaging machinery because packaged products are shaped like pillows. There are various types of pillow packaging, such as self-standing, zipper attached, one with a series of several, with punch holes for hanging. Since it is necessary to correspond to these plural kinds of packaging forms with one packaging machinery as many as possible, various operation changes are required depending on the kind. This motion change can be achieved by changing the locus commanded to the servo motors. However, this system is difficult to control the force in contact with the object because servo motors are controlled by position (or velocity) control. Position control systems are operated regardless of the state of contacting environment; this may result in applying too much force on the object and breaking it. Therefore, it is difficult to adapt to subtle changes in film and products. Actually, depending on the production lot of the film, problems may arise such as film meandering or shift of the pattern of the bag. To over come this problem, the force control by servo motors may become one of the solutions. In this dissertation, force-position hybrid control based on a motion-copying system [22, 23] is introduced. Since

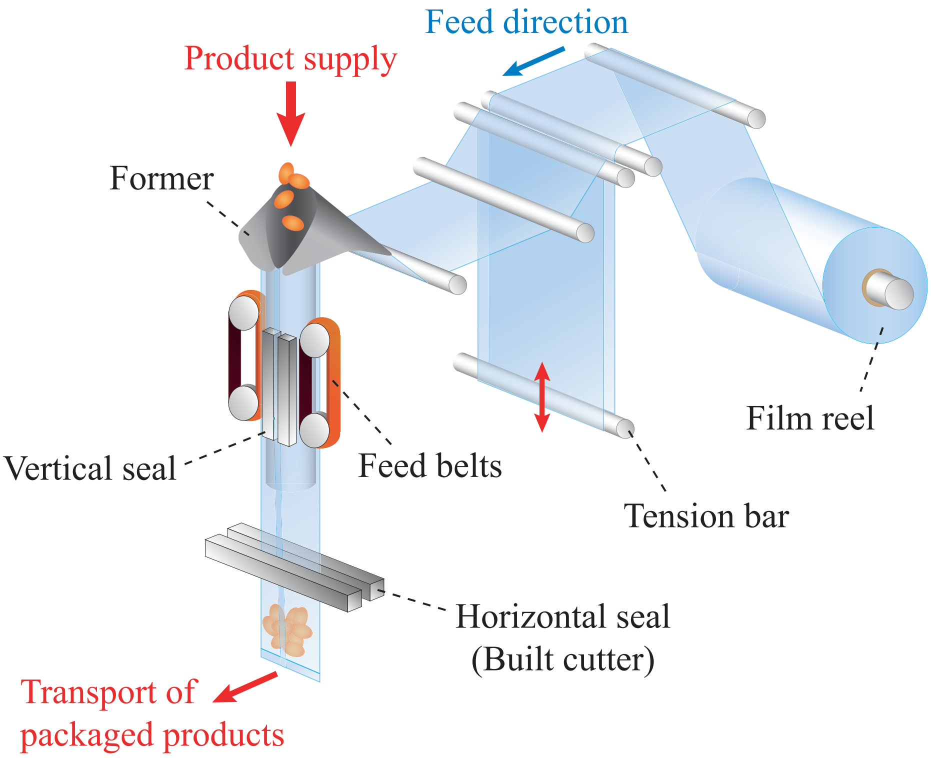

Fig. 1-7: Overview of vertical fill form seal machine.

force control is position indefinite, considering both contact and free motion, a hybrid control system of position and force is desirable. A method to adapt to position variation, which is one of the problems in hybrid control of position and force, is proposed. In addition, packaging machinery has been designed and adjusted for many years based on empirical rules of experienced technicians. In order to satisfy demands for labor saving due to the lack of labor population in recent years, intelligence of machines has been required. This dissertation aims not only to achieve the intelligence of experienced technicians by machinery, but also to abstract them. As a method to achieve it, the EDM is utilized. Here, abstraction is defined as extracting important mathematical expressions in a certain system. Also, there is a possibility that an important rule such as motion equations can be extracted from big data by the EDM. In addition to using abstracted knowledge, it enables inheritance to next generation and inheritance to upper layers and other systems, and achieves the operation of intelligence. Moreover, with the readability that humans can understand, the machine responds within the conditions set by humans, and according to the answers, humans can think about the next setting, make it possible to perform interactive learning.

1.3 Chapter Organization of This Dissertation

Fig. 1-8 shows the chapter organization of this dissertation. In Chapter 2, the EDM is proposed and its basic principle is described. Firstly in Chapter 2, the basic principle is explained. Also, advanced application methods are described. After that, case studies are shown. In the case 1, a first lag system is abstracted by the EDM as a simple example. The case 2 introduces the automatic abstraction method of a compensator for a reaction force observer (RFOB) [59] by the EDM. In addition, the automatic designed of the RFOB is applied to a leak detect machine [60]. In Chapter 3, automatic control design methods are described. At first, an automatic controller design method for a multi-mass resonant system is introduced. Then, angular acceleration control of automatic machinery is described [61]. Angular acceleration control is an important fundamental technology in this dissertation. Since most modern machinery use motion networks for motor control, communication delay occurs. In this Chapter, the effect of this communication delay on an angular acceleration control system is considered. Then, an environmental abstraction method for force control is shown in the case 3. In Chapter 4, automatic generation of command trajectory using the EDM is described. Also, high-precision interpolation using a clothoid curve is proposed [62]. For the intelligence of automatic machinery, it is important not only to abstract knowledge, but also to extract skills. Thereby, a skill extraction method based on the motion-copying system is described in Chapter 5. The motion-copying system is an innovative technology that can extract human's skills. However, there is a problem that stored motion can not be successfully reproduced if an external environment is different between storage and reproduction. Time adaptive control is proposed as the method to overcome this problem [30, 31]. Firstly, it is verified for a single degree of freedom (SDOF) system, and then it is expanded to a multiple degrees of freedom (MDOF) system. In Chapter 6, knowledge abstraction method based on the EDM is explained. The extraction of intelligence is verified by a powder filling machine, because it is being adjusted based on the experience rule of experienced engineers. The EDM abstracts knowledge such as experienced technicians as mathematical expressions. Finally, Chapter 7 concludes this dissertation.

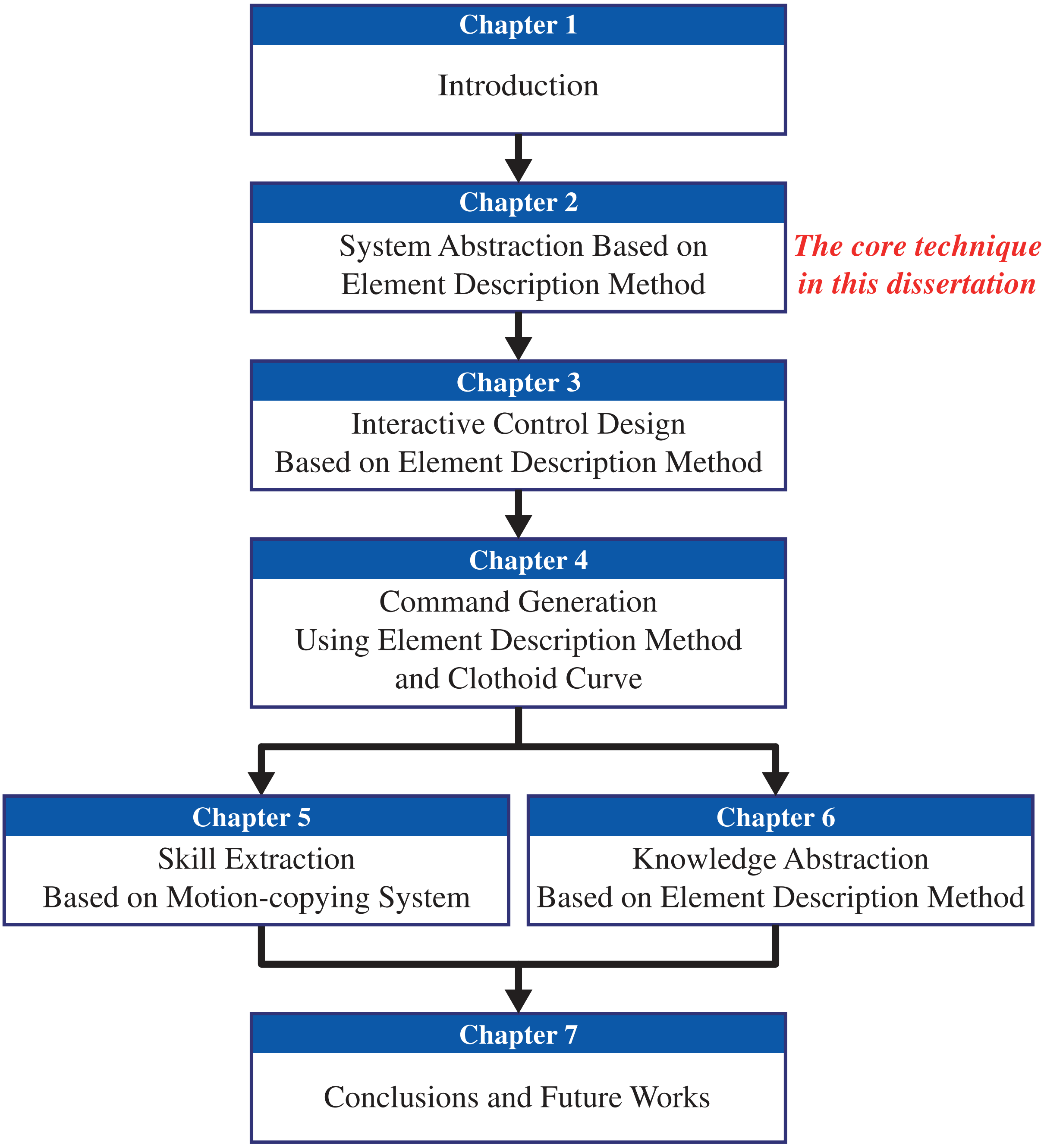

Fig. 1-8: Chapters constructed in this dissertation.

Chapter 2

System Abstraction Based on Element Description Method

2.1 Introduction of Chapter 2

Chapter 2 describes the fundamental principle of the EDM which is the core part of this dissertation. The EDM can be applied to various purposes such as system abstraction, interactive control design, automatic command generation. Chapter 2 introduces the abstraction of systems by EDM. In this dissertation, “abstraction” is defined as extracting the structure and parameters of the physical equations of the system simultaneously. Generally, there are two methods to identify the system using time-series data: one is model-based methods, and the other is data-based methods. Model-based methods are identification methods based on regression equation such as an auto regressive with exogenous (ARX) model and an autoregressive moving average (ARMA) model [37–40]. These type of methods have a merit that the physical meaning of identification results is clear because it is identified based on a human-determined model. However, it is difficult to apply it to a system whose model is unknown because the identification result is restricted by a model decided in advance. Therefore, it is difficult to abstract a system by model-based method. Moreover, the model-based method is generally represented by linear models, so it is difficult to apply them to nonlinear models. In recent years, model-based methods extended to nonlinearities based on Wiener and Hammerstein have been studied [63, 64]. These methods can be applied to nonlinear systems. However, because it is also based on a model, it is difficult to apply it to an unknown system, and it is difficult to abstract a system. The data-based methods are identification methods based

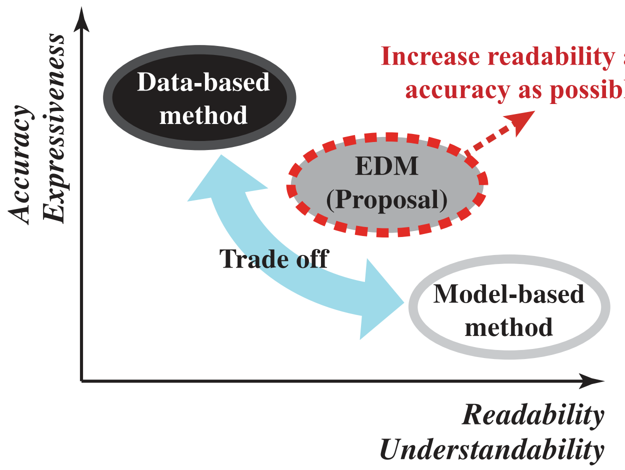

Fig. 2-1: Positioning of the EDM.

on machine learning such as a neural network [45, 46]. An advantage of these type of methods is that it is not necessary to determine the model in advance; therefore, it can be applied to unknown systems with high expression. However, it is difficult to interpret the physical meaning of the identification results. Therefore, it is difficult to abstract a system by data-based method as well as model based method. For example, in the case of a neural network, it is difficult to interpret the physical meaning because the system is represented by neuron model and enumeration of weights. Hence, even if good input/output characteristics are obtained, the system cannot be abstracted. In other words, there is a trade-off relationship between readability and expressibility in these two methods. On the contrary, the EDM of the proposed method does not need to decide a model in advance; therefore it has high expressibility In addition, it is also possible to interpret the physical meaning of the result because it is represented by a combination of prepared models. By using the EDM, since automatic model generation and parameter fitting can be performed simultaneously, system abstraction can be achieved. The positioning of the EDM is depicted in Fig. 2-1. Then, a guideline for proper use are described of the three methods: model-based methods, data-based methods, and the EDM. When an accurate model of a target system is known, model-based methods should be used. When an accurate model of a target system is unknown, data-based methods or the EDM should be used. Moreover, when it is sufficient to obtain only good input/output characteristics, data-based methods should be used. On the contrary, the EDM is should be used when not only achieving the input/output characteristics, but also abstracting the physical model of target system is required.

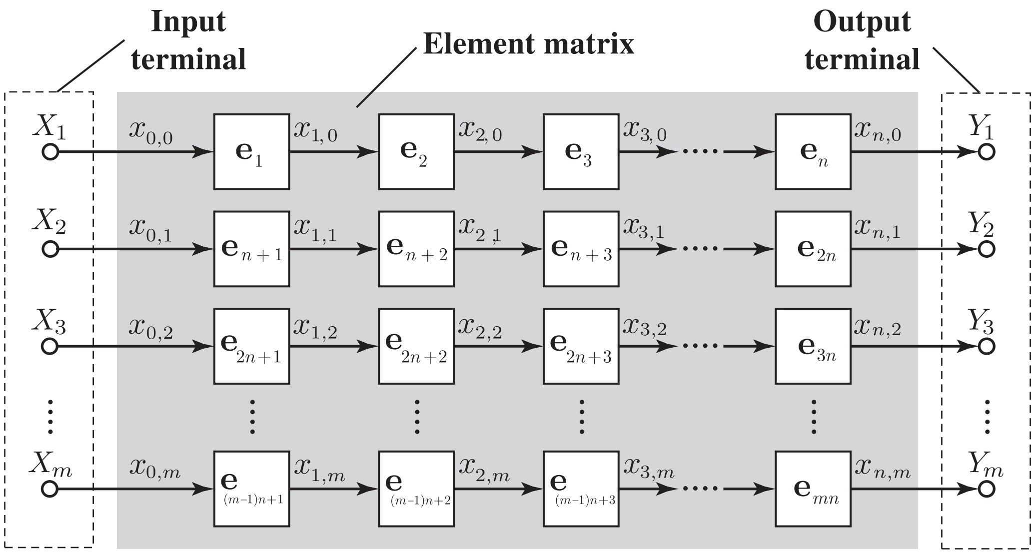

Fig. 2-2: An unidirectional element matrix used for the EDM.

2.2 Hierarchical Abstraction Using Unidirectional Element Matrix

2.2.1 Unidirectional Element Matrix

The EDM can be roughly divided into two types: hierarchical abstraction based on an unidirectional element matrix and overall abstraction based on a multidirectional element matrix. Firstly, the hierarchical abstraction using an unidirectional element matrix is introduced. In the EDM, a system is expressed by an element matrix defined as a combination of simple elements. Fig. 2-2 shows the structure of the unidirectional element matrix for the hierarchical abstraction. In Fig. 2-14, $\mathbf{e}$ and x express the element and signal flow of horizontal directions, respectively. The subscripts stand for the address. The gray area in Fig. 2-2 stands for the element matrix. $n \in \mathbb{N}$ and $m \in \mathbb{N}$ denote the row size of the element matrix and column size of the element matrix, respectively. X and Y stand for the input signals for the system and output signals from the system, respectively. The subscripts denote row and column numbers. Input and output terminals stand for the interface of the element matrix. The input signal is input via the input terminal, and output signal is outputted via the output terminal. Signal definitions of input and output can be decided arbitrarily according to the purpose. As input and output data, usually discrete time data are given. One time series data is associated with one terminal. The calculation is conducted sequentially from the left top to the right bottom in the element matrix. The computation sequence equals to the subscripts of $\mathbf{e}$ (i.e., the address of the element). The output value of each element is calculated from the

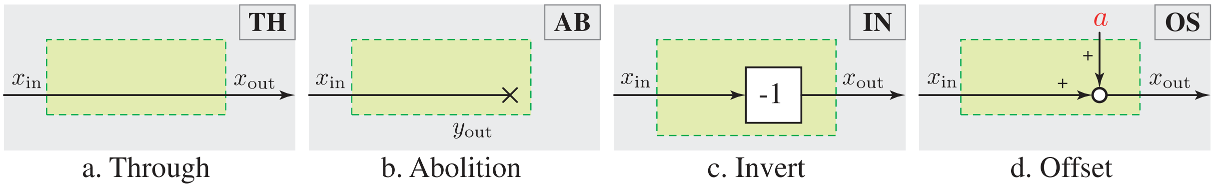

Fig. 2-3: Basic elements for unidirectional element matrix.

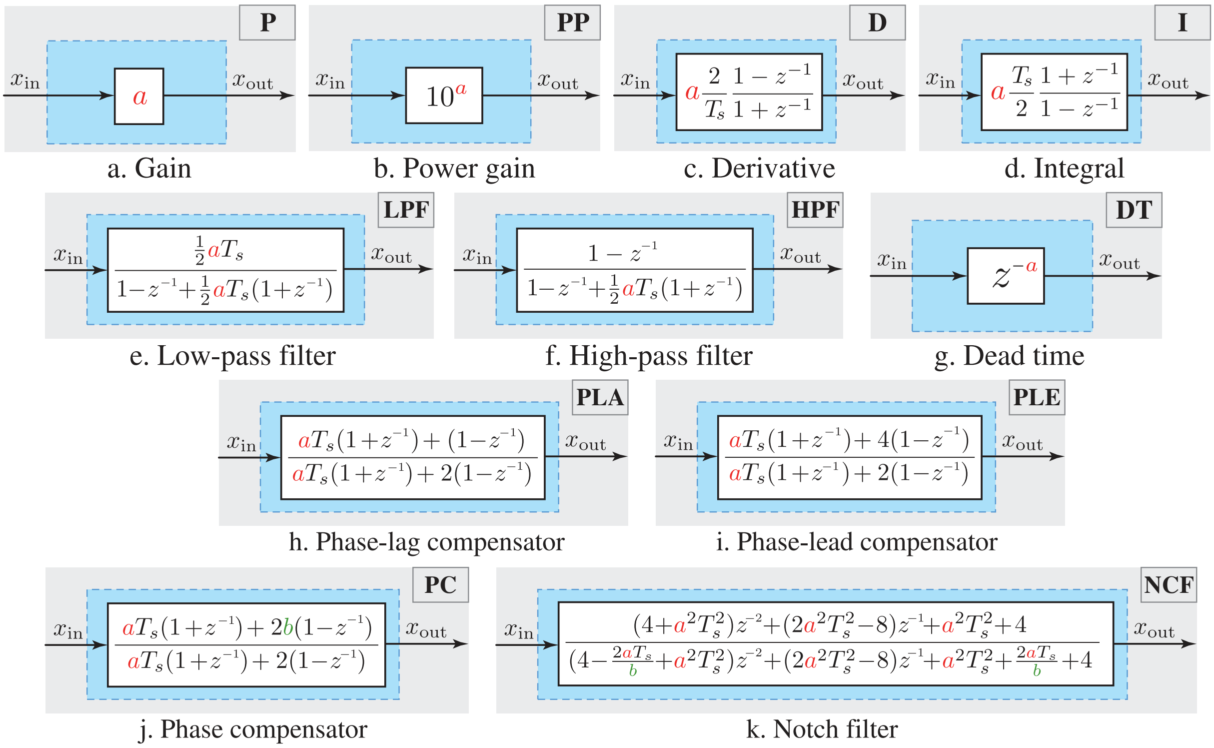

Fig. 2-4: Calculation elements for unidirectional element matrix.

input value as follows:

$$x_{i+1,j} = f_{i,j}(x_{i,j}). \tag{2.1}$$

Each element of the unidirectional element matrix is expressed as a single-input and single-output system. $f(\bullet)$ stands for the calculation function that prescribes input / output relation. The subscripts i and j refer to the row and column of elements, respectively. The output value of each element is used for the adjacent element as an input value. The type of the calculation functions $f_{i,j}$ are automatically selected from the prepared elements. Examples of the elements are shown in Figs. 2-3 to 2-5. Fig. 2-3 expresses basic elements to construct the element matrix structure. The basic elements define the flow of the signal.

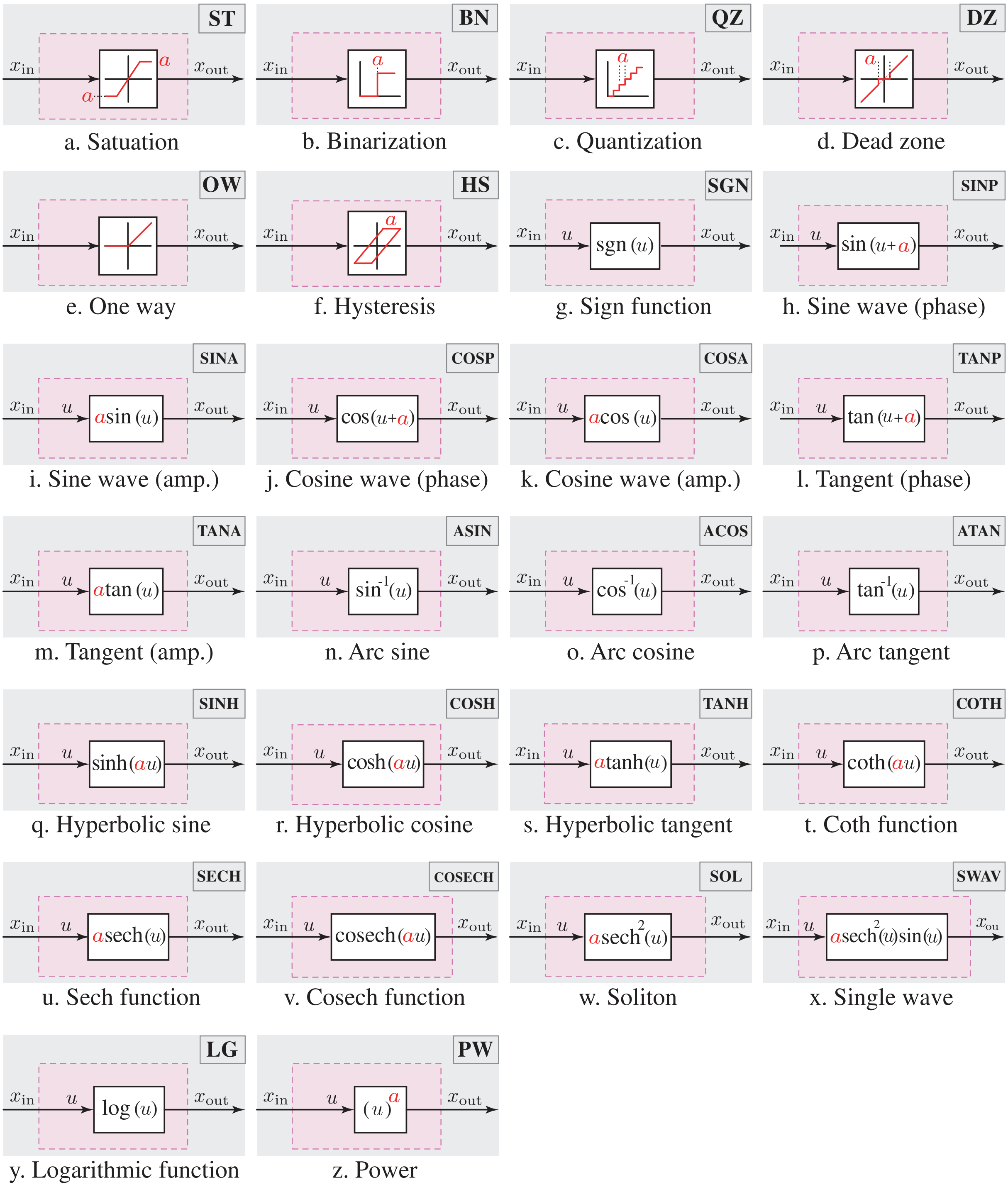

Fig. 2-5: Nonlinear function elements for unidirectional element matrix.

Algorithm 1 Calculation procedure of the unidirectional element matrix.

```
for j = 0 to m − 1 do
  x_{0,j} ⇐ X_j
end for
for j = 0 to m − 1 do
  for i = 0 to n − 1 do
    x_{i+1,j} ⇐ x_{i+1,j} = f_{i,j}(x_{i,j}).
  end for
end for
for j = 0 to m − 1 do
  Y_j ⇐ x_{n,j}
end for
```

Fig. 2-4 depicts the calculation elements. In Fig. 2-4, a and b refer to parameters used for calculation of the element. $z^{-\bullet}$ stands for shift operator. Fig. 2-5 stands for the nonlinear function elements. It is easy to apply nonlinear functions defining them as an element. Moreover, various nonlinear elements can be represented. The calculation algorithm is shown in Algorithm 1. As an example, a calculation method of the first-order low-pass filter element (**LPF**) is explained. Firstly, the transfer function is discretized by bilinear transformation as

$$Y(s) = \frac{a_{\mathrm{lpf}}}{s + a_{\mathrm{lpf}}} X(s), \tag{2.2}$$

$$s \leftarrow \frac{2}{T_{\mathrm{s}}} \frac{1 - z^{-1}}{1 + z^{-1}}, \tag{2.3}$$

$$y[q] = \frac{a_{\mathrm{lpf}} T_{\mathrm{s}}}{2 + a_{\mathrm{lpf}} T_{\mathrm{s}}} \{x[q] + x[q-1]\} + \frac{2 - a_{\mathrm{lpf}} T_{\mathrm{s}}}{2 + a_{\mathrm{lpf}} T_{\mathrm{s}}} y[q-1], \tag{2.4}$$

where a_{lpf}, T_{s}, and $q \in \mathbb{N}$ stand for the cut-off frequency of the low-pass filter, sampling time, and the sampling number of discrete time signal, respectively. The above equation is applied as a function to the actual discrete time signal. From the above, the calculation of the element is as follows:

$$x_{i+1,j}[q] = \frac{a_{\mathrm{lpf}} T_{\mathrm{s}}}{2 + a_{\mathrm{lpf}} T_{\mathrm{s}}} \Big[\big\{ x_{i,j}[q] \big\} + \big\{ x_{i,j}[q-1] \big\} \Big] + \frac{2 - a_{\mathrm{lpf}} T_{\mathrm{s}}}{2 + a_{\mathrm{lpf}} T_{\mathrm{s}}} x_{i+1,j}[q-1]. \tag{2.5}$$

2.2.2 Chromosome Structure

The calculation of each element is conducted by a chromosome vector $\mathbf{e_k}$ expressed as

$$\mathbf{e}_k = \big[c_k, p_k \big]^T, \tag{2.6}$$

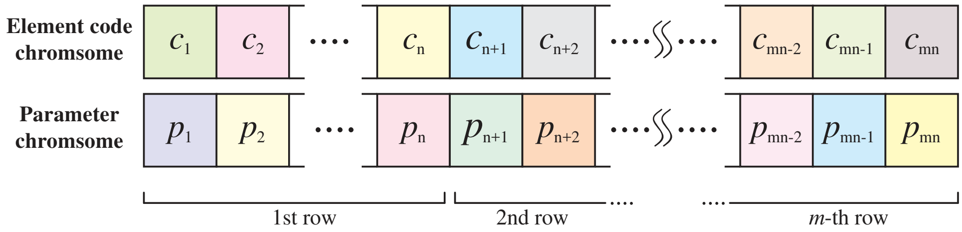

Fig. 2-6: The chromosome structure for the EDM.

where c_k and p_k refer to the element code and the element parameter, respectively. The subscript k denotes the address of the element calculated by

$$k = jn + i. \tag{2.7}$$

In the EDM, the element matrix is optimized by the GA [48–50]. Fig. 2-6 stands for the chromosome structure used for the EDM. There are two chromosomes; one is an element code chromosome, the other is a parameter chromosome. The element chromosome denotes the kind of elements. The parameter chromosome stands for the numerical value for element's calculation. This type of chromosome is needed because some elements in Figs. 2-3 to 2-5 use the parameters for their calculation. The parameter of each element can be designed within the arbitrary range. Also, the number of the parameter in each element can be increased arbitrary by modifying the chromosome structure.

As an example, the parameters of the first-order low-pass filter element $a_{\rm lpf}$ in (2.2) is calculated as follows:

$$a_{\rm lpf} = (p_{\rm lpf}^{\rm max} - p_{\rm lpf}^{\rm min})\, p_{\rm k} + p_{\rm lpf}^{\rm min}, \tag{2.8}$$

where $p_{\rm lpf}^{\rm max}$, $p_{\rm lpf}^{\rm min}$, and $p_{\rm k}$ refer to the maximum value used for the low-pass filter element, the minimum value used for the low-pass filter element, and the random value ranged from 0 to 1, respectively. $p_{\rm lpf}^{\rm max}$ and $p_{\rm lpf}^{\rm min}$ can be designed arbitrarily according to the kind of elements. Moreover, when the element affects the calculation logarithmically, $a_{\rm lpf}$ is set logarithmically as

$$a_{\rm lpf} = 10^{(p_{\rm lpf}^{\rm max} - p_{\rm lpf}^{\rm min})\, p_{\rm k} + p_{\rm lpf}^{\rm min}}. \tag{2.9}$$

In addition, the phase compensator element (**PC**) has two parameters. These parameters are calculated from the parameter chromosome by dividing the parameter into upper and lower bytes.

Algorithm 2 Algorithm of off-line abstraction by the EDM.

```
Initialization ( )
Data Get ( )
while age ≤ N_max × rep do
    for cntr1 = 1 to I_num do
        while t < tN_sum do
            Matrix Calculation
            F ⇐ F + f(t)
        end while
        F [cntr1] = Fit
    end for
    Ranking ( )
    Selection ( )
    Cross Over ( )
    Increase/decrease Parameter ( )
    Mutation ( )
    Make New Age
    if N_max × rep ≤ age then
        if continue = "Yes" then
            rep ⇐ rep +1
        end if
    end if
end while
```

2.2.3 Optimization Procedure of Element Matrix

The element matrix is renewed to minimize or maximize a fitness value. The fitness value is calculated by a fitness function as follows:

$$\Gamma = \frac{1}{N_{\text{sum}}} \sum_{q=1}^{N_{\text{sum}}} \sqrt{\tilde{y}[q]^2}, \tag{2.10}$$

$$\tilde{y}[q] = y[q] - \hat{y}[q], \tag{2.11}$$

where Γ and N_{sum} express the fitness value and number of time-series data, respectively. The superscripts $\tilde{\bullet}$ and $\hat{\bullet}$ show the error value and estimated value, respectively. In other words, $y[q]$ stands for the real value and $\hat{y}[q]$ refers to the calculated value by the element matrix. The fitness function is designed arbitrarily according to the purpose. The algorithm of off-line abstraction by the EDM is shown in Algorithm 2. In Algorithm 2, $N_{\max}$ and I_{num} are the number of repetitions of one trial and number of individuals, respectively. Time-series data of input and output of a system are used for off-line abstraction. In the initialization procedure, first individuals are generated. The number of individual I_{num} can be set

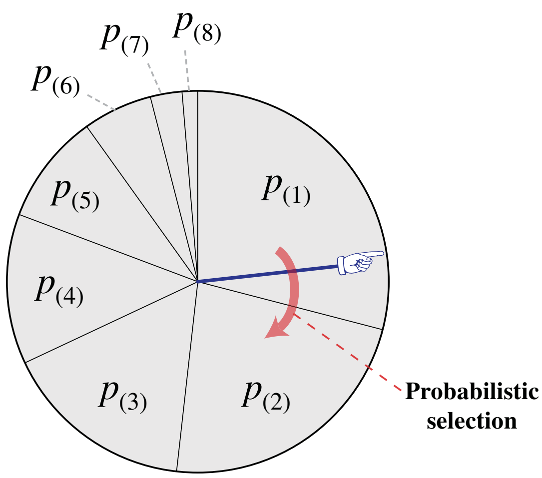

Fig. 2-7: The probability of surviving.

arbitrarily. When there is advanced knowledge about a target system, the code and parameter of the first individual are set by manual input. On the contrary, the code and parameter of the first individual are set at random when a target system is unknown. It is also possible to combine the two setting methods. In the data-get procedure, time-series data for abstraction are obtained. The time-series data consist of input and output of a target system. In the matrix-calculation procedure, Algorithm 3 is conducted. In the ranking procedure, each individual is ranked based on each fitness value. In the selection procedure, individuals for next generation are stochastically selected. Individuals with better fitness value are set to have a higher probability of surviving in the next generation. The rate of the probability can be arbitrarily determined. For example, the probability function is calculated as

$$p_{(n)} = \frac{I_{\text{num}} - n}{I_{\text{num}}!}, \tag{2.12}$$

where $p_{(n)}$ means the survival probability, and the subscripts express the number of individual. Fig. 2-7 stands for the overview of the survival probability when the number of individuals is set to 8. When the value of p is large, the probability of surviving to the next generation becomes large. In addition, by using the "elite preservation strategy" to keep the best individuals as they are in the next generation as it is, the next generation will not become worse than the current generation. In Fig. 2-7, as described above, in the selection process, individuals surviving the next generation are selected and discarded. Then, the crossover procedure is conducted. In the crossover procedure, the occurrence of crossover processing is stochastically determined whether or not crossover occurs based on the crossover

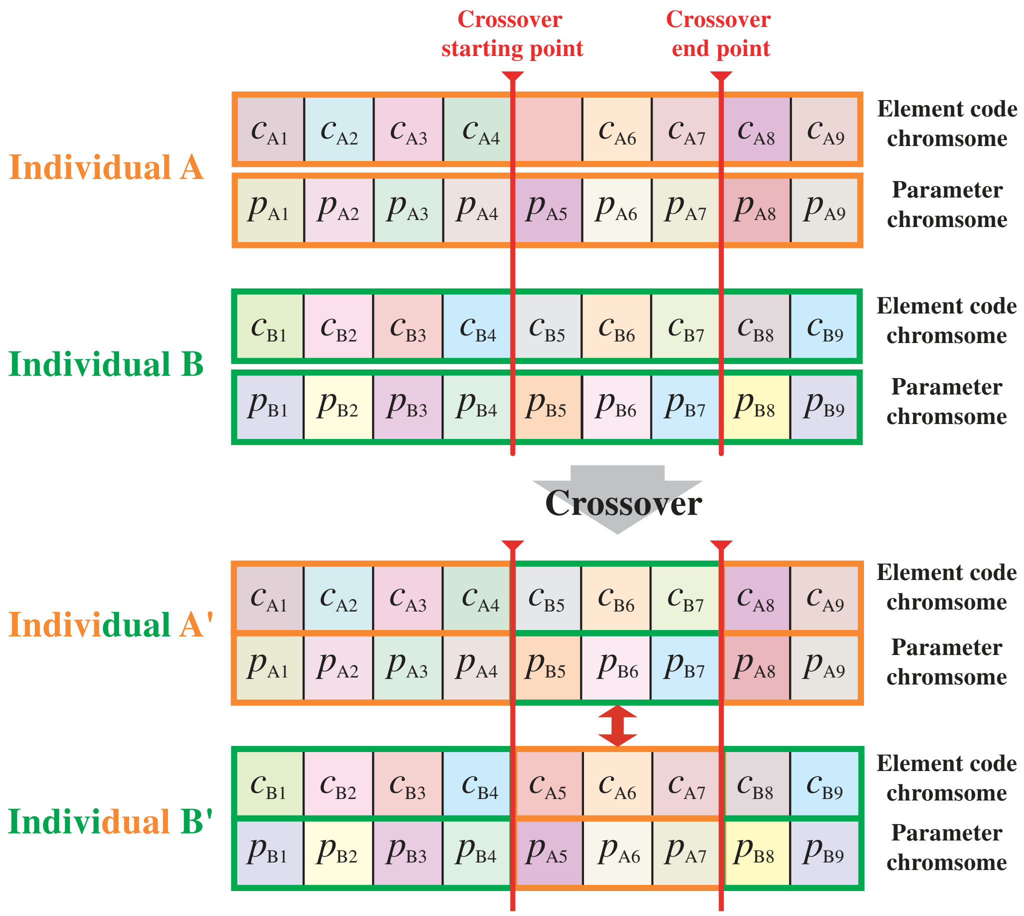

Fig. 2-8: The crossover procedure.

rate. When the crossover occurs, the target individuals for crossover are selected. Moreover, the starting and ending points of the crossover stochastically determined, probabilistically. The overview of the crossover procedure is shown in Fig. 2-8. Chromosomes of excellent individuals are replaced by crossover processing, and there is a possibility that more excellent individuals may be expressed. In the increase/decrease parameter procedure, parameters of randomly chosen chromosomes are increased or decreased. The chromosome selection to increase/decrease the parameters is conducted based on parameter increase/decrease rate η_{id}. This resembles a gradient descent method used for method such as neural network. The point of this method that differs from the gradient descent method used for methods such as neural network is not based on partial differentiation; however, parameters are increased or decreased by trial-and-error in a point as with the gradient descent method. Therefore, this method may converge to a local minimum. A valid process to avoid this is a mutation. In the mutation procedure, there are two

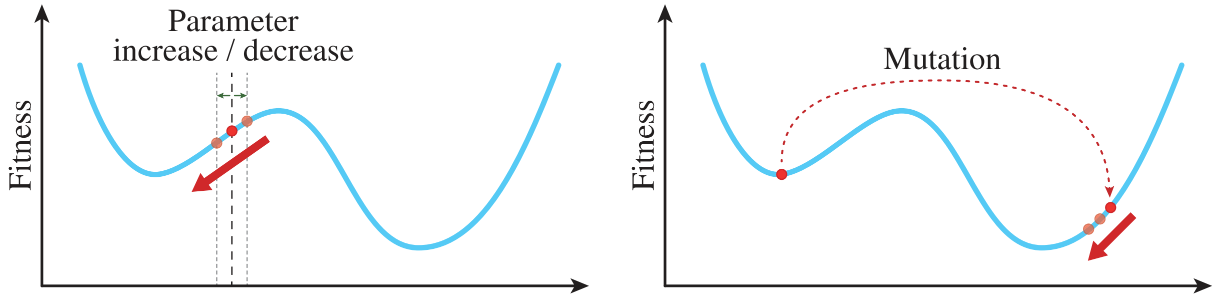

a. Parameter increase / decrease process. b. Mutation process.

Fig. 2-9: Overview of increase/decrease parameter and mutation process.

types of processing; one is element mutation and the other is individual mutation. The element mutation means the mutation of the element code and element parameter. Based on the set of mutation rate of element code $\eta^{\mathrm{c}}_{\mathrm{mut}}$, elements are randomly rewritten with random numbers. In Similarly, parameters are randomly rewritten with random numbers based on the set of mutation rate of parameter $\eta^{\mathrm{p}}_{\mathrm{mut}}$. Mutation rate of the element code and element parameter can be set independently. The individual mutation means mutation of an individual. Based on the set of mutation rate of individual $\eta^{\mathrm{i}}_{\mathrm{mut}}$, individuals are entirely rewritten with random numbers. The overviews of increase/decrease parameter and mutation process are depicted in Fig. 2-9. From the viewpoint that the change in the type of the element greatly changes the result and the change in the parameter finely adjusts the result, it is desirable to set the mutation rate as follows

$$\eta^{\mathrm{i}}_{\mathrm{mut}} < \eta^{\mathrm{c}}_{\mathrm{mut}} < \eta^{\mathrm{p}}_{\mathrm{mut}} < \eta_{\mathrm{id}}. \tag{2.13}$$

By increasing the probability of mutation when the fitness value become constant, the possibility of falling into a more local solution can be reduced. Through these processes, the individuals remaining in the next generation are determined. The optimization is achieved by repeating the above process.

2.2.4 Hierarchical Abstraction Using Unidirectional Element Matrix

As one of the advantages of the EDM, the number of elements in the element matrix can be arbitrarily changed, and the result of the abstraction can be given as the initial value of the next abstraction. By utilizing this advantage, it is possible to hierarchically abstract the elements. In the unidirectional element matrix, each line is independent and the physical meaning becomes clear because there is no vertical connection of signals. The conceptual diagram of the hierarchical abstraction is depicted in Fig. 2-

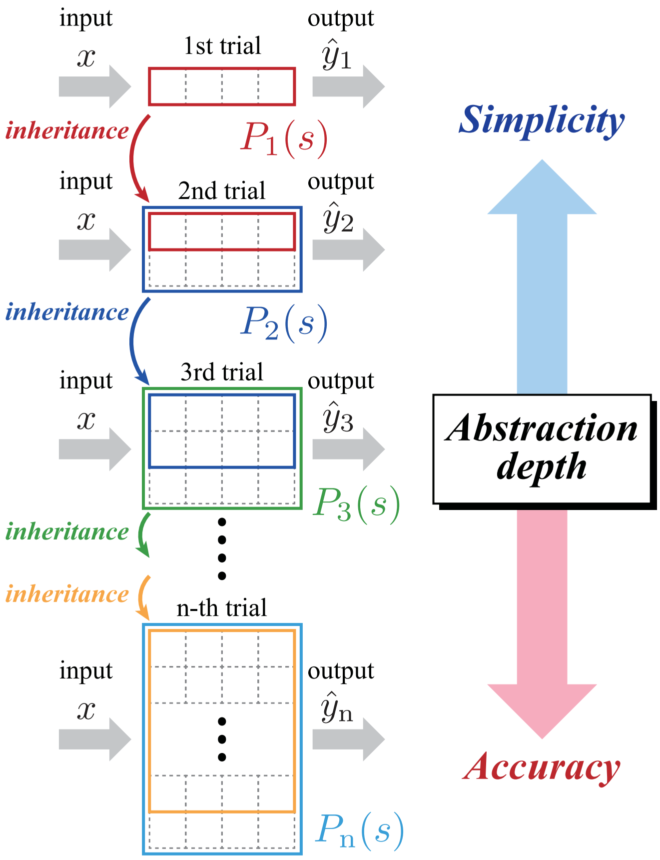

Fig. 2-10: Conceptual diagram of the hierarchical abstraction.

10. When performing hierarchical abstraction, the output of the element matrix uses the sum of the values output from each row. In the first step, the first line extracts the most important elements for a system because it expresses a system more accurately with few elements. In the next step, the result extracted in the first step (line 1) is inherited and the next line is added. This will extract the next most important elements. If retention of inherited results from the previous step is desired, it is designed to update only the added rows. If it is desired to update the results inherited from the previous step taking into account the mutual interaction, it is also possible to update the inherited rows together. It is also possible to fix the structure of the inherited row and update only the parameters. As a result of repeating such hierarchical abstraction, the abstracted systems are arranged in descending order of importance. Therefore, the required accuracy can be aborted where the required accuracy is achieved, and it is possible to extract the necessary and sufficient model. As the abstraction depth increases, accuracy decreases while simplicity declines.

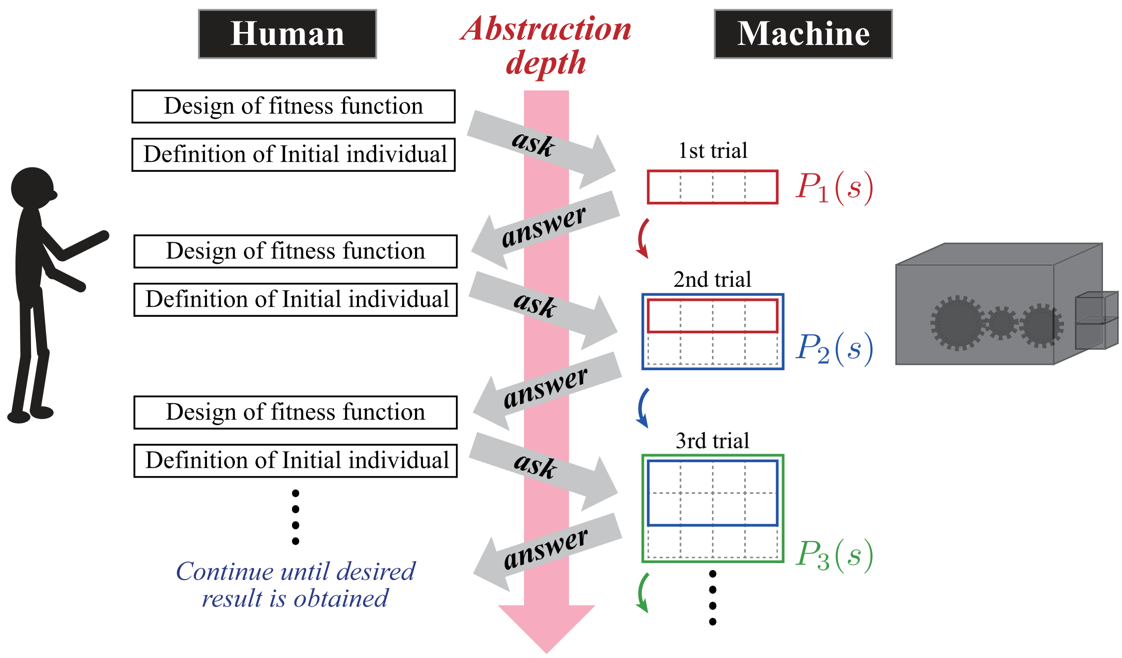

Fig. 2-11: Overview of the interactive system designing based on the EDM.

2.2.5 Interactive Design Based on the EDM

It is possible to design a system interactively between human and machine by taking the advantage of the characteristics of the EDM that the determination of the model is unnecessary and the physical meaning of the obtained mathematical expression is possible. Fig. 2-11 shows the overview of the interaction system designing based on the EDM. In consideration of various possibilities, human can design the EDM. If human has prior knowledge of the target system, human can define its prior knowledge as an initial individual of the GA. If designer wants to completely based on a predetermined model structure, code chromosomes are fixed to those set by designer and only parameters are fitted. If designer wishes to partially based on a predetermined model structure, a part of the code chromosome is fixed to the one set by designer and optimization is executed. By using this strategy, the results become expansion of predetermined model structure designed by designer. By intentionally designing the window function, it is possible to improve by targeting a specific area of the target input/output data. For example, in the first layer, the weight of the area of the steady-state response is increased in order to eliminate the stationary error, and in the second layer, the weight of the area of the transient response is increased in order to improve the transient response. As a result, learning intended by designer can be performed. If the elements that would be needed to improve accuracy become clearly understood, efficient optimization can

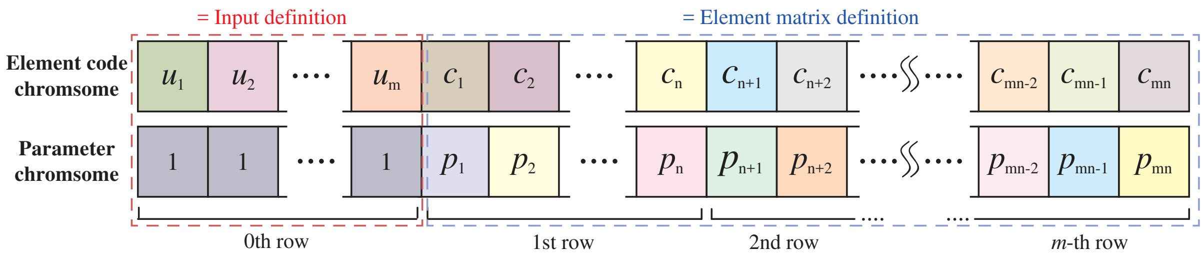

Fig. 2-12: The chromosome structure for the EDM with auto input selection.

be conducted by mixing that element into the chromosome by human at the time of generational change. If only specific elements such as dead time elements are prepared, the system is represented only by the elements decided by designer and the implementation is simplified. Through the interactive design, machine learning is achieved that enables effective use of human knowledge. Moreover, synergistic effect of human knowledge and machine's computing power can be expected.

2.2.6 Automatic Selection of Input Information

Furthermore, when a parameter with strong relevance to an evaluation function is unknown, automatic selection by the EDM becomes possible by including parameters in the chromosome. Fig. 2-12 depicts the chromosome structure including the automatic input selection function. In this case, the beginning part of the code chromosome is used as a parameter selection chromosome. In addition, the parameter chromosome is not used, and it is designed as a fixed value. Parameter chromosomes can also be designed as weights for each parameter. By using automatically selecting input information, only parameters with strong correlation with output are automatically extracted. The number of extracted parameters can be arbitrarily set by the number of prepared chromosomes.

2.2.7 Design of Fitness Function

In addition, a window function $\Lambda(q, l)$ can be designed as follows:

$$\Gamma = \frac{1}{N_{\text{sum}}} \sum_{q=1}^{N_{\text{sum}}} \sqrt{\tilde{y}[q]^2 \cdot \Lambda(q, l)}, \tag{2.14}$$

where $l \in \mathbb{N}$ refers to the number of generational changes. By designing the window function, it becomes possible to perform optimization that tends to converge to a local minimum and optimization that emphasizes the response of a specific part. Examples of window function design are shown in Fig. 2-13.

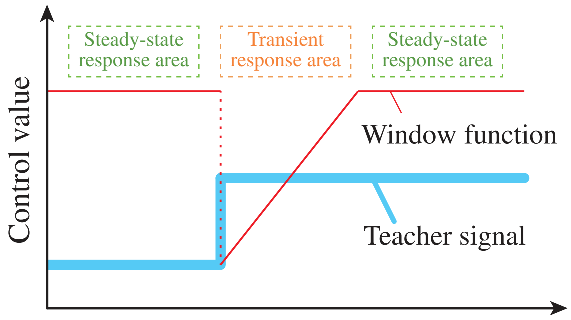

a. Time dependent window design.

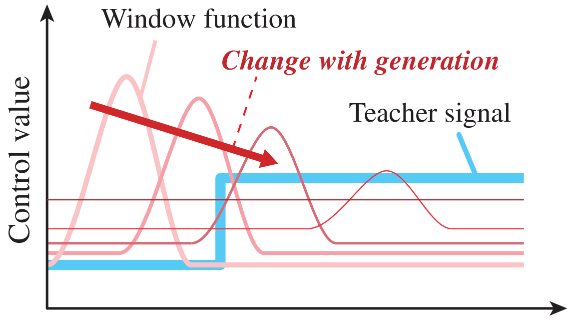

b. Generation dependent window design.

Fig. 2-13: Overview of window function design.

Fig. 2-13a shows the example of a time-dependent window function. As shown in Fig. 2-13a, the weight can be designed based on the importance of a response area. By using the window function, it becomes possible to optimize with emphasis on a specific area. Also, the window function can change by generation. Fig. 2-13b shows the example of a generation-dependent window function. The window function is designed as the function of generation l. However, there is a possibility that the fitness value does not converge to a specific result when the environment (i.e., the fitness function and the window function) continues to change. Therefore, when a target system does not change, it is desirable that the window function is finally fixed. Even using the methods described above, there is a possibility of converging to stagnant local minimum. The reason for this is that if there is only one environment, only one gene that is strong in that environment remains, and the species innovation depends only on mutation. Ideally, it should evolve by crossing strong individuals surviving in various environments. Therefore, apart from the environment used for final evaluation, prepare multiple environments so that strong individuals are always left in each environment. This enables evolution that is rich in diversity and reduces the probability of stagnating at a local minimum. There are various methods such as preparing a plurality of different experimental results, dividing one experimental result into a plurality of sections, partial changing the evaluation function.

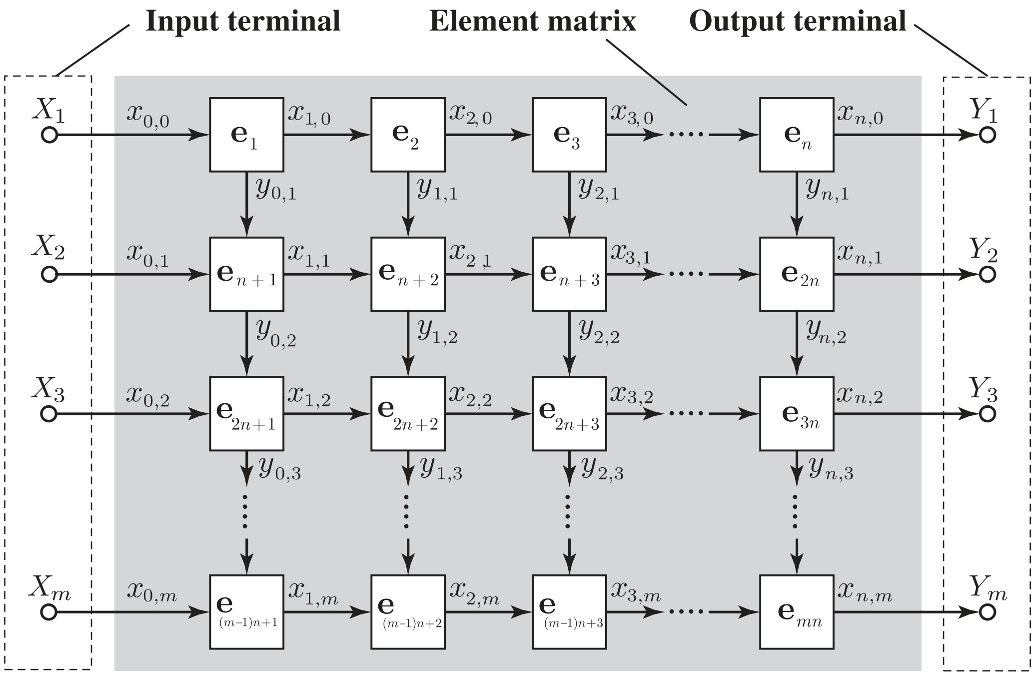

Fig. 2-14: A multidirectional element matrix used for the EDM.

2.3 Overall Abstraction Using Multidirectional Element Matrix

2.3.1 Multidirectional Element Matrix

Signal definitions of input and output can be decided arbitrarily according to the purpose. Then, overall abstraction using a multidirectional element matrix by the EDM is introduced. Fig. 2-14 shows the structure of the multidirectional element matrix. In Fig. 2-14, $\mathbf{e}$, x, and y express the element, signal flow of horizontal and vertical directions, respectively. The kind of elements and the matrix size can be decided arbitrarily according to the purpose. When the size of the element matrix is set large, more correct solution can be derived; however the result becomes complicated. On the contrary, when the size of the element matrix is set small, simple result is abstracted. X and Y stand for the input signals for the system and output signals from the system, respectively. The subscript denotes row numbers. In the same way as the unidirectional element matrix, the calculation is conducted sequentially from the left top to the right bottom in the element matrix. The computation sequence equals to the subscripts of $\mathbf{e}$ (i.e., the address of the element). The output value of each element is calculated from the input value as follows:

$$\begin{bmatrix} x_{i+1,j} \\ y_{i,j+1} \end{bmatrix} = \begin{bmatrix} f_{(x)i,j}(x_{i,j}, y_{i,j}) \\ f_{(y)i,j}(x_{i,j}, y_{i,j}) \end{bmatrix}. \tag{2.15}$$

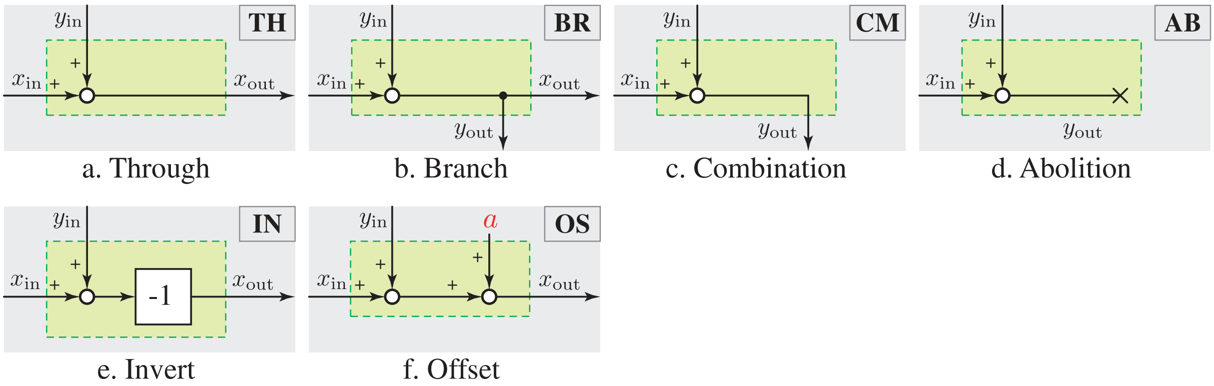

Fig. 2-15: Basic elements for multidirectional element matrix.

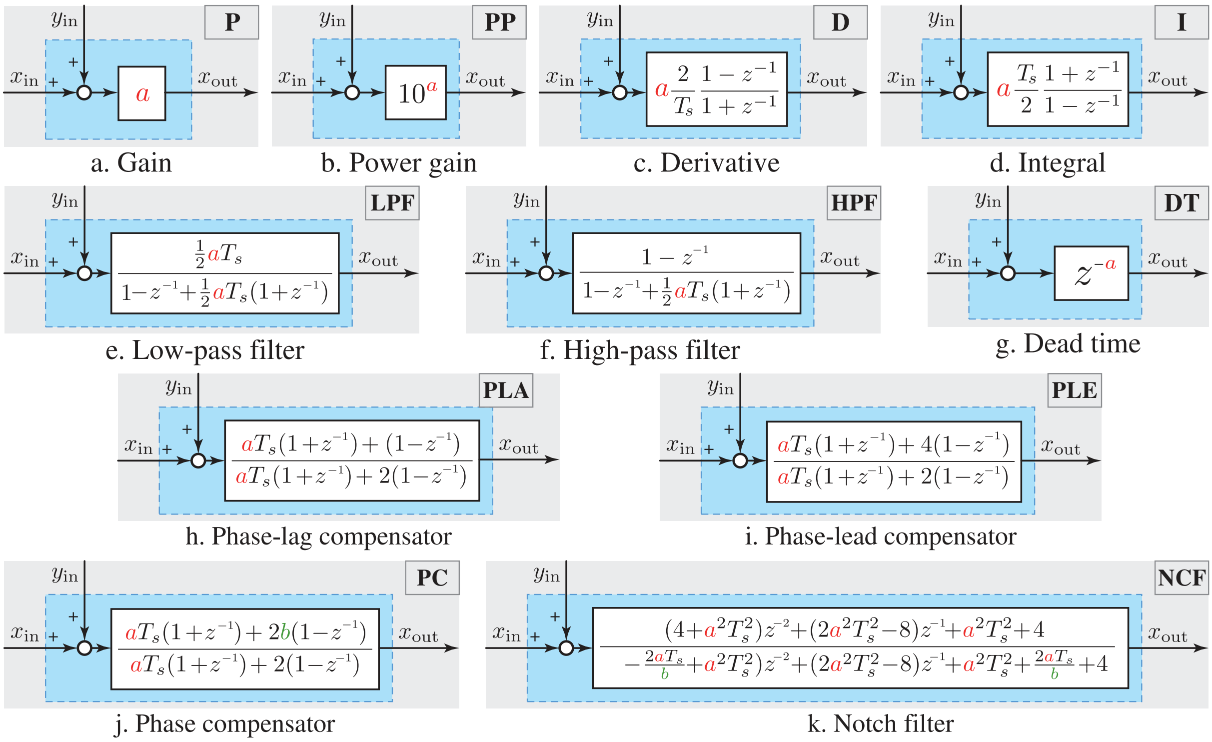

Fig. 2-16: Calculation elements for multidirectional element matrix.

Each element of the multidirectional element matrix is expressed as a two-input and two-output system. $f_{(x)}$ and $f_{(y)}$ stand for the calculation function of horizontal and vertical directions, respectively. The output value of each element is used for the adjacent element as an input value. The calculation algorithm is shown in Algorithm 3. The type of the calculation functions $f_{(x)}$ and $f_{(y)}$ are automatically selected from the prepared elements. Examples of the elements for the multidirectional element matrix are shown

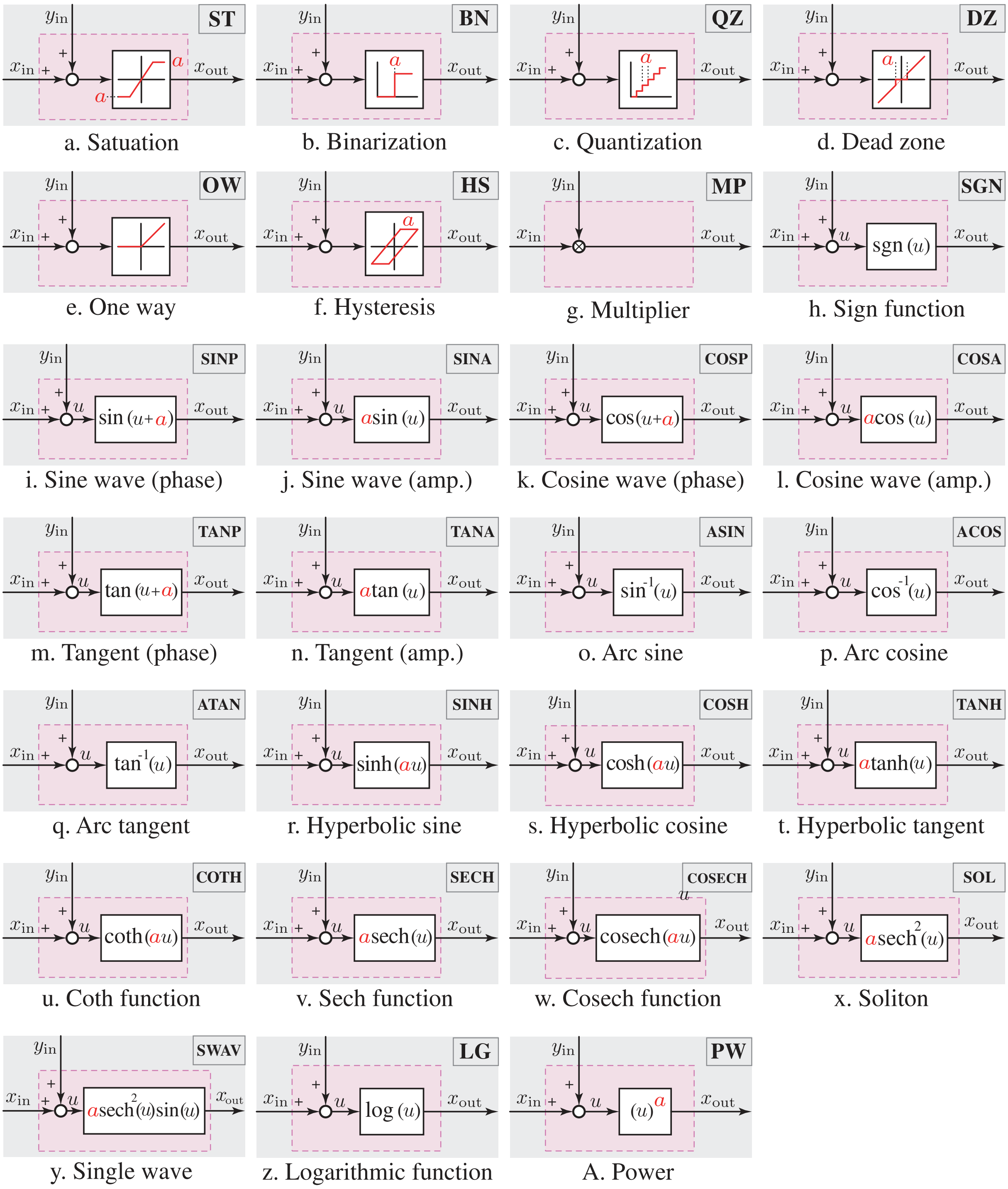

Fig. 2-17: Nonlinear function elements for multidirectional element matrix.

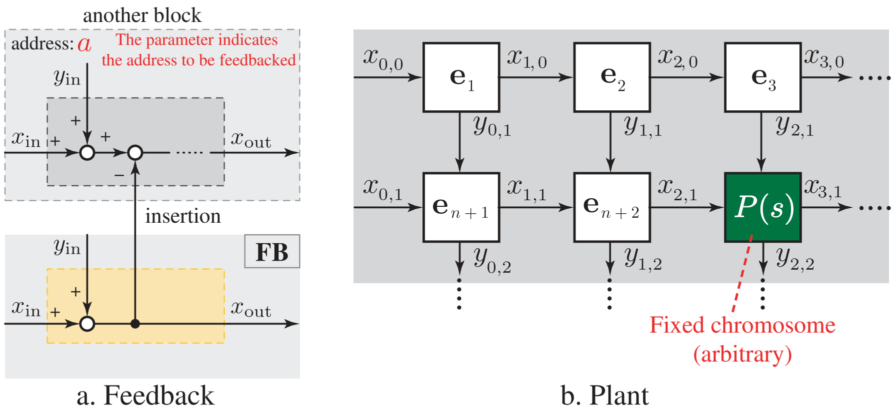

Fig. 2-18: Special elements for multidirectional element matrix.

Algorithm 3 Calculation procedure of element matrix.

for $j = 0$ to $m-1$ **do**
  $x_{0,j} \Leftarrow X_{xj}$
end for
for $i = 0$ to $n-1$ **do**
  $y_{i,0} \Leftarrow X_{yi}$
end for
for $j = 0$ to $m-1$ **do**
  for $i = 0$ to $n-1$ **do**
    $x_{i+1,j} \Leftarrow f_{(x)i,j}(x_{i,j}, y_{i,j})$
    $y_{i,j+1} \Leftarrow f_{(y)i,j}(x_{i,j}, y_{i,j})$
  end for
end for
for $j = 0$ to $m-1$ **do**
  $Y_{xj} \Leftarrow x_{n,j}$
end for
for $i = 0$ to $n-1$ **do**
  $Y_{yi} \Leftarrow y_{i,m}$
end for

in Figs. 2-15 to 2-18. Fig. 2-15 expresses basic elements to construct the element matrix structure. The basic elements define the flow of the signal and make a structure like a block diagram. The structure of the element matrix is designed to represent any block diagram. The structure of the block diagram is represented by basic elements. The branch element (**BR**) is designed to express a take off point of a block diagram, and the combination element (**CM**) is designed to express the summing point of a block diagram. On the contrary, the elements in Figs. 2-16 to 2-17 are defined as a two inputs and one output system. The reason is to clarify the role sharing of the elements that make up the structure

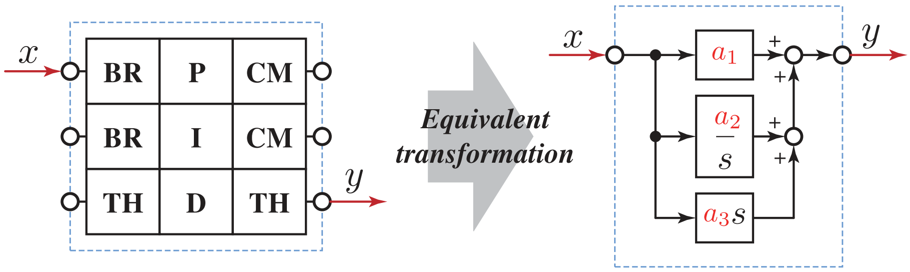

Fig. 2-19: A representation of PID controller.

and the elements that perform the computation. Fig. 2-18 refers to special elements. The feedback element can express a feedback loop. The parameter of the feedback element stands for the address of a feedback target element. The output of the feedback element is inserted as input to the target element. The plant element can express the plant of a system, such as an actuator. The plant is treated with fixed chromosome. As an example, the representation of a PID controller with an element matrix is shown in Fig. 2-19. The input/output definitions indicated by red arrows can be arbitrarily set by engineers.

2.4 Design Procedure of the EDM

Based on the above basic principle, this section describes the actual design procedure.

- Preparation of Input/output Data

  In this dissertation, the EDM is implemented by off-line abstraction shown in Algorithm 2. Firstly, input/output data is prepared for abstraction by the EDM. The number of samples of the input/output data must be the same. Generally, time series data of the discrete time domain is used. Spatial data and frequency domain data can also be used. Also, the EDM can be applied to on-line abstraction. Algorithm 4 stands for the on-line abstraction algorithm. On-line optimization is also basically the same as off-line optimization; however, data used for optimization are acquired by a moving window by ring buffer. By this method, evolution following the changing plant is achieved.

- Definition of Element Matrix

  The number of elements of the element matrix used for the element description method is determined. Increasing the size of the matrix improves the accuracy; however, the readability deteriorates and the calculation load increases. In this dissertation, the number of columns is fixed to

Algorithm 4 Algorithm of on-line abstraction by the EDM.

Initialization ( )
Renew Ring Buffer ( )
if t mod $T_1 = 0$ **then**
  for cntr1 = 1 to I_{num} **do**
    for cntr2 = 0 to t_{sum} **do**
      Matrix Calculation
      $\mathrm{F} \Leftarrow \mathrm{F} + f(\mathrm{cntr2})$
    end for
    F [cntr1] = F
  end for
  Ranking ( )
  Selection ( )
  Cross Over ( )
  Mutation ( )
  Make New Age
end if

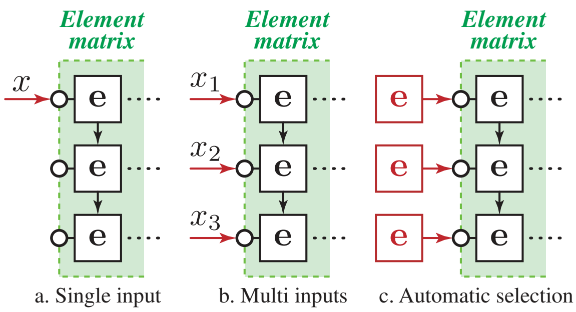

Fig. 2-20: Examples of input definition.

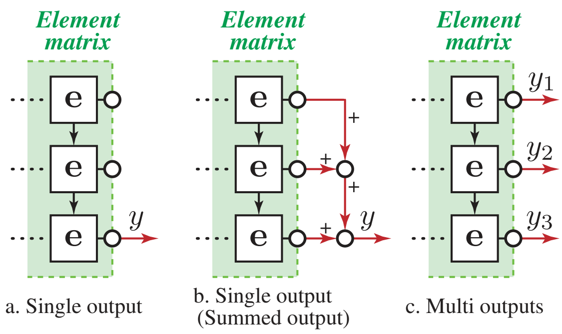

Fig. 2-21: Examples of output definition.

about 3 to 6, and the number of rows is increased to determine the relationship between accuracy and readability. The reason for the above is that the elements of one row can be sufficiently represented by elements of 3 to 6 columns, and they are designed based on the idea of how many rows need to be prepared. In analogy with an approximate expression such as Taylor expansion, the number of rows means the order of approximation, and the number of columns means approximation accuracy per order. Increasing the number of elements too much decreases the readability and makes it impossible to obtain the advantages of the EDM; therefore, it is desirable to keep the number of elements within a certain range. Then, the type of the element matrix (unidirectional, multidirectional) is selected. In the next, input and output are defined. Examples of input/output definition are depicted in Figs. 2-20 and 2-21. Thus, input and output can be freely defined by engineers.

- Preparation of Selectable Elements
  Then, selectable elements are prepared. Selectable elements can be arbitrarily prepared according to a target system. Based on the fitness value, elements suitable for the expression of a system are automatically selected by the GA from the prepared elements. On the contrary, no new elements are created automatically. Therefore, it is possible to express a target system using only limited elements.

- Design of Fitness Function
  Since the element matrix is automatically optimized based on a fitness function, the design of the fitness function is very important. The fitness function can be arbitrarily designed according to the purpose of optimization. By weighting by a window function, it is also possible to focus on some sections. In interactive design with hierarchical abstraction, engineers can redesign the fitness function step by step.

- Generation of Initial Individuals
  Then, it is necessary to generate an initial individual. The method of giving the initial individuals is selected from two methods: random creation and manual input. Although it is common to give initial individuals randomly, in the case where there is prior knowledge about a target system, the initial individual design by manual input is effective. When hierarchical abstraction is performed, the previous result is given as the initial value of the next learning.

- Optimization by the GA
  After the above preparations, an optimization of structure and parameter of a target system using GA is conducted. The method of abstraction is chosen from two methods: overall abstraction and hierarchical abstraction. It is necessary to determine the occurrence probability of crossover, mutation and parameter increase/decrease. In this dissertation, based on the design philosophy that parameters become more optimal values after the structure of the element matrix is decided, the mutation divides the incidence rate by parameter and structure. Thereby, the mutation probability of the parameter and the increase/decrease probability of the parameter are set to be larger than the mutation probability of the code. Optimization is terminated when the predetermined number of

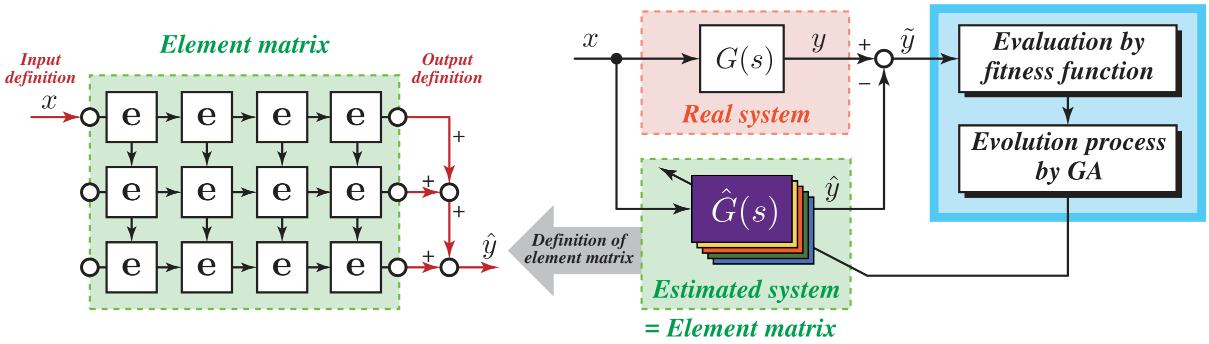

Fig. 2-22: Block diagram of system abstraction based on the EDM.

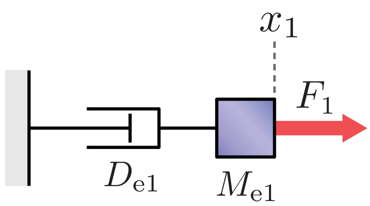

Fig. 2-23: A mechanical first-order lag system.

generations alternation is completed or when a predetermined fitness is obtained. After completion of the process, analyze the chromosome and confirm the abstracted result. Based on this set of design procedures, the system is abstracted.

2.4.1 Abstraction Example of First-order Lag System

In this section, an abstraction example using the EDM is described. The block diagram of system abstraction using the EDM is shown in Fig. 2-22. The fitness function is calculated by

$$\Gamma = \frac{1}{N_{\mathrm{sum}}} \sum_{q=1}^{N_{\mathrm{sum}}} \sqrt{\tilde{y}[q]^2}. \tag{2.16}$$

It is possible to identify various systems by setting input and output to arbitrary physical quantities. In this part, a first-order lag system is abstracted. An example of a mechanical first-order lag system is shown in Fig. 2-23. Here, x_1, F_1, $M_{\mathrm{e}1}$, and $D_{\mathrm{e}1}$ denote the displacement, force, mass, and viscosity, respectively. The transfer function from force to displacement is expressed as

$$\begin{aligned} G(s) &= \frac{x_1}{F_1} \\ &= \frac{1}{M_{\mathrm{e}1}s + D_{\mathrm{e}1}}. \end{aligned} \tag{2.17}$$

Table 2.1: Simulation parameters for abstraction of the first-order lag system.

Parameter	Description	Value
M_{e1}	Mass of the system	2 kg
D_{e1}	Viscosity of the system	100 Ns / m

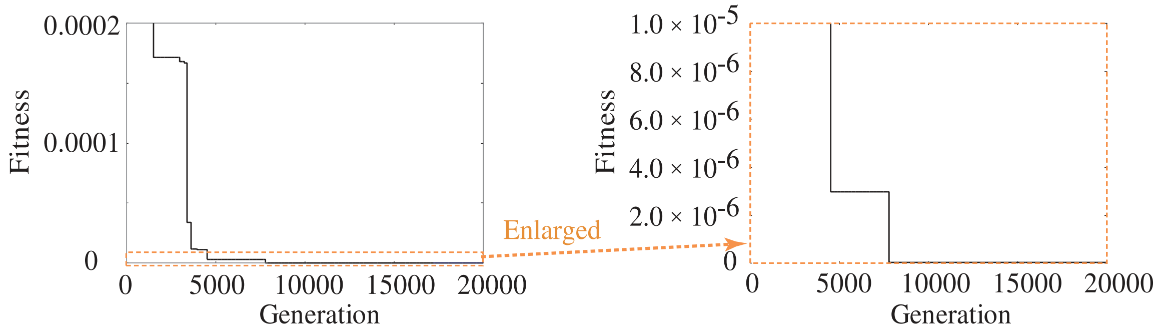

Fig. 2-24: Fitness response of the first-order lag system

The size of the element matrix is designed as 4×3. In this simulation, an overall abstraction is performed using the multidirectional element matrix. Step force is applied to the system for abstraction. Table 2.1 shows the simulation parameters of the EDM for the first-order lag system. The simulation results are shown in Figs. 2-24 to 2-26. The fitness responses are shown in Fig. 2-24. It can be confirmed that the fitness value decreases according to generation change of the GA. Figs. 2-25 and 2-26 show the velocity response and error of velocity responses between the designed model and estimated model, respectively. It can be seen that the velocity response becomes almost same with the designed model by 20,000 th alternation of generations. Table 2.2 shows the abstracted model and parameters by the EDM. The table layout corresponds with the element matrix. By analyzing Table 2.2, Fig. 2-27 is derived. The abstraction result in Fig. 2-27 can be transformed as

$$\hat{G}(s) = \frac{1}{1.898s + 99.85}. \tag{2.18}$$

The estimated system is almost same for an actual system. From this result, the basic performance of the EDM was confirmed.

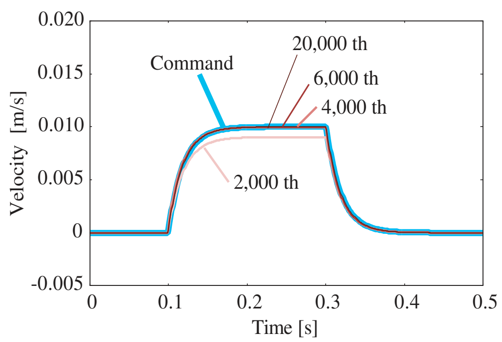

Fig. 2-25: Velocity response of the first-order lag system.

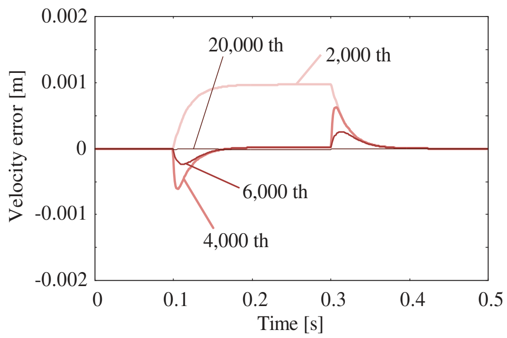

Fig. 2-26: Velocity error of the first-order lag system between designed and estimated models.

Table 2.2: Abstraction result of the first-order lag system.

PP Power gain $a_1 = 2.537 \times 10^4$	**PP** Power gain $a_2 = 8.877 \times 10^{-8}$	**P** Gain $a_3 = 4.447$	**LPF** Low-pass filter $a_4 = 5.260 \times 10$
D Derivative $a_5 = 4.334$	**P** Gain $a_6 = 5.634$	**LPF** Low-pass filter $a_7 = 3.879 \times 10^{-1}$	**I** Integral $a_8 = 1.987 \times 10^4$
TH Through –	**BR** Branch –	**TH** Through –	**CM** Combination –

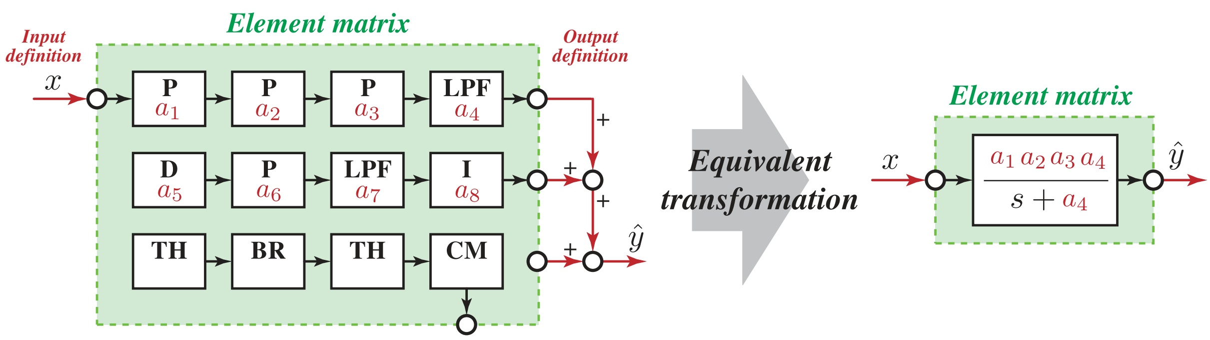

Fig. 2-27: Analysis of Table 2.2

2.5 Hierarchical Abstraction of Compensator for RFOB Based on the EDM

The necessity of the force analysis and control in automatic machinery has been gradually increased according to the increase of the demand to adapt to the fluctuation of the target work as mentioned in Chapter 1. In order to deal with delicate works, force control is necessary [12, 13, 59]. Also, a method to analyze force response is required in order to asset the quality of the target work. Thereby, a force detection method is important to achieve above purposes. There are roughly two methods to detect force: one is to use a force sensor, the other is to use the RFOB. A force sensor has a merit that it can measure the force nearly directly. However, the response frequency domain of a load-cell type is low because the structure of the mechanical system is elastic. Also, a pieszo type and force balance type are relatively expensive although it can detect high frequency domain force. On the contrary, the RFOB has a merit that it can detect the force without additional sensors because it can estimate the force from current information and position (velocity) information. Therefore, this method can implement force control without increasing the cost of the machinery because these information are originally needed for controlling motors. However, it is necessary to compensate disturbance such as coulomb friction, viscosity and gravity because it can not detect force directly. In this dissertation, the RFOB is mainly used in order to detect force information.

2.5.1 Basic Principle of RFOB

The block diagram of the RFOB is expressed as Fig. 2-28. F_{env}, F_{ext}, F_{d}, F_{cmp}, M_{n}, K_{tn}, I_{ref}, $\ddot{x}_{\mathrm{ref}}$, and x_{res} stand for the reaction force from environment, external force, disturbance force, compensation force, nominal mass, nominal thrust constant, current reference, acceleration reference, and position response, respectively. $Q_{\mathrm{r}}(s)$ expresses the low-pass filter of the RFOB. The cut-off frequency of $Q_{\mathrm{r}}(s)$ can be designed separately from the cut-off frequency of the DOB [6, 7]. In order to obtain pure reaction force from an environment, it is necessary to compensate disturbance force F_{d}. Therefore, the accurate calculation method of F_{d} is needed to design the RFOB. Then, estimated F_{d} can be used for compensation force F_{cmp}. Here, calculation methods of F_{cmp} are introduced. As an example, external force is expressed as

$$F_{\mathrm{ext}} = F_{\mathrm{env}} + F_{\mathrm{g}} + F_{\mathrm{fric}}, \tag{2.19}$$

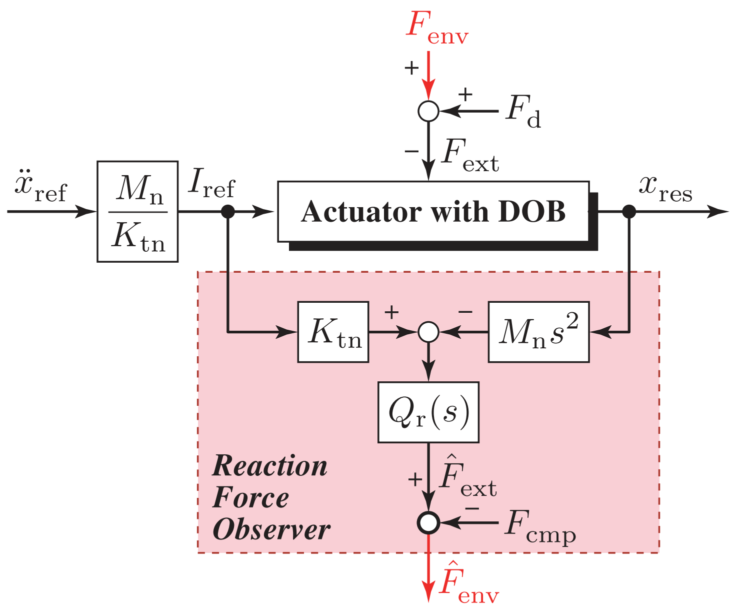

Fig. 2-28: Block diagram of the RFOB.

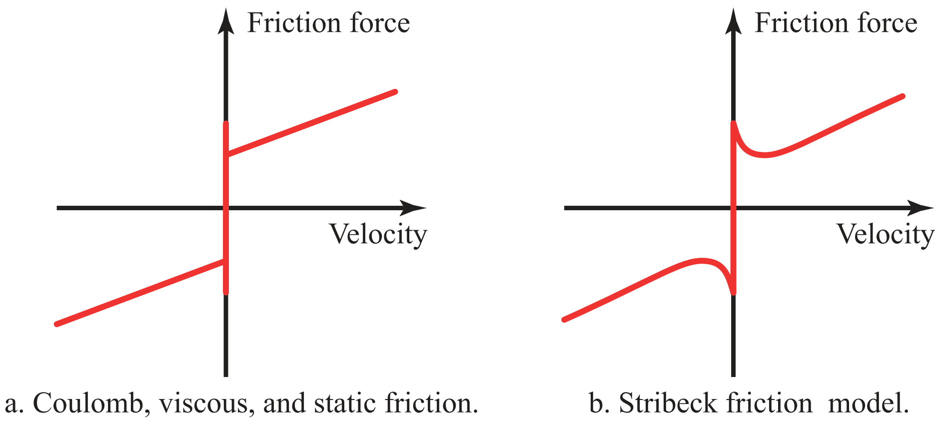

Fig. 2-29: General friction models.

where F_{g} and F_{fric} refer to the gravity and frictional force, respectively. Thereby, in order to extract reaction force from external force, a friction compensation method is needed. One of the calculation method is model based identification. There are several kinds of friction models. Fig. 2-29 shows a general friction model used widely. Fig. 2-29a. depicts a Coulomb, viscous, and static friction model and Fig. 2-29b. depicts a Stribeck friction model [65, 66], respectively. Also, there is a LuGre model [67, 68] as more rigid friction model. The conceptual diagram of the LuGre mode is shown in Fig. 2-30. The frictional force represented by the LuGre model is defined as

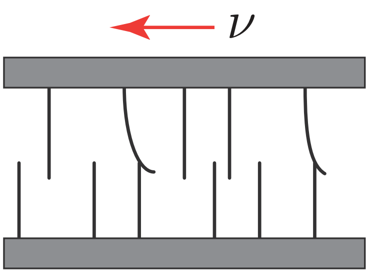

Fig. 2-30: LuGre model.

$$F_{\text{fric}} = \sigma_0 z + \sigma_1 \frac{dz}{dt} + \sigma_2 \nu, \tag{2.20}$$

where z, ν stand for the deflection of the bristles and relative velocity of moving part, respectively. σ_0, σ_1, and σ_2 are friction force parameters, which can be physically interpreted as the stiffness of the bristles between two contact surfaces, damping coefficient of the bristles, and viscous coefficient, respectively. The motion equation about z is represented as

$$\frac{dz}{dt} = \nu - \frac{|\nu|}{g(\nu)} z, \tag{2.21}$$

where $g(\nu)$ is the function indicating the Stribeck effect and is expressed as follows:

$$g(\nu) = \frac{F_{\text{C}} + (F_{\text{S}} - F_{\text{C}}) e^{-(\nu/\nu_{\text{s}})^2}}{\sigma_0}, \tag{2.22}$$

where F_{C}, F_{S}, and ν_{s} stand for the Coulomb friction level, stiction force, and Stribeck velocity, respectively. When ν is constant, z is in steady state as

$$z_{\text{ss}} = g(\nu)\,\text{sgn}(\nu). \tag{2.23}$$

Also, the relationship between the velocity and the frictional force in the steady state is expressed as

$$\begin{aligned} F_{\text{ss}}(\nu) &= \sigma_0 g(\nu)\,\text{sgn}(\nu) + \sigma_2 \nu \\ &= F_{\text{C}}\,\text{sgn}(\nu) + (\mathrm{F_S} - \mathrm{F_C})\mathrm{e}^{-(\nu/\nu_{\text{s}})^2}\,\text{sgn}(\nu) + \sigma_2 \nu. \end{aligned} \tag{2.24}$$

2.5.2 Real-time Disturbance Compensation by Environment Quarrier

Next, an environment quarrier (EQ) [69, 70] is introduced. In the model-based method previously described, there is a limit to the expression of friction. Since the EQ does not require the model of friction, compensation with high accuracy is possible. Moreover, because there is no need to perform

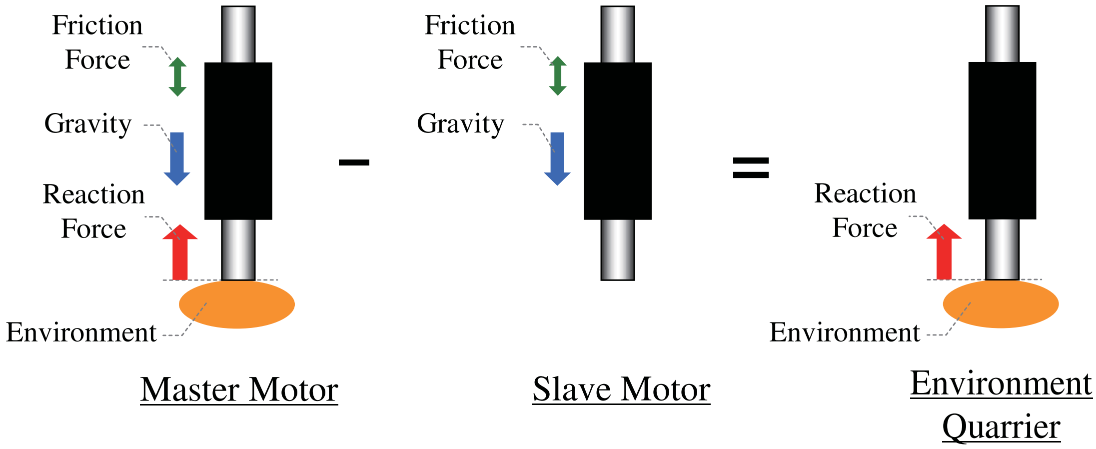

Fig. 2-31: Overview of the EQ.

further identification, design time can be shortened. The EQ consists of a master system for contact and a slave system for gravity/friction compensation. In each system, the DOB is implemented. Only the master system contacts an environment, and the slave system moves in free motion. When compensation for gravity/friction force is not done, the estimated value output from the DOB includes all external forces. Both systems operate in the same structure and synchronously, and only the master system contacts an environment; therefore, the external force of the master system is the external force of the slave system and the reaction force from the environment. Focusing on this point, the reaction force from the product can be obtained by

$$\hat{F}^{\mathrm{M}}_{\mathrm{env}} = \hat{F}^{\mathrm{M}}_{\mathrm{ext}} - \hat{F}^{\mathrm{S}}_{\mathrm{ext}}, \tag{2.25}$$

where superscripts M and S stand for the master system and slave system, respectively. By using the EQ, it becomes possible to compensate disturbance factors such as frictional force which are difficult to identify with high accuracy and in real time. The conceptual diagram of the environmental qualities is shown in Fig. 2-31, and the block diagram is shown in Fig. 2-32, respectively.

On the contrary, in order to achieve compensation using the EQ with high accuracy, synchronism between the master and slave systems becomes important. In order to improve the productivity, tracking performance to the command trajectory is important. Mode transformation is performed by using a

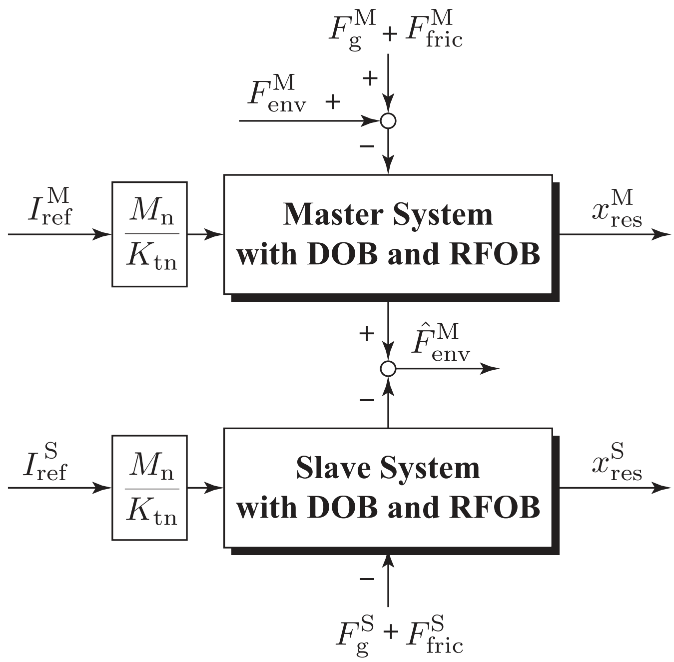

Fig. 2-32: Block diagram of the reaction force extractor by the EQ.

second-order quarry matrix $\mathbf{Q}_2$ to control two variables as follows:

$$\begin{aligned} \begin{bmatrix} x_{\mathrm{res}}^{\mathrm{C}} \\ x_{\mathrm{res}}^{\mathrm{D}} \end{bmatrix} &= \mathbf{Q}_2 \begin{bmatrix} x_{\mathrm{res}}^{\mathrm{M}} \\ x_{\mathrm{res}}^{\mathrm{S}} \end{bmatrix} \\ &= \frac{1}{2}\begin{bmatrix} 1 & 1 \\ 1 & -1 \end{bmatrix} \begin{bmatrix} x_{\mathrm{res}}^{\mathrm{M}} \\ x_{\mathrm{res}}^{\mathrm{S}} \end{bmatrix}, \end{aligned} \tag{2.26}$$

where the superscripts C and D express the common mode and differential mode, respectively. Each of them corresponds to the response value of tracking performance and synchronism. By giving the movement target value $x_{\mathrm{cmd}}^{\mathrm{C}}$ and the synchronization target value $x_{\mathrm{cmd}}^{\mathrm{D}}$ to the response value, the acceleration reference value $\ddot{x}_{\mathrm{ref}}^{\mathrm{C}}$, $\ddot{x}_{\mathrm{ref}}^{\mathrm{D}}$ can be calculated. The acceleration reference value of each mode can be converted to the acceleration reference value of each system by using the quadratic inverse matrix

$$\begin{aligned} \begin{bmatrix} \ddot{x}_{\mathrm{ref}}^{\mathrm{M}} \\ \ddot{x}_{\mathrm{ref}}^{\mathrm{S}} \end{bmatrix} &= \mathbf{Q}_2^{-1} \begin{bmatrix} \ddot{x}_{\mathrm{ref}}^{\mathrm{C}} \\ \ddot{x}_{\mathrm{ref}}^{\mathrm{D}} \end{bmatrix} \\ &= \begin{bmatrix} 1 & 1 \\ 1 & -1 \end{bmatrix} \begin{bmatrix} \ddot{x}_{\mathrm{ref}}^{\mathrm{C}} \\ \ddot{x}_{\mathrm{ref}}^{\mathrm{D}} \end{bmatrix}. \end{aligned} \tag{2.27}$$

Synchronization/trajectory tracking performance can be set independently by converting the sum mode and difference into the mode space. The total block diagram of the EQ is shown in Fig. 2-33.

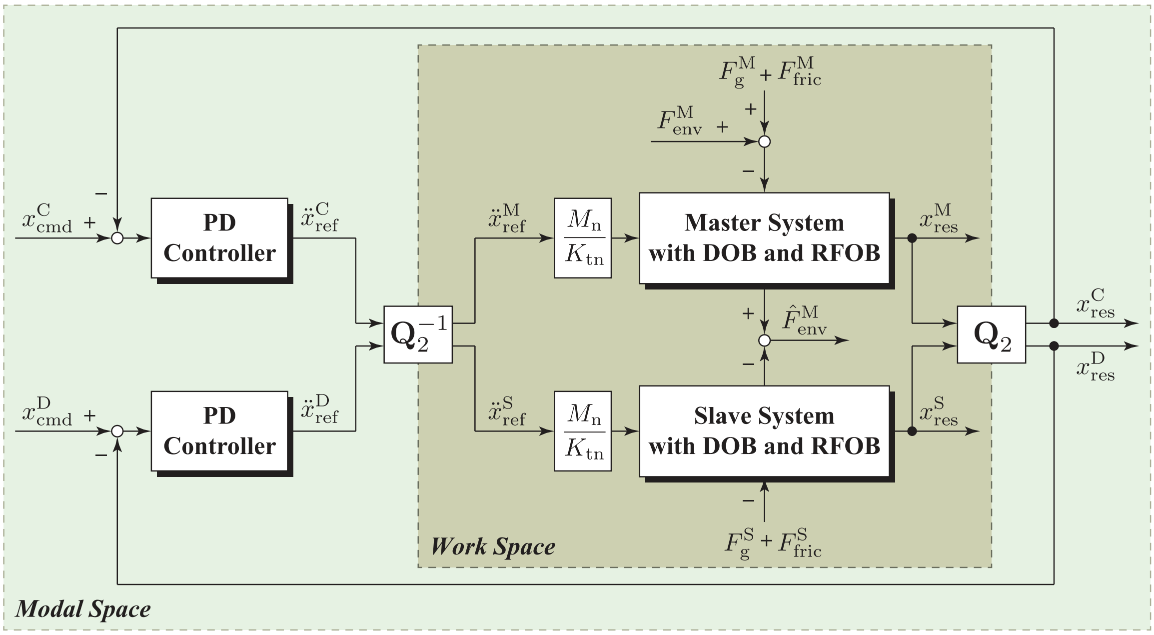

Fig. 2-33: Total block diagram of the EQ.

2.5.3 Compensator Abstraction for RFOB by the EDM

By using an exact model such as the LuGre model, since highly accurate friction compensation can be performed. It is possible to extract the reaction force accurately. However, such exact model has many parameters and takes time and labor to implement. Therefore, in this chapter, an automatic design method of the RFOB using the EDM is proposed. Fig. 2-34 depicts the block diagram of the automatic RFOB compensator generation by the EDM. In Fig. 2-34, I_{ref}, θ_{res}, and $\hat{\tau}_{\mathrm{ext}}$ denote the current reference value, angle response value, and estimated external torque, respectively. The actuator is moved by acceleration control with the DOB. The element matrix in Fig. 2-34 shows the compensator for RFOB. This part is expressed in Fig. 2-35. The input values can be set manually by arbitrary parameters or automatically by the EDM. In this study, the input values are selected automatically using the EDM. In this case, the input and the output of element matrix are designed as status information of an actuator and the compensation torque for the RFOB, respectively. Since the DOB estimates whole disturbance of the system, it is necessary to cancel disturbance other than reaction torque. The objective of the compensator generation is to cancel these disturbances. The compensator is generated using free-motion response of the actuator. At this time, it is desirable to move the motor so as to excite various disturbances. When the RFOB works ideally, torque response of free-motion become always zero. Therefore, the fitness function is

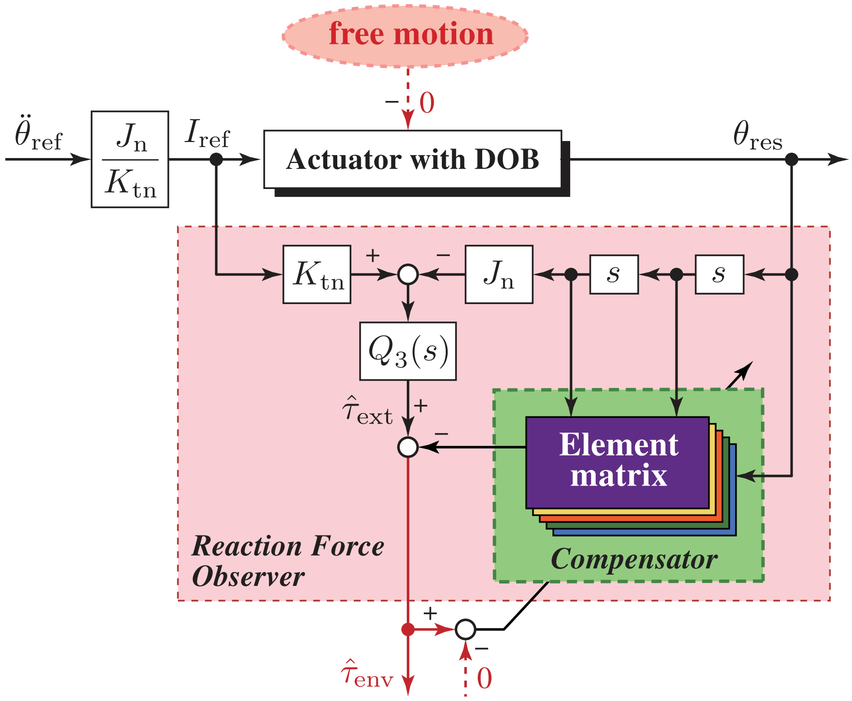

Fig. 2-34: Block diagram of the EDM for compensator abstraction.

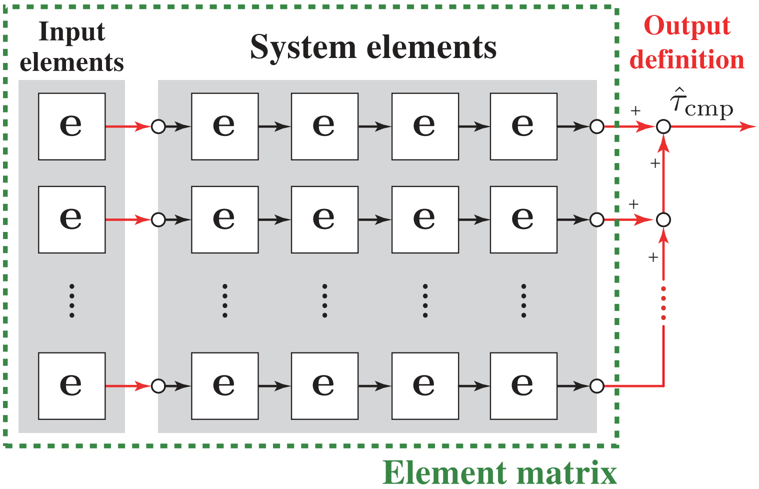

Fig. 2-35: An element matrix for compensator abstraction of RFOB.

defined as

$$\Gamma_{\mathrm{rfob}} = \frac{1}{N_{\mathrm{sum}}} \sum_{q=1}^{N_{\mathrm{sum}}} \sqrt{\hat{F}_{\mathrm{ext}}[q]^2}, \tag{2.28}$$

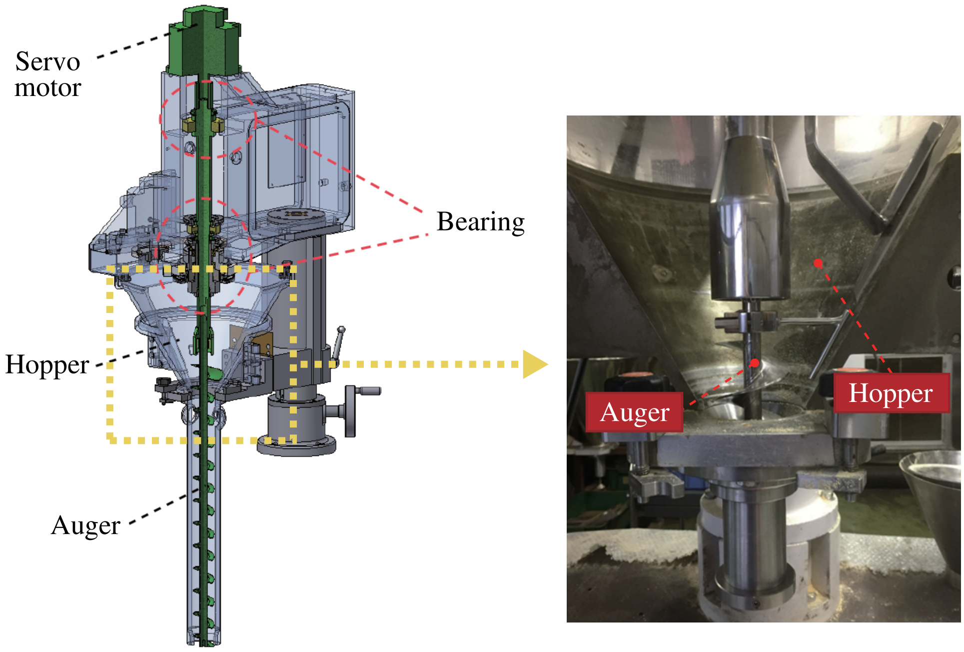

a. Structure of auger filling machine. b. Picture of the auger part.

Fig. 2-36: A powder filling machine.

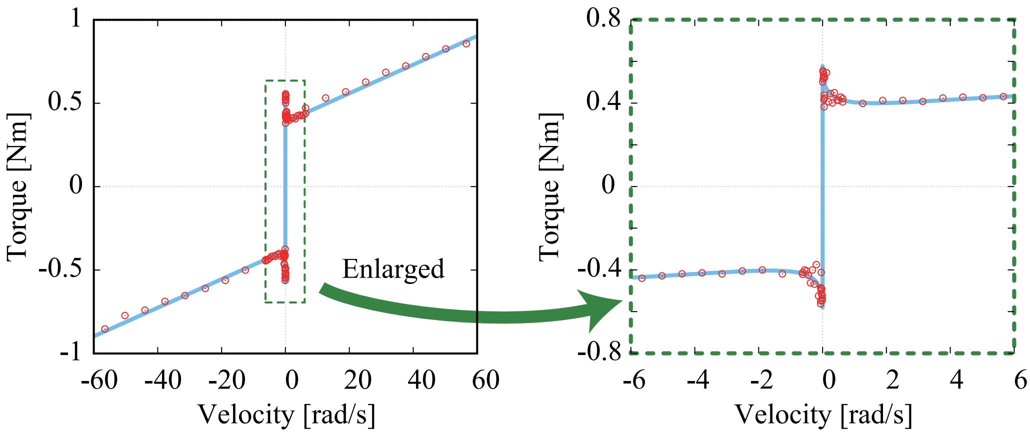

Fig. 2-37: Characteristics of the friction.

where Γ_{rfob} refers to the fitness value of compensator abstraction for the RFOB. Individuals with small fitness values are more likely to survive in the next generation. By repeating the evolution, an equation for calculating the compensation value for zeroing the estimated torque is automatically derived.

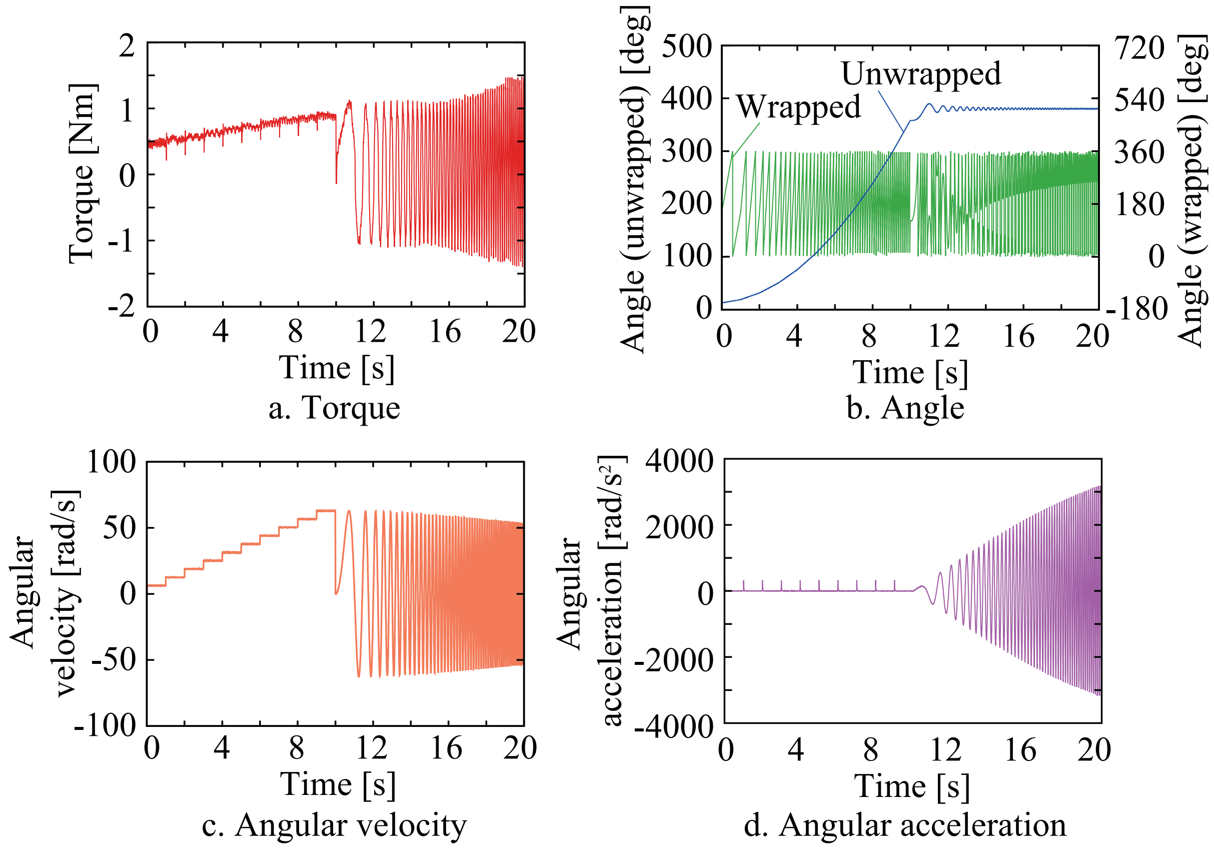

Fig. 2-38: Time-series data for disturbance abstraction.

2.5.4 Experiments of Compensator Abstraction by the EDM

In this part, experiments are conducted in order to confirm the validity of the proposed method. The experimental setup is shown in Fig. 2-36. This equipment is a powder-filling machine. The machine fills powder by a screw shaft called auger. The auger is actuated by a servo motor. Also, the auger axis is supported by bearings in order to reduce the fluctuation. The bearings are sealed to avoid contamination of powder into the actuator. Thereby, friction due to seal parts and bearings exist. The characteristics of the friction are depicted in Fig 2-37. In these experiments, the friction of the auger filling machine are abstracted. The EDM is applied to generate the compensator of this system. The actuator is moved by angle (angular velocity) control. In these experiments, manual designing method of compensator and the proposed method are compared. The abstraction experiments are conducted for deriving the compensator. Time-series data are prepared for abstraction. Fig 2-38 shows the time-series data for abstraction. Four kinds of input signals, unwrapped angle, wrapped angle, angular velocity, angular

Table 2.3: Identification results of the LuGre model.

Parameter	Description	Value
ν_{s}	Stribeck velocity	0.988401 m/s
F_{C}	Coulomb friction level	7.02447×10^{-8}
F_{S}	Stiction force	3.88592×10^{-7}
z	Deflection of the bristles	1.10486×10^{6} m
σ_0	Stiffness of the bristles between two contact surfaces	0.0135702 N/m
σ_1	Damping coefficient of the bristles	8.7536×10^{-8} Ns/m
σ_2	Viscous coefficient	3.74536×10^{-7} Ns/m

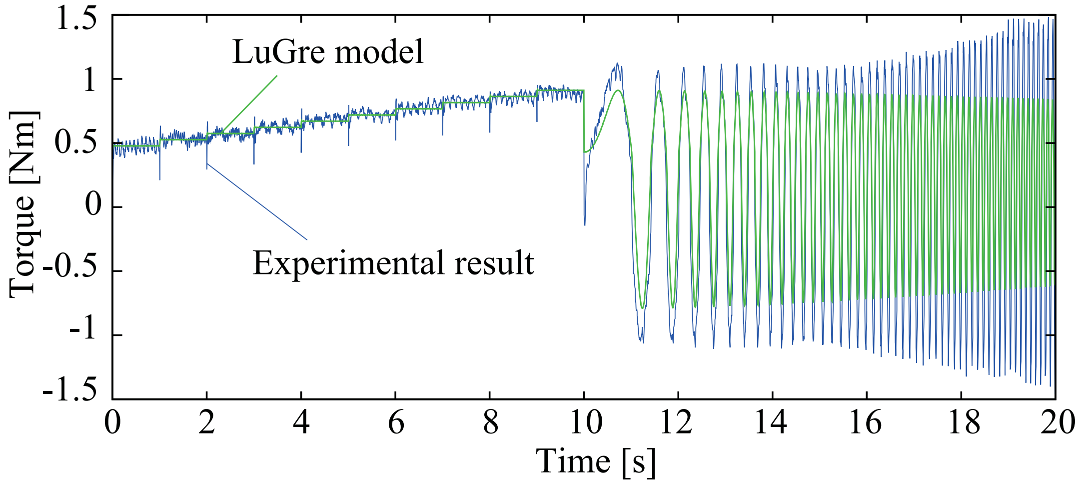

Fig. 2-39: Identification result of the LuGre model.

acceleration are prepared. A torque response is prepared as an output signal. The actuator is moved by angular velocity control. The velocity step command was applied from 0 s to 10 s. Also, velocity charp command was given after 10 s. The charp signal is designed as follows:

$$\omega_{\mathrm{cmd}} = 20\,\pi \sin(2\pi \times 0.5(t-10)^2). \tag{2.29}$$

In this experiment, a conventional method which is explained in the later and the proposed method are compared. In this dissertation, a friction compensator based on LuGre model [67, 68] is applied as the conventional method. The LuGre model is known as a rigid friction model. In this experiment, parameters of the LuGre model are calculated by the GA. Eq. (2.28) was used as the fitness function for the identification of the LuGre model. The derived parameters are shown in Table 2.3. The torque response using the LuGre model is shown in Fig. 2-39. The EDM is applied to abstract a fiction

Table 2.4: The procedure from Steps 1 to 3.

Step	Matrix size	Initial individual	data
Step 1	4×2	Coulomb/viscous friction model	0 s – 10 s
Step 2	4×3	Abstraction result in Step 1	0 s – 10 s
Step 3	4×4	Abstraction result in Step 2	0 s – 10 s
Step 4	4×5	Abstraction result in Step 3	0 s – 20 s

compensator. Firstly, time-series data from 0 s to 10 s was used to abstract angular velocity dependent characteristics. The abstraction is conducted hierarchically as shown in Fig. 2-10. In Step 1, 4×2 element matrix was created. In addition, Coulomb friction/viscous friction, which is known to exist, was given as an initial model. After that, in Steps 2 and 3, the number of rows of the element was increased by one row. The procedure is expressed in Table 2.4. The fitness response in Steps 1 to 3 is shown in Fig. 2-40. The torque response in Steps 1 to 3 is shown in Fig. 2-42. It is shown that the expression ability of the model was improved by increasing the number of element matrix. In Step 1, it can be seen that low-frequency components are represented. In Steps 2 and 3, spatially dependent terms were extracted. Then, time-series data from 0 s to 20 s were used in Step 4 in order to extract angular-acceleration-dependent terms. In Step 4, 4×5 element matrix was used. The fitness response in Step 4 is shown in Fig. 2-41. The torque response in Step 4 is shown in Fig. 2-43. The final abstraction result is shown in Table 2.5. The block diagram of the abstracted compensator by the EDM is shown in Fig 2-44. a_1 to a_{20} in Fig 2-44 refer to the parameters of each element. The subscripts express the address of the parameter. In Fig. 2-44, the first and second lines show the term of Coulomb friction and viscous friction, respectively. The third and fourth lines express the spatially-dependent friction. The fifth line stands for the acceleration-dependent terms. In order to confirm the validity of the abstraction result by the EDM, torque responses using another time-series data from abstraction phase were compared. The command angular velocity is designed as follows:

$$\omega_{\mathrm{cmd}} = 20\,\pi \sin(2\pi \times 0.1t^2). \tag{2.30}$$

Signal flow in the element matrix of the EDM is shown in Fig. 2-45. Correspondence between signal flow and element matrix promotes understanding of the function of each element. Comparison of the torque responses is shown in Fig. 2-46. Enlarged view of Fig. 2-46 is depicted in Fig. 2-47. The black and red lines show the torque response of the LuGre model and the EDM. The light blue line shows

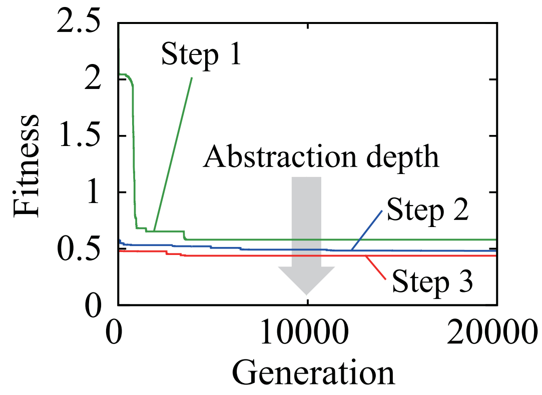

Fig. 2-40: Fitness response of Steps 1 to 3.

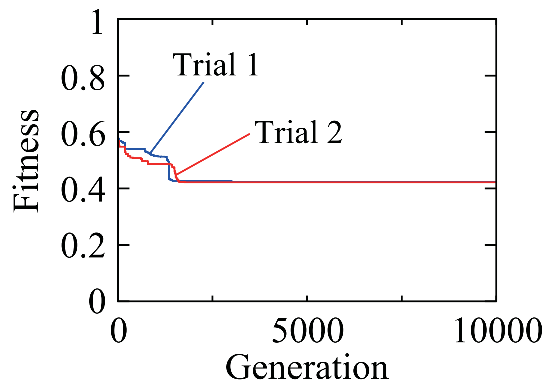

Fig. 2-41: Fitness response of Step 4.

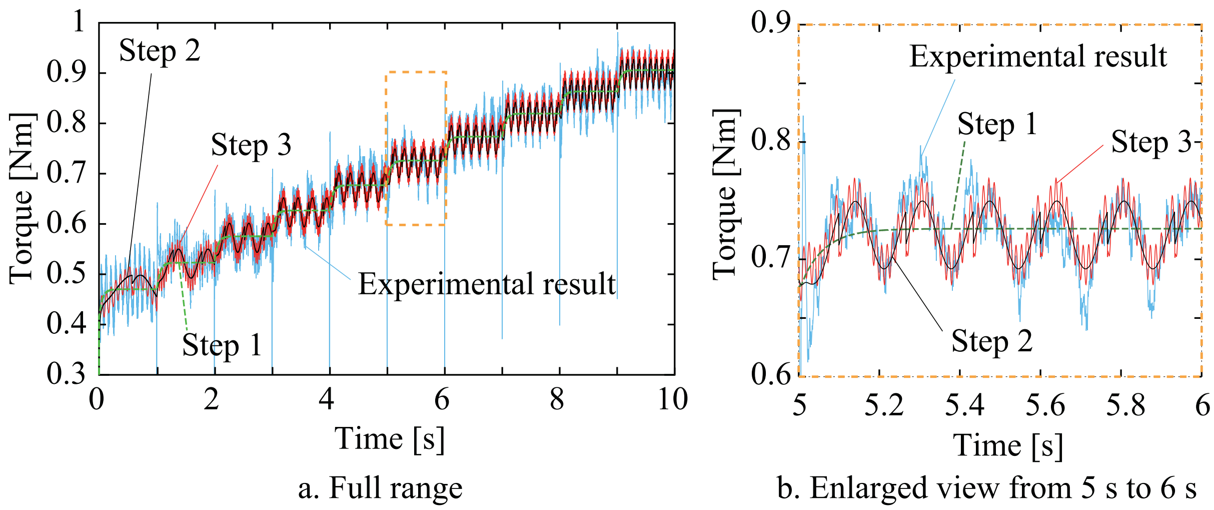

Fig. 2-42: Torque response in Steps 1 to 3.

actural torque response. It was confirmed that the EDM was able to more accurately express the actual response value. Comparison of the root mean square (RMS) of the torque error is shown in Table 2.6. The error value of the proposed method is smaller than that of the LuGre model. Therefore, the estimation accuracy by the EDM is better than model-based method. Moreover, since it was possible to interpret the physical meaning of the calculation formula for obtaining the response, it is more readable than the data-based method such as a neural network. From these results, validity of the proposed method was confirmed by the experiments.

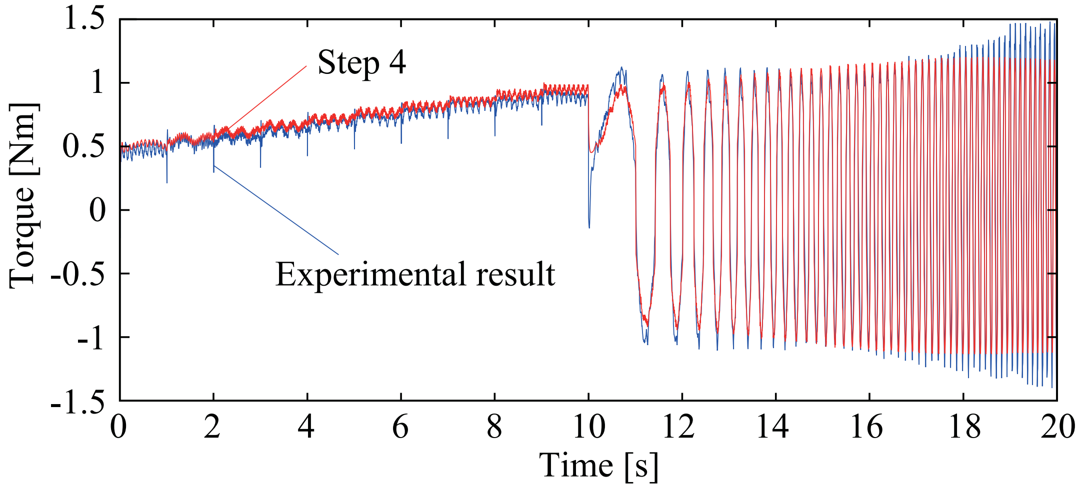

Fig. 2-43: Torque response in Step 4.

Table 2.5: Abstraction result of the RFOB compensator.

$\dot{\theta}_{\mathrm{res}}$ Velocity response	**P** Gain $a_1 = 2.30333$	**ATAN** Arc tangent –	**P** Gain $a_3 = 0.24359$	**TH** Through –
$\dot{\theta}_{\mathrm{res}}$ Velocity response	**TH** Through –	**P** Gain $a_6 = 0.00862$	**ATAN** Arc tangent –	**LPF** Low-pass filter $a_8 = 98.8933$
θ_{res} Angle response	**P** Gain $a_9 = 0.01016$	**PLE** Phase-lead comp. $a_{10} = 0.88240$	**TH** Through –	**COSA** Cosine wave (amp.) $a_{12} = 0.02934$
θ_{res} Angle response	**OFS** Offset $a_{13} = 18.3333$	**P** Gain $a_{14} = 0.21033$	**SINA** Sine wave (amp.) $a_{15} = 0.02304$	**TH** Through –
$\ddot{\theta}_{\mathrm{res}}$ Acc. response	**DT** Dead time $a_{17} = 0.00217$	**P** Gain $a_{18} = 0.00012$	**SINP** Sine wave (phase) $a_{19} = 0.03895$	**DT** Dead time $a_{20} = 0.00154$

Table 2.6: Comparison of torque error RMS.

Step	Matrix size	Unit
LuGre (conv.)	3.91211	Nm
EDM (prop.)	1.88654	Nm

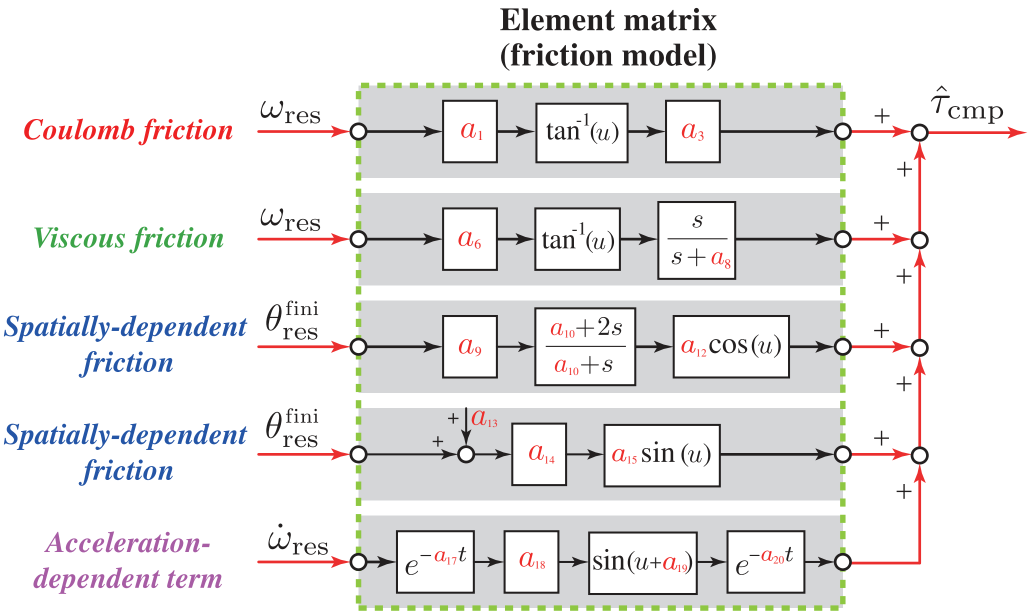

Fig. 2-44: Abstracted compensator by the EDM.

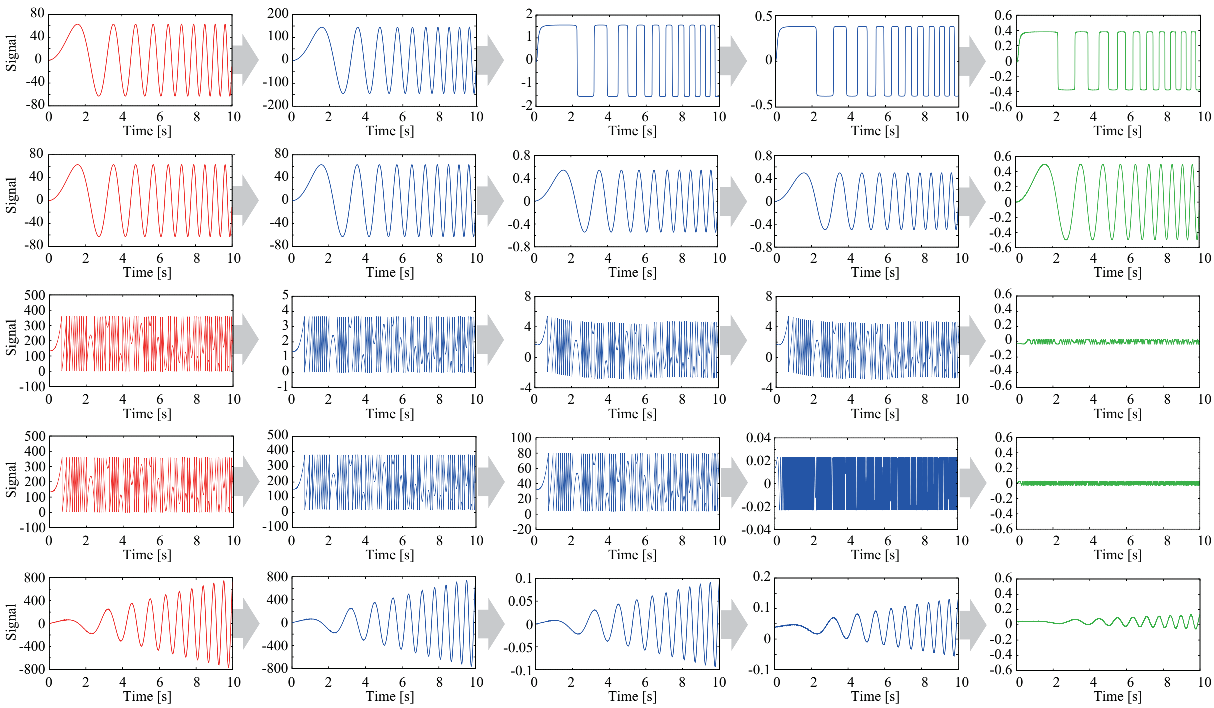

Fig. 2-45: Signal flow of the EDM.

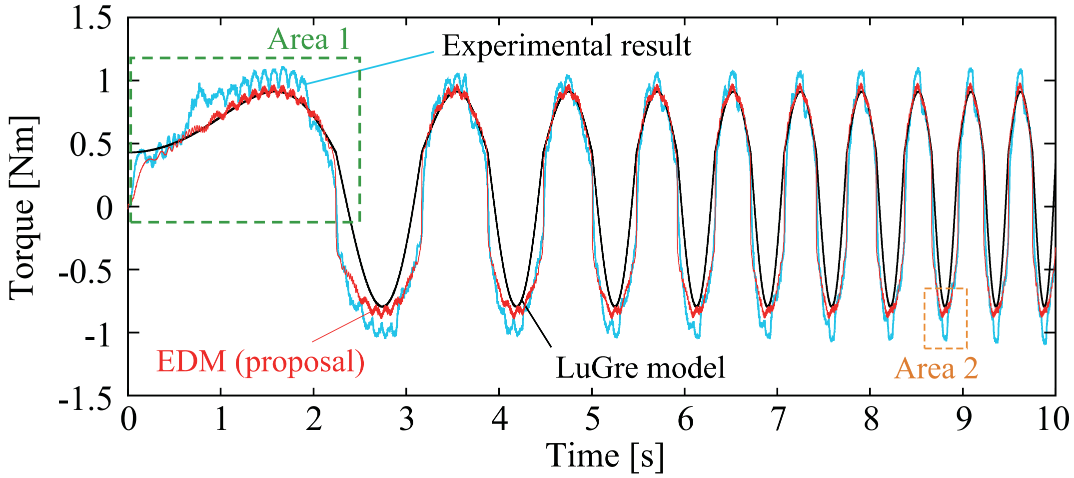

Fig. 2-46: Comparison of torque response between a conventional method and the proposed method.

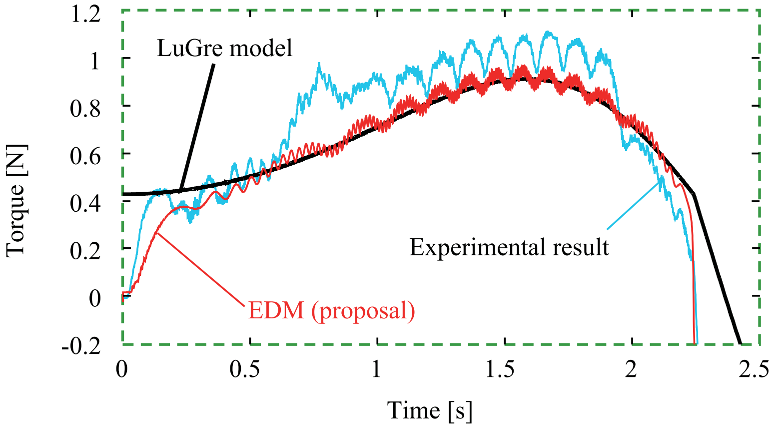

a. Area 1

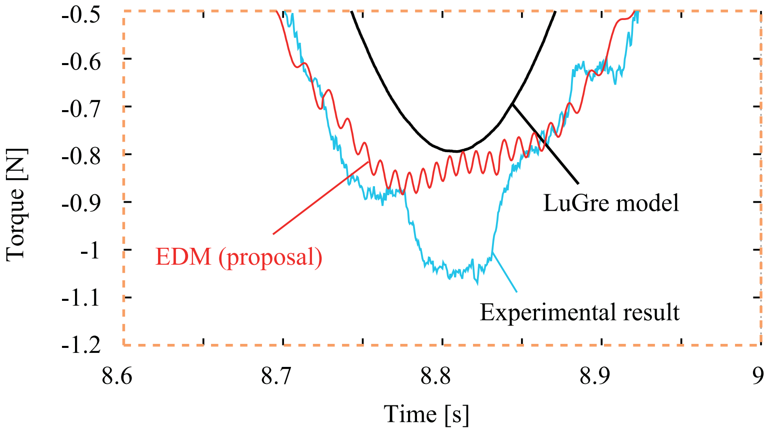

b. Area 2

Fig. 2-47: Enlarged view of Fig. 2-46.

2.6 Packaging Leak Inspection Based on High-accuracy Force Detection

2.6.1 Necessity of Packaging Leak Inspection

In recent years, due to problems such as food poisoning and foreign body contamination, food safety concerns and security awareness are attracting attention. Therefore, various quality inspections are conducted in a food manufacturing process, and one of them is leak inspection. “Leak” means that the degree of the sealing of a bag which is normally completely sealed by packaging is incomplete. When leak occurs in food packaging, there are adverse effects such as moisture absorption and oxidation of grease due to deterioration of taste and aroma and deterioration such as corruption caused by microorganism mold, which is a factor that shakes the food safety and security of consumers. Also, if leak items flow outwardly to the market, food makers will lose the brand image and cause large loss. Therefore, leak inspection has been conducted at the food production site. There are two methods of leak inspection: one is “sampling inspection” and the other is “all-product inspection.” Sampling inspection is a method to inspect a product by extracting several products every predetermined number. Since this method cannot inspect all products, defective products remains a possibility that flows out. On the contrary, an all-product inspection is a method to conduct inspections on all products, which is ideal because of higher safety than a sampling inspection. Therefore, there is a demand for a leak inspection apparatus which can inspect all products at the food production site. As an example, the production speed of a packaging line requiring a leak inspection is generally 30 to 60 pieces per minute in snack confectionery industry. Therefore, in order to achieve automation of all-product inspection, it is necessary to finish one inspection within 2 s. In addition, the installation space that can be used for the leak inspection process is limited in many cases, meaning that a compact machinery is desired. However, there are no leakage inspection apparatuses that can comply with these demands in a small size, high precision and high speed, and automation of all-product inspection has not progressed. Therefore, sampling inspection is usually conducted in recent years. In some cases, bags produced are manually pushed to inspect all items; however it is not easy to inspect with a short time of 2 s, and only obvious leak products such as holes with a few mm open can be detected. The leak testing apparatus for all-product inspection which has been proposed so far has the following problems. There is a method of sandwiching the product on a conveyor arranged in parallel and inspecting it with a pressure sensor, and a method of setting the inside of the container in a vacuum state and detecting the change in pressure requires 10 s or more for one inspection. Hence, in order to conduct all-product inspection, it is necessary to arrange a plurality of inspection sections, and the apparatus becomes large sized. The method of filling a helium gas in bag and detecting gas leak using a helium detector after packaging requires filling with helium gas, resulting in high running cost. In a method of bringing a product into contact with a metal brush to which a voltage is applied and detecting a leak by a change in electric potential, it is difficult to detect a hole at a position where a brush cannot be contacted. In addition, it is necessary to contain much moisture inside. Therefore, it can only be applied to limited products. In this section, a packaging leakage inspection machinery based on force analysis is proposed. The proposed machinery detects a leak by analyzing the force information when pushing the bag. By the proposed machinery, automation of all-product inspection and contribution to food safety and security can be expected because leak inspection can be performed with high precision and high speed in a limited installation space.

2.6.2 High-accuracy Force Detection

The overview of the leak detector is shown in Fig. 2-48. This machinery is commonly used for packaging of snacks, breads, powder products, etc. The machine detects leaks in pillow packaged products (hereinafter referred to as "products") by pushing the product sent by a conveyor with a pusher. It is possible to judge the presence or absence of a leak by extracting and analyzing the haptic information during a pushing time. The pusher consists of a servo control system consisting of a linear motor, linear guide, linear encoder, and end effector, and two control systems are installed for one machine. These two control systems serve as one for inspection to contact with the product and the other for compensation of gravity/friction to increase inspection accuracy. In this dissertation, the inspection system is defined as the master system, and the compensation system is defined as the slave system. In each system of master and slave, the DOB is implemented in order to control the system robustly. Also, the RFOB for estimating the force externally applied to the system are installed, reaction force information from the product can be extracted without a force sensor. Therefore, it is possible to simultaneously achieve high-rigidity control required to achieve high-speed leakage inspection, and wide-band force detection required to achieve highly accurate leakage inspection.

2.6.3 Leak Detection Based on Force Information

Then, a method of extracting information on the presence or absence of leak from the force information of the product obtained is described. At the moment after the end effector contacts with a product, the change of the reaction force due to the deformation of the film is larger than the change in the re-

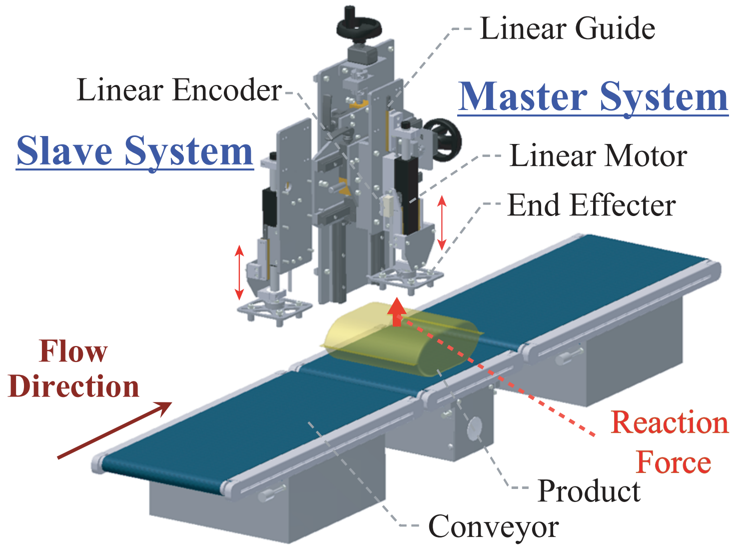

Fig. 2-48: Proposed leak detector.

action force due to the leak. Thereby, it is impossible to determine the leak in transient state. In this study, a robust position control system with high control rigidity is achieved by the DOB; therefore, it is possible to quickly create a stable state independent of the band of the environmental model of a product. Products that are actually inspected differ in the amount of air enclosed, and the thickness is varied by a few millimeters. In this research, it become possible to achieve an inspection which is hardly affected by this variation using the time-derivative of the extracted reaction force. The time-derivative of the extracted reaction force for evaluating the leak detection is defined as equivalent jerk. The equivalent jerk is calculated by time-derivative of the estimated reaction force as

$$\dot{F} = \frac{g_{\mathrm{j}}^2 s}{s^2 + 2g_{\mathrm{j}}s + g_{\mathrm{j}}^2}\hat{F}_{\mathrm{env}}, \tag{2.31}$$

where $\dot{F}$ and g_{j} represent the equivalent jerk and cut-off frequency of the derivative, respectively. Products to be actually inspected differ in the amount of air sealed in each package. There are variations of several mm in thickness; however by evaluating the equivalent jerk, discrimination that is not affected by this thickness variation becomes possible. The presence or absence of leakage is determined from the force information detected by the above method. Also, there are variations of the equivalent jerk, which affects the discrimination accuracy of presence/absence of leak. Therefore, in order to confirm the validity of leak judgment, statistical evaluation is carried out. The accuracy of discrimination is evaluated

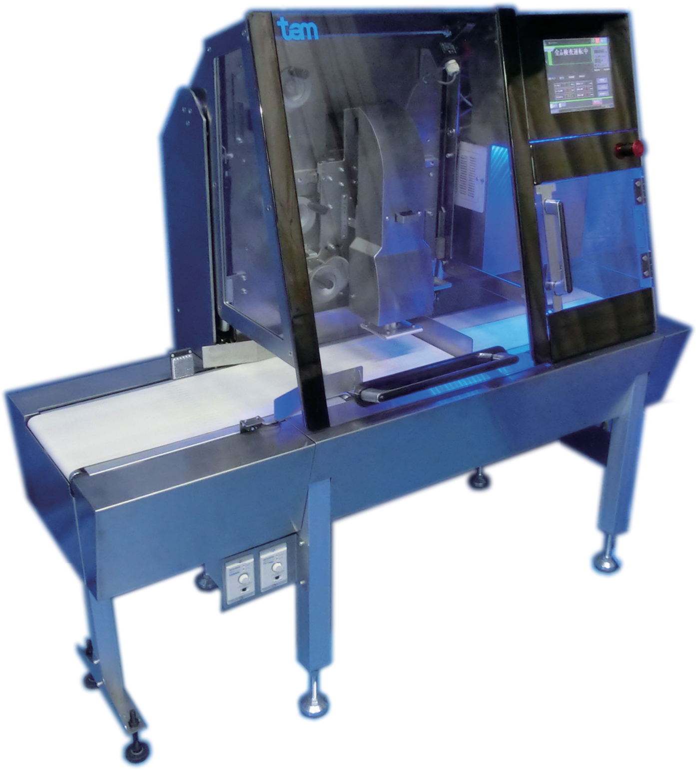

Fig. 2-49: Overall view of prototype leak detector.

by a probability density function calculated from the average value and standard deviation of equivalent jerks at a certain time, and it is evaluated as

$$\Psi(\dot{F}) = \frac{1}{\sqrt{2\pi}\sigma} e^{-\frac{(\dot{F}-\mu)^2}{2\sigma^2}}, \tag{2.32}$$

where $\Psi(\bullet)$, μ, and σ stand for the probability density, the mean value, and the standard deviation, respectively. By expressing using the probability density function, it is possible to evaluate the false detection rate of good products and the error rate of leak products quantitatively.

2.6.4 Experiments of Real-time Disturbance Compensation by EQ

Experiments are conducted to confirm the performance of the leakage inspection apparatus. The prototype of the leak detector is shown in Fig. 2-49. Firstly, the effectiveness of the EQ is confirmed. A ramp command in the direction approaching the product is given to $x^{\mathrm{C}}_{\mathrm{cmd}}$, the end effector comes into contact with a product, and when the reference reaction force is detected, the command is fixed.

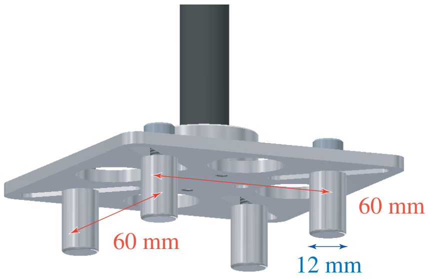

Fig. 2-50: Shape of the end effector.

Table 2.7: Experimental parameters for the EQ.

Parameter	Descriptions	Value
K_{tn}	Force coefficient	33 N/A
M_{n}	Mass of motor	1.35 kg
g_{dis}	Cut-off frequency of the DOB	800 rad/s
g_{ext}	Cut-off frequency of the RFOB	2000 rad/s

A commercially available snack confectionery product is prepared as a sample. After the elapse of 0.6 s, the ramp command in the separation direction is given and the end effector is again moved to the original position. The experiment to analyze the response when performing the above operation and to determine the presence or absence of leak is conducted. The position coordinates are defined as the stand by position of an end effector as the origin (0 mm) and the approach direction as positive. In addition, the end effector in contact with the product is made of the material SUS303 having the shape shown in Fig. 2-50. Each parameter at the time of experiment is shown in Table 2.7. The RFOB output $\hat{F}^{\mathrm{M}}_{\mathrm{ext}}$ when the control command described above is given to the inspection apparatus with a reference reaction force of 20 N. The EQ is evaluated by expressing the output of the quarrier $\hat{F}^{\mathrm{M}}_{\mathrm{env}}$ by position-force coordinates and comparing hysteresis characteristics. The results are shown in Fig. 2-51. Here, the range of 12 mm to 20 mm is the section where the end effector and the product are in contact. From the results, it can be seen that the output from the RFOB that is not compensated includes the steady-state gravity term of about 5 N and the nonlinear element of the Coulomb friction force in the vicinity of 0 mm to 2 mm. On the contrary, the output from the environmental qualifier that compensates in real time shows that these external forces are canceled. From the above, the effectiveness of the EQ was confirmed.

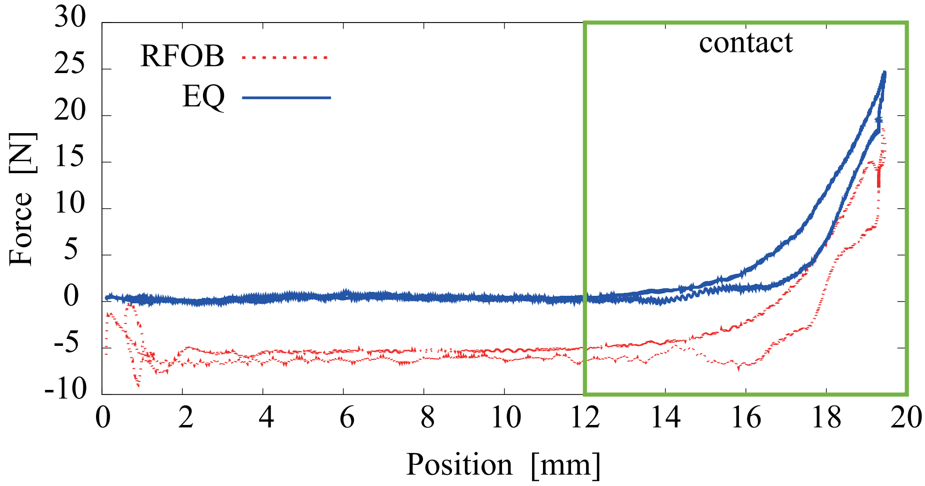

Fig. 2-51: Effect of friction compensation by the EQ.

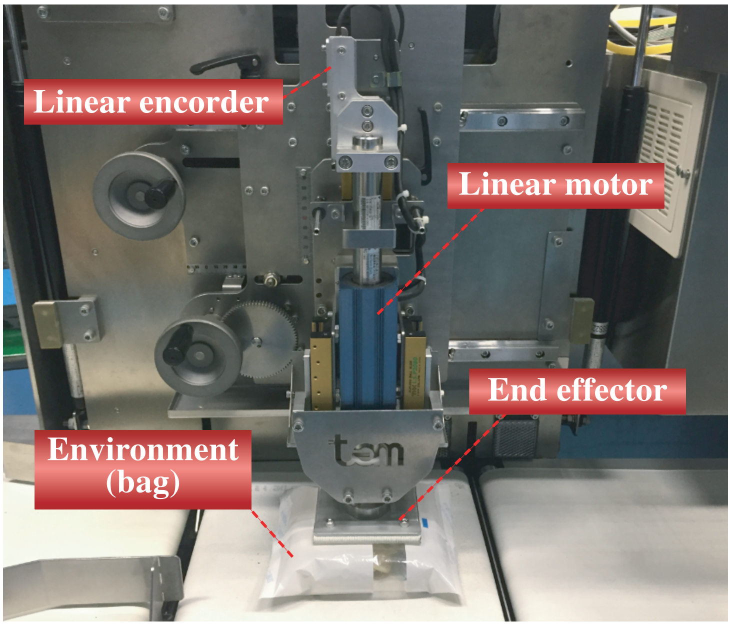

Fig. 2-52: Inspection unit of the prototype of leak detector.

2.6.5 Abstraction of Disturbance Compensator for Leak Detector Based on the EDM

Also, automatic abstraction of the compensator for the RFOB is confirmed. The inspection unit of a prototype leak detector is depicted by Fig. 2-52. In this experiments, hierarchical abstraction using the unidirectional element matrix and overall abstraction using the multidirectional element matrix are compared with changing matrix size. The structure of the element matrix is designed as shown in Fig.

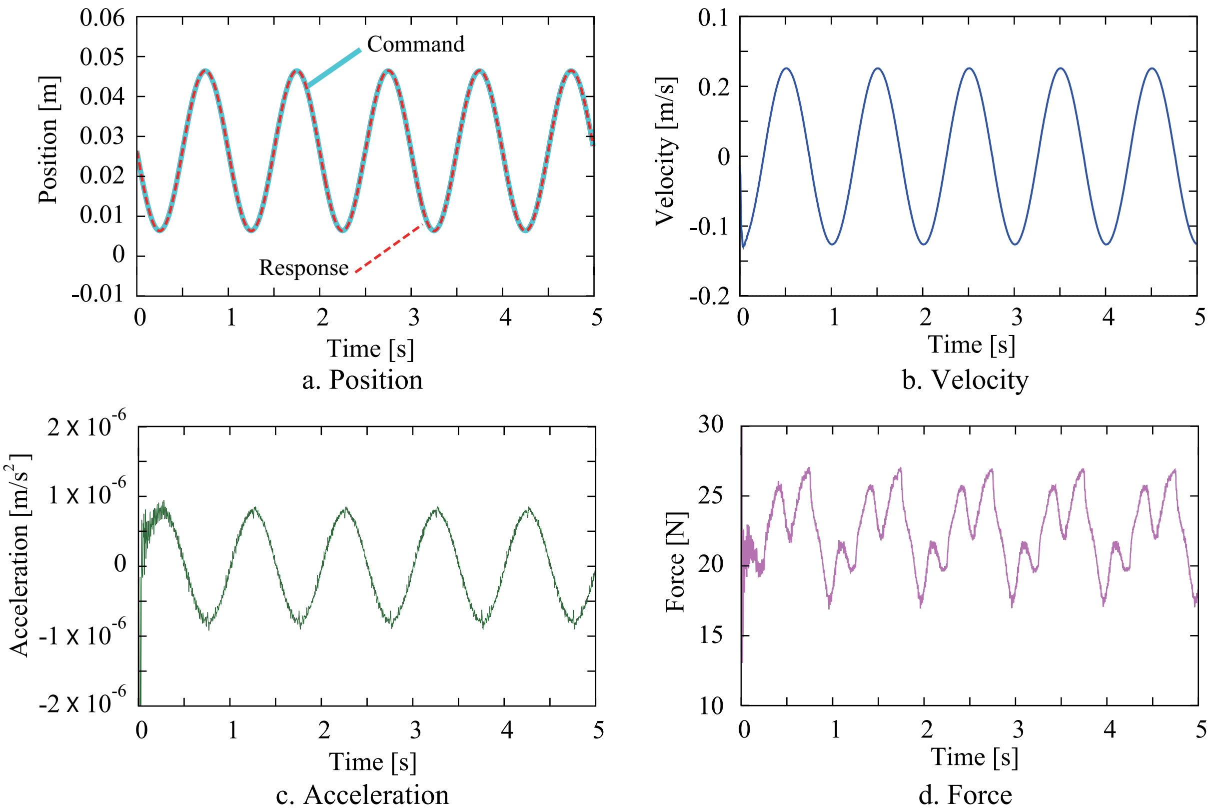

Fig. 2-53: Input data of the EDM for compensator abstraction of leak detector.

2-34. In order to abstract the compensator for the RFOB, measurement data are obtained by free motion. Sinusoidal wave (1 Hz) is applied as position command in the experiment. The prepared data is shown in Fig. 2-53. The fitness value for optimization used for abstraction of the disturbance compensator of the RFOB is calculated by (2.28). In order to avoid convergence to the local solution as much as possible, the mutation rate is designed as follows:

$$\eta_{\mathrm{mut}}^{\mathrm{c}} = \eta_{\mathrm{mut}}^{\mathrm{c,ini}} + \frac{N_{\mathrm{sty}}}{\chi_{\mathrm{c}}}, \tag{2.33}$$

$$\eta_{\mathrm{mut}}^{\mathrm{i}} = \eta_{\mathrm{mut}}^{\mathrm{i,ini}} + \frac{N_{\mathrm{sty}}}{\chi_{\mathrm{i}}}, \tag{2.34}$$

where, N_{sty} and χ_{c}represent the current stagnant number of the GA and mutations increase coefficient, respectively. The subscripts c, i, and ini refer to element code, individual, and initial value, respectively. Table 2.8 shows the simulation parameters of the EDM for compensator abstraction of the leak detector. In the experiments of overall abstraction, matrix size of the multidirectional element matrix is changed

Table 2.8: Experimental parameters for compensator abstraction of the leak detector by the EDM.

Parameter	Description	Value
T_{s}	Sampling time	0.001 s
N_{num}	Data number of time-series data	5000
I_{num}	Number of individual	8
η_{cross}	Crossover rate	0.7
$\eta_{\mathrm{mut}}^{\mathrm{c,ini}}$	Basic value of mutation rate for element code	0.2
$\eta_{\mathrm{mut}}^{\mathrm{i,ini}}$	Basic value of mutation rate for individual	0.06
$\eta_{\mathrm{mut}}^{\mathrm{p}}$	Mutation rate for parameter	0.4
$\eta_{\mathrm{mut}}^{\mathrm{id}}$	Parameter increase/decrease rate	0.7

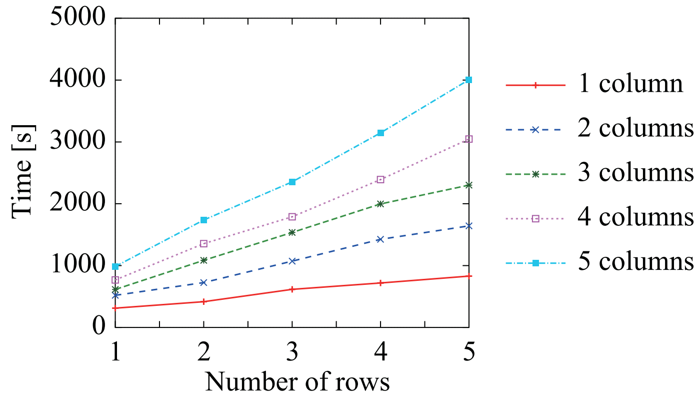

Fig. 2-54: Relationship between matrix size and calculation time.

from 1×1 to 5×5. In the experiments of hierarchical abstraction, matrix size of the unidirectional element matrix is increased from 3×1 to 3×5. The calculation program is implemented based on C++ language. A laptop personal computer (VJP131B01N, VAIO) is used for performance verification of the abstraction by the EDM. The CPU of the laptop personal computer is Core i7-4510U, and memory size is 8 GB. A relationship between matrix size calculation time is shown in Fig. 2-54 when 20,000 times alternation of generations are performed. Firstly, a performance of overall abstraction using the multidirectional element matrix is confirmed. A relationship between fitness value after 20,000 times alternation of generations and matrix size is confirmed experimentally. Fig. 2-55 depicts the relationship between fitness value after 20,000 times alternation of generations and matrix size. Fig. 2-55a shows the average value of final fitness value when trials of optimization for 20,000 times alternation of generations with each matrix size are made three times. From average value of this example, around the 3×3 and 5×2 became good fitness value on average. In the case of overall abstraction using the multidirectional

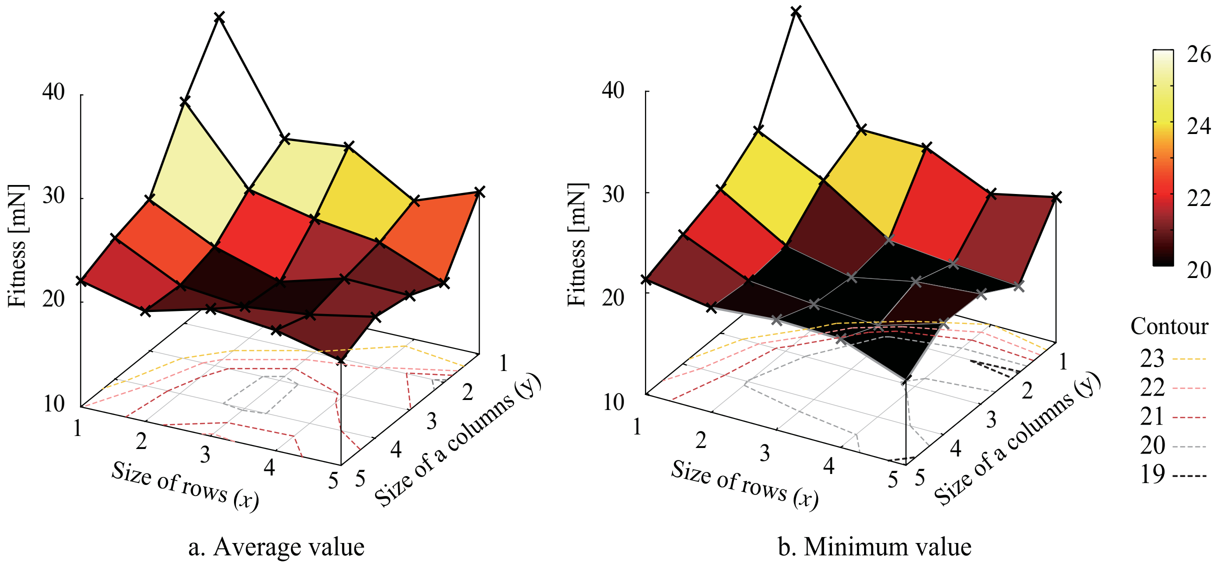

Fig. 2-55: Relationship between matrix size and fitness value.

element matrix, it was confirmed that even if the matrix size was simply increased, the average value of final fitness value would not be improved. Fig. 2-55b shows the minimum value of final fitness value when trials of optimization for 20,000 times alternation of generations with each matrix size are made three times. From Fig. 2-55b, it can be confirmed that 5 $\times$ 5 and 5 $\times$ 2 became the best fitness value.

A matrix with a large element size encompasses expressive power of a matrix with a small element size. Therefore, the larger the element size, the higher the expressive ability. Hence, in the case of 5 $\times$ 5, the minimum value is the smallest. However, the possibility of falling into local optimum is also increased, and the average value is considered to be smaller for 3 $\times$ 3. Since expressiveness increases as the number of elements increases, this is an algorithm limit. Therefore, if improvement of the algorithm can be achieved, the result of optimization is considered to be better as the matrix size is larger. On the other hand, over learning is one of the problems, and it is one of the important issues to continue to optimize. Discrimination between high-precision abstraction and over-learning is one of the important issues in making decisions to end abstraction. In this result, it is desirable to design the number of all abstraction elements in about 3 $\times$ 3 considering the readability of the results and the stability of learning.

Then, a performance of hierarchical abstraction using the unidirectional element matrix is confirmed. Fitness values of hierarchical abstraction is evaluated based on comparison with overall abstraction. Fig. 2-56 shows a comparison of fitness values of overall abstraction and hierarchical abstraction. From Fig. 2-56, it can be seen that the fitness values of the hierarchical abstraction monotonously decreases

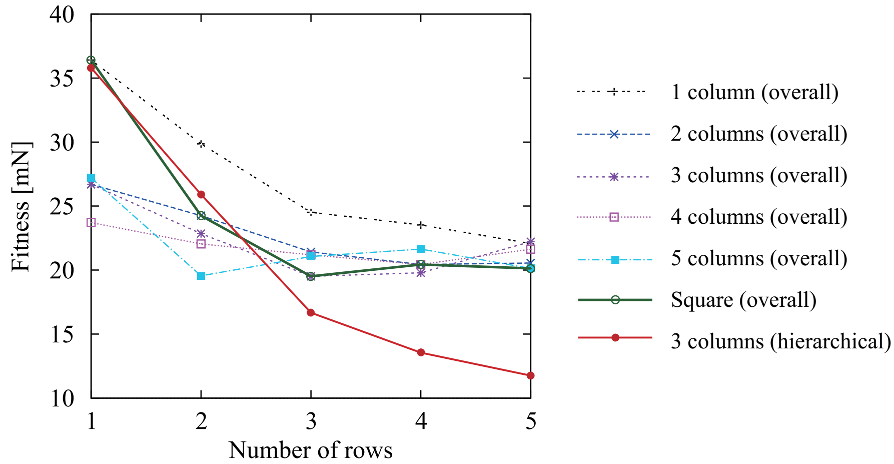

Fig. 2-56: Comparison of fitness values of overall abstraction and hierarchical abstraction.

according to the number of rows. This is because it will never be exacerbated by the elite preservation strategy. In addition, by increasing the number of elements to 3 × 3 or more, it became better than the fitness value of the overall abstraction. From this result, it was confirmed that hierarchical abstraction can achieve wasteful abstraction with a small number of elements.

Here, force responses of disturbance compensator are confirmed. Fig. 2-57 shows force response of disturbance compensation using overall abstraction and hierarchical abstraction. In this confirmation, waveforms of overall abstraction is a result using 5 × 5 matrix because it has smallest fitness value. In addition to the final output from the element matrix, the output from each row is also depicted. Waveforms of hierarchical abstraction is the outputs of 3 × 5 matrix (i.e., fifth hierarch). The output from each row is also shown as well as overall abstraction. As it can be seen, hierarchical abstraction has a clean hierarchical structure, and the output with high importance comes to the upper side. On the contrary, overall abstraction, each row of the importance is not in order. Fig. 2-58 shows enlarged view of compensation values outputted by overall abstraction and hierarchical abstraction that is indicated by orange dotted line in Fig. 2-57. Comparing results of overall abstraction and hierarchical abstraction, the result of hierarchical abstraction grasps the characteristics of the measured values well.

Then, abstraction results by the EDM are analyzed. Firstly, the result of the hierarchical abstraction is shown. Table 2.9 is refers to the abstraction result of disturbance compensator using hierarchical abstraction. The signal flow of each element is shown in Fig. 2-59. Considering the correspondence between Table 2.9 and Fig. 2-59, understanding operation of each element is promoted. From these

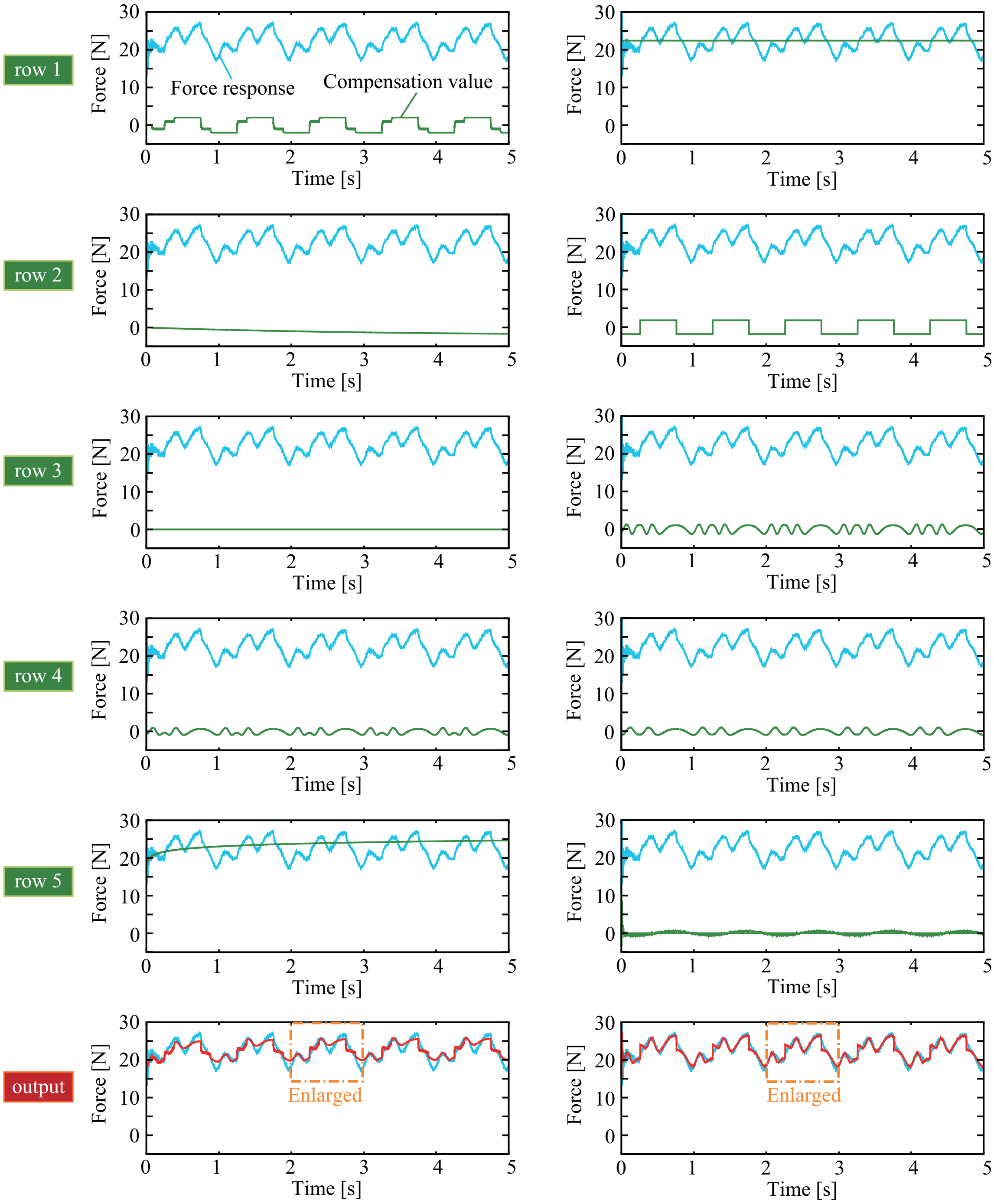

a. Overall abstraction.   b. Hierarchical abstraction.

Fig. 2-57: Compensation values of each row of overall abstraction and hierarchical abstraction.

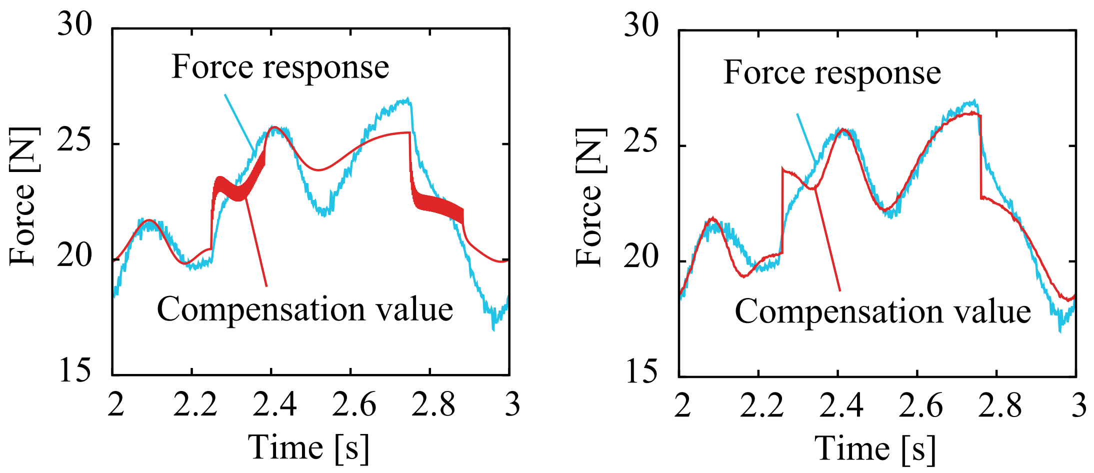

a. overall abstraction. b. hierarchical abstraction.

Fig. 2-58: Enlarged view of compensation values.

Table 2.9: Abstraction result of disturbance compensator using hierarchical abstraction.

$\dot{x}_{\mathrm{res}}$ Velo.	**OFS** Offset $a_1 = 8.50 \times 10^1$	**LOG** Logarithmic $-$	**PP** Power gain $a_3 = 5.04$
$\dot{x}_{\mathrm{res}}$ Velo.	**SINA** Sine wave (amp.) $a_4 = 7.93 \times 10^{-3}$	**SGN** Sign function $--$	**P** Gain $a_6 = 1.83$
x_{res} Pos.	**LOG** Logarithmic $-$	**PP** Power gain $a_8 = 5.82$	**SINA** Sine wave (amp.) $a_9 = 1.26$
x_{res} Pos.	**LOG** Logarithmic $-$	**P** Gain $a_{11} = 4.03$	**SINP** Sine wave (phase) $a_{12} = 4.33 \times 10^{-1}$
$\dot{x}_{\mathrm{res}}$ Velo.	**D** Derivative $a_{13} = 2.55 \times 10^{-1}$	**PLE** Phase-lead comp. $a_{14} = 4.22$	**INV** Invert $-$

results, equivalent transformation is conducted. Fig. 2-60 shows a result of equivalent transformation of Table 2.9. Considering Fig. 2-60, it can be understood that the first line represents gravity and the second line represents Coulomb friction, respectively. The third and fourth lines are considered to be spatially dependent terms. It is possible to understand the spatial frequency from the gain before entering the trigonometric function. In the fifth row, since the compensation value is large in the portion with large acceleration, such as the beginning of movement, it is considered to be an acceleration-dependent term.

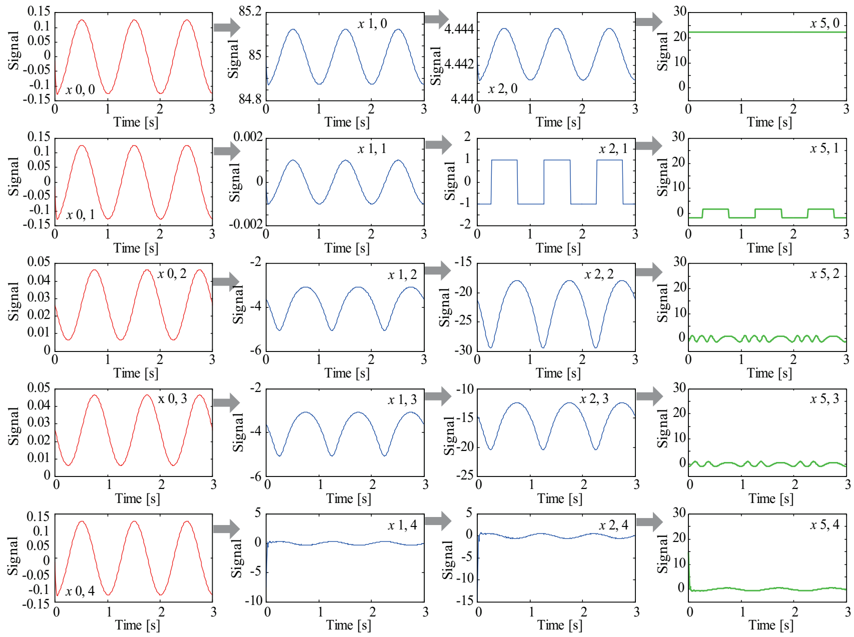

Fig. 2-59: Signal flow of compensator using hierarchical abstraction.

In this way, the results obtained by the hierarchical abstraction are easy to interpret the physical meaning. Then, the result of the overall abstraction is discussed. The abstraction result of disturbance compensator using overall abstraction by 5×5 matrix is shown in Table . The signal flow of each element is shown in Fig. 2-61. The first row is considered to represent the friction term. Since gravity is included in this system, a term that contain constant value should be extracted. However, it could not obtain a line whose output was constant in the whole abstraction. When adding the outputs of the second row and the fifth row, values close to the gravity term are obtained. From this result, it was confirmed that overall abstraction with a large matrix size may not be able to successfully isolate the elements of the true model.

Then, as a result of smaller matrix size, the result of matrix size 3×3 is analyzed. Fig. 2-62 stands for the force response of disturbance compensation using 3×3 overall abstraction. The abstraction result is shown in Table 2.11. The result of equivalent transformation of Table 2.11 is shown in Fig. 2-63. By decoding the result, three compensators are derived: the cogging compensator, friction compensator, and gravity compensator. From this result, a simple compensator of the RFOB was generated automatically by overall abstraction. Based on these results, guidelines on how to properly use hierarchical abstraction and overall abstraction are described. By using hierarchical abstraction, highly accurate models can be abstracted, and interpretation of physical meanings is relatively easy. Therefore, the use of hierarchical

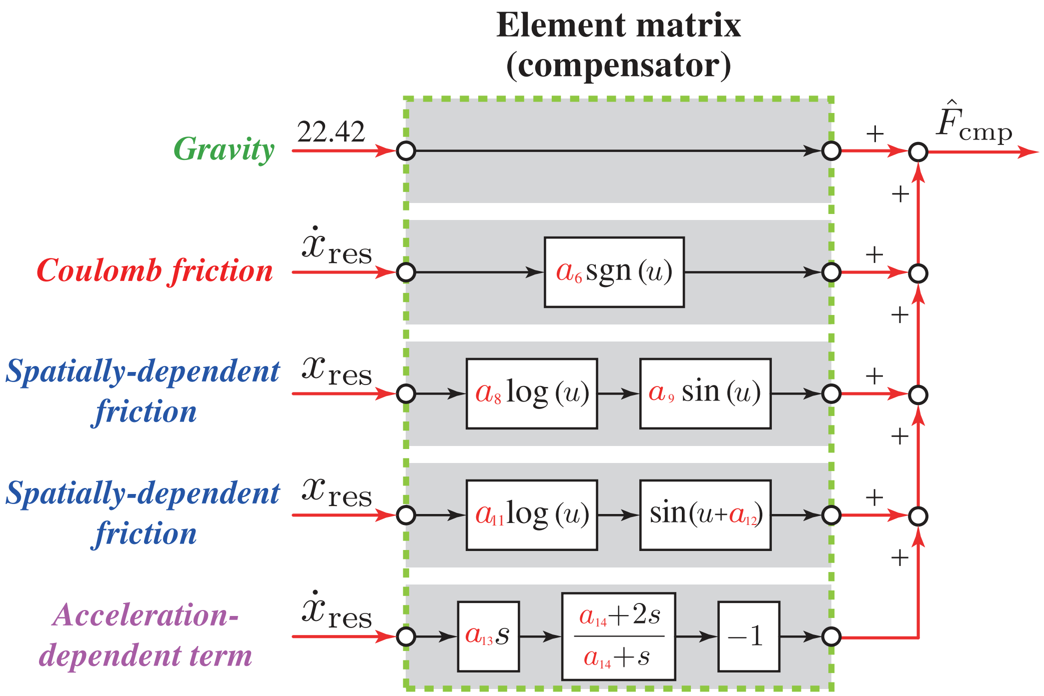

Fig. 2-60: Equivalent transformation of Table 2.9.

Table 2.10: Abstraction result of disturbance compensator using overall abstraction.

$x_{\rm res}$ Pos.	**FB** Feedback $a_1 = 3$	**HYS** Hysteresis $a_2 = 1.44 \times 10^{-2}$	**HYS** Hysteresis $a_3 = 8.55 \times 10^{-2}$	**PC** Phase compensator $a_4 = 1.58 \times 10^2$ $b_4 = 3.31 \times 10^{-1}$	**INV** Invert – –
– None	**P** Gain $a_6 = 1.00 \times 10^1$	**SINA** Sine wave $a_7 = 1.98 \times 10^{-3}$	**OW** One way –	**OFS** Offset $a_9 = 2.09$	**LPF** Low pass filter $a_{10} = 3.17 \times 10^{-1}$
$x_{\rm res}$ Pos.	**CM** Combine –	**DZ** Dead zone $a_{12} = 1.70 \times 10^{-2}$	**ATN** Arc tangent –	**POW** Power $a_{14} = 9.70 \times 10^{-1}$	**DT** Dead time $a_{15} = 2.17 \times 10$
$x_{\rm res}$ Pos.	**log** Logarithmic –	**INV** Invert –	**P** Gain $a_{18} = 4.96$	**INV** Invert –	**SINA** Sine wave $a_{20} = 9.42 \times 10^{-1}$
– None	**HPF** High pass filter $a_{21} = 1.06 \times 10^2$	**SGN** Sign function –	**I** Integral $a_{23} = 9.85 \times 10^{-11}$	**TH** Through –	**log** Logarithmic –

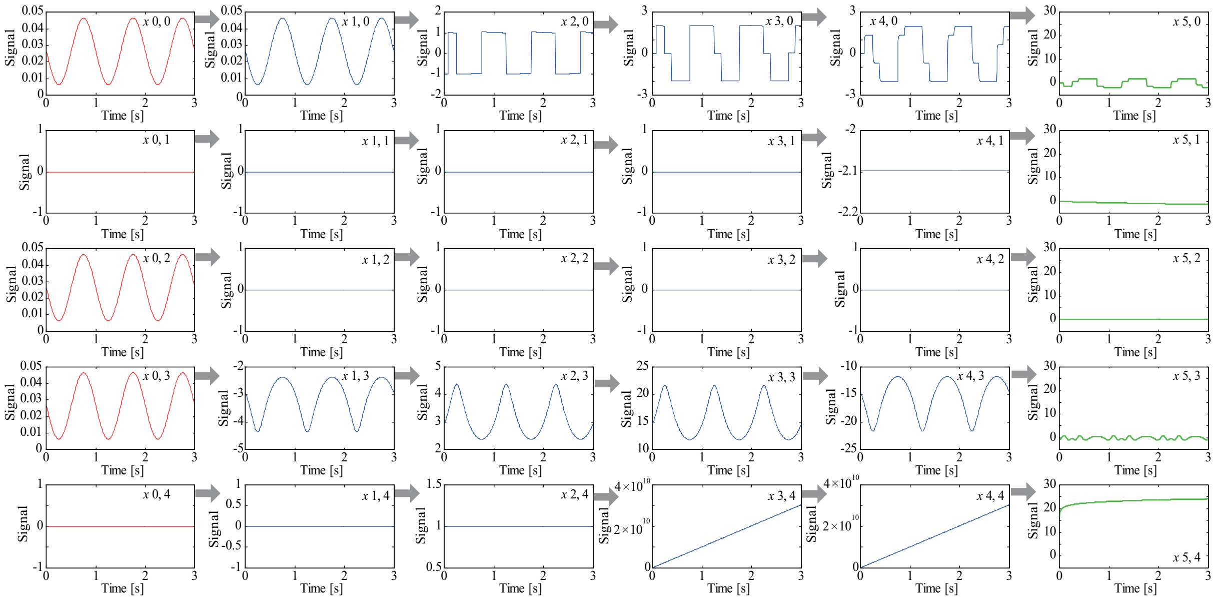

Fig. 2-61: Signal flow of compensator using overall abstraction.

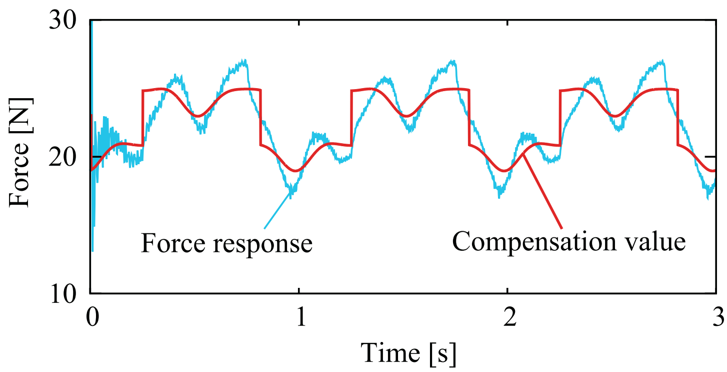

Fig. 2-62: Force response of disturbance compensation using 3×3 overall abstraction.

abstraction is desirable; however, it spends a little time. If time-consuming abstraction is required, overall abstraction should be used. In the case of overall abstraction, it is desirable not to increase the number of elements unnecessarily. Because good results are obtained and relatively easy to understand physical meanings, it is effective to use about 3×3 element matrix.

2.6.6 Experiments of Leak Detection

Then, experiments are conducted to determine the presence or absence of leak based on the obtained haptic information. Samples with no leakage and specimens with pinholes with the diameter of 0.5 mm

Table 2.11: Abstraction result of friction of the leak detector.

x_{res} Position response	**BR** Branch –	**P** Gain $a_2 = 1.66 \times 10^2$	**SIN** Sine wave –
$\dot{x}_{\mathrm{res}}$ Position response	**OS** Offset $a_4 = -4.79 \times 10^{-4}$	**SGN** Sign function –	**BR** Branch –
– –	**OS** Offset $a_7 = 2.98 \times 10^{-1}$	**ATN** Arc tangent –	**OS** Offset $a_9 = 2.17 \times 10$

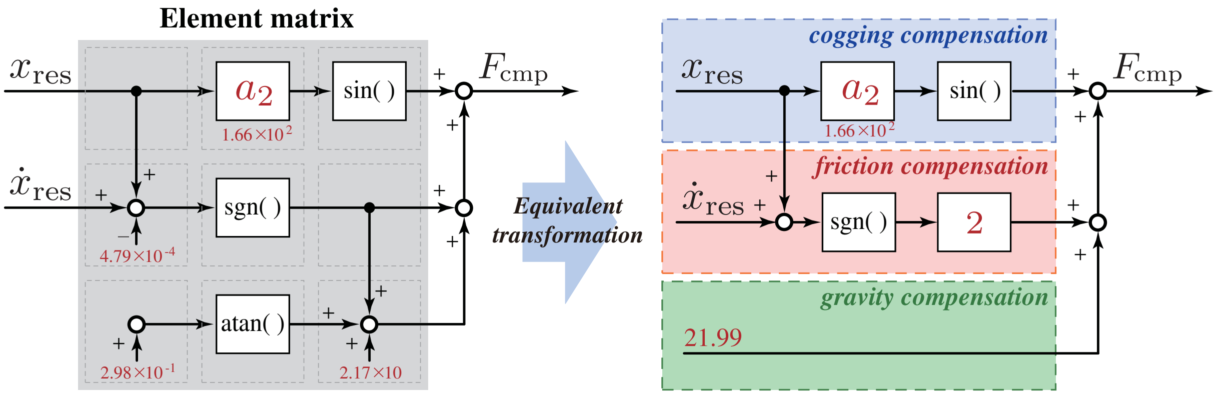

Fig. 2-63: Abstraction result of disturbance compensator using 3×3 overall abstraction.

are prepared, and reaction force estimates are compared. It is difficult to manually detect a pinhole with the diameter of 0.5 mm at a speed equivalent to 30 pieces per minute, and if this detection becomes possible, a leak inspection apparatus with industrial value can be realized. The time when the reaction force response value reaches 60 N is handled as the trigger to start the inspection. Position response and force response are shown in Fig. 2-64. There is no clear difference in the response of reaction force due to the presence or absence of leak. Here, in order to clearly grasp the phenomenon of leakage, the reaction force information is time-differentiated and converted into an equivalent jerk. The converted waveform is shown in Fig. 2-65. From Fig 2-65, it can be seen that a clear difference appears in the waveforms depending on the presence or absence of leak between 0.2 s and 0.6 s by calculating equivalent jerk. By converting the reaction force information into the equivalent jerk, it became possible to judge the presence or absence of leak. In the subsequent experiments, the accuracy of the judgment when judging the presence or absence of leak at 0.5 s was verified.

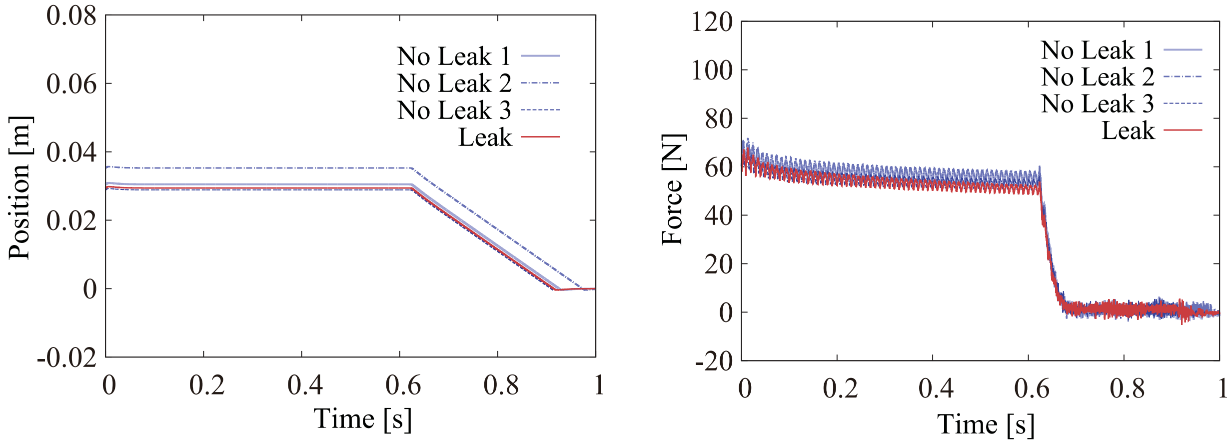

a. Position response.

b. Reaction force.

Fig. 2-64: Experimental results of leak detection.

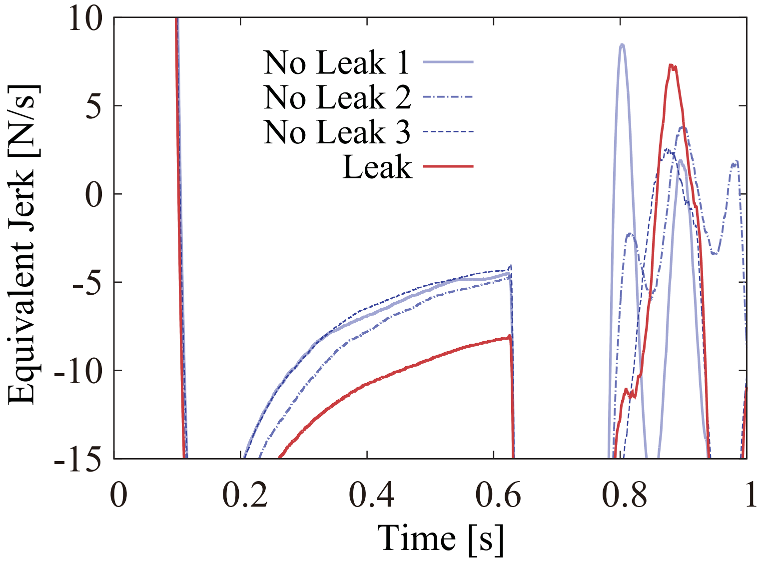

Fig. 2-65: Comparison of equivalent jerks.

Here, the experiments are conducted in order to confirm whether or not the presence or absence of a leak can be detected even when individual differences such as differences in the amount of air sealed in products occur. Three types of specimens with different enclosures in air are prepared, and the equivalent jerk at 0.5 s time point is measured in a state without leakage and a pinhole with the diameter of 0.5 mm opened. The results are shown in Table 2.12. From the experimental results, it was confirmed that the

Table 2.12: Results of equivalent jerk.

Sample	Thickness [m]	Equivalent jerk [N/s]	
		No leak	Leak
1	0.0294	-5.430	-9.380
2	0.0347	-5.908	-9.391
3	0.0289	-5.122	-10.36

Table 2.13: Statistics of equivalent jerk.

Sample	Average [N/s]	Standard deviation [N/s]
No leak	-5.090	0.263
Leak	-10.174	0.383

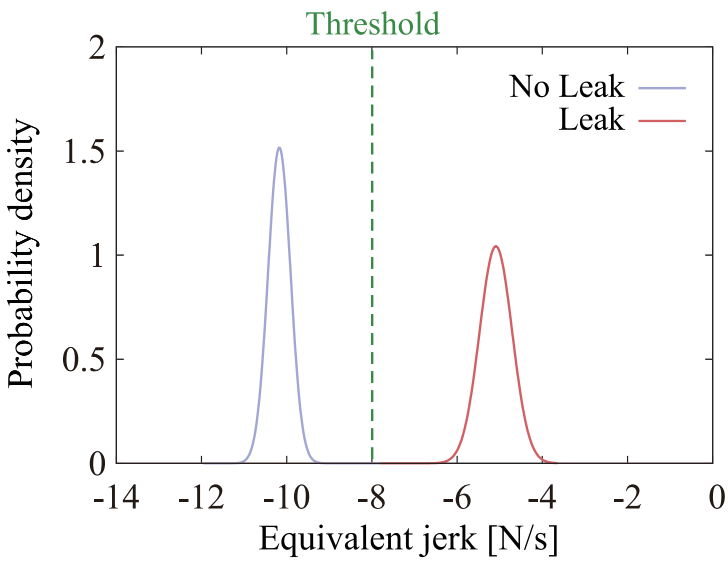

Fig. 2-66: Probability density of equivalent jerk.

presence or absence of leakage can be discriminated even when the bag thickness is different.

Then, in order to confirm the repeatability of leak detection, statistical evaluation is conducted. Samples with no leakage and specimens with the pinholes are prepared one by one, and the equivalent jerk values at 0.5 s are compared. Each individual is measured 20 times, and the probability distribution is calculated from the average value and the standard deviation. The results are shown in Table 2.13 and Fig. 2-66. When the threshold is set at 8 N/s shown in the figure, the false detection rate of non-defective products becomes 1.443×10^{-14} from the probability density, and the misperception rate of leak item becomes 7.261×10^{-17}, respectively. Therefore, it was confirmed that it can be detected with sufficient accuracy.

2.7 Summary of Chapter 2

Chapter 2 described the fundamental structure of the EDM. By using the EDM, model and parameters of a target system can be abstracted simultaneously. Therefore, determination of the model in advance is not needed. Also, the hierarchical abstraction method can extract important physical laws in order. The accuracy of the model is determined based on abstraction depth by using the hierarchical abstraction procedure. Since there is a trade-off between the simplicity and accuracy of the abstraction result, it is necessary to decide the abstraction depth based on accuracy requirement of target application. By using the EDM, it is abstracted with a necessary and sufficient model. In addition, the abstraction result is understandable because it is expressed by the combination of simple elements. As a result, abstracted results can be inherited to different systems, so that knowledge can be utilized. The validity of the proposed hierarchical abstraction based on the EDM was confirmed by generating the compensator for the RFOB of powder filling machine. The disturbance compensator was generated precisely by hierarchical abstraction of the EDM. In addition, when abstraction in a short time is required, overall abstraction is effective. By overall abstraction, it is possible to abstract systems collectively. If the matrix size is made too large, the possibility of falling into a local solution increases due to the constraints of the algorithm. Futhermore, the readability of the abstraction result decreases. Therefore, it is preferable not to increase the matrix size beyond necessity. The validity of the proposed overall abstraction based on the EDM was confirmed by generating the compensator for the RFOB of leak detector. In the experiment of abstraction using the leak detector, it was led that the size of about 3×3 is reasonable. An experimental comparison of hierarchical abstraction and overall abstraction was also conducted. As a result, it was confirmed that it is desirable to use hierarchical abstraction when abstraction precision and readability are required. On the other hand, when system abstraction in short time is required, it is confirmed that overall abstraction is effective.

Chapter 3

Interactive Control Design Based on Element Description Method

3.1 Interactive Control Design for a Multi-mass Resonant System

3.1.1 Overview of Control Generation of Multi-mass Resonant System

In this section, interactive control design using the EDM is described. As mentioned in chapter 2, it is possible to abstract system interactively between human and machine by taking advantage of the characteristics of the EDM that the determination of the model is unnecessary and the physical meaning of the obtained mathematical expression is possible. By performing interactive control design using the EDM, a synergistic effect of human knowledge and machine's computing power can be expected. In this study, position controller for a multi-mass resonant system is created by the EDM. Fig. 3-1 shows the overview of a multi-mass resonant system. Precise position control method of a multi-mass resonant system is one of the important technologies for automatic machinery. There are various conventional researches to control a multi-mass resonant system precisely. A notch filter is one of the most famous methods to reduce a resonant vibration [71]. This method is used for various industrial machine because the structure is simple. Similarly, a phase compensator is used to stabilize a resonant system [72]. Resonant ratio control [73] is one of the famous methods categorized as a phase compensator. One of the problems of the controller designing for a multi-mass resonant system is that a design process becomes complex when a number of mass increases. Moreover, it is difficult to decide the order of the model. A

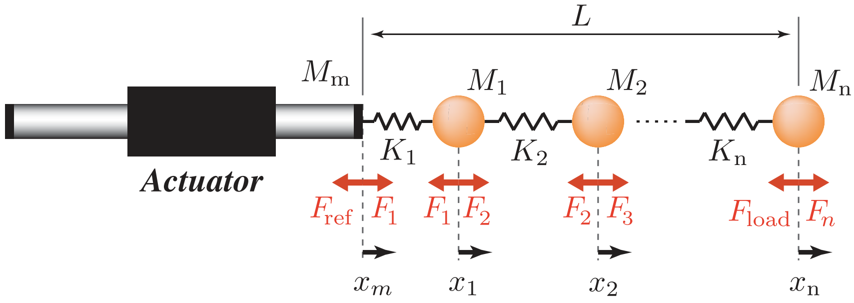

Fig. 3-1: Overview of a multi-mass resonant system.

multi-mass resonant system is generalized as Figs. 3-6 to 3-5. Here, $m_i, i \in \mathbb{N}$ is defined as

$$m_i \triangleq \frac{1}{M_i s^2}, \tag{3.1}$$

where M_i denotes mass of i-th mass. As s Figs. 3-6 to 3-5, multi-mass resonant system is generated using G_a and G_b. From Figs. 3-6 to 3-5, G_a and G_b are generated based on continued fraction as follows:

- Single-mass system

$$G_a^{1,1}(s) = k_1, \tag{3.2}$$

$$G_b^{1,1}(s) = m_1. \tag{3.3}$$

- 2-mass resonant system

$$G_a^{2,2}(s) = \frac{m_1}{1+m_1 k_1}, \tag{3.4}$$

$$G_b^{2,2}(s) = \frac{k_2}{1+k_2 m_2}. \tag{3.5}$$

- 3-mass resonant system

$$G_a^{3,3}(s) = \frac{k2}{1+k_2\dfrac{m_1}{1+m_1 k_1}}, \tag{3.6}$$

$$G_b^{3,3}(s) = \frac{m2}{1+m_2\dfrac{k_2}{1+k_2 m_2}}. \tag{3.7}$$

- 4-mass resonant system

$$G_a^{4,4}(s) = \cfrac{m_2}{1+m_2\cfrac{k2}{1+k_2\cfrac{m_1}{1+m_1k_1}}}, \tag{3.8}$$

$$G_b^{4,4}(s) = \cfrac{k_3}{1+k_3\cfrac{m2}{1+m_2\cfrac{k_2}{1+k_2m_2}}}. \tag{3.9}$$

- general formula of N-mass resonant system
  - In case of even number ($N = 2n, n \in \mathbb{N}$)

$$G_a^{N,N}(s) = \cfrac{m_{\frac{N}{2}}}{1+m_{\frac{N}{2}}\cfrac{k_{\frac{N}{2}}}{1+k_{\frac{N}{2}}\cfrac{m_{\frac{N}{2}-1}}{1+m_{\frac{N}{2}-1}\ddots}}}, \tag{3.10}$$

$$G_b^{N,N}(s) = \cfrac{k_{\frac{N}{2}+1}}{1+k_{\frac{N}{2}+1}\cfrac{m_{\frac{N}{2}+1}}{1+m_{\frac{N}{2}+1}\cfrac{k_{\frac{N}{2}+2}}{1+k_{\frac{N}{2}+2}\ddots}}}. \tag{3.11}$$

  - In case of odd number ($N = 2n + 1$)

$$G_a^{N,N}(s) = \cfrac{k_{\frac{N+1}{2}}}{1+k_{\frac{N+1}{2}}\cfrac{m_{\frac{N+1}{2}-1}}{1+m_{\frac{N+1}{2}-1}\cfrac{k_{\frac{N+1}{2}-1}}{1+k_{\frac{N+1}{2}-1}\ddots}}}, \tag{3.12}$$

$$G_b^{N,N}(s) = \cfrac{m_{\frac{N+1}{2}}}{1+m_{\frac{N+1}{2}}\cfrac{k_{\frac{N+1}{2}+1}}{1+k_{\frac{N+1}{2}+1}\cfrac{m_{\frac{N+1}{2}+1}}{1+m_{\frac{N+1}{2}+1}\ddots}}}. \tag{3.13}$$

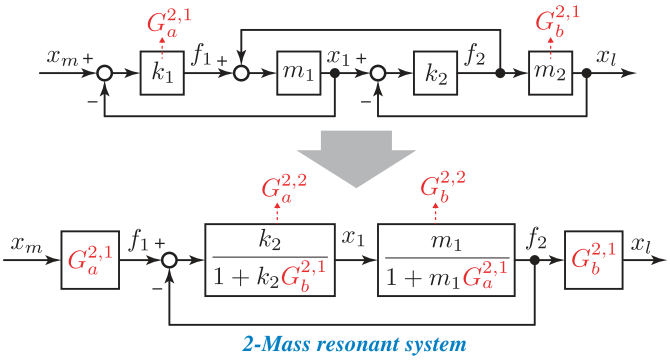

Fig. 3-2: Block diagram of a 2-mass resonant system.

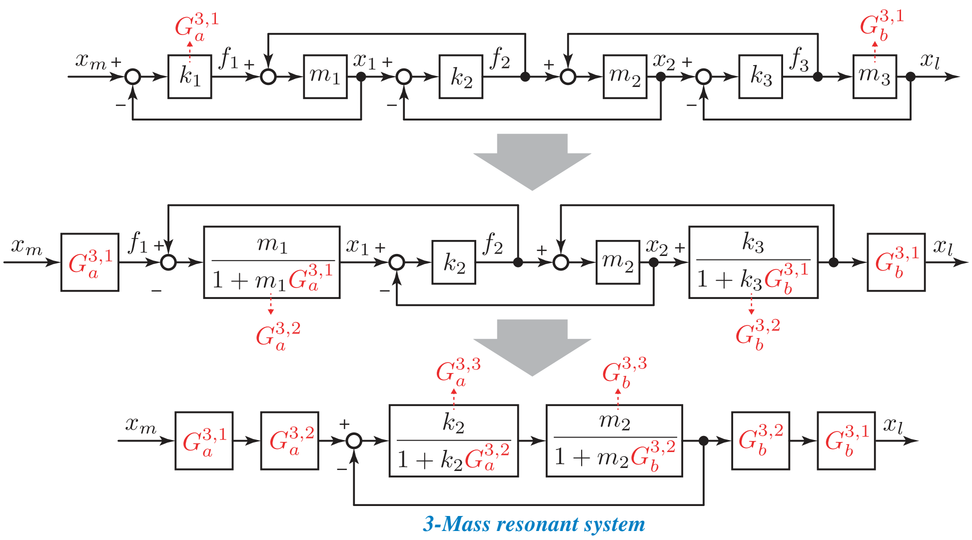

Fig. 3-3: Block diagram of a 3-mass resonant system.

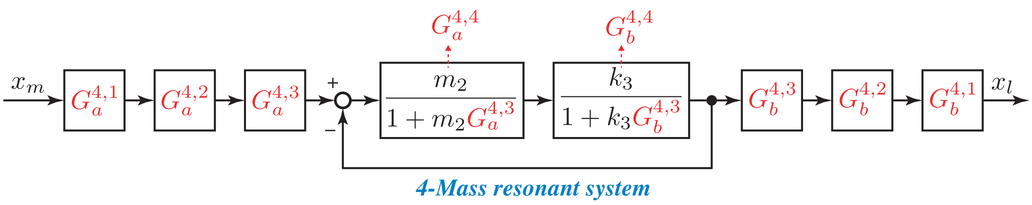

Fig. 3-4: Block diagram of a 4-mass resonant system.

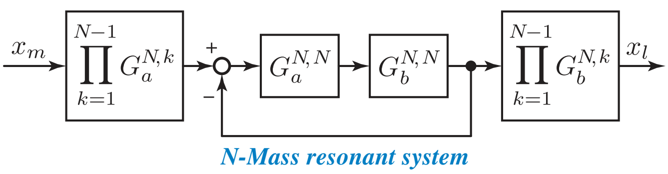

Fig. 3-5: Block diagram of an N-mass resonant system.

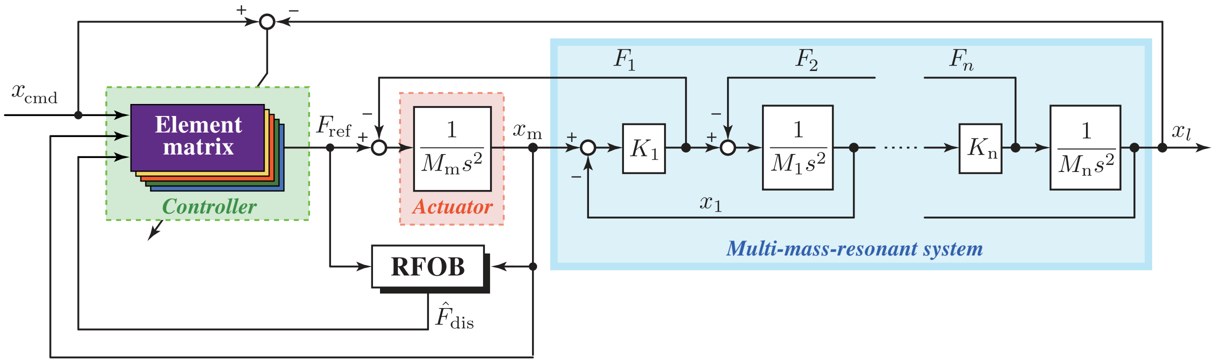

Fig. 3-6: Block diagram of automatic controller design for a multi-mass resonant system.

Table 3.1: Simulation parameters of the EDM for controller synthesis.

Parameter	Description	Value
T_{s}	Sampling time of controller	0.0005 s
P_{s}	Calculation period of plant	0.0001 s
l_{e}	Distance of each mass point	0.05 m
K_{e}	Stiffness between each mass	10,000 N/m
D_{e}	Damper between each mass	50 Ns/m
M_{e}	Weight of each mass point	0.05 kg
M_{m}	Weight of motor mover	0.1 kg

A wave system [74] is one of the effective methods to deal with a high-order multi-mass resonant system. A vibration control by the wave model suppresses up to the high-order vibration with a simple implementation. However, when a deviation occurs in the primary resonance frequency, it is difficult to compensate because the frequencies of higher-order plants and compensator become different. Furthermore, it is difficult to compensate if the high-order resonance point is not a real number multiple of the primary resonance frequency. Fig. 3-6 depicts a block diagram of automatic controller design for a multi-mass resonant system. As the input vector, the load-side position command, the motor position response value, and the estimated disturbance value of the motor are given to the element matrix. The controller designing for a high-order multi-mass resonant system by the EDM is one of the effective method because it can create controllers automatically even if the target system is complicated. In addition, by using hierarchical abstraction, the performance of the controller can be arbitrarily determined. Figs. 3-2 to 3-4 are generalized equivalent transformation of a multi-mass resonant system. In this study, a 5-mass resonant system is applied as the high-order multi-mass resonant system. Table 3.1 refers to simulation conditions.

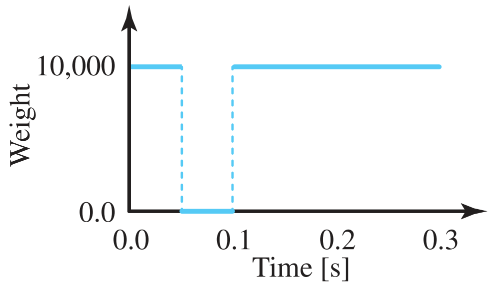

Fig. 3-7: Window function of Step 1.

3.1.2 Example of Interactive Control Design of Multi-mass Resonant System

In this study, position control of a 5-mass resonant system is considered. Position command is applied by a modified sine wave [75] which is generally used in automatic machinery. Since the modified sine wave is possible to calculate the infinite-order derivatives, it is effective to verify the feed-forward controller. The position controller is synthesized by hierarchical abstraction using the EDM. The fitness function is designed as

$$\Gamma_{\mathrm{reso}} = \frac{1}{N_{\mathrm{sum}}} \sum_{q=1}^{N_{\mathrm{sum}}} \Lambda(q) \cdot \sqrt{(x_{\mathrm{cmd}}[q] - x_1[q])^2}. \tag{3.14}$$

As selectable inputs, the position command value x_{cmd}, motor position response x_{m}, position error x_{err}, RFOB disturbance estimated value $\hat{F}_{\mathrm{ext}}$, non-dimensional speed of modified sine (dimensionless differential value of position command) V_{cmd}, dimensionless acceleration of modified sine (the dimensionless second-order differential value of the position command) A_{cmd} are prepared.

Step 1 : Suppression of Vibration

In Step 1, element matrix is designed as 3×1 matrix, and a simple proportional controller is prepared as the initial individual of the EDM. In addition, the window function in Step 1 is designed as

$$\Lambda(q) = \begin{cases} 10,000 & (q < \frac{0.05}{T_{\mathrm{s}}}) \\ 0 & (\frac{0.05}{T_{\mathrm{s}}} \leq q < \frac{0.1}{T_{\mathrm{s}}}) \\ 10,000 & (\frac{0.1}{T_{\mathrm{s}}} \leq q), \end{cases} \tag{3.15}$$

where T_{s} denotes sampling time of time-series data. The window function in Step 1 is depicted in Fig. 3-7. This window function is designed to eliminate steady-state error. Fig. 3-8 denotes fitness response of Step 1. It turns out that fitness decreases according to evolution. The position response in the process of

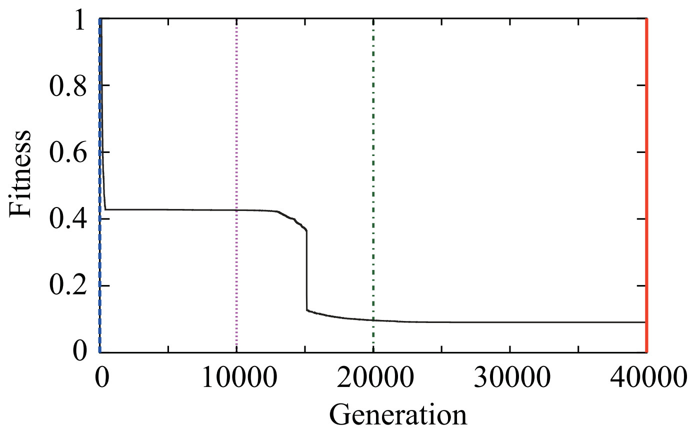

Fig. 3-8: Fitness response of Step 1.

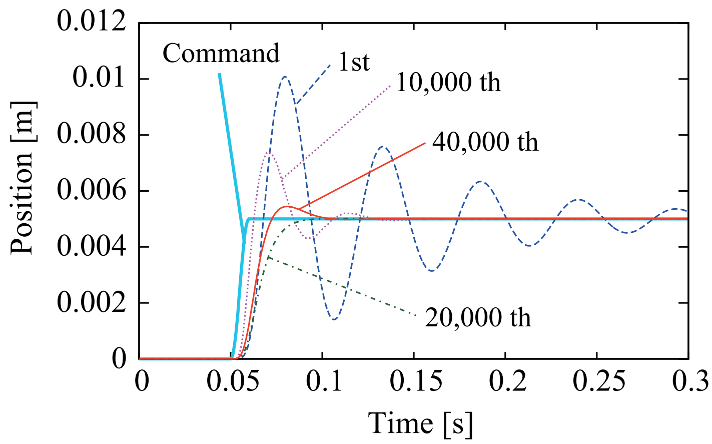

Fig. 3-9: Position response of Step 1.

Table 3.2: The chromosome of the final individual in Step 1.

x_{err}	**P**	**HPF**	**PLA**
Position error	Gain	High-pass filter	Phase-lag comp.
	$a_1 = 7.6325 \times 10^7$	$a_2 = 99501.6$	$a_3 = 0.0281555$

evolution is shown in Fig. 3-9. Since the initial individual is a simple proportional controller, vibrations are generated; however it can be confirmed that the vibration is subsided by learning by the EDM in the final individual. Each mass response of 40,000 th generation in Step 1 is shown in 3-10. The chromosome of the final individual is shown in Table 3.2.

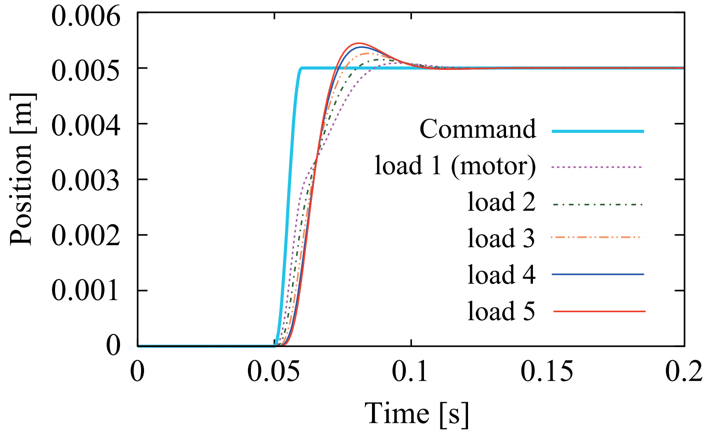

Fig. 3-10: Each mass response of 40,000 th in Step 1.

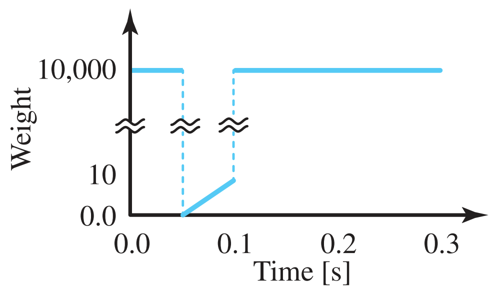

Fig. 3-11: Window function of Step 2.

Step 2 : Improvement of Transient Response

In Step 2, element matrix is designed as 3×2 matrix. The initial individual of Step 2 is given by the abstraction result of Step 1. The window function in Step 2 is designed as

$$\Lambda(q) = \begin{cases} 10,000 & (q < \frac{0.05}{T_s}) \\ 200(qT_s - 0.05) & (\frac{0.05}{T_s} \leq q < \frac{0.1}{T_s}) \\ 10,000 & (\frac{0.1}{T_s} \leq q), \end{cases} \tag{3.16}$$

The weight of transient response area is increased from Step 1 in order to improve transient response. The window function in Step 2 is depicted in Fig. 3-11. To keep the result of the abstraction in Step 1, the mutation and crossover processing applies only to the second line in Step 2. On the contrary, in consideration of the interaction between the parameters of the first row and the second row, the parameter shift processing is applied to all elements. Fig. 3-12 denotes the fitness response of Step 2. It can be seen that fitness by the evolution is decreasing. Fig. 3-13 stands for the position responses in the final

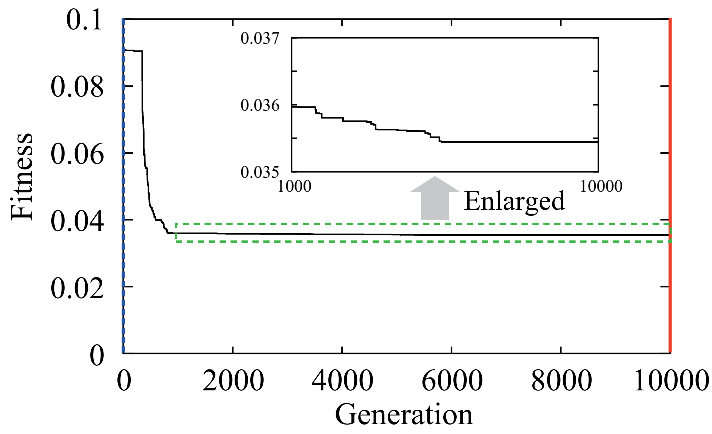

Fig. 3-12: Fitness response of Step 2.

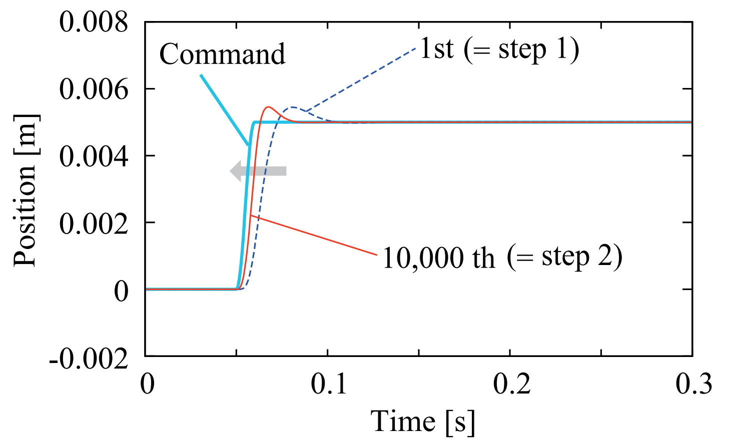

Fig. 3-13: Position response of Step 2.

Table 3.3: The chromosome of the final individual in Step 2.

$x_{\rm err}$ Position error	**P** Gain $a_1 = 3.56451 \times 10^7$	**HPF** High-pass filter $a_2 = 96309$	**PLA** Phase-lag comp. $a_3 = 0.0250167$
$\dot{x}_{\rm cmd}$ Velocity command	**I** Integral $a_4 = 8.14329 \times 10^{-11}$	**POW** Power $a_5 = 0.570767$	**D** Derivative $a_6 = 1.53306 \times 10^{-5}$

individual of Steps 1 and 2. From the position responses, it can be confirmed that the response of the transient response is improved by the evolution of the EDM. The chromosome of the final individual is shown in Table 3.3.

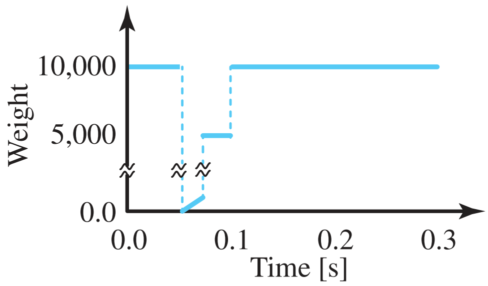

Fig. 3-14: Window function of Step 3.

Step 3 : Suppression of Overshoot

Then, 3×3 elements are applied in Step 3. The initial individual in Step 3 is given by the abstraction result of Step 2. In Step 3, in order to eliminate the overshoot of the transient response, the value of the window function in the section where the overshoot occured is set to be large.

$$\Lambda(q) = \begin{cases} 10,000 & (q < \frac{0.05}{T_\mathrm{s}}) \\ 200(qT_\mathrm{s} - 0.05) & (\frac{0.05}{T_\mathrm{s}} \leq q < \frac{0.064}{T_\mathrm{s}}) \\ 5,000 & (\frac{0.064}{T_\mathrm{s}} \leq q < \frac{0.1}{T_\mathrm{s}}) \\ 10,000 & (\frac{0.1}{T_\mathrm{s}} \leq q), \end{cases} \tag{3.17}$$

The window function in Step 3 is depicted in Fig. 3-14. As in Step 3, in order to keep the result of the abstraction in Steps 1 and 2, the mutation and crossover processing was applied only to the third-line in Step 3. Also, in consideration of the interaction between the parameters of the first row and the second row, the parameter shift processing is applied to all elements. Fig. 3-15 expresses the fitness response of Step 3. It can be seen that fitness by evolution is decreasing. Fig. 3-16 depicts the position response. It can be confirmed that the amount of overshoot is reduced by learning of the EDM. The chromosome of the final individual is shown in Table 3.4.

Step 4 : Adaptability to Parameter Variation

Here, the case where the parameter of the load is varied is verified with respect to the controller obtained in Step 3. Table 3.5 stands for the parameter variation in Step 4. In this verification, the weight of the mass point was changed. Fig. 3-17 shows the fitness response of Step 4. It can be seen that the fitness by evolution is decreasing. The position response of Step 4 is shown in Fig. 3-18. In the case of using the controller synthesized in Step 3, the response speed of the transient response was deteriorated

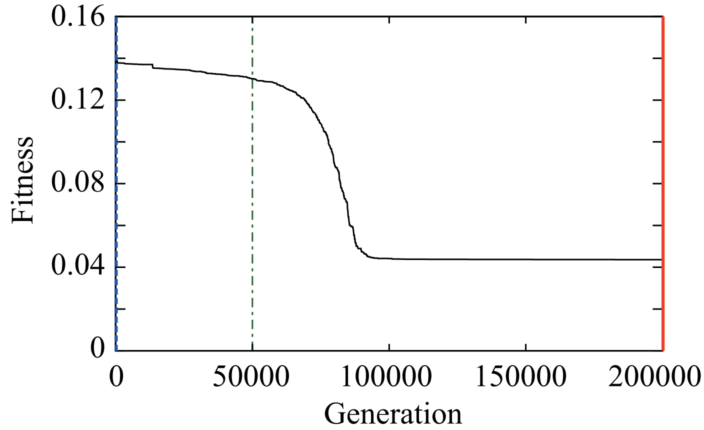

Fig. 3-15: Fitness response of Step 3.

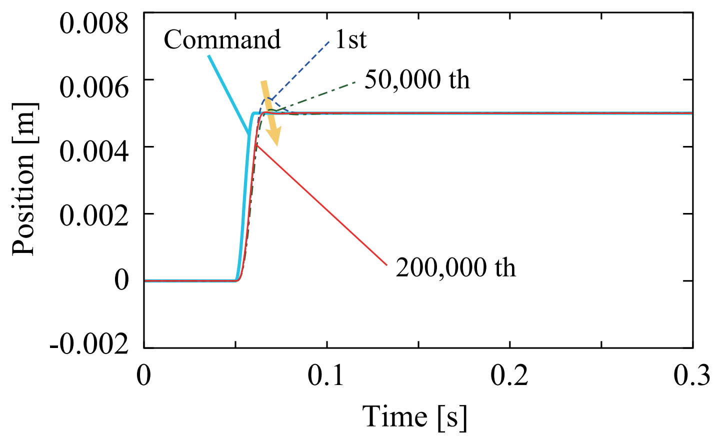

Fig. 3-16: Position response of Step 3.

Table 3.4: The chromosome of the final individual in Step 3.

x_{err} Position error	**P** Gain $a_1 = 2.92864 \times 10^7$	**HPF** High-pass filter $a_2 = 94769.1$	**PLA** Phase-lag comp. $a_3 = 0.0293921$
$\dot{x}_{\mathrm{cmd}}$ Velocity command	**I** Integral $a_4 = 1.22124 \times 10^{-10}$	**POW** Power $a_5 = 0.632433$	**D** Derivative $a_6 = 6.15971 \times 10^{-6}$
x_{err} Position error	**D** Derivative $a_7 = 0.000873454$	**PLE** Phase-lead comp. $a_8 = 0.0274136$	**TH** Through –

due to the change in the mass. On the contrary, the controller which synthesized in Step 4 improved

Table 3.5: Parameter variation in Step 4.

Parameter	Description	Step 1 – 3	Step 4
M_{m}	Weight of motor mover	0.1 kg	0.1 kg
M_2	Weight of mass 2	0.05 kg	0.1 kg
M_3	Weight of mass 3	0.05 kg	0.07 kg
M_4	Weight of mass 4	0.05 kg	0.05 kg
M_5	Weight of mass 5	0.05 kg	0.03 kg

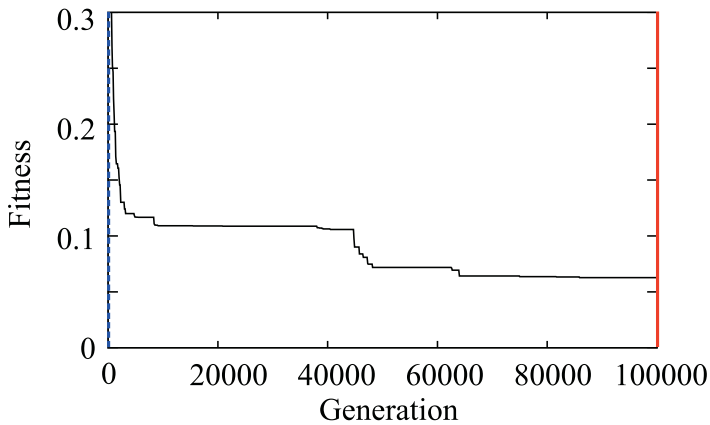

Fig. 3-17: Fitness response of Step 4.

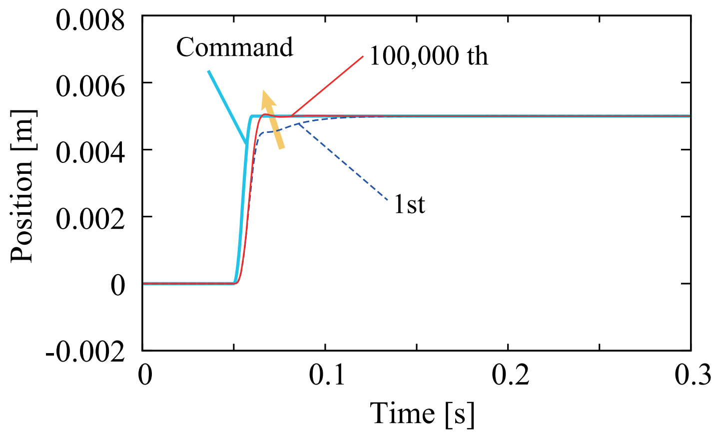

Fig. 3-18: Position response of Step 4.

the transient response according to the load fluctuation. These validations showed the effectiveness of controller design by the EDM.

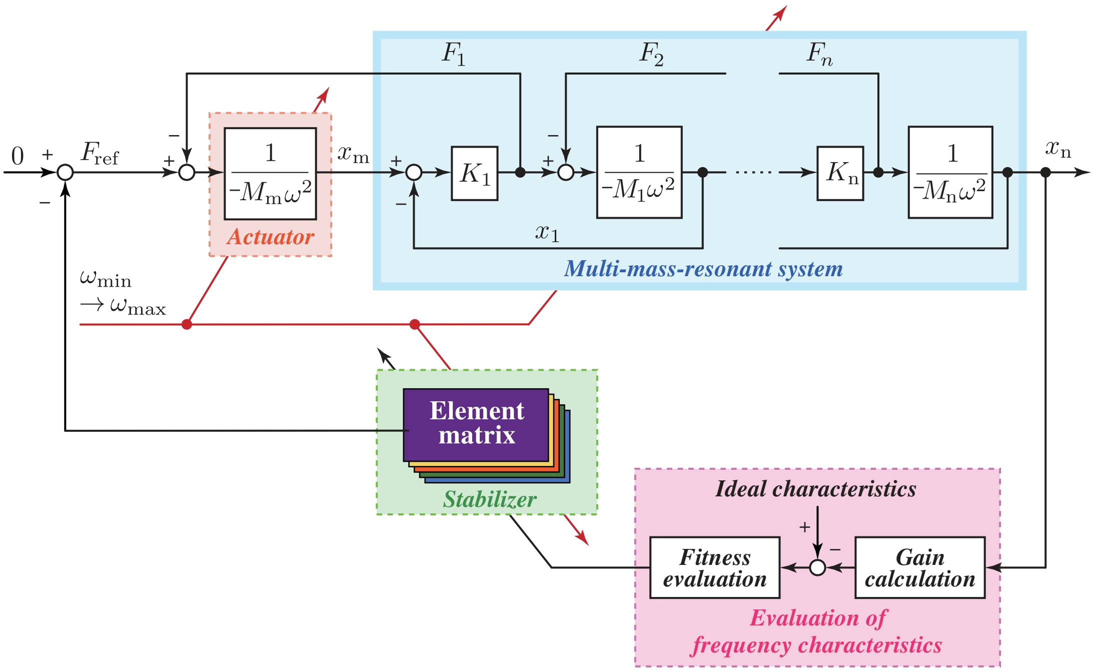

Fig. 3-19: Block diagram of feedback compensator abstraction for multi-mass resonant system.

3.1.3 Automatic Design of Feedback Compensator Based on the EDM

This section describe a automatic design of stabilized feedback compensator of multi-mass resonant system using the EDM. The automatic design is conducted based on frequency characteristics. The control design method described in previous section, feedback controller and feed-forward controller were generated simultaneously. In this section, an independent design method of feedback controller is proposed. A feedback controller is generated to stabilize the system based on frequency characteristics. The block diagram of the proposed method is shown in Fig. 3-19. This block diagram is expressed in frequency domain. In an evaluation part in Fig. 3-19, gain characteristics of loop transfer function, sensitivity function, and complementary sensitivity function are calculated. Moreover, fitness is evaluated based on fitness function. The fitness function is expressed as

$$\Gamma_{\mathrm{fb}} = \frac{1}{N_{\max}} \sum_{q=1}^{N_{\max}} \sqrt{\Lambda \left[\xi_{\mathrm{des}} - 20\log_{10}\left|G_{\mathrm{sys}}\{\omega[q]\}\right|\right]^2}, \tag{3.18}$$

$$\Lambda = \begin{cases} \frac{\Lambda_1}{\omega} & (0 < 20\log_{10}\left|G_{\mathrm{sys}}\{\omega[q]\}\right| \\ \frac{1}{\omega} & 20\log_{10}\left|G_{\mathrm{sys}}\{\omega[q]\}\right| \leq 0 \end{cases}, \tag{3.19}$$

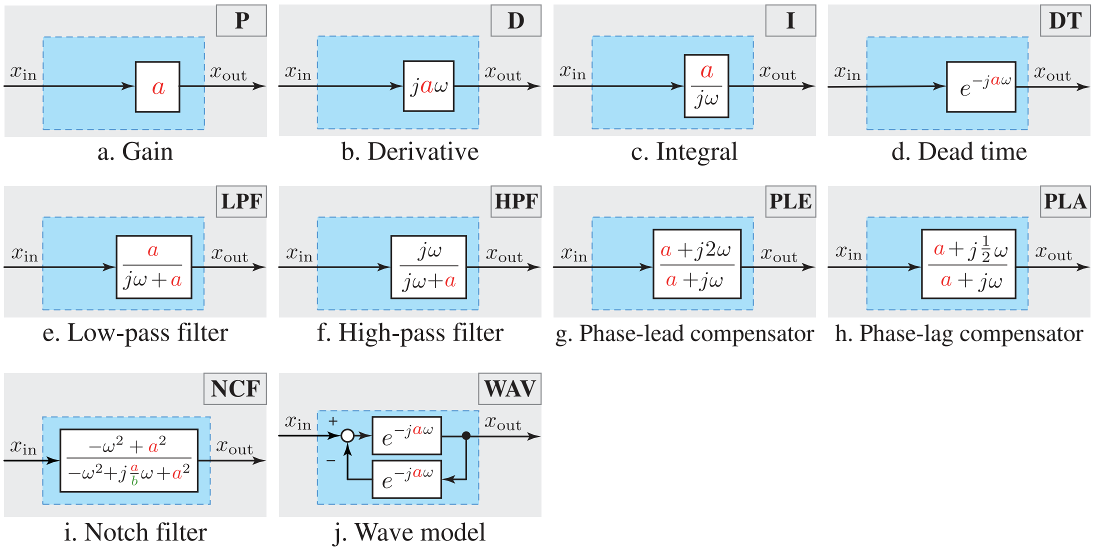

Fig. 3-20: Elements for automatic designing of stabilized feedback compensator.

where ξ_{des}, Λ, $G_{\mathrm{lp}}(\bullet)$, and $\omega(q)$ denote the desired gain characteristics, the weighting factor, the loop transfer function, and exponentially increasing frequency, respectively. Then, the following input values in the frequency domain is considered as

$$u_1(\omega) = \frac{A + jB}{C + jD}, \tag{3.20}$$

where $A \in \mathbb{R}$, $B \in \mathbb{R}$, $C \in \mathbb{R}$, and $D \in \mathbb{R}$ represent the real component of the numerator, the imaginary component of the numerator, the real component of the denominator, and the imaginary component of the denominator, respectively The calculation formula on the complex plane of the frequency transfer function of each element shown in Fig. 3-20 is as follows:

- Derivative $(j\omega)$

$$y(\omega) = \frac{-B\omega + jA\omega}{C + jD} \tag{3.21}$$

- Integral $\left(\frac{1}{j\omega}\right)$

$$y(\omega) = \frac{A + jB}{-D\omega + jC\omega} \tag{3.22}$$

- First-order low-pass filter $\left(\frac{g}{j\omega+g}\right)$

$$y(\omega) = \frac{gA + jgB}{Ca - D\omega + j\{C\omega + Da\}} \tag{3.23}$$

- First-order high-pass filter $\left(\frac{j\omega}{j\omega+g}\right)$

$$y(\omega) = \frac{-B\omega + j\omega A}{Ca - D\omega + j\{C\omega + Da\}} \tag{3.24}$$

- Phase compensator $\left(\frac{a+jb\omega}{a+j\omega}\right)$

$$y(\omega) = \frac{Aa - Bb\omega + j\{Ab\omega + Ba\}}{Ca - D\omega + j\{C\omega + Da\}} \tag{3.25}$$

- Notch filter $\left(\frac{s^2+a^2}{s^2+\frac{a}{b}s+a^2}\right)$

$$y(\omega) = \frac{Aa^2 - A\omega^2 + j\{Ba^2 - B\omega^2\}}{Ca^2 - C\omega^2 - \frac{a}{b}D\omega + j\{\frac{a}{b}C\omega - D\omega^2 + Da^2\}} \tag{3.26}$$

- Dead time $(e^{-jT\omega})$

$$y(\omega) = \frac{A\cos(-T\omega) - B\sin(-T\omega) + j\{A\sin(-T\omega) + B\cos(-T\omega)\}}{C + jD} \tag{3.27}$$

- Wave model $\left(\frac{e^{-jT\omega}}{1+e^{-j2T\omega}}\right)$

$$y(\omega) = \frac{A\cos(-T\omega) - B\sin(-T\omega) + j\{A\sin(-T\omega) + B\cos(-T\omega)\}}{C\cos(-2T\omega) - D\sin(-2T\omega) + C + j\{C\sin(-2T\omega) + D\cos(-2T\omega) + D\}} \tag{3.28}$$

In addition, the following input values in the frequency domain is defined as

$$u_2(\omega) = \frac{E + jF}{G + jH}, \tag{3.29}$$

where $E \in \mathbb{R}$, $F \in \mathbb{R}$, $G \in \mathbb{R}$, and $H \in \mathbb{R}$ represent the real component of the numerator, the imaginary component of the numerator, the real component of the denominator, and the imaginary component of

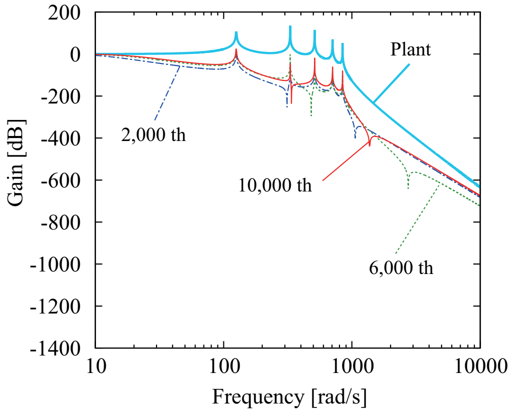

Fig. 3-21: Bode diagram of feedback compensator generation based on loop transfer function.

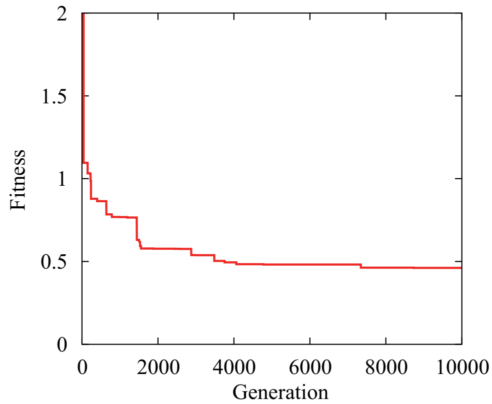

Fig. 3-22: Fitness response of feedback compensator generation based on loop transfer function.

the denominator, respectively From $u_1(\omega)$ and $u_2(\omega)$, summing calculation is expressed as

$$\begin{aligned} u_1(\omega) + u_2(\omega) &= \frac{A + jB}{C + jD} + \frac{E + jF}{G + jH} \\ &= \frac{AG - BH + CE - DF + j(AH + BG + CF + DE)}{CG - DH + j(DG + CH)}. \end{aligned} \tag{3.30}$$

From the above preparation, optimization of a feedback controller based on the frequency domain by the EDM is implemented.

Firstly, a feedback controller is generated based on loop transfer function. In the case of loop transfer function, desired gain characteristics ξ_{des} is set to 0. In order to avoid the gain from becoming larger than 0, Λ_1 is set to larger than 1. In this simulation, Λ_1 is set to 1000. Simulation results feedback compensator generation based on loop transfer function are shown in Fig. 3-21. The fitness response of is shown in Fig 3-22. According to evolution, it was confirmed that the gain characteristic approached zero. From this result, it was confirmed that EDM can be used for optimization of loop transfer function.

Then, a feedback controller is generated based on complementary sensitivity function. The weighting factor of fitness function is designed as follows:

$$\Lambda = \begin{cases} \frac{\Lambda_2}{\omega} & (\xi_{\text{des}} < 20\log_{10}\left|G_{\text{sys}}\{\omega[q]\}\right| \\ \frac{1}{\omega} & 20\log_{10}\left|G_{\text{sys}}\{\omega[q]\}\right| \leq \xi_{\text{des}} \end{cases}, \tag{3.31}$$

In the case of complementary sensitivity function, low pass characteristics is desired for gain character-

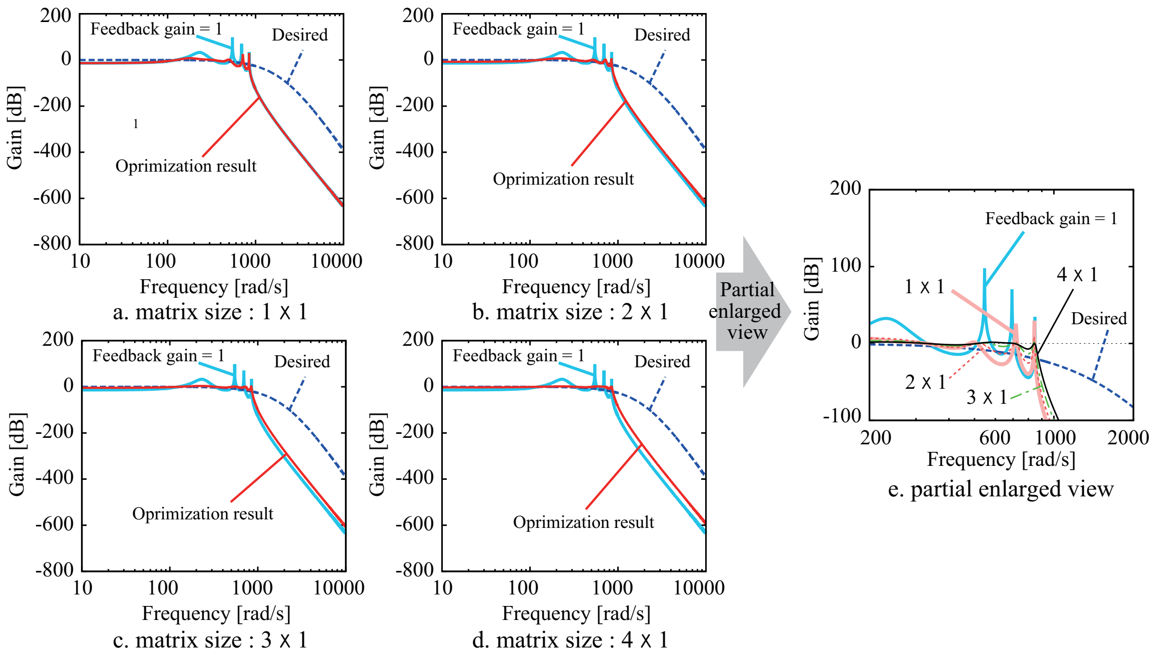

Fig. 3-23: Optimization results of complementary sensitivity function (columns increasing).

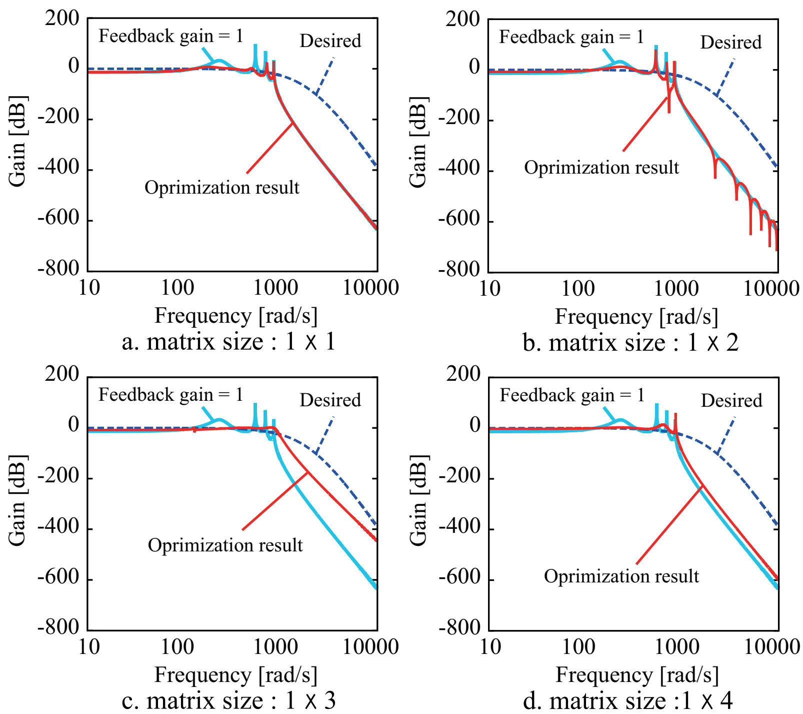

Fig. 3-24: Optimization results of complementary sensitivity function (rows increasing).

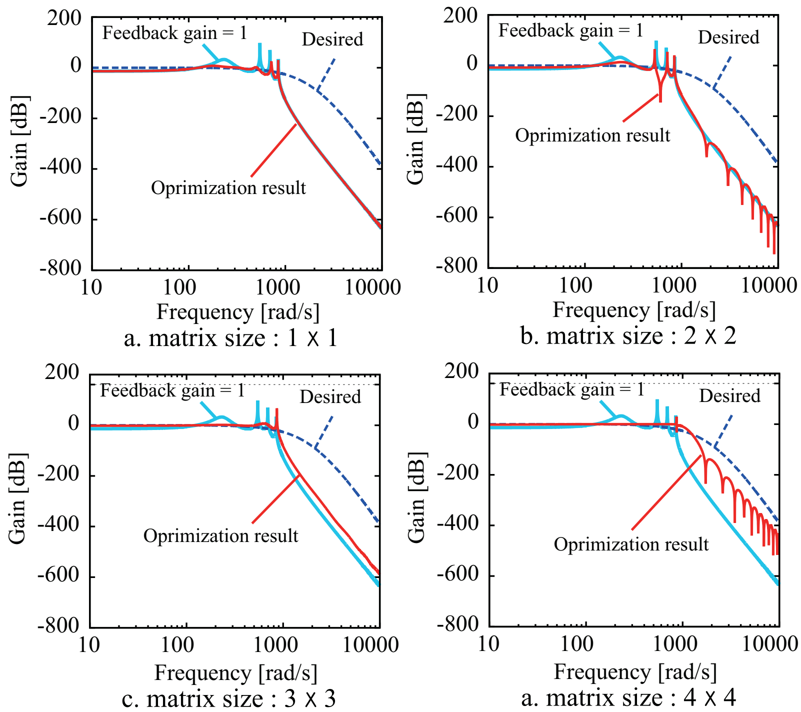

Fig. 3-25: Optimization results of complementary sensitivity function (square increasing).

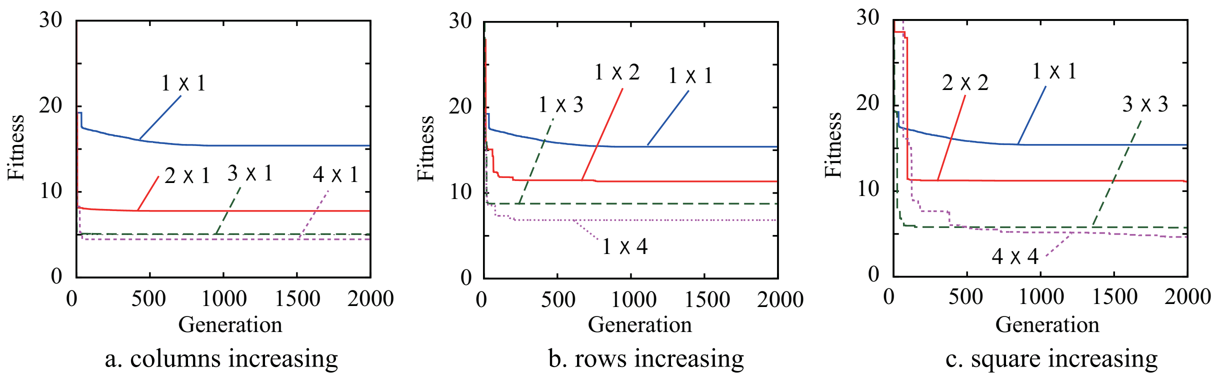

Fig. 3-26: Fitness response of feedback compensator optimization based on complementary sensitivity function.

istics ξ_{des}. Therefore, ξ_{des} is designed as follows:

$$\xi_{\text{des}} = \left| \left(\frac{g_{\text{des}}}{j\omega + g_{\text{des}}} \right)^{12} \right|, \tag{3.32}$$

where g_{des} refer to desired cut-off frequency of complementary sensitivity function. The size of element matrix is changed in three ways: the first is from 1×1 to 4×1 (columns increasing), the second is

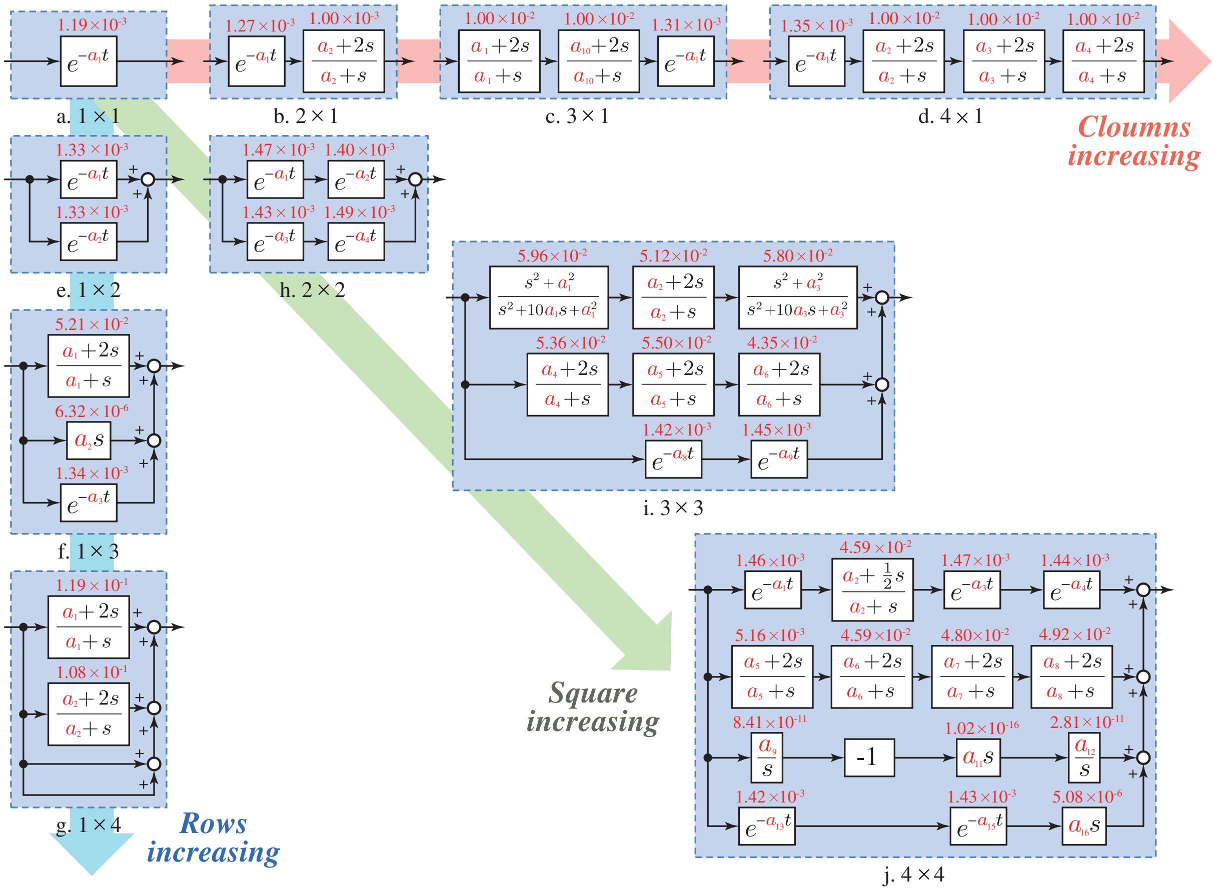

Fig. 3-27: Feedback compensator extracted by the EDM based on complementary sensitivity function.

from 1×1 to 1×4 (rows increasing), and the third is from 1×1 to 4×4 (square increasing). In this optimization, g_{des} is set to 2000. The fitness response complementary sensitivity function optimization is shown in Fig. 3-26. Optimization results of complementary sensitivity function are shown in Figs. 3-23 to 3-25. The light blue lines in Figs. 3-23 to 3-25 show complementary sensitivity function when the feedback gain equal to 1. From Figs. 3-23 to 3-25, it was confirmed that EDM can be used for optimization of complementary sensitivity function. It was confirmed that the fitness value was effectively improved when the number of columns was increased. This is because the order of the transfer function increases. Moreover, it can be confirmed that the convergence of 4×4 fitness has not ended. In addition, abstraction results are confirmed. Fig. 3-27 depicts the feedback compensator extracted by the EDM based on complementary sensitivity function The numbers above each element stands for parameter of the element. As the size of the matrix increases, it turns out that the order of feedback

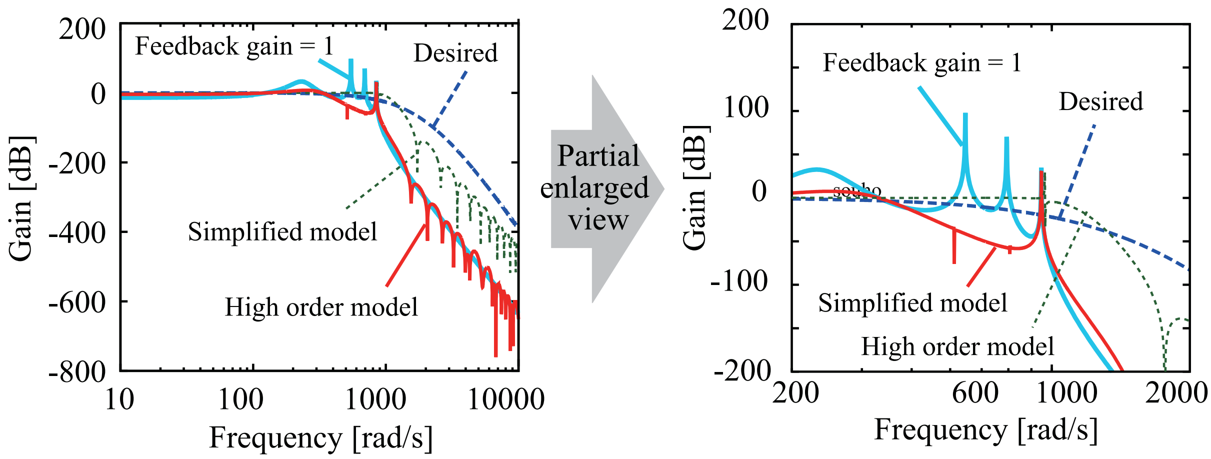

Fig. 3-28: Comparison of optimization results between high-order model and simplified model.

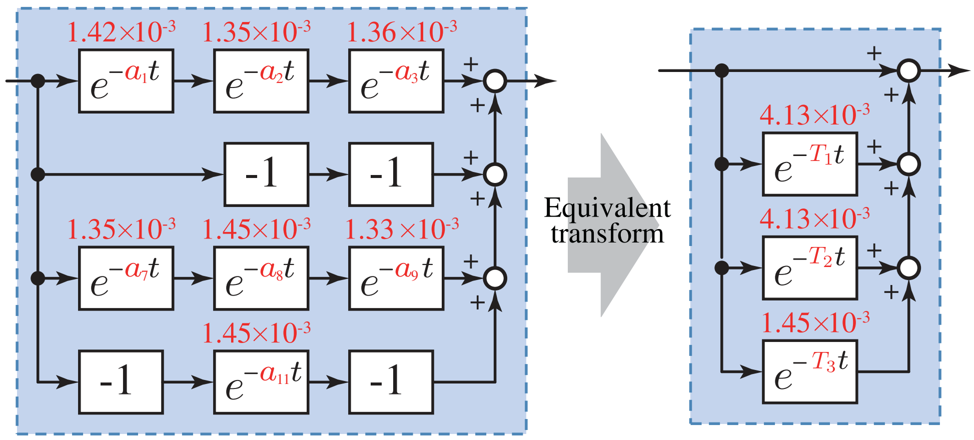

Fig. 3-29: Simplified feedback compensator abstracted by the EDM.

compensator increases which makes it difficult to implement. Then, in order to simplify the implementation, abstraction was performed by preparing only dead time for the element. In this way, a simplified feedback compensator is extracted. The comparison of optimization results between high-order model and simplified model is shown in Fig. 3-28. The red line shows the result of simplified model. Fig. 3-29 depicts a simplified feedback compensator abstracted by the EDM. From these results, it was confirmed that a simplified feedback compensator easy to implement can be abstracted by EDM.

3.2 Acceleration Control of Automatic Machinery via Motion Network

In this section, acceleration control of an automatic machinery is described. As mentioned in the previous section, the position control and force control are the most important control structure for motion control. An ideal position (velocity) control system has infinity control stiffness because it is the system to actuate arbitrary position (velocity) regardless of disturbances. It can be called as a position (velocity) determinate-force indeterminate system. On the contrary, an ideal force control system has zero infinity control stiffness because it is the system to actuate with arbitrary force regardless of position. It can be called as a force determinate-position (velocity) indeterminate system. They have duality relationship. By expanding position control and force control, various advanced controls can be achieved, such as hybrid control [14], compliance (impedance) control [15–18], and bilateral control [19–21]. All of these control methods are achieved based on the acceleration control. The conceptual diagram of acceleration control and its expansion are depicts in Fig. 3-30. By including a wide-bandwidth acceleration control system in the inner loop, various control systems can be constructed. The control method in this dissertation is also based on acceleration control. Firstly, the effectiveness and the basic principle of acceleration control are described. Next, a case where an attempt was made to achieve an acceleration control system of automatic machinery by using a general DOB is described. Since most recent automatic machinery is driven through the motion network, there is communication delay in the control system. Hence, it leads the problems in the case that the acceleration control system is installed for the automatic machinery. From this reason, the method to install the acceleration control under time delay is described. Finally, how to incorporate the acceleration control system into the machine and its design guidelines are explained. In this section, velocity control is shown as an example. An the acceleration control of a linear motion system and angular acceleration control of a rotational motion system are collectively called as “acceleration control.” Similarly, position control of a linear motion system and a angle control of a rotational motion system are collectively called as “position control,” velocity control of a linear motion system and angular velocity control of a rotational motion system are collectively called as “velocity control,” and force control of a linear motion system and a torque control of a rotational motion system are collectively called as “force control,” respectively.

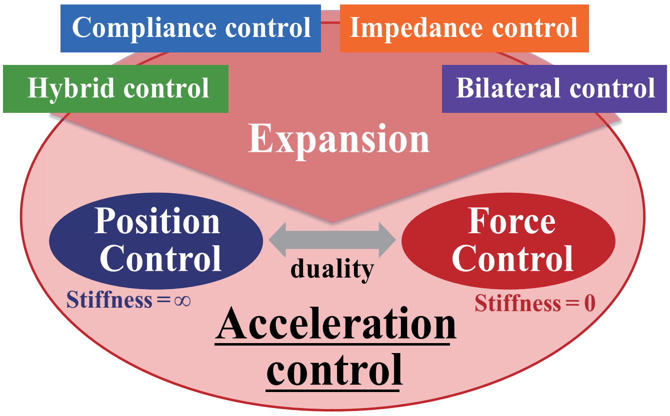

Fig. 3-30: Conceptual diagram of acceleration control and its expansion.

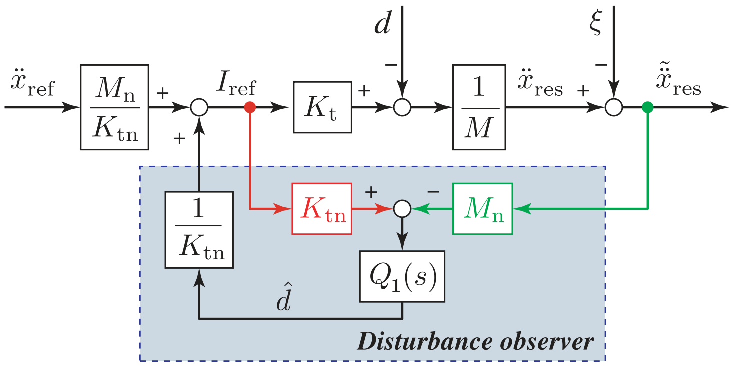

Fig. 3-31: Block diagram of an acceleration control using the DOB.

3.2.1 Acceleration Control Using DOB

As mentioned in the previous part, various control systems with high accuracy can be achieved by an acceleration control system. An ideal acceleration control system is a system whose the transfer function from the acceleration reference value to the acceleration response value is 1. The acceleration control system can be achieved by implementing the DOB. Fig. 3-31 shows block diagram of acceleration control using the DOB. In Fig. 3-31, d, ξ, and $Q_1(s)$ refer to the disturbance, sensing noise, low-pass filter of the DOB, respectively. The superscripts $\ddot{\bullet}$ and $\tilde{\bullet}$ express second derivative of time and sensing value, respectively. The subscripts ref, res, and n denote the reference value, response value, nominal value, respectively. Figs. 3-32 and 3-33 stand for the equivalent transformation of Fig. 3-31. The loop transfer function is expressed as

$$L_{a1}(s) = \frac{Q_1(s)}{1 - Q_1(s)}\alpha, \tag{3.33}$$

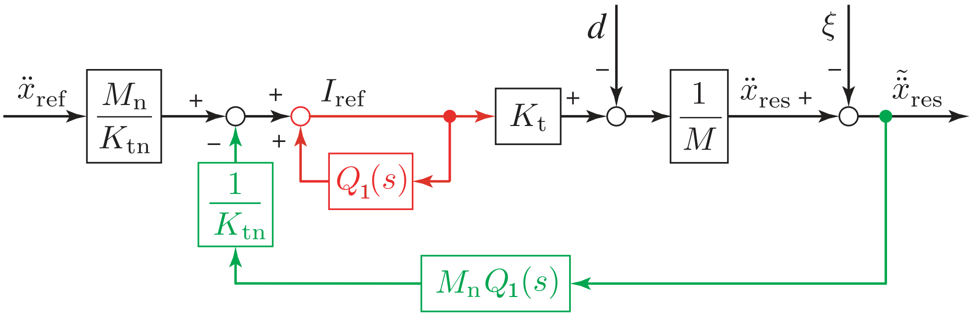

Fig. 3-32: Equivalent transformation of Fig. 3-31.

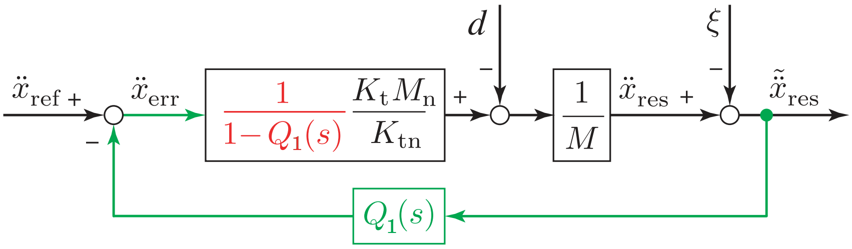

Fig. 3-33: Equivalent transformation of Fig. 3-32.

where

$$\alpha \triangleq \frac{K_{\mathrm{t}}}{K_{\mathrm{tn}}}\frac{M_{\mathrm{n}}}{M}, \tag{3.34}$$

$$\epsilon_{\mathrm{m}} \triangleq \frac{M}{M_{\mathrm{n}}}, \tag{3.35}$$

$$\epsilon_{\mathrm{k}} \triangleq \frac{K_{\mathrm{t}}}{K_{\mathrm{tn}}}. \tag{3.36}$$

From Fig. 3-33, the acceleration error and acceleration response are expressed as follows:

$$\begin{aligned}\ddot{x}_{\mathrm{err}} &= \frac{1}{1+\frac{Q_1(s)}{1-Q_1(s)}\alpha}\ddot{x}_{\mathrm{ref}} - \frac{\frac{Q_1(s)}{M}}{1+\frac{Q_1(s)}{1-Q_1(s)}\alpha}d - \frac{Q_1(s)}{1+\frac{Q_1(s)}{1-Q_1(s)}\alpha}\xi \\ &= \frac{1-Q_1(s)}{1-Q_1(s)+Q_1(s)\alpha}\ddot{x}_{\mathrm{ref}} - \frac{\{1-Q_1(s)\}\frac{Q_1(s)}{M}}{1-Q_1(s)+Q_1(s)\alpha}d - \frac{\{1-Q_1(s)\}Q_1(s)}{1-Q_1(s)+Q_1(s)\alpha}\xi,\end{aligned} \tag{3.37}$$

$$\begin{aligned}\ddot{x}_{\mathrm{res}} &= \frac{\frac{1}{1-Q_1(s)}\alpha}{1+\frac{Q_1(s)}{1-Q_1(s)}\alpha}\ddot{x}_{\mathrm{ref}} - \frac{\frac{1}{M}}{1+\frac{Q_1(s)}{1-Q_1(s)}\alpha}d + \frac{\frac{Q_1(s)}{1-Q_1(s)}\alpha}{1+\frac{Q_1(s)}{1-Q_1(s)}\alpha}\xi \\ &= \frac{\alpha}{1-Q_1(s)+Q_1(s)\alpha}\ddot{x}_{\mathrm{ref}} - \frac{\{1-Q_1(s)\}\frac{1}{M}}{1-Q_1(s)+Q_1(s)\alpha}d + \frac{Q_1(s)\alpha}{1-Q_1(s)+Q_1(s)\alpha}\xi.\end{aligned} \tag{3.38}$$

Acceleration Control without the DOB

Here, the case that $Q_1(s)$ is set to 0 is considered. This means the case without the DOB. (3.37) and (3.38) are rewritten as

$$\ddot{x}_{\mathrm{err}} = \ddot{x}_{\mathrm{ref}}, \tag{3.39}$$

$$\ddot{x}_{\mathrm{res}} = \alpha\ddot{x}_{\mathrm{ref}} - \frac{1}{M}d. \tag{3.40}$$

From (3.39) and (3.40), disturbance and nominal error affect acceleration reference when the DOB is not implemented. These equations mean open-loop control of acceleration.

Acceleration Control with Ideal DOB

On the contrary, the case that $Q_1(s)$ is set to 1 is considered. This means the case with the ideal DOB.

$$\ddot{x}_{\mathrm{err}} = 0, \tag{3.41}$$

$$\ddot{x}_{\mathrm{res}} = \ddot{x}_{\mathrm{ref}} + \xi. \tag{3.42}$$

From (3.41) and (3.42), the influence of disturbance is eliminated when $Q_1(s)$ is set to 1. Hence, the effectiveness of disturbance rejection by the DOB is confirmed. However, a sensing noise affects acceleration response.

Acceleration Control with Actual DOB

In actual case, influence of a sensing noise cannot be ignored. Therefore, $Q_1(s)$ is set as a low-pass filter as

$$Q_1(s) = \frac{g_{\mathrm{dis}}}{s + g_{\mathrm{dis}}}, \tag{3.43}$$

where g_{dis} stands for the cut-off frequency of the low-pass filter. From (3.43), (3.37) and (3.38) are rewritten as

$$\ddot{x}_{\mathrm{err}} = \frac{s}{s + g_{\mathrm{dis}}\alpha}\ddot{x}_{\mathrm{ref}} - \frac{\frac{s}{s+g_{\mathrm{dis}}}\frac{g_{\mathrm{dis}}}{M}}{s + g_{\mathrm{dis}}\alpha}d - \frac{\frac{s}{s+g_{\mathrm{dis}}}g_{\mathrm{dis}}}{s + g_{\mathrm{dis}}\alpha}\xi, \tag{3.44}$$

$$\ddot{x}_{\mathrm{res}} = \frac{(s + g_{\mathrm{dis}})\alpha}{s + g_{\mathrm{dis}}\alpha}\ddot{x}_{\mathrm{ref}} - \frac{1}{M}\frac{s}{s + g_{\mathrm{dis}}\alpha}d - \frac{g_{\mathrm{dis}}\alpha}{s + g_{\mathrm{dis}}\alpha}\xi. \tag{3.45}$$

The Bode diagrams from each input to $\ddot{x}_{\mathrm{err}}$ and $\ddot{x}_{\mathrm{res}}$ are shown in Fig. 3-34. It can be seen that if

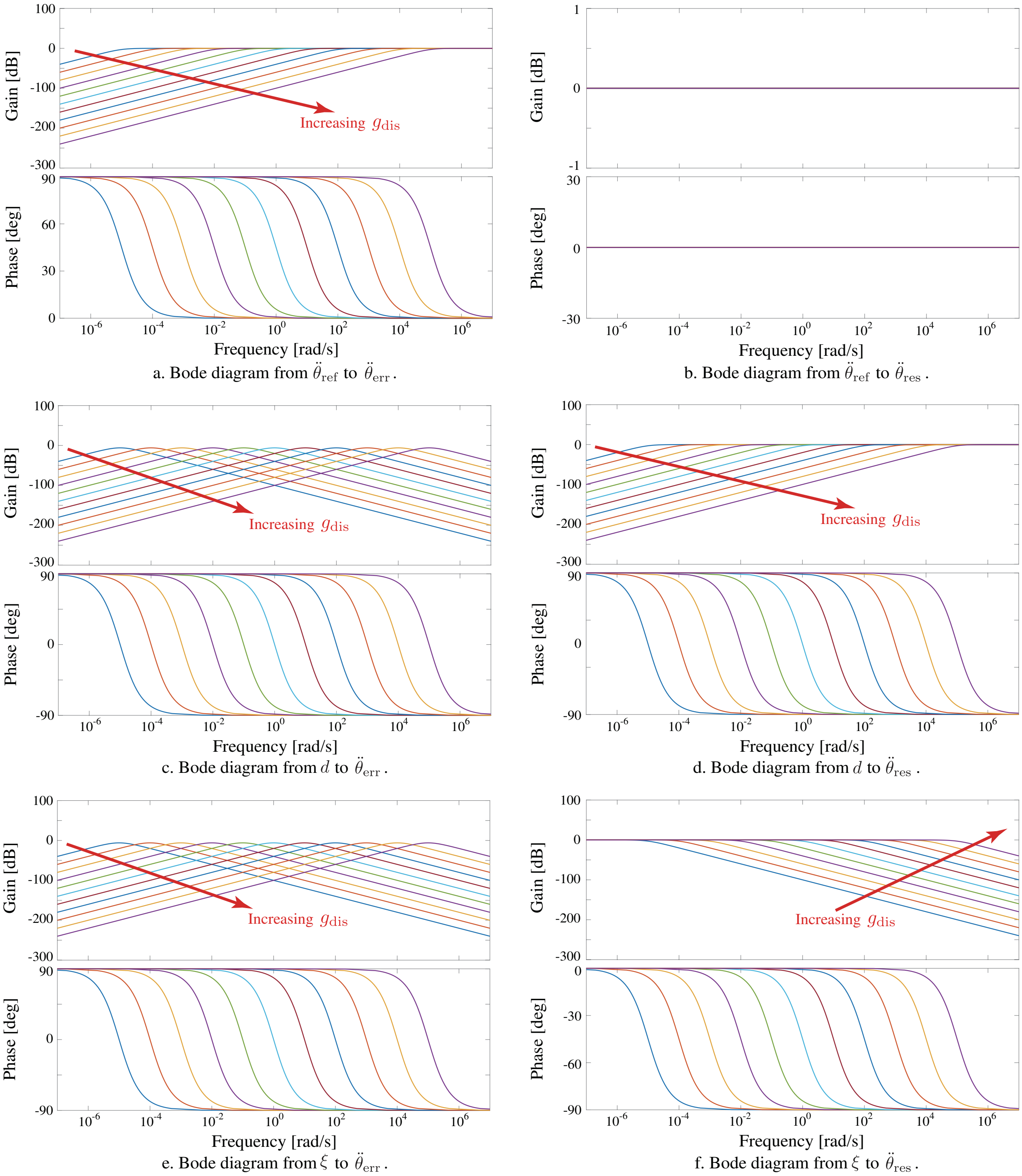

a. Bode diagram from $\ddot{\theta}_{\mathrm{ref}}$ to $\ddot{\theta}_{\mathrm{err}}$.

b. Bode diagram from $\ddot{\theta}_{\mathrm{ref}}$ to $\ddot{\theta}_{\mathrm{res}}$.

c. Bode diagram from d to $\ddot{\theta}_{\mathrm{err}}$.

d. Bode diagram from d to $\ddot{\theta}_{\mathrm{res}}$.

e. Bode diagram from ξ to $\ddot{\theta}_{\mathrm{err}}$.

f. Bode diagram from ξ to $\ddot{\theta}_{\mathrm{res}}$.

Fig. 3-34: Bode diagram of closed loop transfer function when g_{dis} is changed.

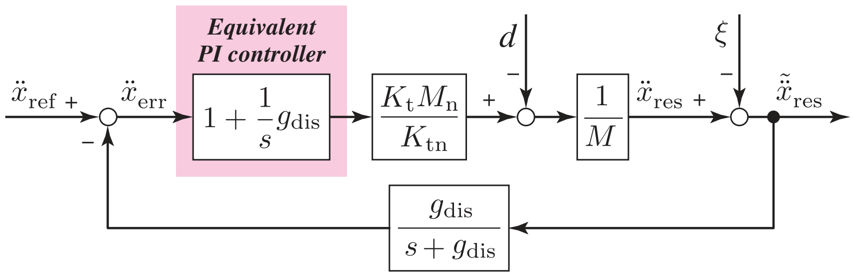

Fig. 3-35: Equivalent transformation of Fig. 3-33 in the case of $Q_1(s) = \frac{g_{\mathrm{dis}}}{s+g_{\mathrm{dis}}}$.

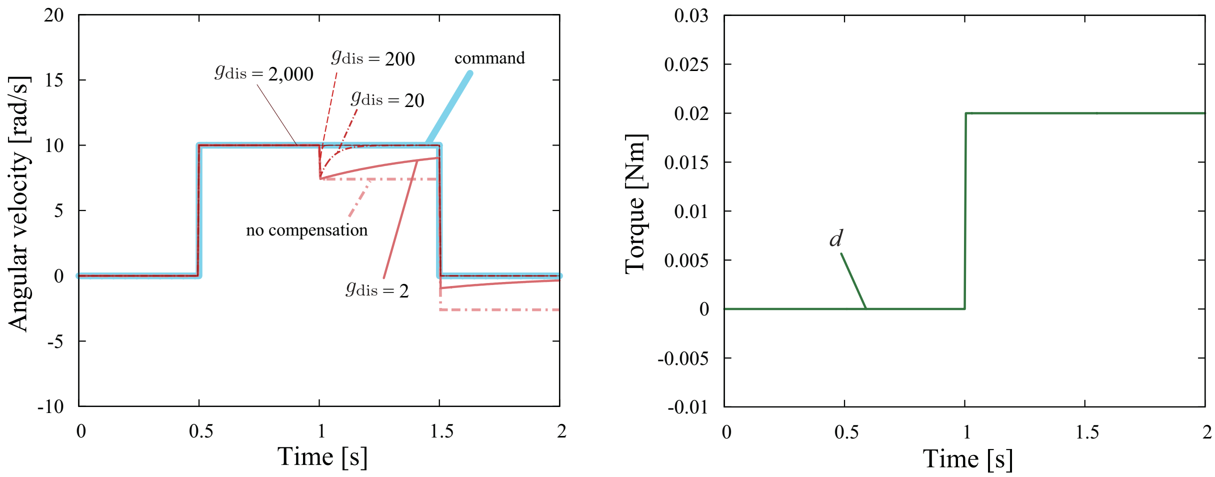

a. Angular accerelation response

b. Disturbance

Fig. 3-36: Acceleration response when T_1 and T_2 are changed.

g_{dis} is increased, higher-frequency disturbance is rejected. On the contrary, since the noise sensitivity is increased by increasing g_{dis}, it is susceptible to noise. By deciding g_{dis} according to the target system, an acceleration control system can be constructed. In the case of actual DOB, Fig. 3-33 can be transformed to Fig. 3-35. This block diagram indicates that the DOB works as an equivalent PI controller in the acceleration control system. The acceleration response of the simulation is shown in Fig. 3-36. In this simulation, 10 $\mathrm{rad/s^2}$ step command is given from 0.5 s. The disturbance torque is applied from 1 s. From this result, the influence of the disturbance in the acceleration control system is removed by the DOB, and as the value of g_{dis} is set large, the disturbance was immediately removed. On the contrary, the noise sensitivity from ξ become higher due to increasing of g_{dis}. It is known as trade-off between a sensitivity function and a complementary sensitivity function [76].

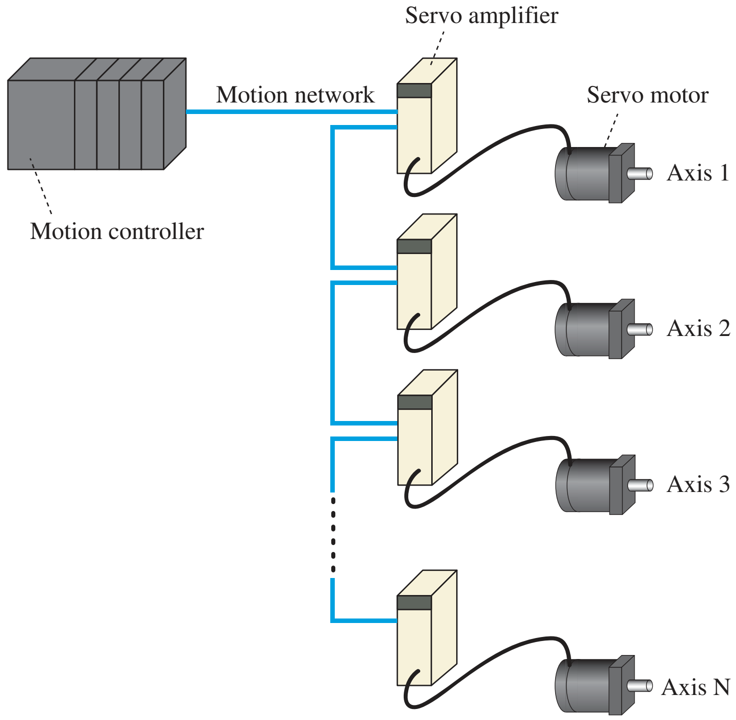

Fig. 3-37: Overview of control system using motion network.

3.2.2 Acceleration Control via Motion Network

Overview of Control System for Automatic Machinery

As mentioned in Chapter 1, general automatic machinery is worked by servo motors. Initial servo motors had transmitted commands and response values by pulse signals and analog signals. Although this method allows information to be exchanged immediately, there is a disadvantage that the wiring becomes complicated and there are few information that can be shared. In recent years, with the development of information and communication technology, delivery of information of motion by communication, which can exchange a lot of information by wire saving, has become popular. Fig. 3-37 shows the overview of the control system through the motion network. Various methods are available depending on the vender, such as EtherCAT [77], Powerlink [78], and Mechatrolink [79] as a method of communication of servo motors. However, when motion information is exchanged by communication, a delay occurs. In this dissertation, the influence of the motion communication delay when constructing an acceleration control system is analyzed.

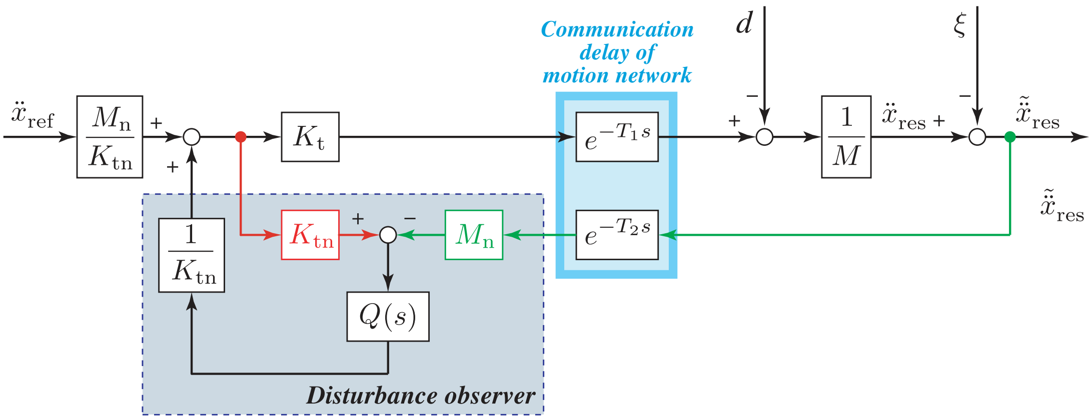

Fig. 3-38: Block diagram of acceleration control system via motion network.

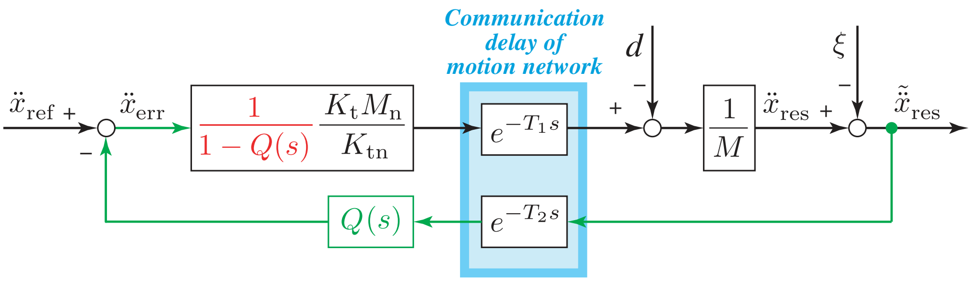

Fig. 3-39: Equivalent transformation of Fig. 3-38.

Acceleration Control via Motion Network

The block diagrams of acceleration control system with the DOB via motion network are shown in Figs. 3-38 and 3-39. In these figures, T_1 and T_2 refer to delay time of the forward path and delay time of the return path, respectively. The influence of communication delay of motion network is expressed as

$$\epsilon_k = e^{-T_1 s}, \tag{3.46}$$

$$\epsilon_m = \frac{1}{e^{-T_2 s}}. \tag{3.47}$$

The loop transfer function is expressed as

$$L_{\mathrm{a2}}(s) = \frac{Q_1(s)}{1 - Q_1(s)} \alpha e^{-(T_1+T_2)s}. \tag{3.48}$$

Table 3.6: Parameters for stability analysis (changing T_1 and T_2).

Parameter	Description	Value
T_{s}	Sampling time	500×10^{-6} s
g_{dis}	Cut-off frequency of the DOB	600 rad / s

From Fig. 3-39, the acceleration error and acceleration response are expressed as follows:

$$\begin{aligned}
\ddot{x}_{\mathrm{err}} &= \frac{1}{1+\frac{Q_1(s)}{1-Q_1(s)}\alpha e^{-(T_1+T_2)s}}\ddot{x}_{\mathrm{ref}} - \frac{\frac{Q_1(s)}{M}e^{-T_2 s}}{1+\frac{Q_1(s)}{1-Q_1(s)}\alpha e^{-(T_1+T_2)s}}d \\
&\quad -\frac{Q_1(s)e^{-T_2 s}}{1+\frac{Q_1(s)}{1-Q_1(s)}\alpha e^{-(T_1+T_2)s}}\xi \\
&= \frac{1-Q_1(s)}{D_{\mathrm{a2}}(s)}\ddot{x}_{\mathrm{ref}} - \frac{\{1-Q_1(s)\}\frac{Q_1(s)}{M}e^{-T_2 s}}{D_{\mathrm{a2}}(s)}d - \frac{\{1-Q_1(s)\}Q_1(s)e^{-T_2 s}}{D_{\mathrm{a2}}(s)}\xi, \qquad (3.49)
\end{aligned}$$

$$\begin{aligned}
\ddot{x}_{\mathrm{res}} &= \frac{\frac{1}{1-Q_1(s)}\alpha e^{-T_1 s}}{1+\frac{Q_1(s)}{1-Q_1(s)}\alpha e^{-(T_1+T_2)s}}\ddot{x}_{\mathrm{ref}} - \frac{\frac{1}{M}}{1+\frac{Q_1(s)}{1-Q_1(s)}\alpha e^{-(T_1+T_2)s}}d \\
&\quad +\frac{\frac{Q_1(s)}{1-Q_1(s)}\alpha e^{-(T_1+T_2)s}}{1+\frac{Q_1(s)}{1-Q_1(s)}\alpha e^{-(T_1+T_2)s}}\xi \\
&= \frac{\alpha e^{-T_1 s}}{D_{\mathrm{a2}}(s)}\ddot{x}_{\mathrm{ref}} - \frac{\{1-Q_1(s)\}\frac{1}{M}}{D_{\mathrm{a2}}(s)}d + \frac{Q_1(s)\alpha e^{-(T_1+T_2)s}}{D_{\mathrm{a2}}(s)}\xi, \qquad (3.50)
\end{aligned}$$

$$D_{\mathrm{a2}}(s) = 1-Q_1(s)+Q_1(s)\alpha e^{-(T_1+T_2)s}. \qquad (3.51)$$

Stability Analysis of Acceleration Control System

Then, stability of an acceleration control system is analyzed. In this analysis, T_1 and T_2 are assumed as same value as $T_1 = T_2 = nT_{\mathrm{s}}$. Here, T_{s} stands for sampling time of the controller. The Nyquist diagram when n is varied from 0 to 5 are shown in Fig. 3-40. Parameters of this analysis is shown in Table 3.6. From Fig. 3-40, even when ideal acceleration feedback can be made, the system becomes unstable when there is a time-delay of 3 cycles or more. On the contrary, the system becomes stable in the case that there is no time-delay. Therefore, the time-delay of the motion network has a fatal influence on the stability of the acceleration control system. The acceleration response when a step input is given is shown in Fig. 3-41. Fig. 3-42 shows the Nyquist diagram of the loop transfer function with normal DOB in the case of changing the cut-off frequency of the DOB. In this figure, delay time of motion

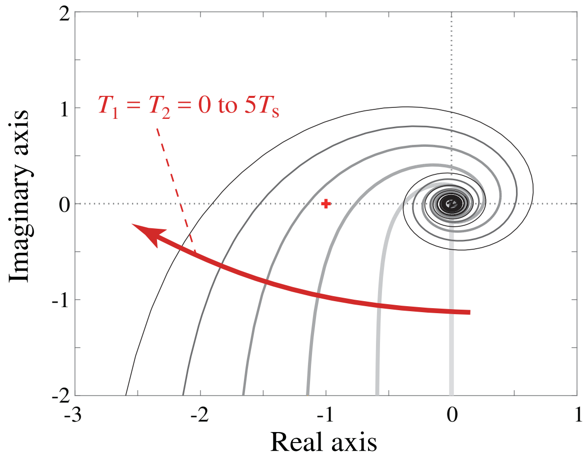

Fig. 3-40: Stability analysis of acceleration control under time delay when T_1 and T_2 are changed.

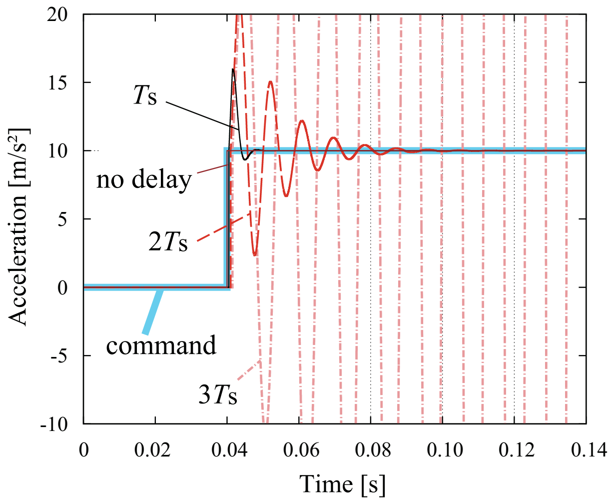

Fig. 3-41: Acceleration response when T_1 and T_2 are changed.

network T_1, T_2 are set to $2T_s$. The cut-off frequency of the low-pass filter used in the DOB is changed from 200 to 1,400 rad/s. From Fig. 3-42, it can be seen that the cut-off frequency can only be increased up to 400 due to the influence of the delay of the motion network. Therefore, in order to increase the bandwidth of acceleration control system, it is necessary to decrease the influence of the time-delay of motion network. Then, characteristics of the closed loop are analyzed in the case of (3.43). From (3.56)

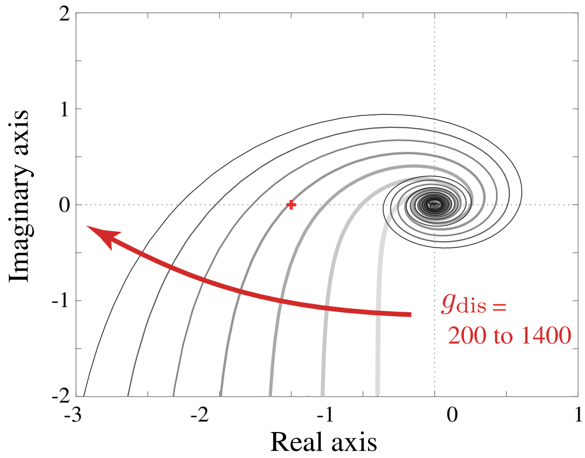

Fig. 3-42: Stability analysis of acceleration control under time delay when $g_{\rm dis}$ is changed.

and (3.60), the acceleration error and acceleration response are rewritten as follows:

$$\ddot{x}_{\rm err} = \frac{s}{d_{\rm a2}(s)}\ddot{x}_{\rm ref} - \frac{\left(1-\frac{g_{\rm dis}}{s+g_{\rm dis}}\right)\frac{g_{\rm dis}}{M}e^{-T_2 s}}{d_{\rm a2}(s)}d - \frac{\left(1-\frac{g_{\rm dis}}{s+g_{\rm dis}}\right)g_{\rm dis}e^{-T_2 s}}{d_{\rm a2}(s)}\xi, \tag{3.52}$$

$$\ddot{x}_{\rm res} = \frac{(s+g_{\rm dis})\alpha e^{-T_1 s}}{d_{\rm a2}(s)}\ddot{x}_{\rm ref} - \frac{\frac{s}{M}}{d_{\rm a2}(s)}d + \frac{g_{\rm dis}\alpha e^{-(T_1+T_2)s}}{d_{\rm a2}(s)}\xi, \tag{3.53}$$

$$d_{\rm a2}(s) = s + g_{\rm dis}\alpha e^{-(T_1+T_2)s}. \tag{3.54}$$

Bode diagrams from each input to $\ddot{x}_{\rm err}$ and $\ddot{x}_{\rm res}$ are shown in Fig. 3-43. From these results, it can be seen that the time-delay affects the high-frequency domain.

Delay Compensation the DOB

As described above, the bandwidth of the acceleration control system is significantly lowered due to the time delay of the motion network. Therefore, in order to achieve an acceleration control system with an automatic machinery, a method capable of increasing the bandwidth is required even when the motion network is used. The delay-compensation-type DOB is shown in Figs. 3-44 and 3-45. Each signal in the DOB (i.e., total motor output force and acceleration force) is synchronized by the time delay compensation. The loop transfer function is expressed as

$$L_{\rm a3}(s) = \frac{Q_1(s)}{1-Q_1(s)e^{-T_3 s}}\alpha e^{-(T_1+T_2)s}. \tag{3.55}$$

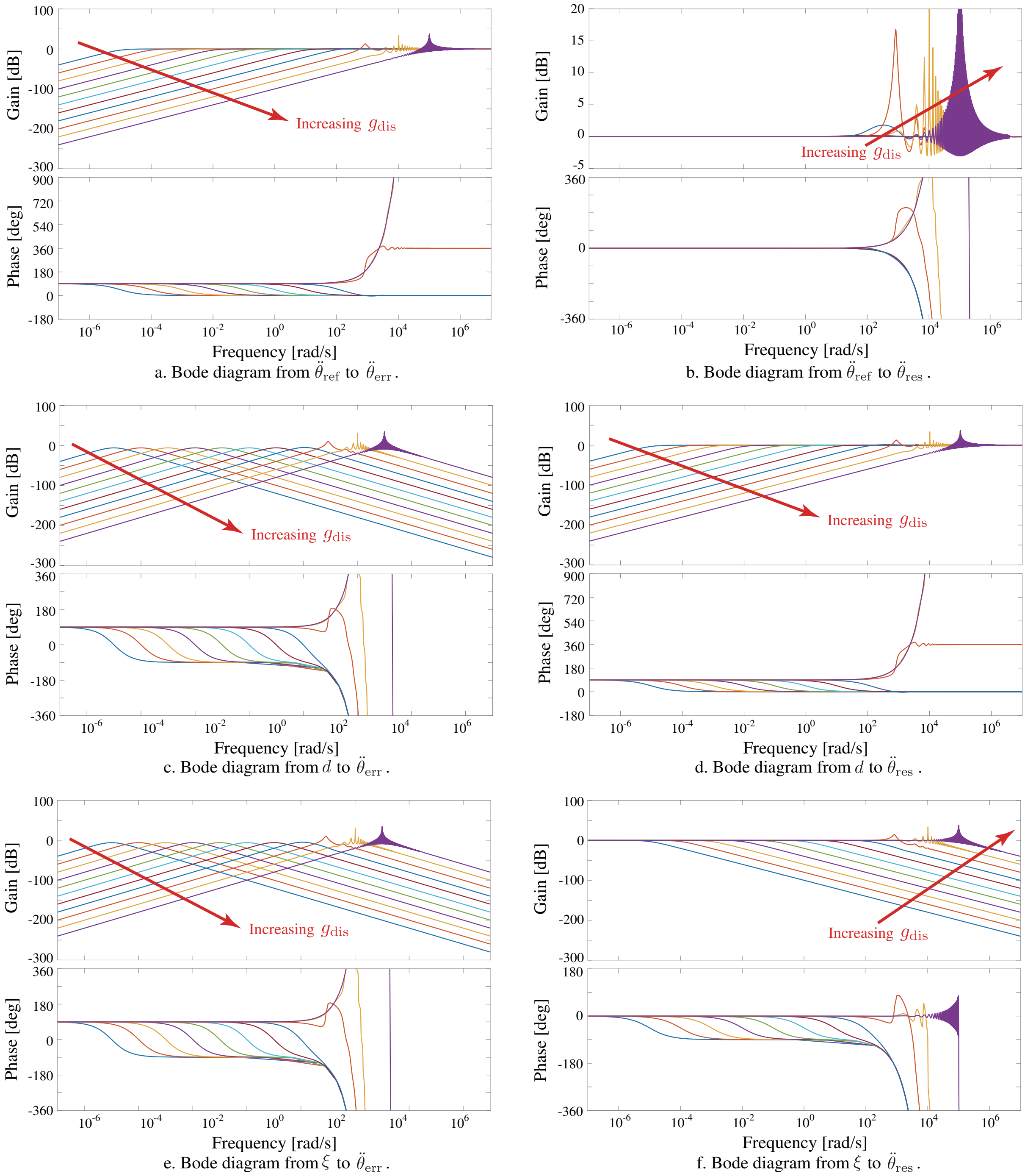

Fig. 3-43: Bode diagram of closed loop transfer function under time delay when $g_{\rm dis}$ is changed.

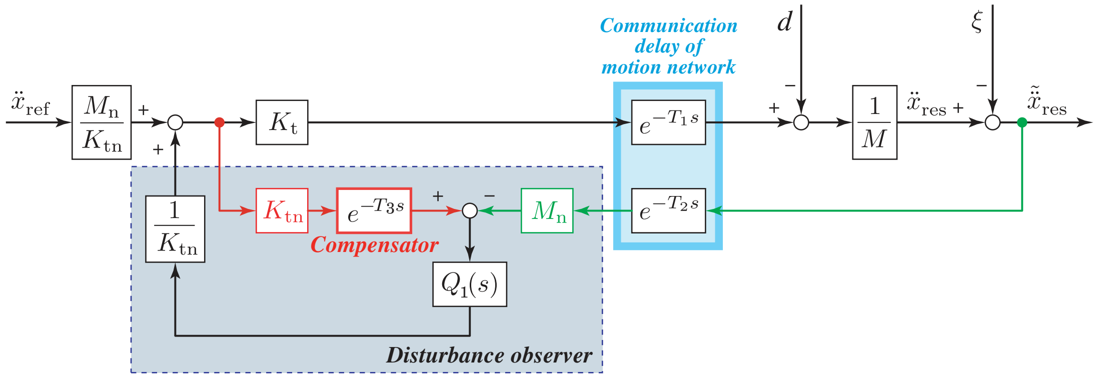

Fig. 3-44: Block diagram of acceleration control system via motion network.

From Fig. 3-45, the acceleration error and acceleration response of the closed loop system are expressed as

$$\begin{aligned}\ddot{x}_{\mathrm{err}} &= \frac{1}{1+\frac{Q_1(s)}{1-Q_1(s)e^{-T_3 s}}\alpha e^{-(T_1+T_2)s}}\ddot{x}_{\mathrm{ref}} - \frac{\frac{Q_1(s)}{M}e^{-T_2 s}}{1+\frac{Q_1(s)}{1-Q_1(s)e^{-T_3 s}}\alpha e^{-(T_1+T_2)s}}d \\ &\quad - \frac{Q_1(s)e^{-T_2 s}}{1+\frac{Q_1(s)}{1-Q_1(s)e^{-T_3 s}}\alpha e^{-(T_1+T_2)s}}\xi \\ &= \frac{1-Q_1(s)e^{-T_3 s}}{D_{\mathrm{a3}}(s)}\ddot{x}_{\mathrm{ref}} - \frac{\left\{1-Q_1(s)e^{-T_3 s}\right\}\frac{Q_1(s)}{M}e^{-T_2 s}}{D_{\mathrm{a3}}(s)}d \\ &\quad - \frac{\left\{1-Q_1(s)e^{-T_3 s}\right\}Q_1(s)e^{-T_2 s}}{D_{\mathrm{a3}}(s)}\xi, \end{aligned} \tag{3.56}$$

$$\begin{aligned}\ddot{x}_{\mathrm{res}} &= \frac{\frac{1}{1-Q_1(s)e^{-T_3 s}}\alpha e^{-T_1 s}}{1+\frac{Q_1(s)}{1-Q_1(s)e^{-T_3 s}}\alpha e^{-(T_1+T_2)s}}\ddot{x}_{\mathrm{ref}} - \frac{\frac{1}{M}}{1+\frac{Q_1(s)}{1-Q_1(s)e^{-T_3 s}}\alpha e^{-(T_1+T_2)s}}d \\ &\quad + \frac{\frac{Q_1(s)}{1-Q_1(s)e^{-T_3 s}}\alpha e^{-(T_1+T_2)s}}{1+\frac{Q_1(s)}{1-Q_1(s)e^{-T_3 s}}\alpha e^{-(T_1+T_2)s}}\xi \\ &= \frac{\alpha e^{-T_1 s}}{D_{\mathrm{a3}}(s)}\ddot{x}_{\mathrm{ref}} - \frac{\left\{1-Q_1(s)e^{-T_3 s}\right\}\frac{1}{M}}{D_{\mathrm{a3}}(s)}d + \frac{Q_1(s)\alpha e^{-(T_1+T_2)s}}{D_{\mathrm{a3}}(s)}\xi, \end{aligned} \tag{3.57}$$

$$D_{\mathrm{a3}}(s) = 1 - Q_1(s)e^{-T_3 s} + Q_1(s)\alpha e^{-(T_1+T_2)s}. \tag{3.58}$$

Then, the characteristics of the closed loop are analyzed in the case of (3.43). From (3.56) and (3.57),

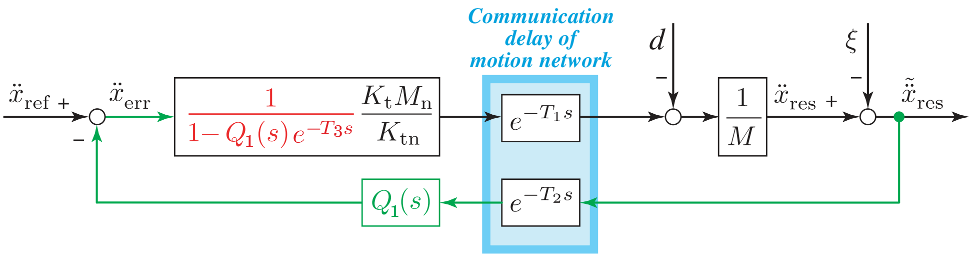

Fig. 3-45: Equivalent transformation of Fig. 3-44.

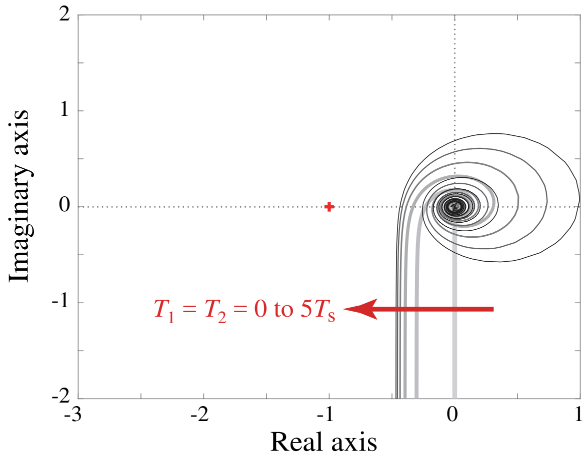

Fig. 3-46: Stability analysis of acceleration control under time delay with compensator when T_1 and T_2 are changed.

the acceleration error and acceleration response are rewritten as follows

$$\begin{aligned}\ddot{x}_{\mathrm{err}} &= \frac{s+g_{\mathrm{dis}}-g_{\mathrm{dis}}e^{-T_3 s}}{d_{\mathrm{a3}}(s)}\ddot{x}_{\mathrm{ref}} \\ &\quad -\frac{\left(1-\frac{g_{\mathrm{dis}}}{s+g_{\mathrm{dis}}}e^{-T_3 s}\right)\frac{g_{\mathrm{dis}}}{M}e^{-T_2 s}}{d_{\mathrm{a3}}(s)}d-\frac{\left(1-\frac{g_{\mathrm{dis}}}{s+g_{\mathrm{dis}}}e^{-T_3 s}\right)g_{\mathrm{dis}}e^{-T_2 s}}{d_{\mathrm{a3}}(s)}\xi, \end{aligned} \tag{3.59}$$

$$\ddot{x}_{\mathrm{res}} = \frac{(s+g_{\mathrm{dis}})\alpha e^{-T_1 s}}{d_{\mathrm{a3}}(s)}\ddot{x}_{\mathrm{ref}}-\frac{\frac{s+g_{\mathrm{dis}}-g_{\mathrm{dis}}e^{-T_3 s}}{M}}{d_{\mathrm{a3}}(s)}d+\frac{g_{\mathrm{dis}}\alpha e^{-(T_1+T_2)s}}{d_{\mathrm{a3}}(s)}\xi, \tag{3.60}$$

$$d_{\mathrm{a3}}(s) = s+g_{\mathrm{dis}}-g_{\mathrm{dis}}e^{-T_3 s}+g_{\mathrm{dis}}\alpha e^{-(T_1+T_2)s}. \tag{3.61}$$

Bode diagrams from each input to $\ddot{x}_{\mathrm{err}}$ and $\ddot{x}_{\mathrm{res}}$ are shown in Fig 3-47. Stability in high-frequency domain is improved by the delay compensation. Therefore, the effectiveness of the delay compensator is confirmed.

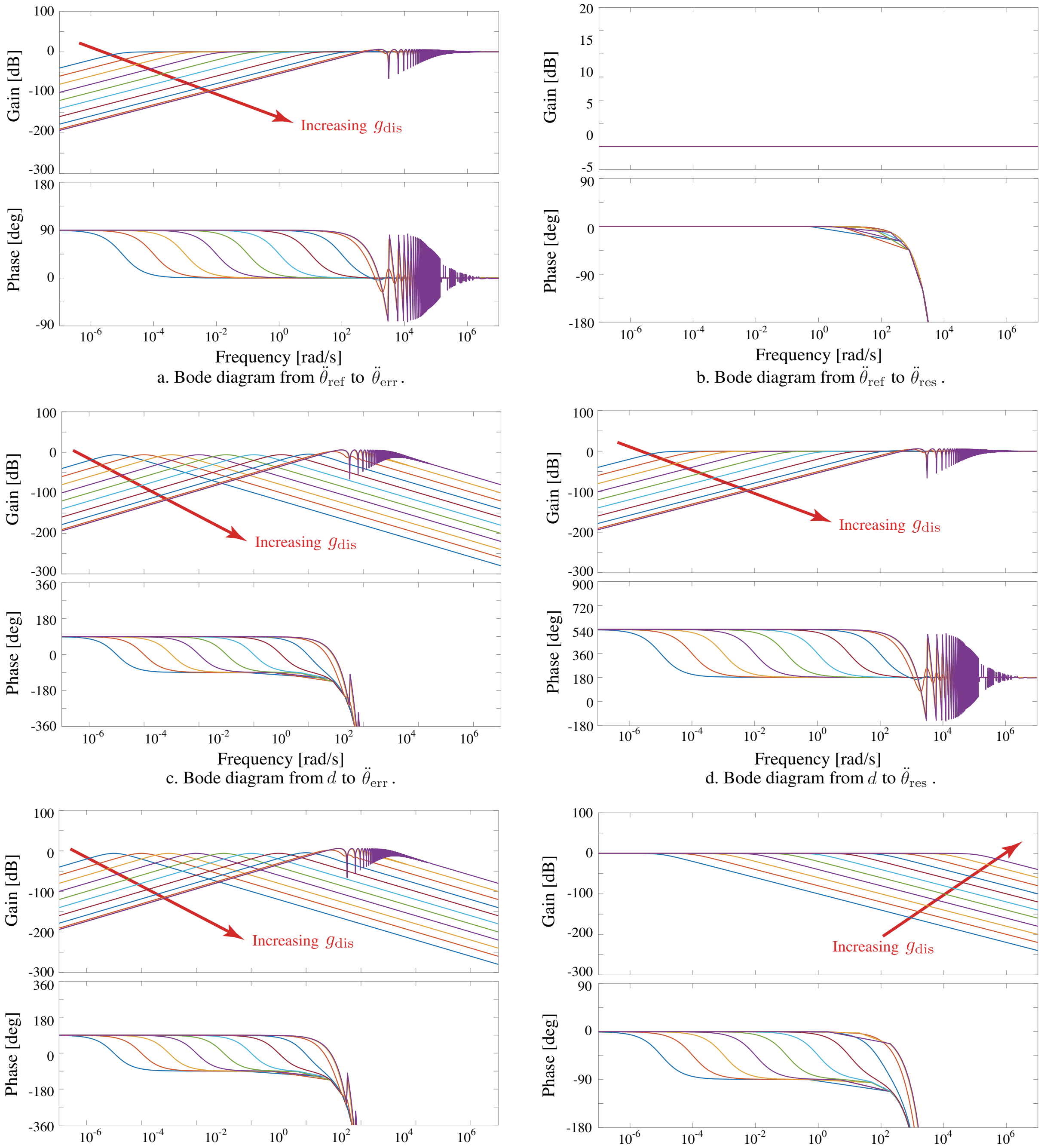

a. Bode diagram from $\ddot{\theta}_{\rm ref}$ to $\ddot{\theta}_{\rm err}$.

b. Bode diagram from $\ddot{\theta}_{\rm ref}$ to $\ddot{\theta}_{\rm res}$.

c. Bode diagram from d to $\ddot{\theta}_{\rm err}$.

d. Bode diagram from d to $\ddot{\theta}_{\rm res}$.

e. Bode diagram from ξ to $\ddot{\theta}_{\rm err}$.

f. Bode diagram from ξ to $\ddot{\theta}_{\rm res}$.

Fig. 3-47: Bode diagram of closed loop transfer function under time delay when $g_{\rm dis}$ is changed.

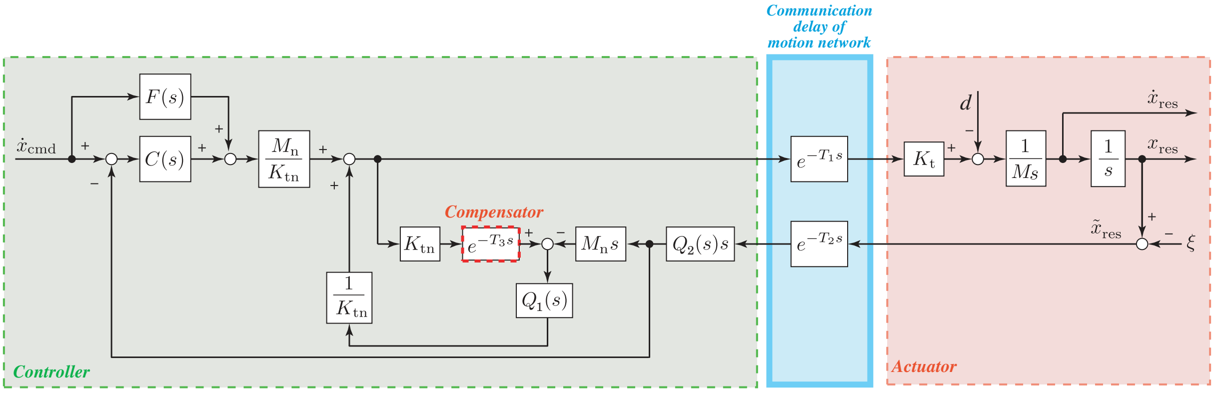

Fig. 3-48: Block diagram of velocity control via motion network.

3.2.3 Velocity Control of Automatic Machinery via Motion Network Based on Acceleration Control

In this subsection, a design method about velocity control via motion network is described. Fig. 3-48 shows the block diagram of velocity control via motion network. It contains the acceleration control system that is described in the previous subsection in a minor loop. The equivalent block diagram is derived as Fig. 3-49. When the disturbance d and sensor noise ξ are ignored, the block diagram can be rewritten as Fig. 3-50. From Fig. 3-48, the loop transfer function is expressed as follows:

$$L_{\mathrm{velo}}(s) = \frac{C(s)Q_2(s)\alpha e^{-(T_1+T_2)s}}{\left\{1 - Q_1(s)e^{-T_3 s} + \alpha Q_1(s)Q_2(s)e^{-(T_1+T_2)s}\right\}s}. \tag{3.62}$$

Also, $Q_2(s)$ is designed as follows:

$$Q_2(s) = \frac{g_{\mathrm{d}}}{s+g_{\mathrm{d}}}, \tag{3.63}$$

where g_{d} stands for the cut-off frequency of the pseudo-differentiator. Then, design guidelines of controller $C(s)$ is considered. Firstly, simple proportional control is described. The proportional controller of velocity is designed as follows:

$$C(s) \triangleq K_{\mathrm{v}}, \tag{3.64}$$

where K_{v} refers to the proportional gain of velocity controller. In order to analyze the stability of the velocity control system, Nyquist diagram is used. The case of normal DOB is shown in Fig. 3-51. In this Nyquist diagram, the delay times T_1 and T_2 are gradually changed to large value. The system becomes

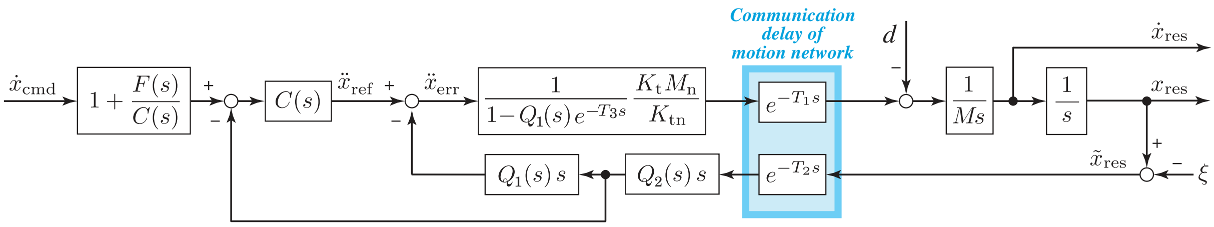

Fig. 3-49: Equivalent transformation of Fig. 3-48.

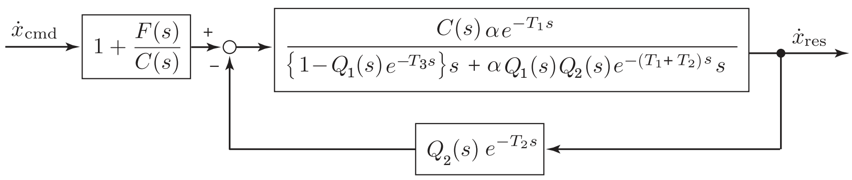

Fig. 3-50: Equivalent transformation of Fig. 3-49.

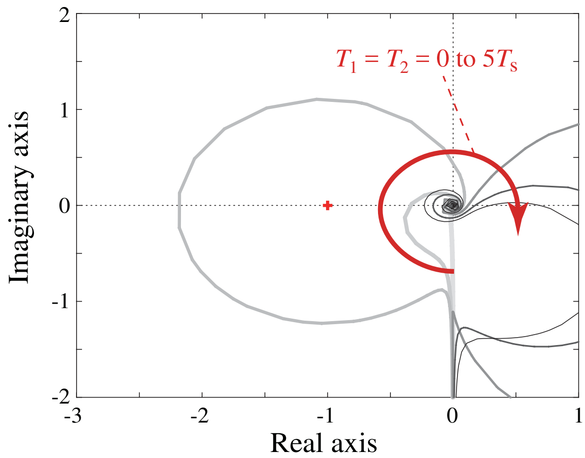

Fig. 3-51: Stability analysis of velocity control under time delay when T_1 and T_2 are changed.

unstable due to the increase of delay time. The velocity response in the case using the normal DOB when T_1 and T_2 are changed is shown in Fig. 3-52. It can be seen that the velocity response diverges when the time delay set to $2T_{\mathrm{s}}$. The Nyquist diagram of velocity control system using the delay-compensation DOB is shown in Fig. 3-53. The system keeps stability even if the time delay becomes large. However, as the delay time increases, the system is gradually becoming unstable. The cause of this destabilization is because of the time delay of the plant. The velocity response in the case using the delay-compensation DOB when T_1 and T_2 are changed is shown in Fig. 3-54. The response becomes oscillatory when the

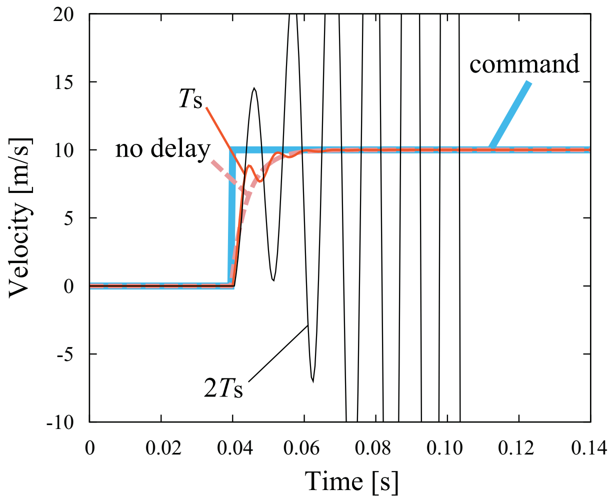

Fig. 3-52: Velocity response under time delay by the normal DOB when T_1 and T_2 are changed.

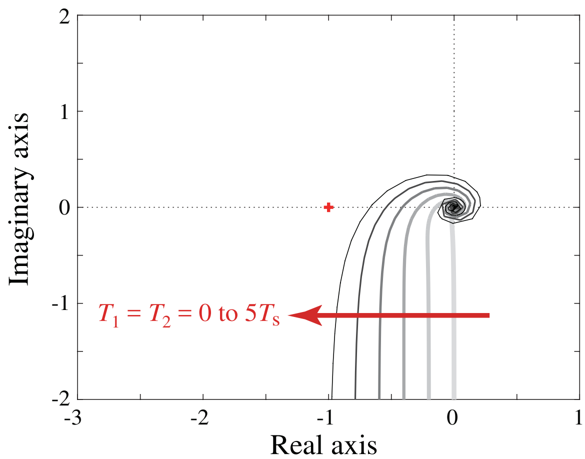

Fig. 3-53: Stability analysis of velocity control under time delay with compensator when T_1 and T_2 are changed.

time delay set large. The closed loop transfer function is derived as follows:

$$G_1(s) \quad = \quad \frac{K_{\mathrm{v}}P(s)}{1 + K_{\mathrm{v}}P_{\mathrm{n}}(s)Q_2(s)e^{-(T_1+T_2)s}}e^{-T_1 s}. \tag{3.65}$$

Since the characteristic polynomial of (3.65) contain the time delay, it is causing instability of the system. As designing methods of controllers for systems including dead time, a Smith predictor [80] and a communication disturbance observer (CDOB) [81] are known. In this dissertation, a Smith predictor is

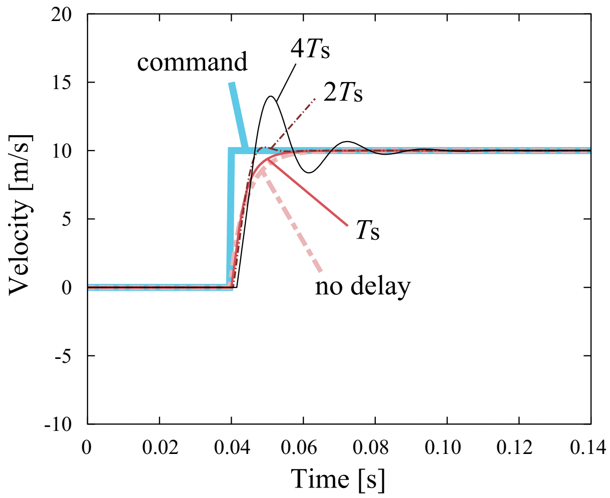

Fig. 3-54: Velocity response under time delay by the delay compensation DOB when T_1 and T_2 are changed.

applied to stabilize the time-delay system. A Smith predictor is designed as follows:

$$C_2(s) \triangleq \frac{K_{\mathrm{v}}}{1+K_{\mathrm{v}}(1-Q_2(s)e^{-(T_1+T_2)s})P_{\mathrm{n}}(s)}, \tag{3.66}$$

$$P_{\mathrm{n}}(s) = P(s) = \frac{\alpha}{\left\{1-Q_1(s)e^{-T_3 s}+\alpha Q_1(s)Q_2(s)e^{-(T_1+T_2)s}\right\}s}. \tag{3.67}$$

When $T_3 = T_1 + T_2$ and $\alpha = 1$ are assumed, $P_{\mathrm{n}}(s)$ is rewritten as follows:

$$P_{\mathrm{n}}(s) = P(s) = \frac{1}{s-(1-Q_2(s))Q_1(s)e^{-(T_1+T_2)s}s}. \tag{3.68}$$

Block diagram in the case of using the Smith predictor is shown in Fig 3-55. The closed loop transfer function is calculated by

$$\begin{aligned} G_2(s) &= \frac{K_{\mathrm{v}}P(s)}{1+K_{\mathrm{v}}P_{\mathrm{n}}(s)-K_{\mathrm{v}}P_{\mathrm{n}}(s)Q_2(s)e^{-(T_1+T_2)s}+K_{\mathrm{v}}P(s)Q_2(s)e^{-(T_1+T_2)s}}e^{-T_1 s} \\ &= \frac{K_{\mathrm{v}}P(s)}{1+K_{\mathrm{v}}P_{\mathrm{n}}(s)}e^{-T_1 s}. \end{aligned} \tag{3.69}$$

It can be seen that the time delay of the characteristic polynomial has disappeared by the Smith predictor. A Nyquist diagram in the case of using the Smith predictor is shown in Fig 3-56. From the Nyquist diagram, it can be seen that the system becomes stable by the Smith predictor. The velocity response in the case using the delay-compensation DOB with Smith predictor when T_1 and T_2 are changed is

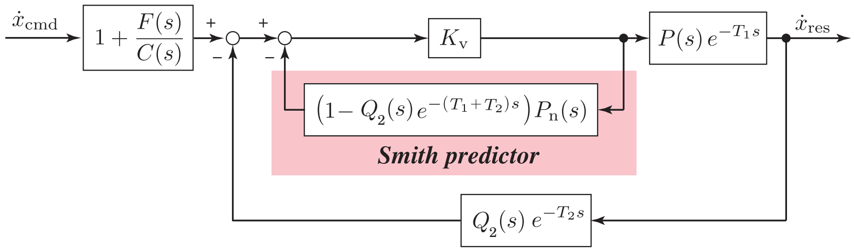

Fig. 3-55: Block diagram of velocity control via motion network with Smith predictor.

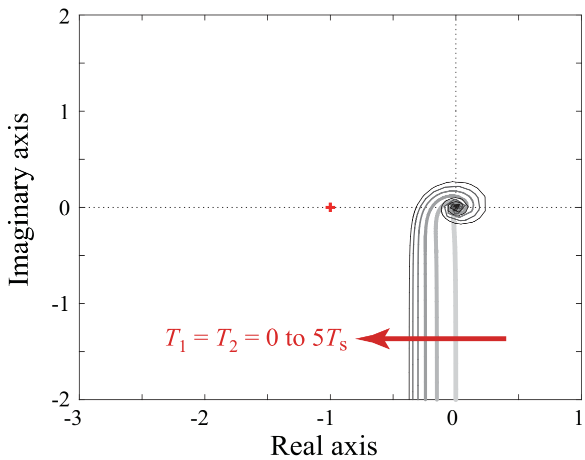

Fig. 3-56: Stability analysis of velocity control under time delay with the Smith predictor when T_1 and T_2 are changed.

shown in Fig. 3-57. When the cut-off frequency of Q_s is set to large enough, the plant $P(s)$ can be assumed $\frac{1}{s}$. In this simulation, plant model in the Smith predictor is implemented as $\frac{1}{s}$ for simplicity. From this simulation result, it can be seen that the system becomes stable by the Smith predictor and the delay-compensation DOB. Parameters for the analysis of velocity control are shown in Table 3.7. Then, the feed-forward controller $F(s)$ is considered. From (3.69), an ideal feed-forward controller can be designed as follows:

$$\frac{\dot{x}_{\mathrm{res}}}{\dot{x}_{\mathrm{ref}}} = \left\{1+\frac{F(s)}{C_2(s)}\right\}\frac{K_{\mathrm{v}}P(s)}{1+K_{\mathrm{v}}P_{\mathrm{n}}(s)}e^{-T_1 s} = e^{-T_1 s}. \tag{3.70}$$

Therefore,

$$\frac{F(s)}{C_2(s)} = \frac{1}{K_{\mathrm{v}}P_{\mathrm{n}}(s)}, \tag{3.71}$$

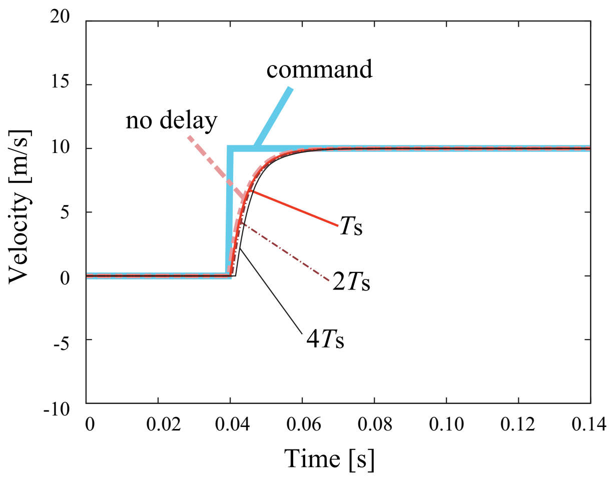

Fig. 3-57: Velocity response under time delay by the delay-compensation DOB with the Smith predictor when T_1 and T_2 are changed.

Table 3.7: Parameters for stability analysis of velocity control under time delay.

Parameter	Description	Value
T_{s}	Sampling time	500×10^{-6} s
g_{dis}	Cut-off frequency of the DOB	600 rad/s
g_{d}	Cut-off frequency of pseudo-differentiator for velocity calculation	10,000 rad/s
K_{v}	Velocity proportional gain	200

is the condition of ideal feed-forward controller design. From (3.71), $F(s)$ is designed as follows:

$$F(s) = \frac{s^2}{s + K_{\mathrm{v}} - K_{\mathrm{v}} Q_2(s) e^{-(T_1+T_2)s}}. \tag{3.72}$$

By using these control methods, precise velocity control can be achieved even if there is a round trip time delay.

3.2.4 Automatic Controller Design Under Time-delay Based on the EDM

Here, the velocity controller is designed automatically by the EDM. The block diagram of automatic generation of velocity controller is depicted as Fig. 3-58. The fitness function for the EDM is defined as follows:

$$\Gamma_{\mathrm{td}} = \frac{1}{N_{\mathrm{sum}}} \sum_{q=1}^{N_{\mathrm{sum}}} \sqrt{\left\{ \dot{x}_{\mathrm{cmd}}(q) - \dot{x}_{\mathrm{res}}(q) \right\}^2}, \tag{3.73}$$

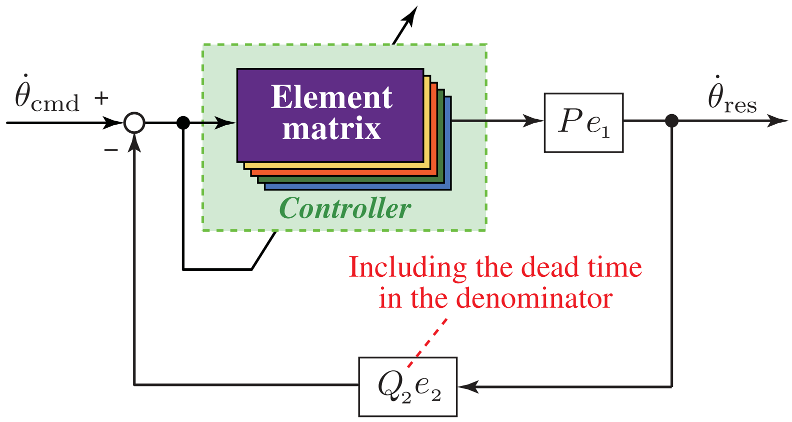

Fig. 3-58: Block diagram of automatic controller generation by the EDM.

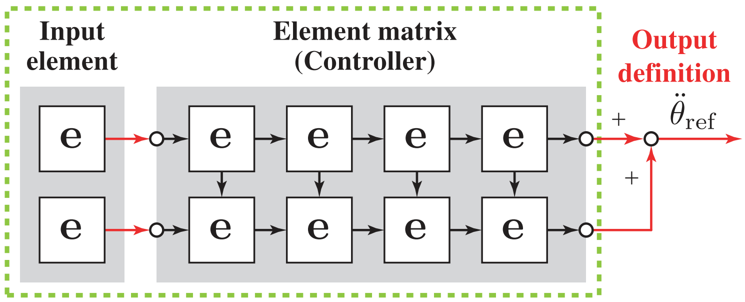

Fig. 3-59: Design of element matrix.

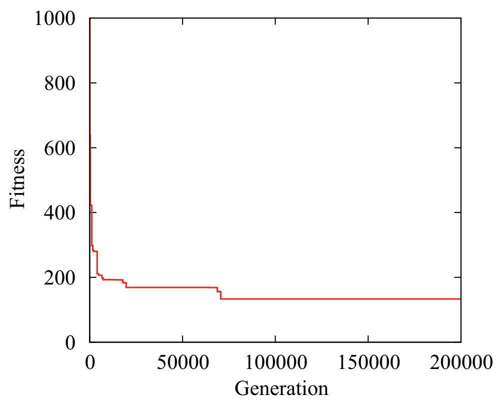

Fig. 3-60: Fitness response of automatic velocity controller design under time delay.

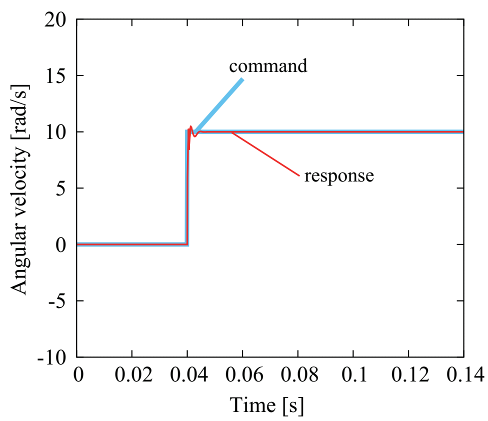

Fig. 3-61: Velocity response using the EDM controller.

where Γ_{td} and N_{sum} express the fitness value and number of the time-series data, respectively. The element matrix of the EDM is designed as Fig 3-59. Inputs of the element matrix are selected from

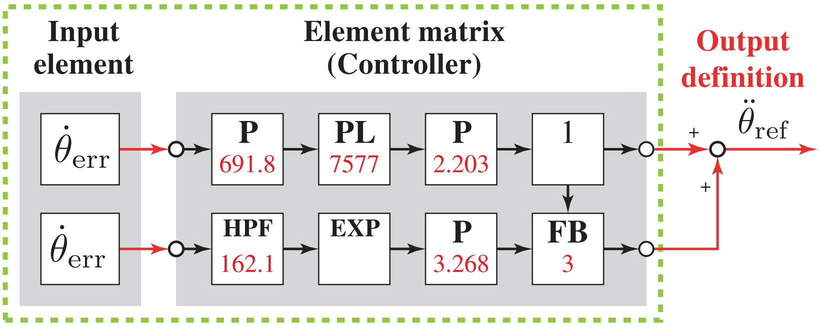

Fig. 3-62: Velocity controller abstracted by the EDM.

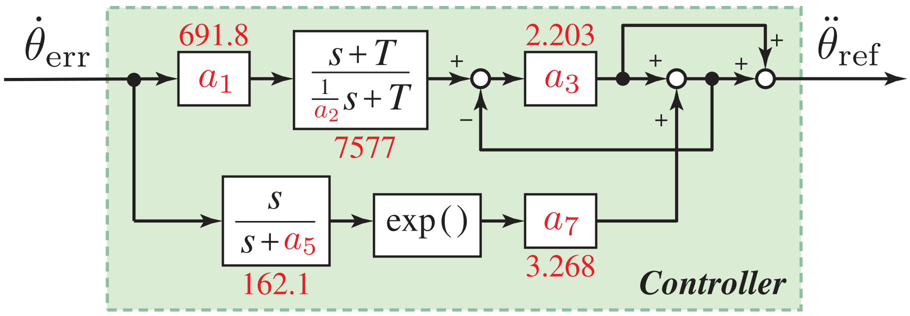

Fig. 3-63: Equivalent transformation of Fig. 3-62.

$\theta_{\rm err}$ or $\ddot{\theta}_{\rm ref}$. Fig. 3-60 depicts the fitness response of automatic velocity controller design under time delay. The response of angular velocity after evolution for 200,000 times is shown in the Fig. 3-61. It was confirmed that the transient response of the angular velocity was improved. The combination of the element matrix of 200,000 generations is shown in Fig. 3-62. The equivalent conversion of Fig. 3-62 leads to Fig. 3-63.

3.2.5 Experiments of Velocity Control via Motion Network

In order to confirm the proposed method, experiments are conducted. Fig. 3-64 shows the experimental setup. A servo motor SGMGV-30A (Yaskawa Electric) implemented in a powder filling machinery is used for experiments. The servo motor is controlled via Mechatrolink III. The step response of each control method is compared. The velocity command is set to 2 π rad/s from 0.04 s. Table 3.8 shows parameters for the experiment of velocity control via motion network. The experimental result is shown in Fig. 3-65. It can be seen that the proposed method suppresses vibration and obtains a better response. Therefore, the effectiveness of the proposed method was confirmed by experiments.

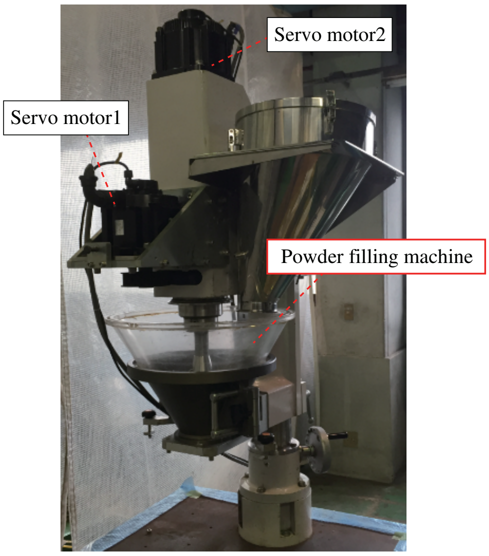

Fig. 3-64: Experimental setup using motion network.

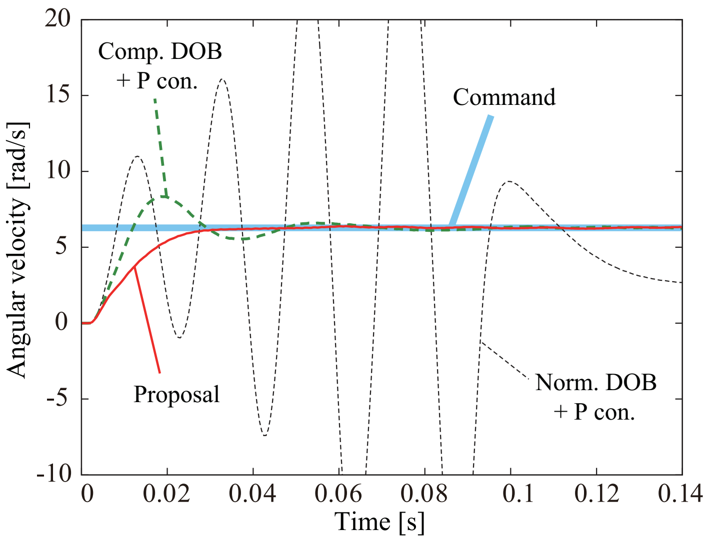

Fig. 3-65: Velocity responses via motion network in experiment .

3.3 Model-based Force Control Considering Unknown Environment

The schematic of position control and force control is shown in Fig. 3-66. It is a well-known fact that the performance of a force control system depends on the impedance of a contacting environment. This figure indicates the force control system includes environmental impedance in its transfer function. Hence, in order to obtain good response of force, recognition of the environmental impedance is im-

Table 3.8: Parameters for experiment of velocity control via motion network.

Parameter	Description	Value
T_{s}	Sampling time	500×10^{-6} s
g_1	Cut-off frequency of the DOB	400 rad / s
g_2	Cut-off frequency of velocity calculation	400 rad / s
K_{v}	Velocity proportional gain	200
J_{n}	Nominal value of inertia	0.005 kg m^2
K_{tn}	Nominal value of torque constant	0.848 Nm / A

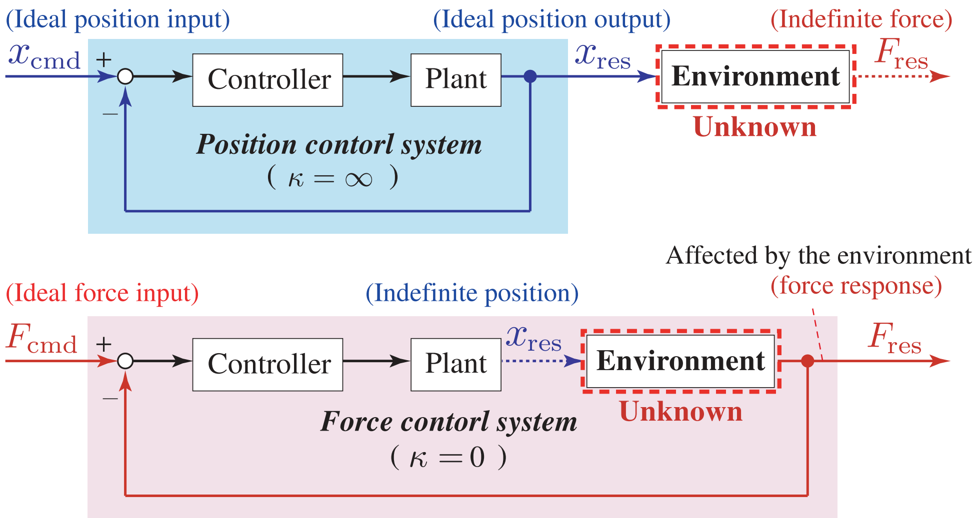

Fig. 3-66: Comparison with position control and force control.

portant. Admittance feed-forward control based on the environmental impedance is one of the effective methods to control the force precisely. In this section, the necessity of environment identification in a force control system is explained. The block diagram of a force control system using admittance feed-forward control is shown in Fig. 3-67. Assuming the ideal condition, the filter value of a system can be expressed as follows

$$G_{\mathrm{dis}}(s) = 0, \tag{3.74}$$

$$G_{\mathrm{ext}}(s) = 1, \tag{3.75}$$

$$M = M_{\mathrm{n}}, \tag{3.76}$$

$$C(s) = C_{\mathrm{p}}, \tag{3.77}$$

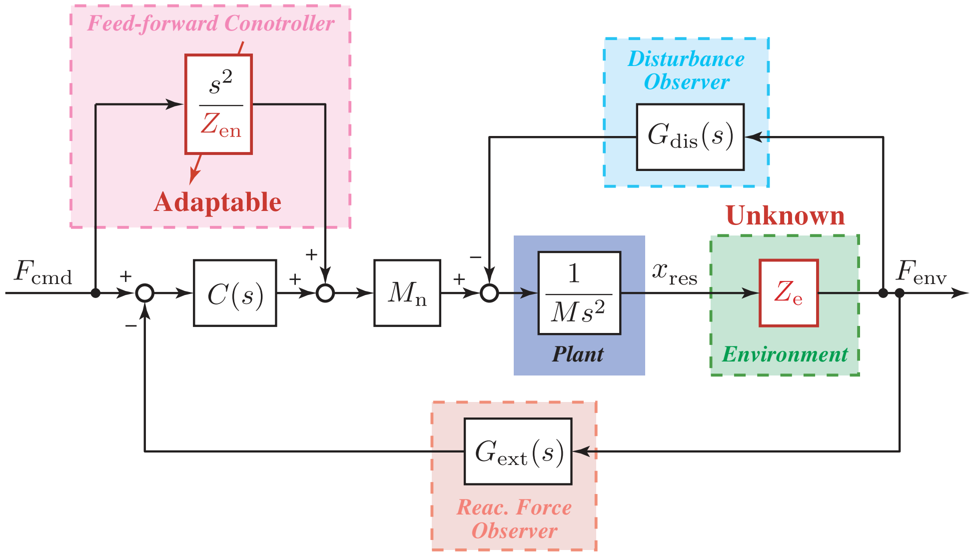

Fig. 3-67: Block diagram of force control with feed-forward controller.

where $G_{\mathrm{dis}}(s)$, $G_{\mathrm{ext}}(s)$, M, $C(s)$ and C_p refer to the high-pass filter of the DOB, the low-pass filter of the RFOB, mass of plant, force controller and proportional gain, respectively. The subscript n expresses as the nominal value. The transfer function of this system is given by

$$\frac{F_{\mathrm{env}}}{F_{\mathrm{cmd}}} = \frac{C_{\mathrm{p}} Z_{\mathrm{e}}(s)\{s^2 + C_{\mathrm{p}} Z_{\mathrm{en}}(s)\}}{C_{\mathrm{p}} Z_{\mathrm{en}}(s)\{s^2 + C_{\mathrm{p}} Z_{\mathrm{e}}(s)\}}, \tag{3.78}$$

$$Z_{\mathrm{e}}(s) = D_{\mathrm{e}} s + K_{\mathrm{e}}, \tag{3.79}$$

$$Z_{\mathrm{en}}(s) = D_{\mathrm{en}} s + K_{\mathrm{en}}, \tag{3.80}$$

where F_{env}, F_{cmd}, Z_{e}, D_{e} and K_{e} stand for the reaction force from environment, command force, environmental impedance, damper coefficient, and spring coefficient, respectively. The subscript cmd, res, e and n refer to the command value, response value, value of actual environment, and value of nominal environment, respectively. From (3.78), when the nominal environmental impedance equal to actual environmental impedance, the transfer function of system becomes 1. Therefore, perfect tracking of force control can be achieved. However, since the environmental impedance is unknown and the parameters vary, identification of the environmental impedance for feed-forward control is indispensable. Hence, the instantaneous identification method of environmental impedance is needed to control contact force precisely.

3.3.1 Recursive Least-square Method

A major identification method of environmental impedance is the recursive least-square method [82]. The recursive least square method is widely used for on-line identification purpose. The recursive least square method is calculated as

$$\boldsymbol{P}_{(k+1)} = \frac{1}{\mu}\left\{\boldsymbol{P}_{(k)} + \frac{\boldsymbol{P}_{(k)}\boldsymbol{m}_{(k+1)}\boldsymbol{m}^T_{(k+1)}\boldsymbol{P}_{(k)}}{\mu + m^T_{(k+1)}\boldsymbol{P}_{(k)}\boldsymbol{m}_{(k+1)}}\right\}, \tag{3.81}$$

$$\hat{\boldsymbol{z}}_{(k+1)} = \hat{\boldsymbol{z}}_{(k)} + \frac{\boldsymbol{P}_{(k)}\boldsymbol{m}_{(k+1)}}{\mu + m^T_{(k+1)}\boldsymbol{P}_{(k)}\boldsymbol{m}_{(k+1)}}\epsilon, \tag{3.82}$$

$$\epsilon = f_{\mathrm{env(k+1)}} - \boldsymbol{m}^T_{(k+1)}\hat{\boldsymbol{z}}_{(k)}, \tag{3.83}$$

$$\boldsymbol{m}_{(k)} = [x_{\mathrm{e(k)}} \quad \dot{x}_{\mathrm{e(k)}}]^T, \tag{3.84}$$

where $\boldsymbol{P}$ and μ stands for the coefficient matrix and forgetting factor, respectively. By using this method, environmental impedance can be identified. However, this method has a trade-off between the identification speed and noise sensitivity. Moreover, it spends time to apply because there are a lot of design elements.

3.3.2 Instantaneous Identification Considering Rotation Center of Impedance Plane

In this section, instantaneous identification of an environment considering rotation center of impedance plane is proposed. Overview of the proposed identification method is shown in Fig. 3-68. $E(k)$ stands for the existing range of true value. In this study, the environmental impedance is assumed as spring and damper model

$$F_{\mathrm{env}(k)} = D_{\mathrm{e}(k)}\dot{x}_{\mathrm{e}(k)} + K_{\mathrm{e}(k)}x_{\mathrm{e}(k)}, \tag{3.85}$$

$$\mathbf{z}_{\mathrm{e}(k)} = [K_{\mathrm{e}(k)} \quad D_{\mathrm{e}(k)}]^T, \tag{3.86}$$

where x_e expresses as deformation length of an environment. The subscript (k) defines sampling number of control. By considering the environmental parameters on impedance plane, stiffness and damper

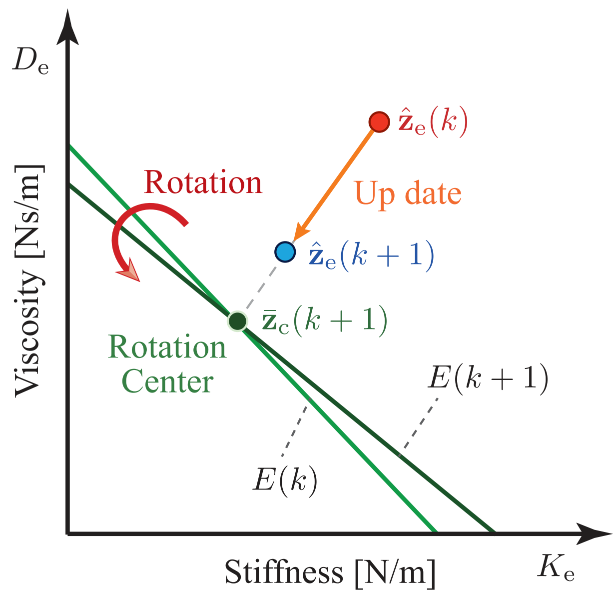

Fig. 3-68: Concept diagram of the proposed method.

coefficients are derived by

$$\tilde{K}_{\mathrm{e}(k+1)} = \frac{F_{\mathrm{env}(k)}\dot{x}_{\mathrm{e}(k+1)} - F_{\mathrm{env}(k+1)}\dot{x}_{\mathrm{e}(k)}}{x_{\mathrm{e}(k)}\dot{x}_{\mathrm{e}(k+1)} - \dot{x}_{\mathrm{e}(k)}x_{\mathrm{e}(k+1)}}, \tag{3.87}$$

$$\tilde{D}_{\mathrm{e}(k+1)} = \frac{F_{\mathrm{env}(k+1)}}{\dot{x}_{\mathrm{e}(k+1)}} - \frac{x_{\mathrm{e}(k+1)}}{\dot{x}_{\mathrm{e}(k+1)}}\tilde{K}_{\mathrm{e}(k+1)}, \tag{3.88}$$

$$\bar{\mathbf{z}}_{\mathrm{e}(k)} = \frac{1}{n}\sum_{q=k-n}^{k} \tilde{\mathbf{z}}_{\mathrm{e(q)}}, \tag{3.89}$$

$$\hat{\mathbf{z}}_{\mathrm{e}(k+1)} = \left\{\bar{\mathbf{z}}_{\mathrm{e}(k)} - \hat{\mathbf{z}}_{\mathrm{e}(k)}\right\}\alpha + \hat{\mathbf{z}}_{\mathrm{e}(k)}, \tag{3.90}$$

where n and α refer to the mean number and convergence coefficient, respectively. The superscript $\tilde{\bullet}$, $\bar{\bullet}$ and $\hat{\bullet}$ refer to intersection value, the value of center of gravity and estimated value. (3.89) stands for the moving center of gravity of intersection value. When the system has noise, the noise influence is decreased by setting n and α. Next, it is shown that the estimate value converges to true value in ideal condition. In the case of ideal condition, n and α set 1. The environmental impedance can be estimated as

$$\begin{aligned}\tilde{K}_{\mathrm{e}(1)} &= \frac{F_{\mathrm{env}(0)}\dot{x}_{\mathrm{e}(1)} - F_{\mathrm{env}(1)}\dot{x}_{\mathrm{e}(0)}}{x_{\mathrm{e}(0)}\dot{x}_{\mathrm{e}(1)} - \dot{x}_{\mathrm{e}(0)}x_{\mathrm{e}(1)}} \\ &= \frac{\dot{x}_{\mathrm{e}(0)}x_{\mathrm{e}(1)} - x_{\mathrm{e}(0)}\dot{x}_{\mathrm{e}(1)}}{\dot{x}_{\mathrm{e}(0)}x_{\mathrm{e}(1)} - x_{\mathrm{e}(0)}\dot{x}_{\mathrm{e}(1)}}K_{\mathrm{e}(1)} \\ &\quad + \frac{\dot{x}_{\mathrm{e}(0)}\dot{x}_{\mathrm{e}(1)} - \dot{x}_{\mathrm{e}(0)}\dot{x}_{\mathrm{e}(1)}}{\dot{x}_{\mathrm{e}(0)}x_{\mathrm{e}(1)} - x_{\mathrm{e}(0)}\dot{x}_{\mathrm{e}(1)}}D_{\mathrm{e}(1)} \\ &= K_{\mathrm{e}(1)}, \end{aligned} \tag{3.91}$$

$$\begin{aligned}\tilde{D}_{\mathrm{e}(1)} &= \frac{D_{\mathrm{e}(1)}\dot{x}_{\mathrm{e}(1)} + K_{\mathrm{e}(1)}x_{\mathrm{e}(1)}}{\dot{x}_{\mathrm{e}(1)}} - \frac{x_{\mathrm{e}(1)}}{\dot{x}_{\mathrm{e}(1)}}K_{\mathrm{e}(1)} \\ &= D_{\mathrm{e}(1)}. \end{aligned} \tag{3.92}$$

The proposed method can estimate the true value of impedance until 2 scan in ideal condition. Then, influence of a low-pass filter using force sensing is considered. In actual situations, force information is obtained via a low-pass filter. The influence of the low-pass filter is considered in this section. Considering the low-pass filter, (3.87) and (3.88) are expressed as

$$\tilde{K}^{\mathrm{lpf}}_{\mathrm{e}(k+1)} = \frac{G_{\mathrm{dis}}F_{\mathrm{env}(k)}\dot{x}^{\mathrm{lpf}}_{\mathrm{e}(k+1)} - G_{\mathrm{dis}}F_{\mathrm{env}(k+1)}\dot{x}^{\mathrm{lpf}}_{\mathrm{e}(k)}}{x^{\mathrm{lpf}}_{\mathrm{e}(k)}\dot{x}^{\mathrm{lpf}}_{\mathrm{e}(k+1)} - \dot{x}^{\mathrm{lpf}}_{\mathrm{e}(k)}x^{\mathrm{lpf}}_{\mathrm{e}(k+1)}}, \tag{3.93}$$

$$\tilde{D}^{\mathrm{lpf}}_{\mathrm{e}(k+1)} = \frac{G_{\mathrm{dis}}F_{\mathrm{env}(k+1)}}{\dot{x}^{\mathrm{lpf}}_{\mathrm{e}(k+1)}} - \frac{x^{\mathrm{lpf}}_{\mathrm{e}(k+1)}}{\dot{x}^{\mathrm{lpf}}_{\mathrm{e}(k+1)}}\tilde{K}^{\mathrm{lpf}}_{\mathrm{e}(k+1)}, \tag{3.94}$$

where G_{dis} refers to the low-pass filter. The superscript lpf expresses modified value in order to consider the influence of the low-pass filter. By setting $\dot{x}^{\mathrm{lpf}}_{\mathrm{e}(k)}$ and $x^{\mathrm{lpf}}_{\mathrm{e}(k)}$ as

$$x^{\mathrm{lpf}}_{\mathrm{e}(k)} = G_{\mathrm{dis}}x_{\mathrm{e}(k)}, \tag{3.95}$$

$$\dot{x}^{\mathrm{lpf}}_{\mathrm{e}(k)} = G_{\mathrm{dis}}\dot{x}_{\mathrm{e}(k)}, \tag{3.96}$$

the influence of the low-pass filter can be suppressed. Also, in order to apply to real situations, sensing noises and disturbances (e.g., friction force and nominal error) must be considered. In real situations, external force can be expressed as

$$F_{\mathrm{ext}} = F_{\mathrm{env}} + w, \tag{3.97}$$

where w defines the noise and disturbance except the reaction force from an environment. The estimation error can be expressed as

$$K_{e(k)} = \tilde{K}_{e(k)} + \Delta K_{e(k)}, \tag{3.98}$$

$$D_{e(k)} = \tilde{D}_{e(k)} + \Delta D_{e(k)}. \tag{3.99}$$

(3.87) and (3.88) are redefined as

$$\begin{aligned} \tilde{K}_{e(k+1)} &= \frac{F_{env(k)} - F_{env(k+1)}r}{x_{e(k)} - x_{e(k+1)}r} + \frac{w_{(k)} - w_{(k+1)}r}{x_{e(k)} - x_{e(k+1)}r} \\ &= K_{e(k+1)} + \frac{w_{(k)} - w_{(k+1)}r}{x_{e(k)} - x_{e(k+1)}r}, \end{aligned} \tag{3.100}$$

$$\Delta K_{e(k+1)} = \frac{w_{(k)} - w_{(k+1)}r}{x_{e(k)} - x_{e(k+1)}r}, \tag{3.101}$$

$$\Delta D_{e(k+1)} = \frac{w_{(k+1)}}{\dot{x}_{e(k+1)}} - \frac{x_{e(k+1)}}{\dot{x}_{e(k+1)}}\Delta K_{e(k+1)}, \tag{3.102}$$

$$r = \frac{\dot{x}_{e(k)}}{\dot{x}_{e(k+1)}}. \tag{3.103}$$

In order to analyze the proposed method, r is assumed nearly equal 1 (i.e., acceleration $\simeq 0$).

$$\begin{aligned} \Delta K_{e(k+1)} &= \frac{w_{(k)} - w_{(k+1)}}{x_{e(k)} - x_{e(k+1)}} \\ &= \frac{w_{(k)} - w_{(k+1)}}{x_{e(k)} - (\dot{x}_{e(k)}\Delta t + x_{e(k)})} \\ &= \frac{w_{(k)} - w_{(k+1)}}{\dot{x}_{e(k)}\Delta t}, \end{aligned} \tag{3.104}$$

$$\Delta D_{e(k+1)} = \frac{x_{e(k)}(w_{(k)} - w_{(k+1)}) + \dot{x}_{e(k)}w_{(k)}\Delta t}{\dot{x}^2_{e(k)}\Delta t}. \tag{3.105}$$

Therefore, the estimation error becomes small in the case that $\dot{x}_e$ is large and x_e is small. The above condition is consistent with the conditions immediately after contact. Since the impedance should be obtained immediately after the contact, the performance of the proposed method is consistent with the request. From the above reason, the parameter α is set as

$$\alpha = 1 - e^{-\left|\frac{\dot{x}_{e(k)}}{x_{e(k)}}\right|\beta}, \tag{3.106}$$

where β defines sensitivity gain.

Table 3.9: Common parameter for the simulations of impedance identification.

Parameter	Descriptions	Value
T_{s}	Control period	10^{-4} s
P_{s}	Plant calculation period	10^{-6} s
K_{p}	Proportional gain	90000
K_{d}	Differential gain	600
g_{dis}	Cut-off frequency of the DOB	1000 rad/s
g_{ext}	Cut-off frequency of the RFOB	1000 rad/s
$\dot{x}_{\mathrm{cmd}}$	Velocity command	0.1 m/s
F_{lim}	Limited force	10 N
x_{ini}	Initial position	0.001 m
β	Sensitivity gain of the proposed method	0.01
n	Average number of intersection points	10
K_{ini}	Estimation initial value of stiffness	1000 N/m
D_{ini}	Estimation initial value of viscosity	20 Ns/m

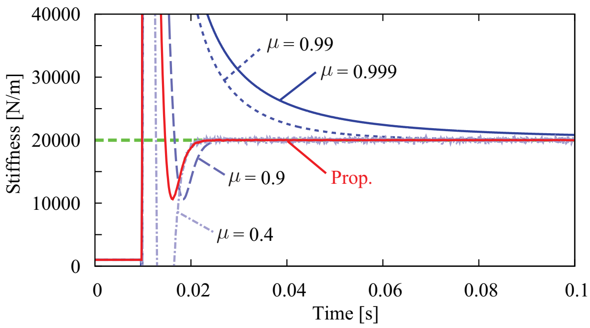

a. Stiffness estimation.

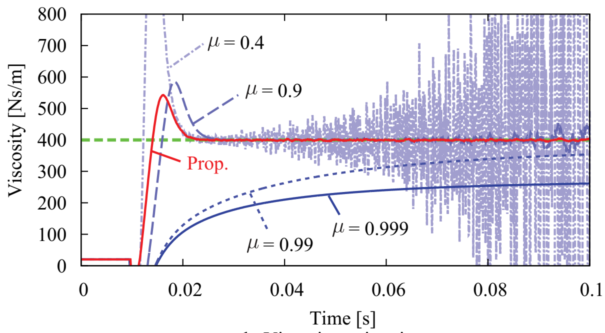

b. Viscosity estimation.

Fig. 3-69: Simulation results with changing μ.

3.3.3 Simulations of Impedance Identification

In this part, simulations are conducted in order to verify the performance of the proposed method. In this study, the proposed method is compared with an recursive least square method as a conventional method.

Simulation Setup of Impedance Identification

This part explains simulation conditions. Simulation is implemented by Visual Basic. In order to evaluate the proposed method quantitatively, optimal setting of the simulation parameter is important. $\boldsymbol{P}_{(0)}$ and μ in recursive least square method affects the performance of the identification speed and noise sensitivity. In order to generate the system noise w, uniform distribution noise is added to the position

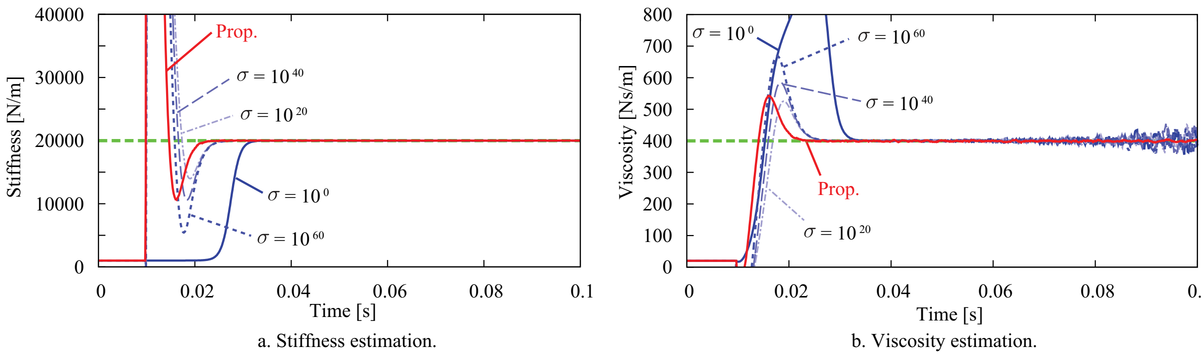

Fig. 3-70: Simulation results with changing σ.

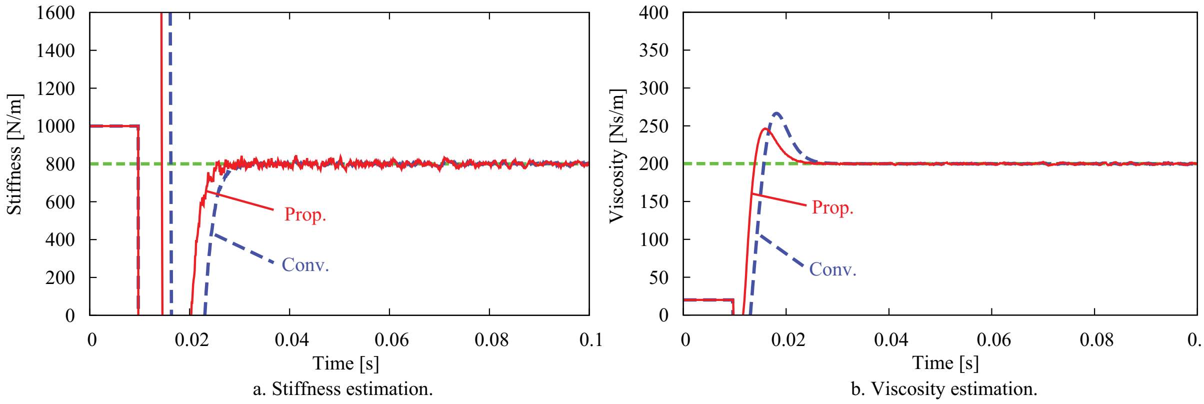

Fig. 3-71: Simulation results of Simulation 2.

response value using “rnd” function of Visual Basic. This noise assumes the sensing noise of a position sensor. The range of noise is set $\pm 10^{-8}$ m. In this simulation, the initial value of coefficient matrix $\boldsymbol{P}_{(0)}$ is designed as

$$\boldsymbol{P}_0 = \begin{bmatrix} \sigma & 0 \\ 0 & \sigma \end{bmatrix}. \tag{3.107}$$

The actuator is moved by position control. Position command is applied as

$$x_{\mathrm{cmd}} = \dot{x}_{\mathrm{cmd}} t. \tag{3.108}$$

In order to contact to environments, the output force is limited by

$$F_{\mathrm{ref}} = \begin{cases} F_{\mathrm{lim}} & (F_{\mathrm{lim}} < F_{\mathrm{ref}}) \\ -F_{\mathrm{lim}} & (-F_{\mathrm{lim}} > F_{\mathrm{ref}}) \end{cases} . \tag{3.109}$$

Table 3.10: Parameters of conventional method for the simulations of impedance identification.

Sim. No.	σ	μ	K_{e}	D_{e}
Sim. 1. 1	10^{40}	$0.4 \to 0.999$	20000	400
Sim. 1. 2	$10^{0} \to 10^{60}$	0.9	20000	400
Sim. 2	10^{40}	0.9	1000	200

In simulation 1, the identification speed and noise sensitivity are compared between the proposed method and conventional method. The optimal parameter of the conventional method is confirmed simultaneously in this simulation. In simulation 2, influence of environmental impedance value is confirmed. The common parameters of simulations are shown in Table 3.9. Parameters of the conventional method for simulations of impedance identification are shown in Table 3.10.

Simulation Results of Impedance Identification

Figs. 3-69 and 3-70 show the results of simulation 1. When the value of μ is set as large value, noise sensitivity becomes low, and the identification speed becomes slow. On the contrary, the value of μ is set as small value, the noise sensitivity becomes high, and the identification speed becomes fast. The identification speed of the conventional method becomes faster, by increasing σ. However, the identification speed converged from σ set 10^{20}. Fig. 3-71 shows the results of simulation 2. The proposed method estimates the impedance faster than the conventional method with common condition. Therefore, validity of the proposed method is verified.

3.3.4 Experiments of Impedance Identification

In this part, in order to confirm the validity of the proposed method, experiments are conducted.

Experimental Setup of Impedance Identification

Fig. 3-72 shows the experimental setup of impedance identification. In this study, a single actuator system is used. The environments are shown in Fig. 3-73. In the experiments, the position ramp command was applied as well as simulations. Parameters for the experiments are shown in Table 3.11.

Experimental Results of Impedance Identification

Fig. 3-74 shows the position and force response of the experiments. Figs. 3-75 and 3-76 show the identification results of rubber block and tennis ball. The parameters of the conventional method are

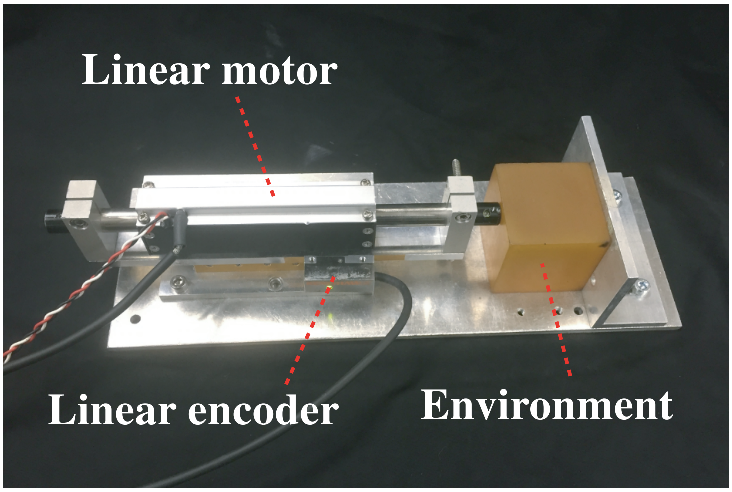

Fig. 3-72: Experimental setup of impedance identification.

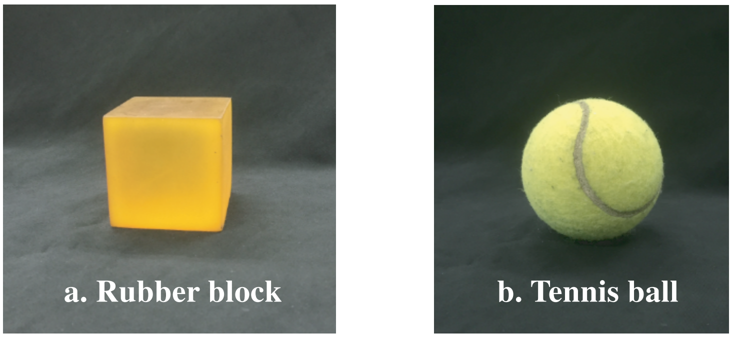

Fig. 3-73: Environments for impedance identification.

Table 3.11: Parameters for the experiments of impedance identification.

Parameter	Description	Value
T_{s}	Control period	10^{-4} s
K_{p}	Proportional gain	10000
K_{d}	Differential gain	200
g_{dis}	Cut-off frequency of the DOB	1000
g_{ext}	Cut-off frequency of the RFOB	1000
$\dot{x}_{\mathrm{cmd}}$	Velocity command	0.04 m/s
F_{lim}	Limited force	10 N
β	Sensitivity gain of the proposed method	0.01
n	Mean number of the proposed method	10
K_{ini}	Estimation initial value of stiffness	1000 N/m
D_{ini}	Estimation initial value of viscosity	20 Ns/m

Table 3.12: Parameters of the conventional method for experiment.

No.	σ	μ
Conv. 1	10^{40}	0.9
Conv. 2	10^{20}	0.999

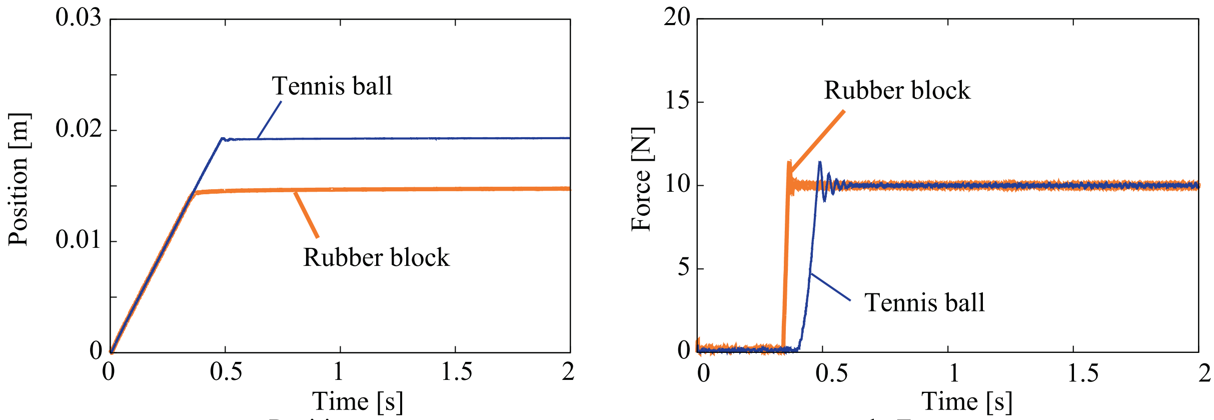

a. Position response. b. Force response.

Fig. 3-74: Actuator responses in the experiments.

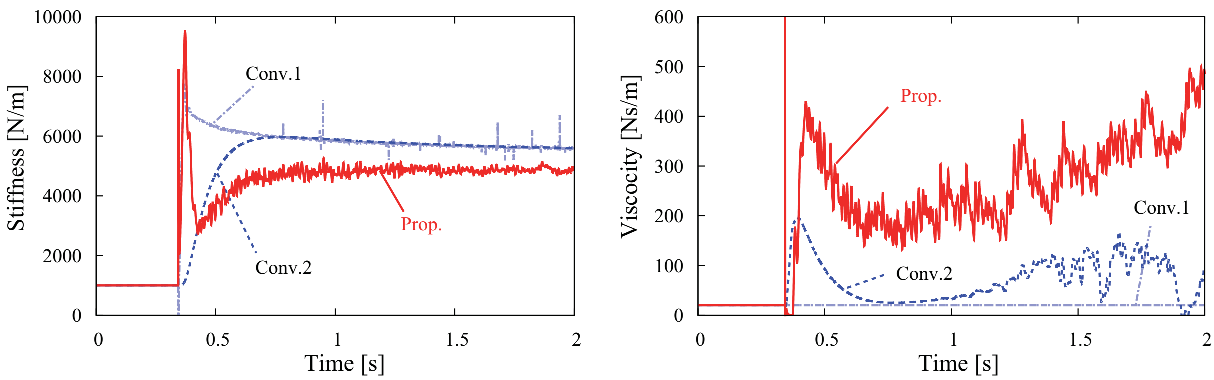

a. Stiffness estimation. b. Viscosity estimation.

Fig. 3-75: Experimental results of rubber block.

shown in Table 3.12. The parameters of Conv. 1 are the same as optimal parameter in simulation. However, using this parameter, viscosity cannot be identified. From the above reason, the parameter of Conv. 2 is modified. By using the parameter of Conv. 2, viscosity can be identified. Each method can estimate the stiffness of contact objects immediately. The proposed method estimated the viscosity about 0.8 s; on the other hand, the conventional method spend a time until estimating viscosity. Moreover, viscosity identification result of the proposed method increases gradually. It is expected that this phenomenon is

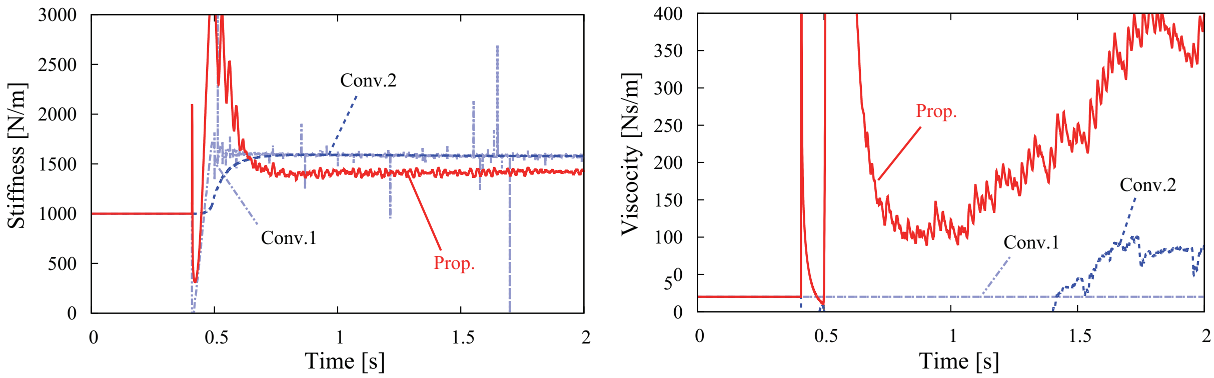

a. Stiffness estimation.
b. Viscosity estimation.

Fig. 3-76: Experimental results of tennis ball.

caused by low-speed state. Therefore, the identification of the proposed method should be stopped in low-velocity area.

3.4 Model Generation and Parameter Identification Using the EDM

3.4.1 Principle of Impedance Abstraction

In this part, an environmental identification method using the EDM is proposed. There are roughly two methods how to use the environment characteristics. One is a model-based method (white-box modeling), and the other is a data-based method (black-box modeling). The mainstream method of environmental identification is parameter identification using a least-square method [37]. This method is one of the model-based methods. This method can identify environmental impedances according to the designed model. However, this method needs to decide the model of an environment before identification. Thus, it is difficult to apply the method to an environment whose model is unknown. As another approach, black-box modeling method has been researched [41–44]. Neural network, fuzzy logic, and the method based on database can achieve input-output characteristics. However, physical meaning of target systems is difficult to understand. Komada *et. al.* proposed a robust force control method based on an environment observer [83]. This method can attain target following performance adapting to variation of environment. However, since the external force estimated by environmental observer contains several term of force, this method is difficult to know the environmental model from estimated force. Although this method uses simple spring model for feed-forward controller, more precise model should be applied for delicate control. On the contrary, a physical model and its parameter can be estimated simultaneously

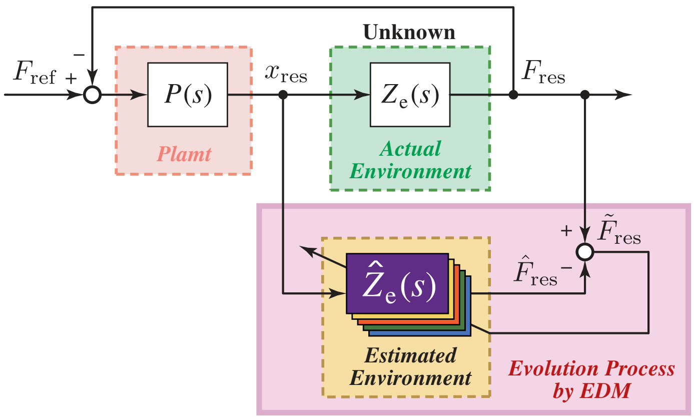

Fig. 3-77: Block diagram of environmental identification by the proposal.

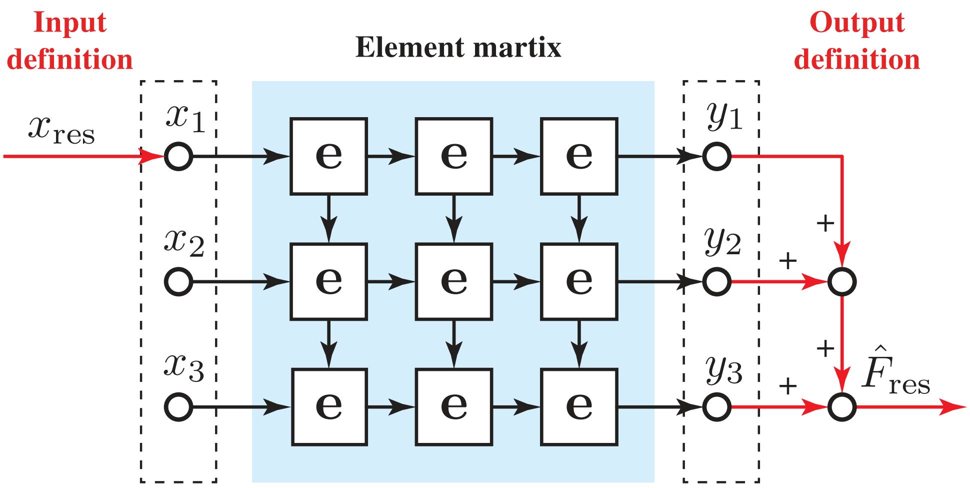

Fig. 3-78: Element matrix for environmental identification using 3 $\times$ 3 matrix.

by using the EDM. Therefore, model definition in previous is not required. In addition, physical meaning of target environment is understandable by element description. It may be possible to discover a new physical property of an environment. The block diagram of environmental identification is shown in Fig. 3-77. The environment behaves as a function between position (or velocity) and force

$$F = g(x). \tag{3.110}$$

Thus, position information is an input, and force information is an output for the element matrix in the case of environmental identification. Fig. 3-78 shows force calculation by the element matrix. This figure shows a case of using 3 $\times$ 3 matrix. In this case, the fitness function is designed as

Table 3.13: Common parameter for simulations of impedance abstraction.

Parameter	Descriptions	Value
T_{s}	Control period	10^{-4} s
K_{p}	Proportional gain	10000
K_{d}	Differential gain	500
M	Mass of actuator	0.3 kg
K_{t}	Force coefficient	0.24 N/A
x_{ini}	Location of environment	0.0 m
K_{e}	Environmental stiffness	2000 N/m
D_{e}	Environmental viscosity	500 Ns/m
x_{st}	Stroke of positioning	0.001 m
t_{ini}	Waiting time	0.2 s
t_{mv}	Moving time	0.2 s

$$\tilde{F}_{\mathrm{res}} = \hat{F}_{\mathrm{res}} - F_{\mathrm{res}}, \tag{3.111}$$

$$\Gamma_{\mathrm{ide}} = \frac{1}{T}\sum_{t=0}^{T} \tilde{F}_{\mathrm{res}}{}^{2}, \tag{3.112}$$

where $\tilde{F}_{\mathrm{res}}$, $\hat{F}_{\mathrm{res}}$, F_{res}, and T stand for the error force, estimated force, actual force, and total time of motion, respectively. When the value of the fitness function F is small, it is evaluated as a better individual. In this part, simulations and experiments are conducted in order to verify the performance of the proposed method using known environment.

3.4.2 Simulation of Impedance Abstraction

Simulation Setup of Impedance Abstraction

This section explains the simulation conditions. The simulation is implemented by C Language. In this simulation, the actuator is moved by position control. The position command is applied as

$$x_{\mathrm{cmd}} = \begin{cases} 0 & (t < t_{\mathrm{ini}}) \\ H\left(\frac{t-t_{\mathrm{ini}}}{t_{\mathrm{mv}}}\right) x_{\mathrm{st}} & (t_{\mathrm{ini}} \leq t < t_{\mathrm{ini}} + t_{\mathrm{mv}}) \\ x_{\mathrm{st}} & (t_{\mathrm{ini}} + t_{\mathrm{mv}} \leq t) \end{cases}, \tag{3.113}$$

where x_{st}, H, t_{ini}, and t_{mv} stands for the stroke distance, a function of cam curve, starting time of positioning, and moving time of positioning, respectively. The kind of cam curve is set as the distorted sine curve. Also, a PD controller is used as the position controller. In this simulation, environment is given

Table 3.14: Common parameters for the GA.

Descriptions	Value
Population size	8
Crossover rate	0.7
Mutation rate for element code	0.2
Mutation rate for element parameter	0.2

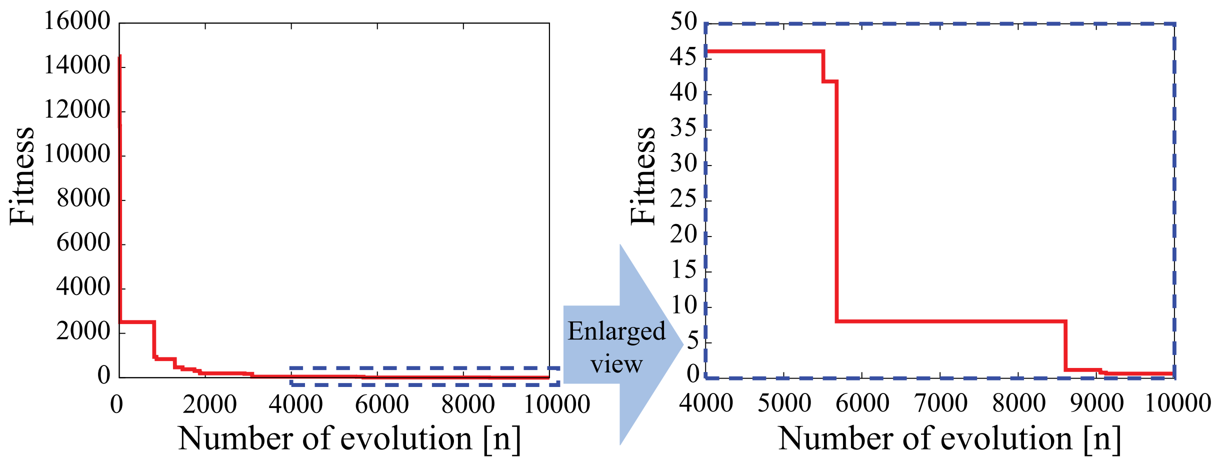

Fig. 3-79: Fitness variation in simulation.

as a spring-damper model as

$$Z_{\rm e} = D_{\rm e}s + K_{\rm e}, \tag{3.114}$$

where $Z_{\rm e}$, $D_{\rm e}$, and $K_{\rm e}$ refer to environmental impedance, environmental viscosity, and environmental stiffness, respectively. Parameters for the simulation are shown in Table 3.13. The common parameters for the GA are shown in Table 3.14.

Simulation Results of Impedance Abstraction

The fitness value of simulation is shown in Fig. 3-79. By increasing the number of evolution, fitness value became small. The force response of the simulation is shown in Fig. 3-80. In Fig. 3-80, graph legends stand for the number of evolution. By 1000 times of evolution, the actual response and estimated response became almost the same. From these figures, the effect of the evolution can be confirmed. Fig. 3-81 shows the element matrix of final individual. The lower number of each block refers to parameters used for the calculation of each block. Then, by decrypting each element of Fig. 3-81, the block diagram

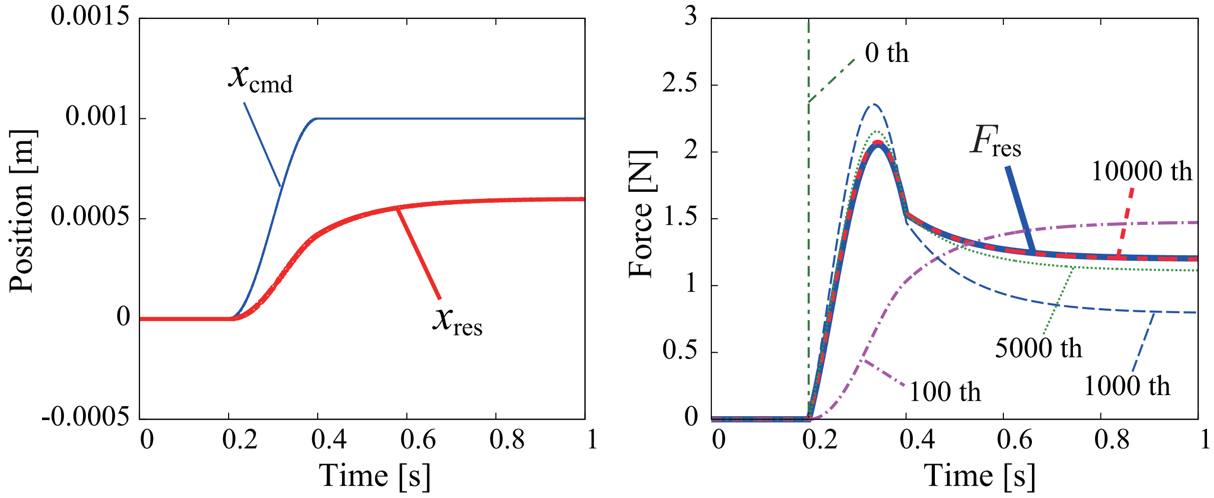

a. Position response for identification. b. Force response with evolution.

Fig. 3-80: Force response with increasing evolution.

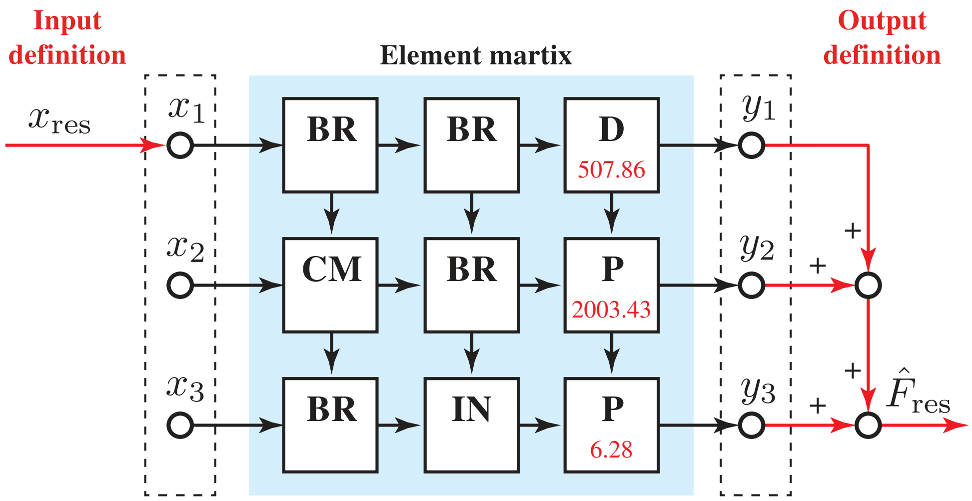

Fig. 3-81: Final individual of the simulation.

of Fig. 3-82 can be derived. This estimated model of environment matches to actual model used in the simulation. Therefore, validity of the proposed method can be verified.

3.4.3 Experiments of Impedance Abstraction

In order to verify the performance of the proposed method, experiments are conducted.

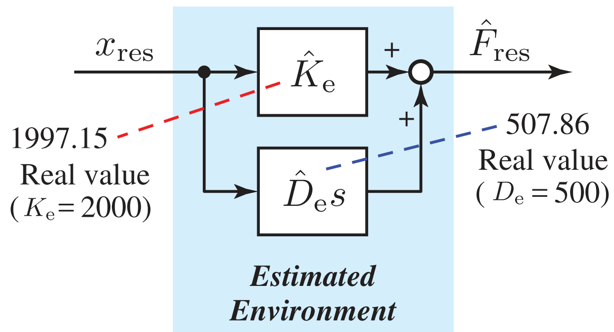

Fig. 3-82: Equivalent block diagram of Fig 3-81.

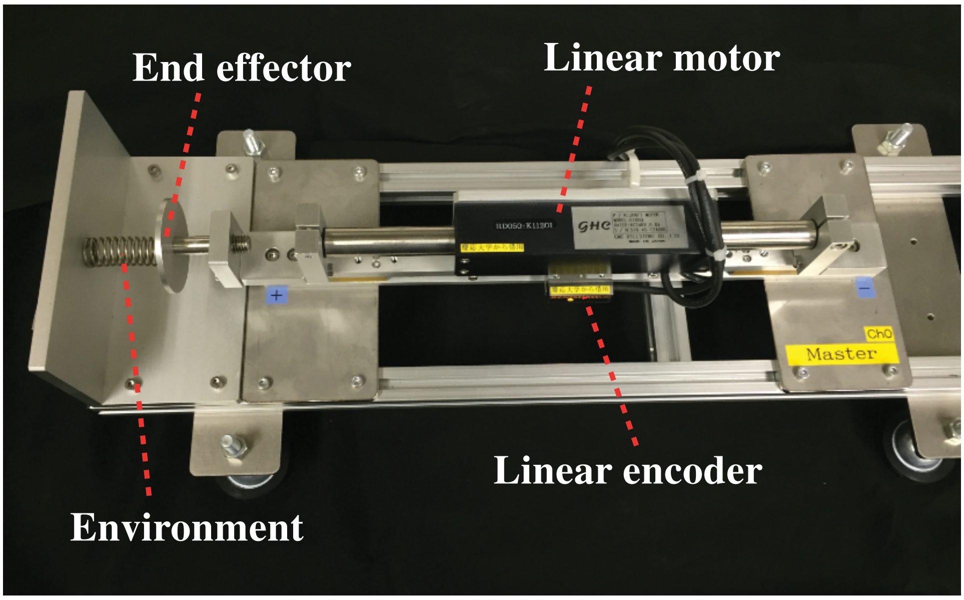

Fig. 3-83: Experimental setup for impedance abstraction.

Experimental Setup

Fig. 3-83 shows the experimental setup. In this study, a single actuator system is used. This system consists of a linear motor, a linear encoder, and an end effector. The linear motor contacts to an environment. Environments used in the experiment are shown in Fig. 3-84. The actuator is moved by position control. In order to achieve high-stiff control, the DOB is implemented. In the experiments, the position command applying to the actuator is designed sine wave command (2 Hz). Parameters for the experiments are shown in Table 3.15. In this experiments, the reaction force from the environment is acquired by the RFOB. From the position response and the force response, identification is conducted.

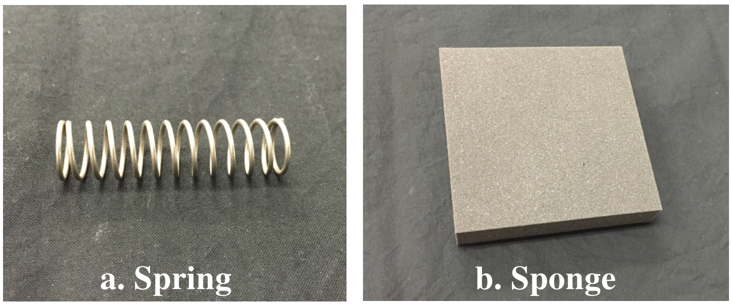

Fig. 3-84: Environments for the experiments of impedance abstraction.

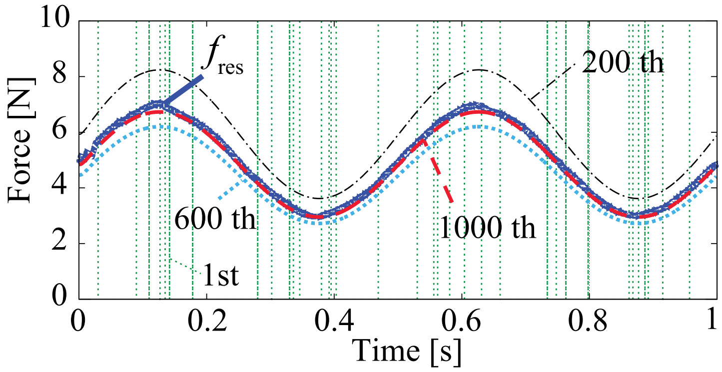

Fig. 3-85: Force response with increasing evolution (spring).

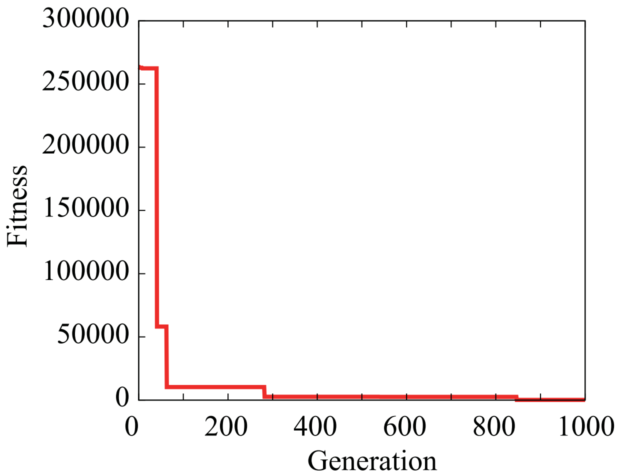

Fig. 3-86: Fitness variation in the experiment (spring).

Experimental Results

Fig. 3-85 shows the force response of the experiments using spring with increasing evolution. The fitness variation is shown in Fig. 3-86. From these figures, the actual response and estimated response

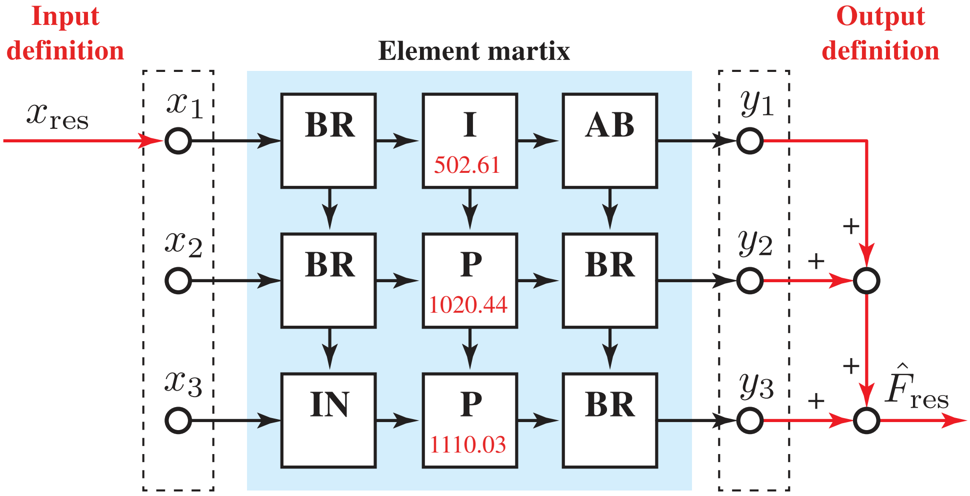

Fig. 3-87: Final individual of experiment (spring).

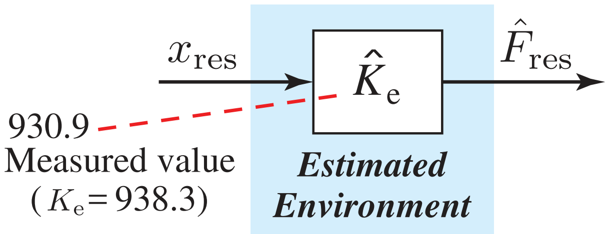

Fig. 3-88: Equivalent block diagram of Fig. 3-87.

Table 3.15: Common parameter for experiments of impedance abstraction.

Parameters	Descriptions	Value
$T_{\rm s}$	Control period	10^{-4} s
$K_{\rm p}$	Proportional gain	10000
$K_{\rm d}$	Differential gain	200
$g_{\rm dis}$	Cut-off frequency of the DOB	500 rad/s
$g_{\rm ext}$	Cut-off frequency of the RFOB	500 rad/s
$M_{\rm n}$	Nominal mass of actuator	0.7 kg
$K_{\rm tn}$	Nominal force coefficient	33.0 N/A
$x_{\rm ini}$	Location of environment	0.0 m

became almost the same by 850 times of evolution. Fig. 3-87 shows the final individual of spring identification. By decoding Fig. 3-87, a simple spring model shown in Fig. 3-88 can be derived. Fig. 3-89 shows the force response of experiments using sponge with increasing evolution. The fitness variation is shown in Fig. 3-90. The identification error becomes small by increasing the evolution

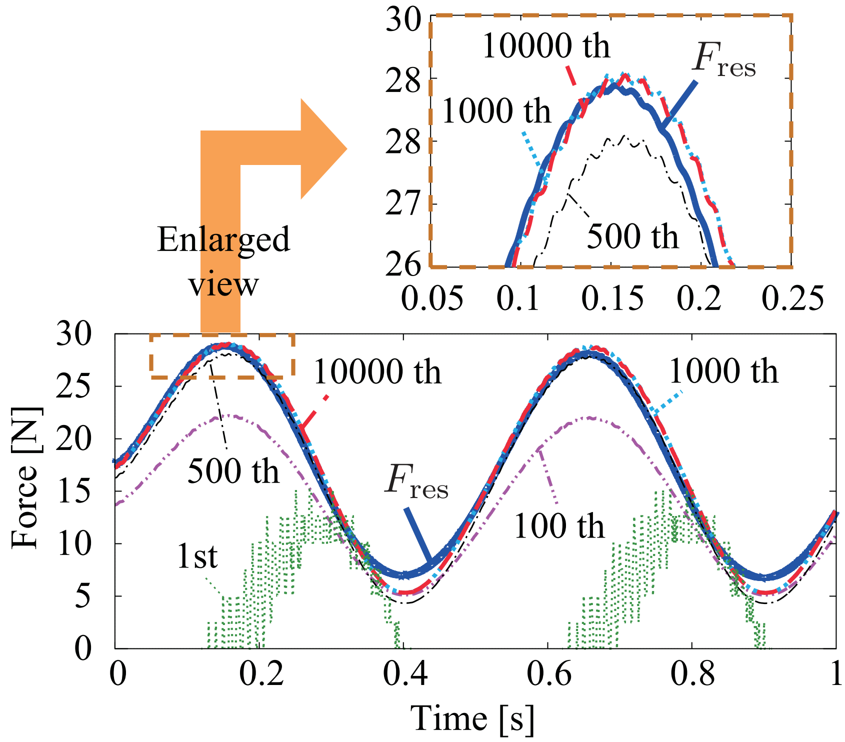

Fig. 3-89: Force response with increasing evolution (sponge).

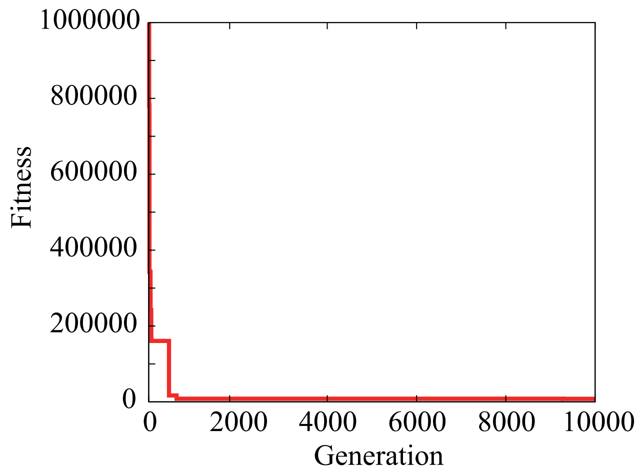

Fig. 3-90: Fitness variation in the experiment (sponge).

number. The identification result is kept constant after 1,000 times of evolution. Fig. 3-91 shows the final individual of sponge identification, and Fig. 3-92 shows the equivalent block diagram of Fig. 3-91. Oscillation of real force response is well expressed by the identification result. On the contrary, small

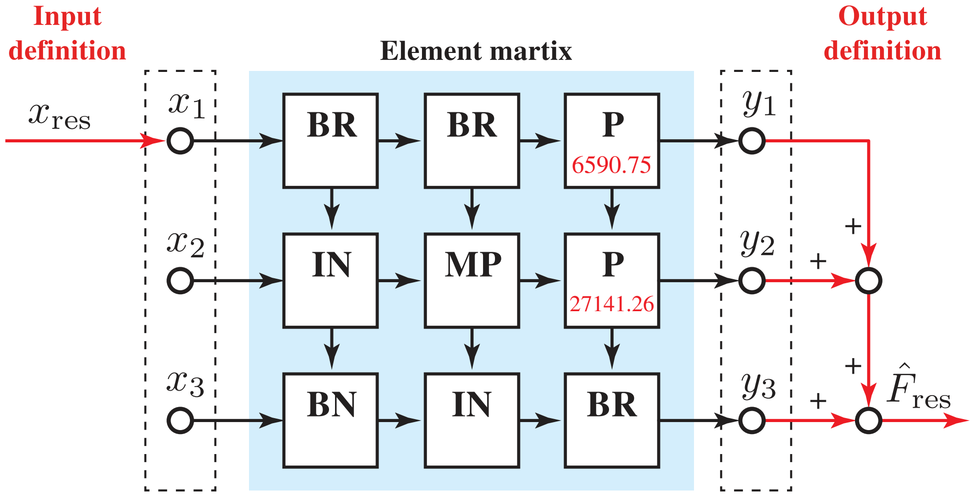

Fig. 3-91: Final individual of experiment (sponge).

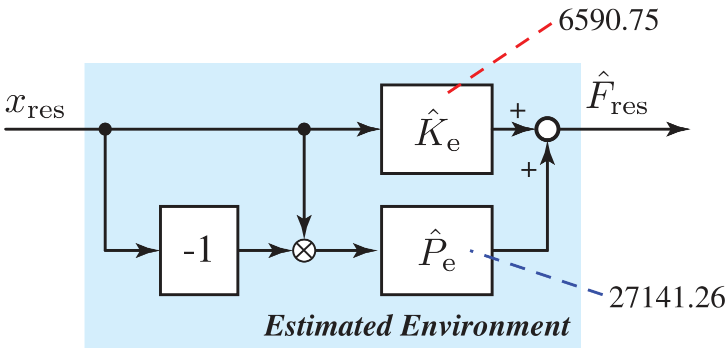

Fig. 3-92: Equivalent block diagram of Fig. 3-91.

error is remained as shown in the enlarged view in Fig. 3-89. To overcome this error, designing of an element is needed suitable for environment description. From these experiments, validity and limits of the proposed method are confirmed.

3.5 Summary of Chapter 3

In Chapter 3, the interactive control design method was described. The machine responds based on initial individuals and fitness functions designed by human. Based on the answers derived by the machine, humans design the initial individuals and the fitness function. By repeating this process to deepen the abstraction depth, it is possible to design a desired controller interactively. The effectiveness of the proposed method was confirmed by the controller design of the multi-mass resonant system, the time delay system, and force control system. In addition, automatic design of feedback conmensator was proposed by the EDM in frequency domain. The feedback compensator was generated based on gain characteristics of loop transfer function or complementary sensitivity function. Also, the identification method of unknown environment for motion control was proposed. Firstly, impedance identification method of environment was proposed considering impedance plane. Next, abstraction method of environment was described. The proposed method can estimate a physical model and its parameter using the EDM. General identification methods needed to decide a physical model of target in advance. On the contrary, the proposed method can generate a physical model of an environment, and it can identify its parameter simultaneously. The proposed method has a merit that the physical meaning of identification result is understandable according to element description. Moreover, the proposed method can treat a nonlinear system and multiple-input and multiple-output (MIMO) system easily. By using the proposed method, an ideal controller for contact task can be designed based on an environmental model and its parameter. It may be possible to discover a new physical property of an environment.

Chapter 4

Command Generation Using Element Description Method and Clothoid Curve

Command value generation technique is one of the most important technologies for automatic machinery. Basically, automatic machinery and industrial robots keep repeating motions all the time based on preset command values. Therefore, depending on the command value generated, the productivity and yield of the factory change dramatically. Generally, a machine designer manually designates the command value. For example, in the operation of the working tip of a machine, elements such as coordinates, velocity, and time, determined from the requested operation of the entire machine are taken as boundary conditions, and the curve connecting the points is connected by a cam curve based on trigonometric function [75] or polynomial spline. For industrial robots, manual designation by an operator using a teaching pendant is common. However, it is difficult to ensure optimality of curves used for setting and interpolating each coordinate. Also, since the designer manually designs the curves, it takes time and labor. In this dissertation, an automatic command generation method using the EDM is proposed In addition, an interpolation method using the clothoid curve is proposed as an example of the command value generation method of the automatic machinery. By using the proposed methods, it is expected to ensure optimality of command value design and shortening design time.

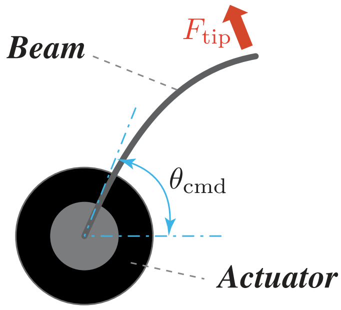

Fig. 4-1: Overview of the beam system.

4.1 Automatic Command Generation Using EDM for Beam System

4.1.1 Command Generation Method for Beam System

In this subsection, automatic command generation using the EDM is proposed. By placing the element matrix to the generation of the command values can be applied to a variety of command value generation problems. Here, as an example, the maximizing control of the tip velocity assuming a hitting operation using a beam [84] is conducted. A schematic view of the beam is shown in Fig. 4-1. In this verification, the beam is approximated as a multi-mass resonant model for simplicity. In this verification, consideration is made using 5-mass resonant system. The block diagram of automatic command generation using the EDM for multi-mass resonant system is depicted in Fig. 4-2. Here, t, x_{cmd}, x_{ref}, x_{m}, x_{tip}, F_{ref}, F_{act}, and, F_{l} denote time, position command, position reference, position response of actuator, position response of tip, force reference, actuation force, and load force, respectively. The transfer functions $C(s)$, $P(s)$, and $L(s)$ represent position controller, actuator, and multi-mass resonant system, respectively. The superscripts $\hat{\bullet}$ and $\dot{\bullet}$ refer to estimated value and time-differential value, respectively. t is prepared as input of element matrix. Also, learning is done with the goal of maximizing the velocity of the tip at a certain time. The objective function is defined as follows:

$$\begin{aligned} \text{maximize} \quad & \Gamma_{\mathrm{hit}}(x_{\mathrm{cmd}}) = \dot{x}_{\mathrm{tip}}(t_{\mathrm{hit}}, x_{\mathrm{cmd}}), \\ \text{subject to} \quad & |F_{\mathrm{ref}}| \le F_{\mathrm{lim}}, \\ & x_{\mathrm{min}} \le x_{\mathrm{cmd}} \le x_{\mathrm{max}}, \end{aligned}$$

where Γ_{hit}, t_{hit}, F_{lim}, x_{min}, and x_{max} stand for the fitness value of command generation, the time of hitting, force limitation, minimum position, and maximum position, respectively. Here, although the velocity at a certain time is optimized, it is also possible to optimize the velocity at a certain spatial

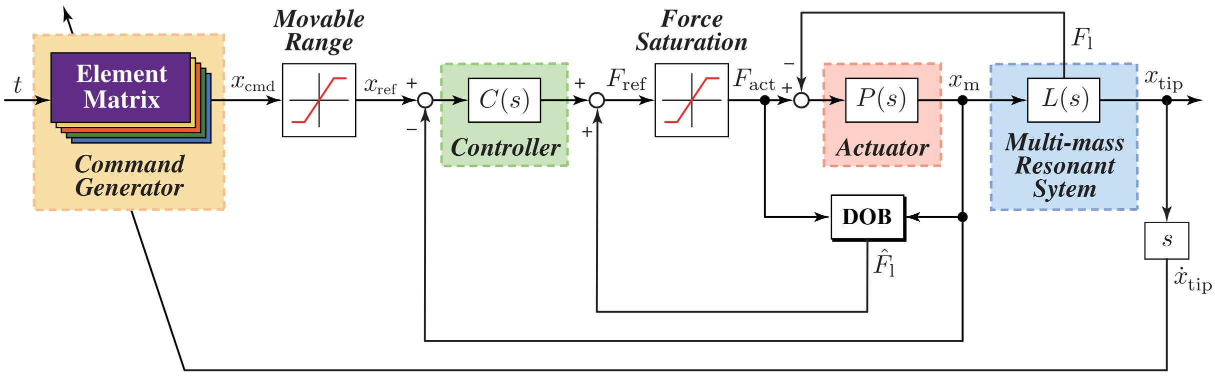

Fig. 4-2: Block diagram of automatic command generation using the EDM for multi-mass resonant system.

Table 4.1: Simulation parameters for velocity maximization.

Parameter	Description	Value
t_{hit}	Time of hitting	0.2 s
F_{lim}	Maximum value of output force	15 N
x_{max}	Maximum value of position command	0.1 m
x_{min}	Minimum value of position command	-0.1 m
M_{m}	Weight of motor mover	0.3 kg
M_{l}	Total mass of load	0.2 kg
K_{l}	Stiffness of load	1000 N/m
D_{l}	Viscosity of load	50 Ns/m

position.

4.1.2 Simulation of Automatic Command Generation

In this validation, tip velocity at 0.2 s is maximized. In simulation 1, parameters shown in Table. 4.1 are used. When there is no restriction on force or velocity, there is no need to conduct optimization. This is because that equal acceleration motion become the optimal solution. Hence, a limit value of force and velocity that can be output is defined. In order to confirm the optimality of synthesis results, simulation 1 was put into effect 3 times by the same condition. The fitness response of simulation 1 is shown in Fig. 4-3. Since the results converged to almost the same value for all three times, it is considered that values close to optimum are obtained.

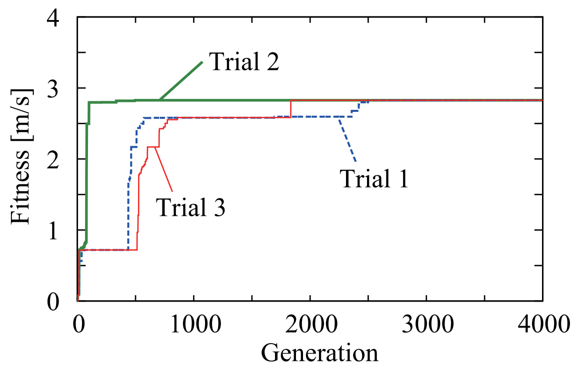

Fig. 4-3: Fitness response of beam system in simulation 1.

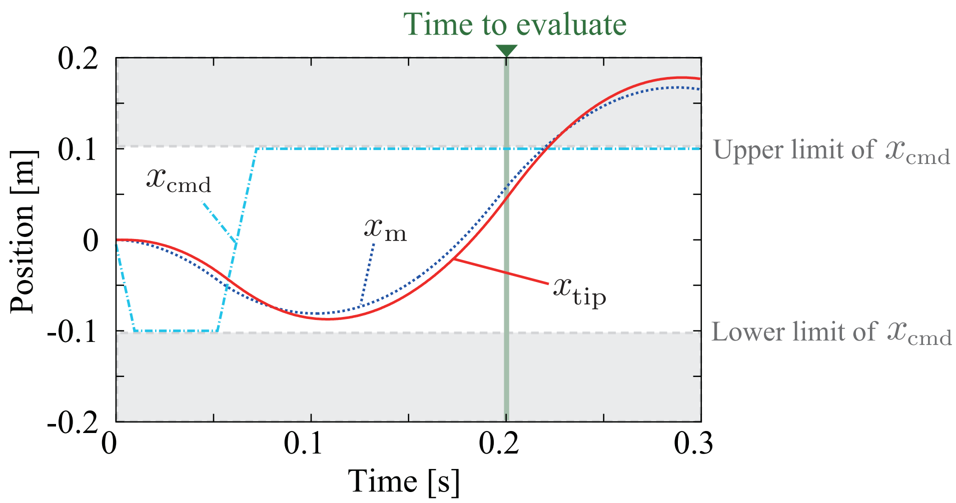

Fig. 4-4: Position response of beam system in simulation 1.

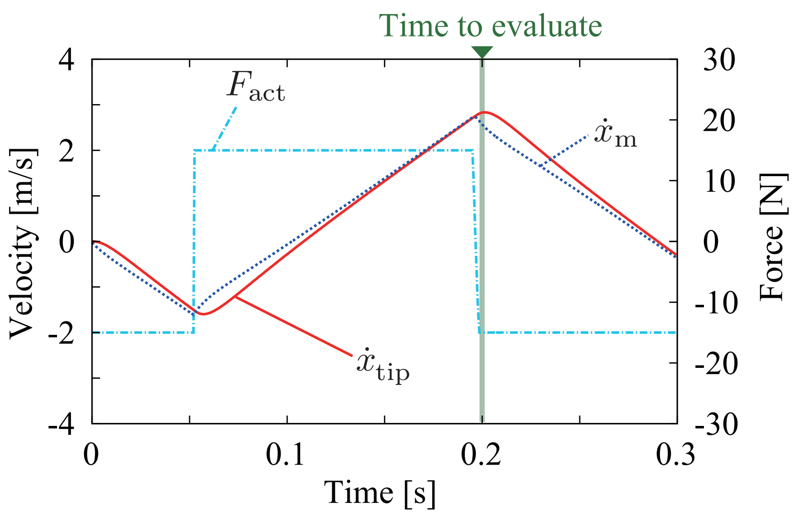

Fig. 4-5: Velocity response of beam system in simulation 1.

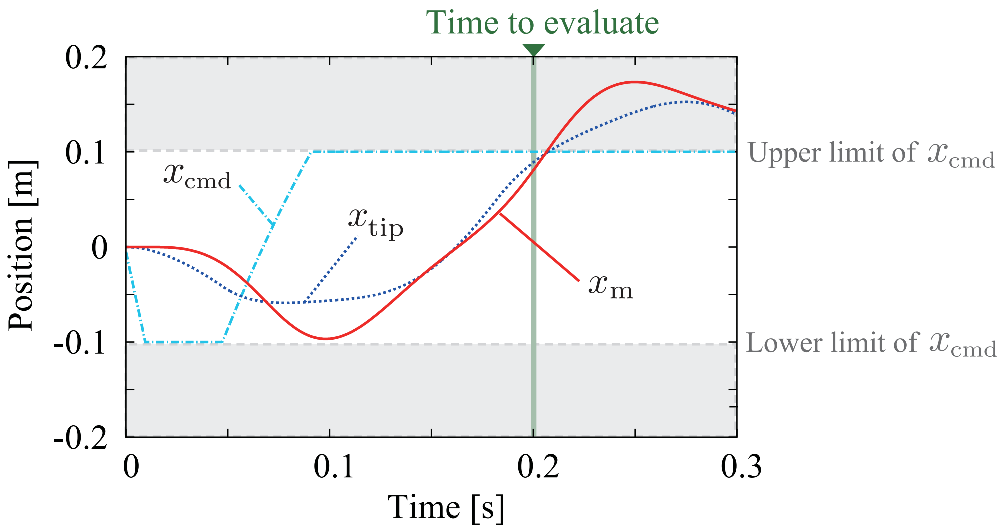

Fig. 4-6: Position response of beam system in simulation 2.

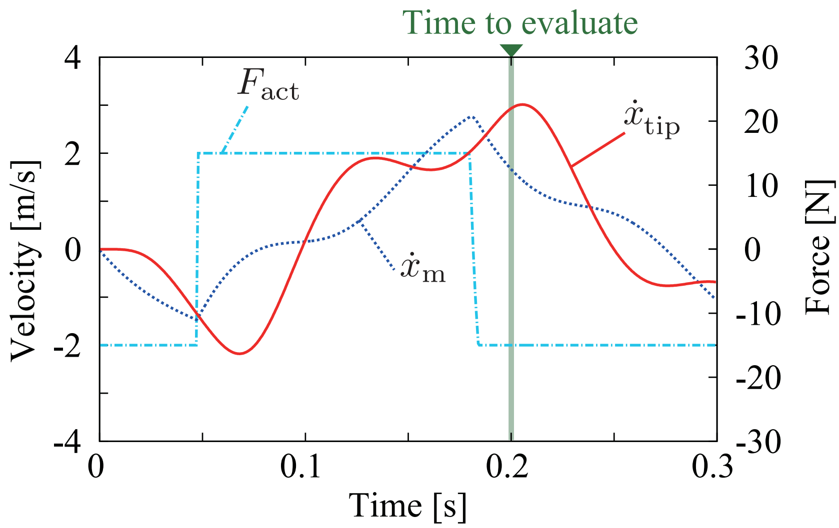

Fig. 4-7: Velocity response of beam system in simulation 2.

Fig. 4-4 refers to the position response of simulation 1. Fig. 4-5 denotes velocity response of simulation 1. It was confirmed that the velocity was controlled to increase at the time point of 0.2 s. Since overshoot occurs at the position due to the force limit value, it is necessary to set a limit value in anticipation of the overshoot amount. Next, from the parameters of the Table. 4.1, simulation 2 is performed when only the damper constant is changed to 5 Ns/m. Fig. 4-6 expresses position response of simulation 2. Fig. 4-7 depicts velocity response of simulation 2. In the simulation 2, a beam behaves like a spring

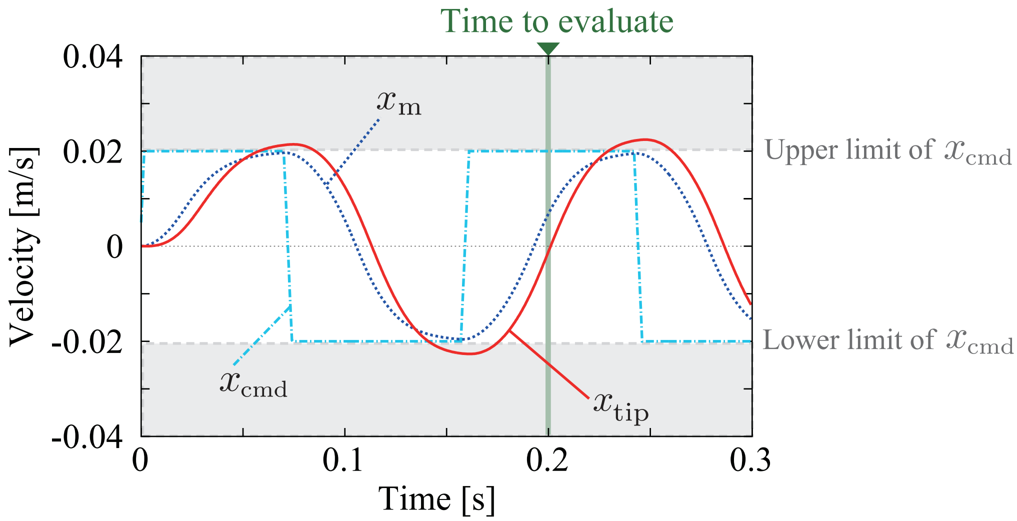

Fig. 4-8: Position response of beam system in simulation 3.

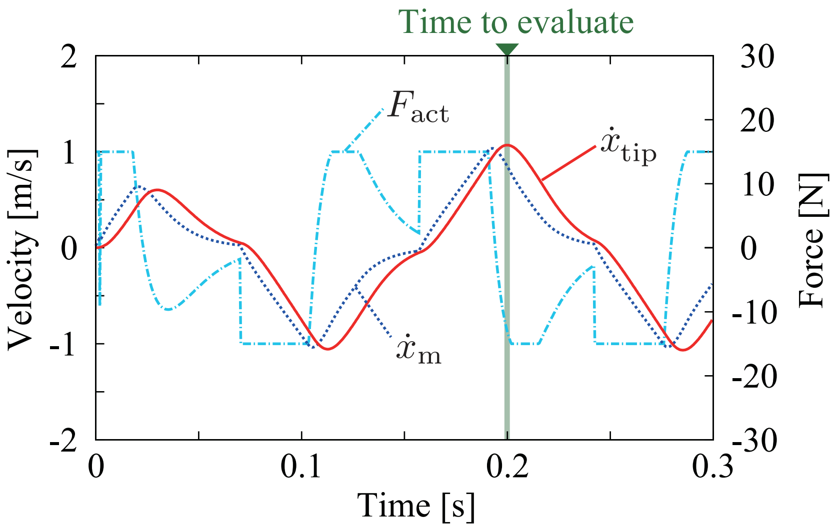

Fig. 4-9: Velocity response of beam system in simulation 3.

because the damper constant is made smaller. Therefore, it can be seen that the vibration is excited by the response. From Fig. 4-7, it can be seen that the force reference value is negative from around 0.18 s in order to make use of the bending of the beam. Then, from the parameters of the Table. 4.1, simulation 3 is performed when only the minimum and maximum value of position command are changed to -0.02 m and 0.02 m. Figs. 4-8 and 4-9 show the position and velocity response of simulation 3, respectively. When shortening the movable range, you can see that you have entered back swing action after moving in the positive direction once to bounce beam's stretches.

4.2 Spatio-temporal Interpolation Using Clothoid Curve

4.2.1 Overview of Interpolation Technology

The processing technology, which is a fundamental technology that supports the manufacturing industry, has made remarkable progress in recent times. The position control technology [8–10] is being widely researched to improve the processing quality. In particular, computerized numerical control (CNC) [85–87] systems are widely used to manufacture products, such as machining centers, 3D printers, chip mounter, laser process machines, painting robots, and welding robots. The key technology of the CNC system is the interpolation technology that connects the desired start and stop points. Fig. 4-10 shows the overview of the CNC system interpolation. The interpolation methods can be separated into two groups based on its purpose. The first group represents the case of obtaining a smooth approximate curve of the point group, except starting and ending points (e.g., Bezier spline, B-spline [86, 87], and NURBS [88].) These methods have merits of easily designing a smooth curve from a large amount of point data. The other group is the case of obtaining a smooth curve connecting the point to another point in the point group (e.g., linear, circular [89, 90], algebraic function [91], and clothoid [62, 92, 93] interpolation). These methods can easily design the smooth curve from a small amount of point data by manual entry. These methods each have a merit. Therefore, selective usage depending on the application is necessary. This chapter focuses on the latter method. These methods are required in the case of setting only important path points.

A clothoid interpolation is one of the most effective methods among these approach because it can connect the spatial points with a smooth curve by only setting path points and tangential angle on the points. On the contrary, the other methods are difficult to simultaneously achieve arbitrary point and tangent angle. Hence, discontinuous points or approximate points are generated. Since the clothoid curve can continuously change curvature, it can apply easily to nonholonomic system [94]. Moreover the time function can be independently designed because the clothoid curve can directly define the tangential velocity as a time function. Therefore, the synthesis between time and space can easily be achieved. This chapter deals with an interpolation method using a clothoid curve from these reasons. The clothoid curve has one problem that cannot be analytically expressed [95]. The curve also needs to be calculated for having a numerical solution. Hence, the discretization error of the clothoid curve should be considered to achieve a more precise task. A few studies have considered the discretization error of the clothoid curve [96]. Accordingly, the discretization error is suppressed by increasing the calculation resolution

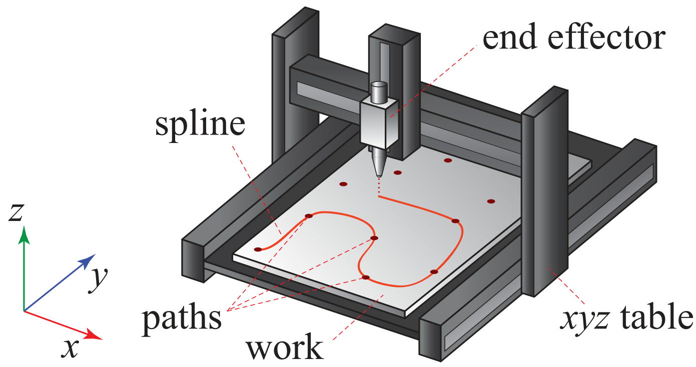

Fig. 4-10: Overview of interpolation in industrial applications.

because the clothoid curve is a spatial function. However, the calculation resolution of the clothoid curve is limited by the sampling time of the controller and the tangential velocity of the actuator in the actual case of application to equipment.

This study proposes a clothoid interpolation based on an iterative true-value prediction. This method can immediately estimate a true value of the clothoid curve by pinching integration and Aitken acceleration, thereby suppressing the discretization error of the clothoid curve. A smooth interpolation can be achieved using the proposed method even in the case, where the calculation resolution is limited. Furthermore, the DOB and a feed-forward controller are implemented to control the clothoid curve. The robust acceleration control can be achieved because the DOB suppresses the system disturbance. The feed-forward controller enhances the position tracking ability. Meanwhile, the feed-forward commands are calculated from the information on the clothoid curve and the tangential velocity. The trajectory can be completely controlled based on the clothoid interpolation using the DOB and the feed-forward controller thereon. Thus, the high-quality processing of precise tasks can be expected.

4.2.2 Spatial Interpolation Using Clothoid Interpolation

Clothoid Curve Definition

A clothoid curve is a spatial function smoothly connecting a point to another point. A spline on the polar coordinates is expressed as follows:

$$\boldsymbol{p} = \boldsymbol{p}_0 + \int_0^{q_e} \boldsymbol{u} dq, \tag{4.1}$$

where $\boldsymbol{p}$, q, q_e,and $\boldsymbol{u}$ denote the position vector, curve length from $\boldsymbol{p}_0$ to $\boldsymbol{p}$, total curve length from $\boldsymbol{p}_0$ to $\boldsymbol{p}_{\mathrm{n}}$, and unit vector of the tangential angle, respectively. The integral of q means spatial integration with respect to the tangent length. The subscript 0 refers to the starting point. The $\boldsymbol{u}$ of the clothoid curve in a three-dimensional space is defined as follows:

$$\boldsymbol{u} = E^{j\alpha}E^{k\beta} = \left\{ \begin{array}{c} \cos\alpha\cos\beta \\ \sin\alpha\cos\beta \\ -\sin\beta \end{array} \right\}, \tag{4.2}$$

where $E^{j\alpha}$ and $E^{k\beta}$ denote the rotation matrices around the j axis (i.e., z axis) and the k axis (i.e., y axis), respectively. The rotation angles α and β are calculated as follows:

$$\alpha = a_0 + a_1 q + a_2 q^2, \tag{4.3}$$

$$\beta = b_0 + b_1 q + b_2 q^2, \tag{4.4}$$

where a_0, a_1, a_2, b_0, b_1, and b_2 denote coefficients of clothoid curve, respectively. Meanwhile, the $\boldsymbol{u}$ of the clothoid curve in a two-dimensional space is defined by the following equation:

$$\boldsymbol{u} = e^{j\phi}. \tag{4.5}$$

The rotation angle ϕ is calculated as follows:

$$\phi = \phi_0 + c_1 q + c_2 q^2, \tag{4.6}$$

where ϕ_0, c_1, and c_2 denote the initial angle, initial curvature, and half of the value of the scaling factor, respectively. This study considers the interpolation method on a two-dimensional space for simplicity because the issue about the discretization error is common in spite of its dimension. In addition, the clothoid interpolation can apply to several equipment such as laser processor, pick and place manipulator, and chip mounter. These machines can use the simple interpolation method for the z axis command.

Clothoid Interpolation Calculation

Fig. 4-11 shows a curve on the polar coordinates. The differential value of ϕ is then given as follows:

$$c_{\mathrm{v}} = \frac{d\phi}{dq} = c_1 + 2c_2 q, \tag{4.7}$$

$$c_{\mathrm{u}} = \frac{d^{\,2}\phi}{dq^2} = 2c_2 = const., \tag{4.8}$$

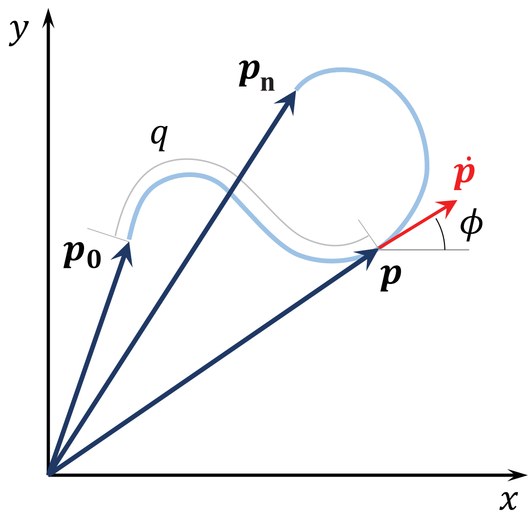

Fig. 4-11: A curve on polar coordinate.

where c_{v} and c_{u} denote the curvature and the reduction ratio, respectively. The normalized displacement is then defined as follows:

$$Q \triangleq \frac{q}{h} \quad (0 \leq Q \leq 1), \tag{4.9}$$

where h denotes the length of the interpolation curve connecting two points. Subsequently, $\boldsymbol{p}$ and ϕ are redefined as follows using (4.9):

$$\boldsymbol{p} = \boldsymbol{p}_0 + h\int_0^1 e^{j\phi} dQ, \tag{4.10}$$
$$\phi = \phi_0 + \phi_{\mathrm{v}}\mathrm{Q} + \phi_{\mathrm{u}}\mathrm{Q}^2, \tag{4.11}$$

where ϕ_{v} and ϕ_{u} represent the normalized initial curvature and the half value of the normalized scaling factor, respectively. Fig. 4-12 shows the clothoid curve, where λ, ψ, and l denote the chord-arc ratio, the view angle, and distance between $\boldsymbol{p_0}$ and $\boldsymbol{p_1}$, respectively. The chord-arc ratio λ and the view angle ψ herein are defined as follows:

$$\boldsymbol{p}_1 - \boldsymbol{p}_0 = \lambda h e^{j(\phi_0+\psi)}. \tag{4.12}$$

The interpolation method using the clothoid curve [62, 92, 93] is described in this section. The tangential angle herein is continuously designed using the clothoid curves. The clothoid interpolation can set an arbitrary coordinate and arbitrary tangent angle at the points to pass through. From (4.11), the tangential

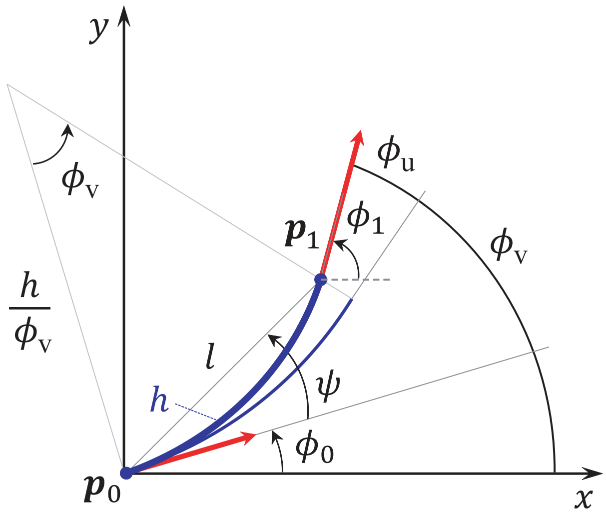

Fig. 4-12: Clothoid curve.

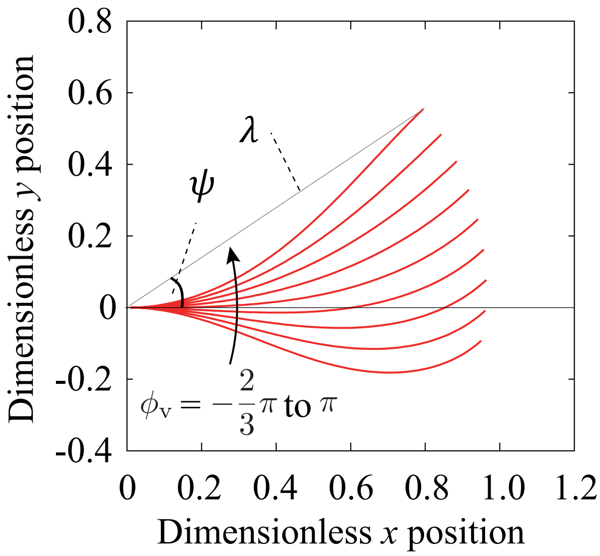

Fig. 4-13: Fundamental clothoid.

angle of the ending point ϕ_1 is calculated as follows:

$$\phi_1 \quad = \quad \phi_0 + \phi_v + \phi_u. \tag{4.13}$$

Solving the equation analytically is impossible because the clothoid curve is defined in terms of Fresnel integrals [95]. Accordingly, ϕ_v and ϕ_u are derived by a search algorithm shown in algorithm 1. Fig.

Algorithm 5 Searching method for ϕ_v and ϕ_u

while $e > a$ **do**
  $\phi_{\mathrm{v}} \Leftarrow s$
  $\phi_{\mathrm{u}} \Leftarrow \phi_1 - \phi_0 - \phi_{\mathrm{v}}$
  for $i = 0$ to $n - 1$ **do**
    $m \Leftarrow \frac{1}{n}$
    $q \Leftarrow mi$
    $\phi \Leftarrow \phi_0 + \phi_{\mathrm{v}} q + \phi_{\mathrm{u}} q^2$
    $dx \Leftarrow m \cos \phi$
    $dy \Leftarrow m \sin \phi$
    $x \Leftarrow x + dx$
    $y \Leftarrow y + dy$
  end for
  $\psi_{\mathrm{res}} \Leftarrow \tan^{-1} \frac{y}{x}$
    $\lambda \Leftarrow \sqrt{x^2 + y^2}$
  if $(\psi_{\mathrm{res}} \leq \psi_{\mathrm{n}}) \wedge (\psi_{\mathrm{res}} > \psi_{\mathrm{n}})$ **then**
    $i \Leftarrow \frac{1}{2} i$
    $s \Leftarrow s_{\mathrm{pre}}$
    $e \Leftarrow |\psi_{\mathrm{n}} - \psi_{\mathrm{res}}|$
  else
    $s_{\mathrm{pre}} \Leftarrow \mathrm{s}$
    $s \Leftarrow s + i$
  end if
  $\psi_{\mathrm{pre}} \Leftarrow \psi_{\mathrm{res}}$
end while

4-13 shows the fundamental clothoid. In Fig. 4-13, ϕ_0 and ϕ_1 are set to 0 and $\frac{\pi}{4}$, respectively, and ϕ_{v} is set from $-\frac{2}{3}\pi$ to π. ϕ_{v} and ϕ_{u} can be obtained using the search algorithm by setting ϕ_0 and ϕ_1 as the boundary conditions. The curve size is affected only by h. Also ϕ_0, ϕ_1, ϕ_{v}, and ϕ_{u} are not affected by the curve size. Hence, the clothoid curve in the actual scale can be obtained as follows:

$$\lambda = \frac{l}{h}. \tag{4.14}$$

Consequently, the clothoid curve connecting the points can be obtained. Fig. 4-13 indicates that λ also means chord length of the fundamental clothoid.

4.2.3 Temporal Interpolation Using Minimum Jerk Model

Binding of Time and Space

The curve becomes spatially smooth when the clothoid function is used. However, the curve does not have the temporal smoothness. Designing the time length of the trajectory is necessary for the time smoothness. The merit in using the clothoid curve is that the tangential angle and velocity are obvious and can be directly controlled. The tangential velocity is expressed as follows:

$$\dot{q}(t) = \sqrt{\dot{x}^2(t) + \dot{y}^2(t)}. \tag{4.15}$$

Accordingly, $\dot{q}(t)$ should be set as a constant value when constant velocity is required. Furthermore, $q(t)$ should be given by a smooth curve such as a cam curve [5] or a spline curve [97], when a smooth motion is required. The position trajectory herein is generated by the minimum jerk model [98]. The interpolation method using the minimum jerk model is explained as follows. The cost function of minimum jerk model on SDOF is expressed as

$$C = \int_0^1 \frac{d^3Q(t)}{dt^3} dT = \int_0^1 L\, dT, \tag{4.16}$$

where S and T refer to the normalized position and normalized time, respectively. The position and time were normalized for simplification in this study. The normalized values are expressed as follows:

$$Q(T) = \frac{q(t)}{h}, \tag{4.17}$$

$$T = \frac{t}{t_{\mathrm{h}}}, \tag{4.18}$$

$$t_{\mathrm{h}} = t_{\mathrm{e}} - \mathrm{t_s}, \tag{4.19}$$

where t_{e} and t_{s} denote the end point time and start point time, respectively. The normalized velocity $V(T)$, normalized acceleration $A(T)$, and normalized jerk $J(T)$ are calculated as follows using the above mentioned values:

$$V(T) = \frac{dQ(T)}{dT}, \tag{4.20}$$

$$A(T) = \frac{dV(T)}{dT}, \tag{4.21}$$

$$J(T) = \frac{dA(T)}{dT}. \tag{4.22}$$

Furthermore, velocity $v(t)$, acceleration $a(t)$, and jerk $j(t)$ are calculated as follows:

$$v(t) = \frac{h}{t_\mathrm{h}}V(T), \tag{4.23}$$

$$a(t) = \frac{h}{{t_\mathrm{h}}^2}A(T), \tag{4.24}$$

$$j(t) = \frac{h}{{t_\mathrm{h}}^3}J(T). \tag{4.25}$$

The Euler equation is expressed as follows:

$$\frac{d^3}{dt^3}\left(\frac{\partial L}{\partial x'''}\right) = 0 \tag{4.26}$$

$$\frac{d^6x}{dt^6} = 0, \tag{4.27}$$

where x refers to position. The boundary conditions are represented as follows:

$$V(0) = v_0,\ V(1) = v_1, \tag{4.28}$$

$$A(0) = a_0,\ A(1) = a_1, \tag{4.29}$$

where subscripts 0 and 1 denote the starting and ending values, respectively. The spline function is expressed as follows using these boundary conditions:

$$Q(T) = k_0 + k_1T + k_2T^2 + k_3T^3 + k_4T^4 + k_5T^5, \tag{4.30}$$

$$V(T) = k_1 + 2k_2T + 3k_3T^2 + 4k_4T^3 + 5k_5T^4, \tag{4.31}$$

$$A(T) = 2k_2 + 6k_3T + 12k_4T^2 + 20k_5T^3, \tag{4.32}$$

where k_0 to k_5 are calculated as follows:

$$k_0 = 0, \tag{4.33}$$

$$k_1 = V_0, \tag{4.34}$$

$$k_2 = \frac{A_0}{2}, \tag{4.35}$$

$$k_3 = -\frac{3}{2}A_0 + \frac{1}{2}A_1 - 6V_0 - 4V_1, \tag{4.36}$$

$$k_4 = -\frac{3}{2}A_0 - A_1 + 7A_1 + 8V_0, \tag{4.37}$$

$$k_5 = -\frac{1}{2}A_0 + \frac{1}{2}A_1 - 3V_0 - 3V_1. \tag{4.38}$$

The time-position trajectory based on minimum jerk model is generated by using above mentioned equations. The position, velocity, and acceleration can be continuously tracked for each point using the minimum jerk model. However, the discretization error occurs depending on the tangential velocity and sampling time because a clothoid curve solution cannot be analytically expressed. Therefore, the discretization error in the numerical calculation must be considered in the implementation phase.

4.2.4 Control Method of Clothoid Interpolation Considering Discretization Error

Command Generation with True Value Estimation

(4.1) and (4.6) can be re-defined as follows in the discrete space:

$$\begin{aligned} \boldsymbol{p}(u) &= \boldsymbol{p}(0) + \sum_{k=0}^{n} e^{j\phi(k)} \Delta q, && (4.39) \\ \phi(k) &= \phi(0) + c_1 q(k) + c_2 q^2(k), && (4.40) \\ q(k) &= \Delta q k, && (4.41) \\ \Delta q &= \frac{h}{n}, && (4.42) \end{aligned}$$

where k and n denote the sampling counter and the division number, respectively. A normalized clothoid in the discrete space is given as follows:

$$S_n^{(-)} \triangleq \sum_{k=0}^{n-1} e^{j\left\{c_1(\frac{k}{n})+c_2(\frac{k}{n})^2\right\}} \Delta q. \tag{4.43}$$

The true value of the clothoid curve S_{tr} can be calculated as follows:

$$S_{\mathrm{tr}} = \lim_{n\to\infty} S_n^{(-)}. \tag{4.44}$$

However, the calculation volume increases with an increase in the number of divisions n. A normalized clothoid curve in the discrete space using the future value is expressed as follows:

$$S_n^{(+)} \triangleq \sum_{k=1}^{n} e^{j\left\{c_1(\frac{k}{n})+c_2(\frac{k}{n})^2\right\}} \Delta q. \tag{4.45}$$

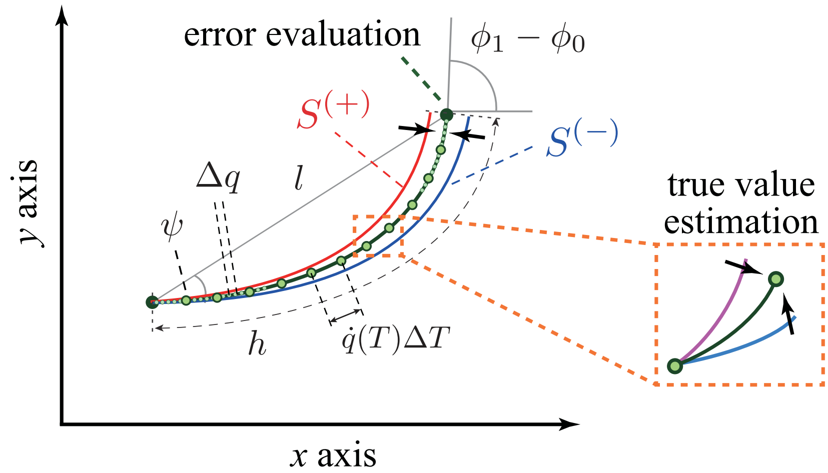

Fig. 4-14: Overview of true value estimation.

The curve can then be more accurately calculated using numerical integration with a smaller volume of calculation by pinching as follows:

$$\begin{aligned} S_n^{(m)} &\triangleq \frac{S_n^{(-)} + S_n^{(+)}}{2} \\ &= \sum_{k=1}^{n} e^{j\left\{c_1\left(\frac{k+0.5}{n}\right)+c_2\left(\frac{k+0.5}{n}\right)^2\right\}} \Delta q. \end{aligned} \tag{4.46}$$

A value closer to the true value can be calculated using (4.46). This calculation method is similar to the trapezoidal integration. The overview of true value estimation is depicted in Fig. 4-14. In addition, the Aitken acceleration method [99] is applied to estimate the true value more quickly. The Aitken acceleration method is an acceleration method used to rapidly estimate the convergence value by defining another series from one series. The acceleration method to predict convergence value of the sequence is described. The sequence is defined as follows:

$$s_n = \alpha + C\gamma^n, n \in \mathbb{N}, \tag{4.47}$$

where α, C, and γ stand for the convergence value of the sequence, unknown coefficient, and known coefficient, respectively. From (4.47), α is obtained by deleting C as follows:

$$\alpha = \frac{s_{n+1} - \gamma s_n}{1 - \gamma}. \tag{4.48}$$

From (4.48), a new sequence z_n can be defined as follows:

$$z_n \triangleq \frac{s_{n+1} - \gamma s_n}{1-\gamma}. \tag{4.49}$$

This method is known as Richardson acceleration method. In addition, the case of γ is unknown is considered.

From (4.47), γ is expressed as

$$\gamma = \frac{s_{n+2} - s_{n+1}}{x_{n+1} - x_n}. \tag{4.50}$$

Therefore, z_n can be defined as follows:

$$z_n \triangleq \frac{s_n s_{n+2} - s_{n+1}^2}{x_{n+2} + s_n - 2s_{n+1}}. \tag{4.51}$$

This method is known as Aitken acceleration method. The true value estimation using the Aitken acceleration method is given by the following equation:

$$S_n^{(m)}(K+1) = \frac{S_{n+1}^{(m)}(K) S_{n-1}^{(m)}(K) - S_n^{(m)2}(K)}{S_{n+1}^{(m)}(K) + S_{n-1}^{(m)}(K) - 2S_n^{(m)}(K)}, \tag{4.52}$$

where K is the counter of the series using the Aitken acceleration method. The true value of the clothoid curve can be quickly estimated using (4.52).

Control Structure of the Spatio-temporal Spline

Fig. 4-15 shows the block diagram of the control system for the spatio-temporal spline, where, $\boldsymbol{x}$, $\boldsymbol{C}_{\mathrm{p}}$, $\boldsymbol{C}_{\mathrm{v}}$, $\boldsymbol{M}$, $\boldsymbol{K}_{\mathrm{t}}$, and $\boldsymbol{Z}_{\mathrm{e}}$ refer to the position vector and position controller, velocity controller, mass, force coefficient, and impedance matrices, respectively. The subscripts cmd, res, and n refer to the command, response, and nominal values, respectively. $\boldsymbol{x}$ is defined as

$$\boldsymbol{x} \triangleq [x, y]^T, \tag{4.53}$$

The DOB [6,7] is implemented herein to achieve the disturbance suppression performance. The transfer function of the x axis system in which the DOB is implemented, is given as follows:

$$P_x(s) = \frac{x_{\mathrm{res}}}{\ddot{x}_{\mathrm{ref}}} = \frac{s}{s+g_{\mathrm{dis}}} \frac{1}{s^2}, \tag{4.54}$$

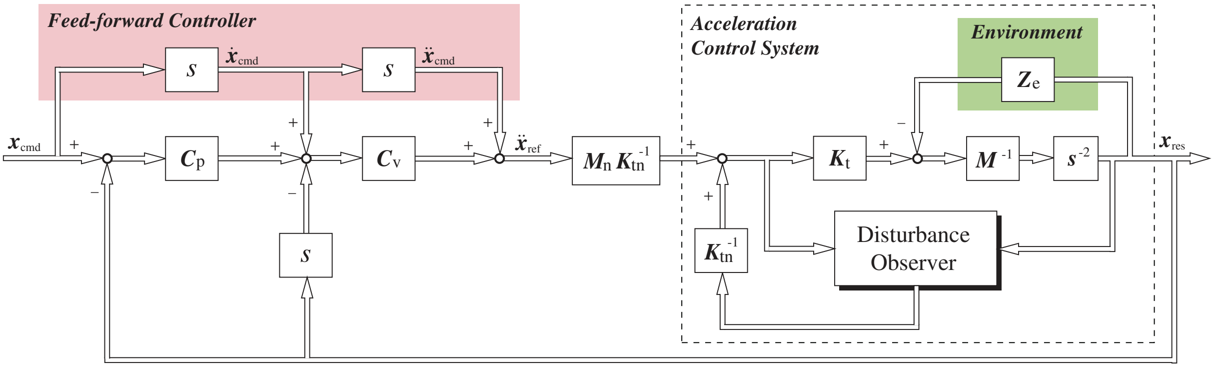

Fig. 4-15: Block diagram of feed-forward control.

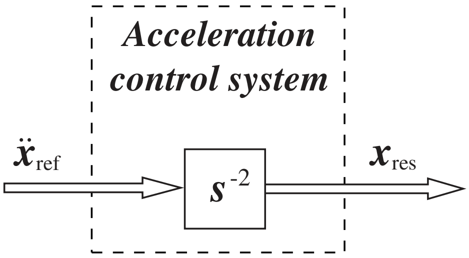

Fig. 4-16: Acceleration control system.

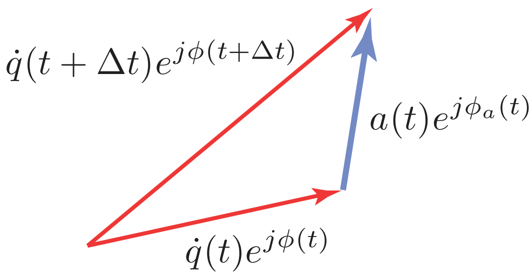

Fig. 4-17: Acceleration vector.

where $P_x(s)$ and g_{dis} stand for the transfer function of the plant with the DOB and cut-off frequency of the DOB, respectively. The acceleration control plant model is obtained if the cut-off frequency of the low-pass filter in the DOB is assumed as to be infinite. $P_x(s)$ can then be represented by a simple second-order integration in the form shown in Fig. 4-16. The DOB is implemented on the y axis as well as the x axis.

The feed-forward control is applied to achieve a precise trajectory tracking with an arbitrary tangential velocity. The feed-forward controller has three command values: position, velocity, and acceleration commands. The acceleration vector can be obtained as follows:

$$a(t)e^{j\phi_a(t)} = \dot{q}(t+\Delta t)e^{j\phi(t+\Delta t)} - \dot{q}(t)e^{j\phi(t)}, \tag{4.55}$$

where $a(t)$ and ϕ_a stand for the absolute value of the acceleration vector and the angle of the acceleration

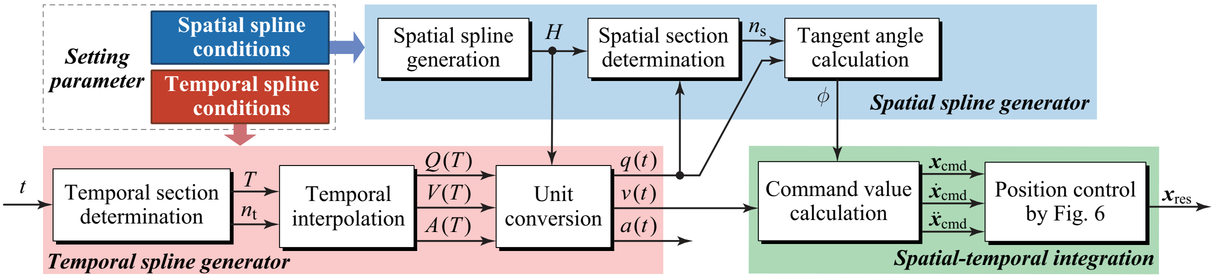

Fig. 4-18: Procedure for the design of the spatio-temporal spline.

vector, respectively, which are expressed as follows:

$$a(t) = \frac{1}{\Delta t}\Big[\dot{q}(t+\Delta t)\cos\Big\{\phi(t+\Delta t)-\phi_a(t)\Big\} + \dot{q}(t)\cos\Big\{\phi(t)-\phi_a(t)\Big\}\Big], \tag{4.56}$$

$$\phi_a(t) = \tan^{-1}\left\{\frac{\dot{q}(t+\Delta t)\sin\phi(t+\Delta t)+\dot{q}(t)\sin\phi(t+\pi)}{\dot{q}(t+\Delta t)\cos\phi(t+\Delta t)+\dot{q}(t)\cos\phi(t+\pi)}\right\}, \tag{4.57}$$

The acceleration vector is shown in Fig. 4-17. The transfer function from $\boldsymbol{x}_{\mathrm{cmd}}$ to $\boldsymbol{x}_{\mathrm{res}}$ in this control system is expressed as follows:

$$G_x(s) = \frac{x_{\mathrm{cmd}}}{x_{\mathrm{res}}} = 1, \tag{4.58}$$

$$G_y(s) = \frac{y_{\mathrm{cmd}}}{y_{\mathrm{res}}} = 1, \tag{4.59}$$

where superscripts x and y refer to the x and y components, respectively. Obtaining a superior characteristic of the position response is possible from the above equations. An accurate trajectory tracking can be achieved by combining the spatio-temporal spline, the DOB, and feed-forward control. Fig. 4-18 shows the utilization flow of the spatio-temporal spline. Accordingly, n_{t}, T, and $\boldsymbol{D}^T$ stand for the temporal section number, normalized time, and coefficient matrix, respectively.

An instance of clothoid interpolation is introduced in this section. Table 4.2 shows the boundary conditions for the spatial interpolation. The clothoid function values are calculated from these parameters, as listed in Table 4.3. Fig. 4-19 represents the calculated curve of the spatial interpolation. The solid arrows shows the velocity vector and the dotted arrow shows the acceleration vector, respectively. Meanwhile, Table 4.4 lists the boundary conditions for the temporal interpolation. Fig. 4-20 illustrates the calculated curve of the temporal interpolation. This curve has a constant velocity section and an acceleration–deceleration section. The spatio-temporal spline can be obtained from synthesizing of

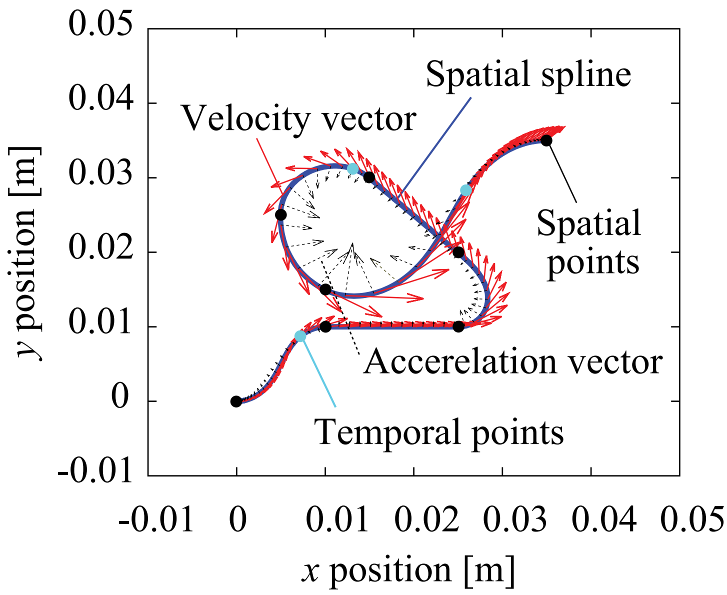

Fig. 4-19: X - Y plane trajectory.

Table 4.2: Boundary conditions of spatial interpolation.

	Coordinates x	Coordinates y	ϕ
point 1	0 m	0 m	0 rad
point 2	0.010 m	0.010 m	0 rad
point 3	0.025 m	0.010 m	0 rad
point 4	0.025 m	0.020 m	$\frac{3}{4}\pi$ rad
point 5	0.015 m	0.030 m	$\frac{3}{4}\pi$ rad
point 6	0.005 m	0.025 m	$-\frac{1}{6}\pi$ rad
point 7	0.010 m	0.015 m	$\frac{1}{3}\pi$ rad
point 8	0.035 m	0.035 m	0 rad

these interpolations. Fig. 4-21 shows the designed spatio-temporal spline.

4.2.5 Simulations of Spatio-temporal Interpolation

The validity of the iterative true value prediction is confirmed in this section. Table 4.5 presents the setting parameters. Fig. 4-23 shows the simulation results of the true value estimation indicating that the estimated value converges to the true value in approximately 10 scans using the proposed method.

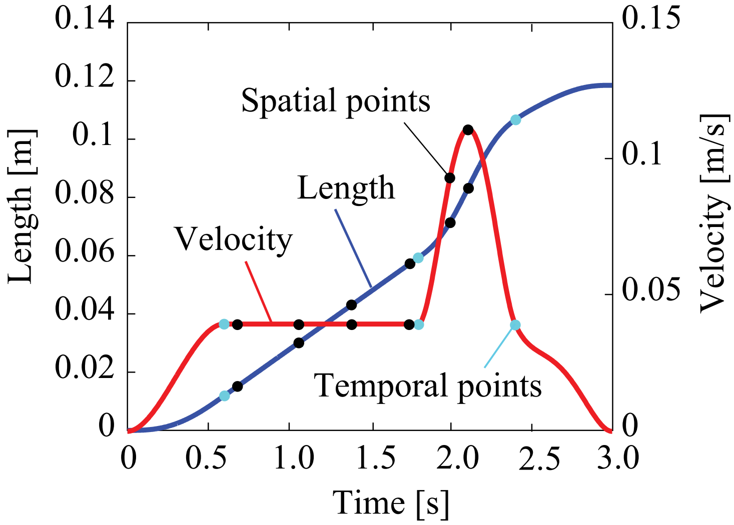

Fig. 4-20: An instance of temporal interpolation.

Table 4.3: Calculated values of spatial interpolation.

	$\phi_{\rm v}$	$\phi_{\rm u}$	h
section 1	4.68 rad	−4.68 rad	0.01504 m
section 2	0.00 rad	0.00 rad	0.01500 m
section 3	4.54 rad	−2.19 rad	0.01295 m
section 4	0.00 rad	0.00 rad	0.01414 m
section 5	2.80 rad	−0.45 rad	0.01428 m
section 6	0.72 rad	0.32 rad	0.01171 m
section 7	6.08 rad	−5.56 rad	0.03538 m

Hence, the proposed method can immediately estimate the true value of the clothoid curve. The error of the clothoid curve is then evaluated. Fig. 4-24 demonstrates the error evaluation results of the clothoid curve. Table 4.6 presents the simulation parameters. The tangential velocity $\dot{q}$ is varied from 0.005 to 0.1. The accurate results can be obtained using the proposed method, regardless of the tangential velocity setting. A precise trajectory tracking can be expected when the proposed method is used.

4.2.6 Experiments of Spatio-temporal Interpolation

The experiments were conducted as explained below to confirm the validity of the proposed method.

Table 4.4: Boundary conditions of temporal interpolation.

	T	S	V	A
time 0	0	0	0	0
time 1	0.2	0.1	1	0
time 2	0.6	0.5	1	0
time 3	0.8	0.9	1	-10
time 4	1	1	0	0

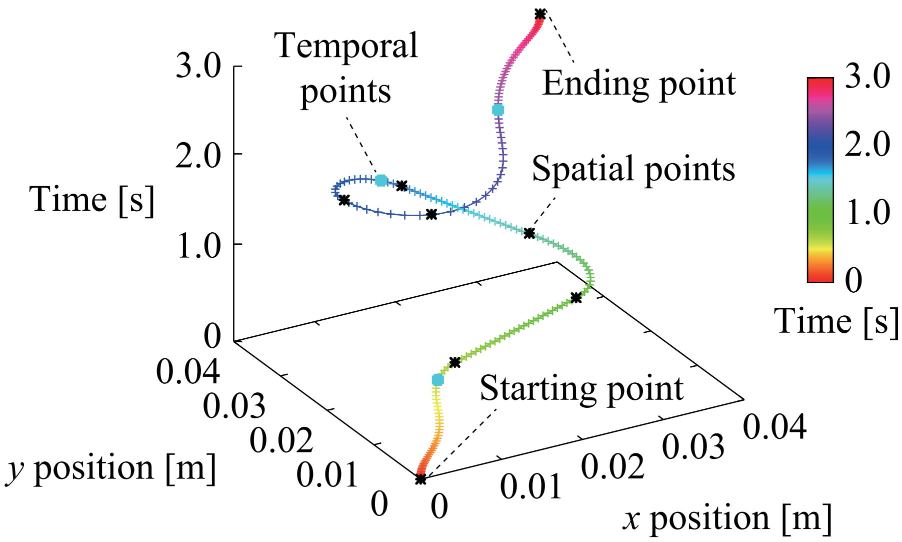

Fig. 4-21: Spatio-temporal interpolation using the proposed method.

Table 4.5: Simulation conditions of true value estimation.

Parameter	Description	Value
ϕ_0	Tangential angle in starting point	0 rad
ϕ_1	Tangential angle in ending point	$\frac{\pi}{4}$ rad
$\phi_{\rm v}$	Normalized initial curvature	0
n	Division number	$0 \to 1000$

Experimental Setup

A gantry machine, in which four actuators are mounted, is used in the experiments. Fig. 4-26 shows the experimental setup. Each actuator comprised a linear motor, a linear guide, and a linear encoder. Only actuators 1–3 are used for the x–y table system because this research focused only on x–y plane trajectory design. Actuators 1 and 2 are controlled in a modal space [100]. Transformation from actual

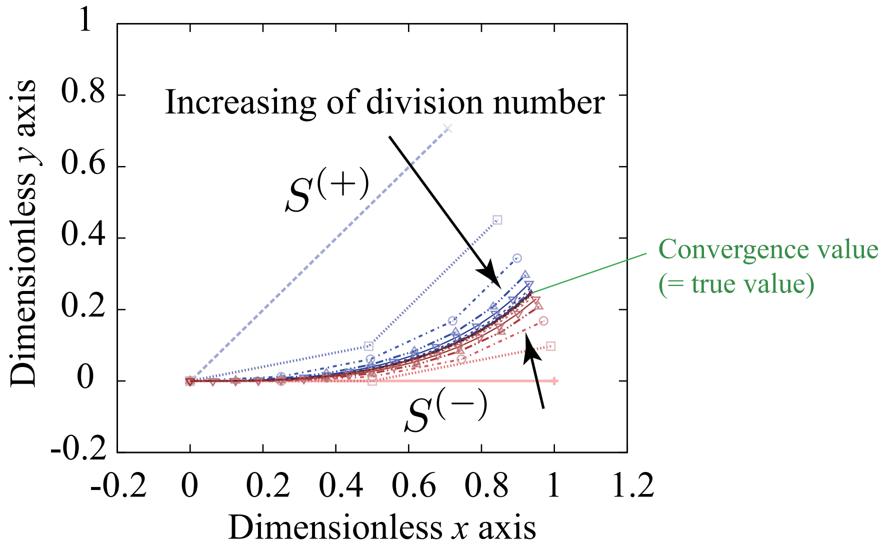

Fig. 4-22: Overview of simulation.

Table 4.6: Simulation conditions of error evaluation.

Parameter	Description	Value
ϕ_0	Tangential angle in starting point	$\frac{\pi}{6}$ rad
ϕ_1	Tangential angle in ending point	$\frac{\pi}{2}$ rad
ϕ_{v}	Normalized initial curvature	0
h	Length of curve	0.1 m
$K_{\max}$	Series number of Aitken	10

space to modal space is achieved by a quarry matrix. The modal transformation of position information in 2-degree-of-freedom system is expressed as

$$\begin{bmatrix} x_{\mathrm{c}} \\ x_{\mathrm{d}} \end{bmatrix} = \mathbf{Q}_2 \begin{bmatrix} x_1 \\ x_2 \end{bmatrix}, \tag{4.60}$$

$$\mathbf{Q}_2 = \frac{1}{2}\begin{bmatrix} 1 & 1 \\ 1 & -1 \end{bmatrix}, \tag{4.61}$$

where, $\mathbf{Q}_2$ stands for the second-order quarry matrix. The subscripts, c, d, 1, and 2 refer to information of common mode, differential mode, actuator 1, and actuator 2, respectively. In the same way, the modal transformation of force information in 2-degree-of-freedom system is calculated by

$$\begin{bmatrix} f_{\mathrm{c}} \\ f_{\mathrm{d}} \end{bmatrix} = \mathbf{Q}_2 \begin{bmatrix} f_1 \\ f_2 \end{bmatrix}. \tag{4.62}$$

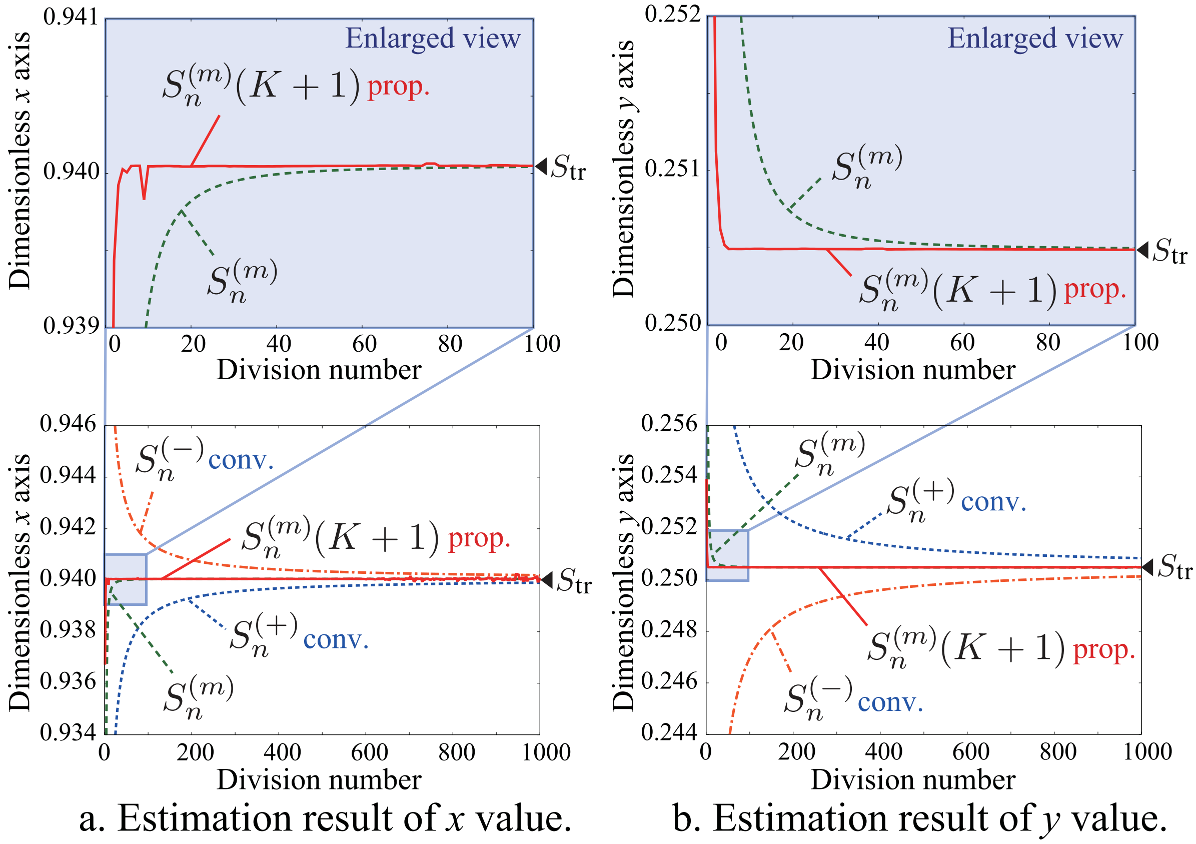

Fig. 4-23: Simulation result of true value estimation.

The differential mode is controlled by force control, while the force command in the differential mode is set to 0 N. The common mode is controlled by position control, while the position command in the common mode is set as the y axis command. The force of differential mode and the position of common mode mean torsional force and center of gravity position, respectively. The command value is used the spline shown in Fig. 4-21. The experiments are conducted by using RT-Linux. Accordingly, the controller's sampling time is 0.1 ms. The experimental parameters of spatio-temporal interpolation are shown in Table 4.7. Firstly, the effectiveness of command value generation by true-value prediction, which is the main proposal of this dissertation, is confirmed. Then, the validity of the feed-forward control is evaluated in comparison with the general conventional method. PD control without the DOB (PD), Cross-coupled Control (CCC) [101], PD control with the DOB (PD + DOB), and the proposed feed-forward control with the DOB (Proposal) are compared in the experiments. The block diagram of the CCC is shown in 4-25.

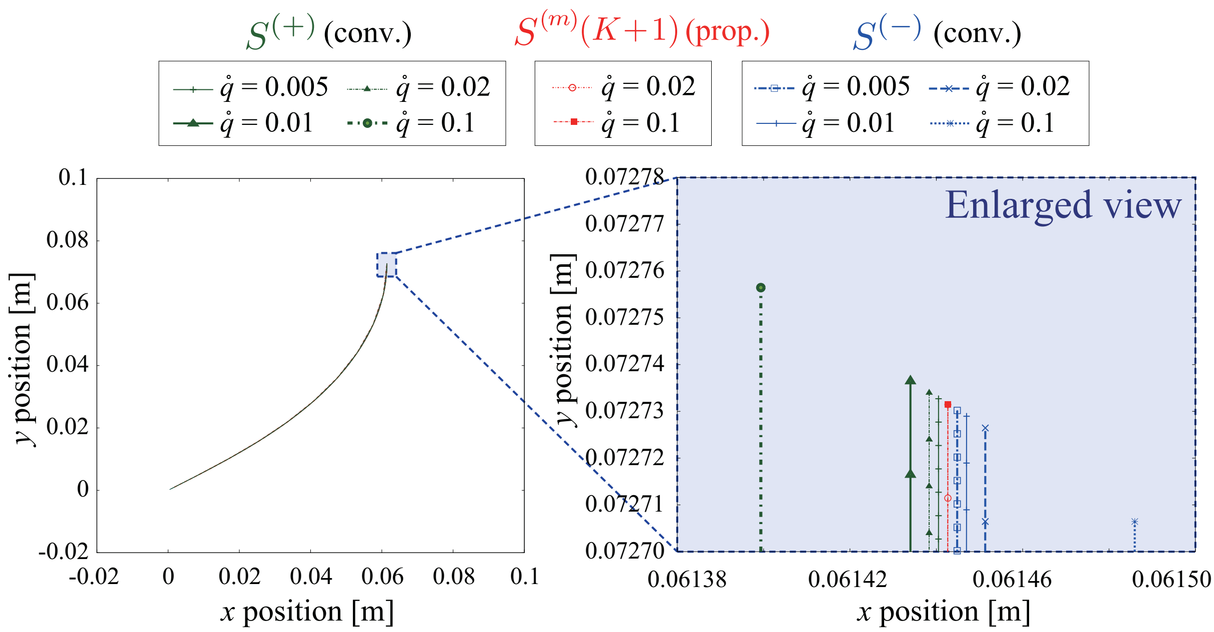

Fig. 4-24: Error evaluation of clothoid curve.

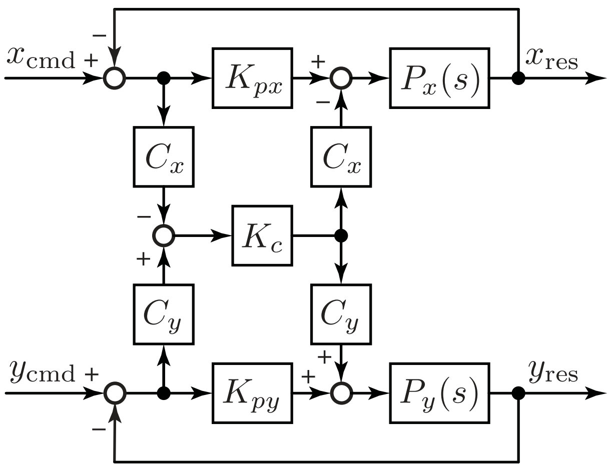

Fig. 4-25: Block diagram of the CCC.

Effectiveness of the True Value Prediction

In this section, the effectiveness of the true-value prediction is confirmed. True-value prediction is used for command generation of control. To evaluate its effect, the error with the true value of the clothoid curve is compared. The command value is the clothoid curve of section 1 in Fig. 4-19. In case study 1, tangential velocity is set to constant value. The result of the case study 1 is depicted in Fig.

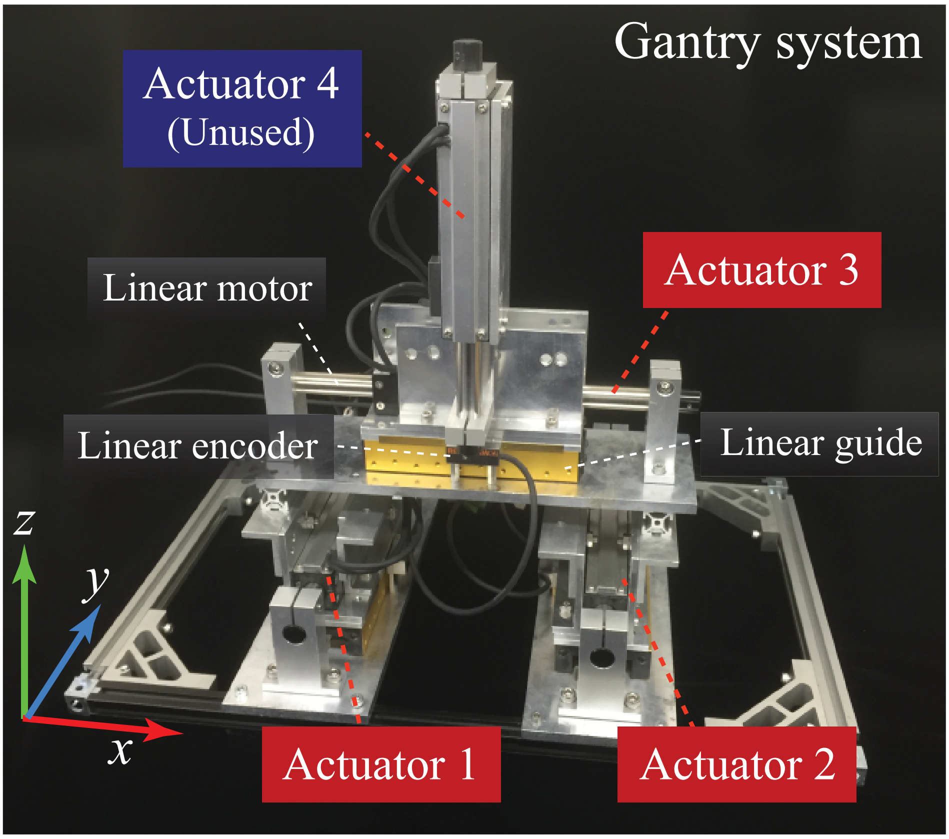

Fig. 4-26: Experimental setup of spatio-temporal interpolation.

4-27. In the case study 1, the tangential velocity and sampling time T_s are set to 0.5 $\mathrm{m/s}$ and 0.001 s, respectively. The black line in Fig. 4-27 means true value of clothoid curve (i.e., the case of very slow tangential velocity). The proposed method coincided with the true value, even when the resolution of calculation is low. Case study 2 is conducted to make sure the case that the tangential velocity is changed. The result of the case study 2 is shown in Fig. 4-28. The acceleration of the case study 2 is set to 30 $\mathrm{m/s^2}$. The initial tangential velocity and sampling time are set to 0 $\mathrm{m/s}$ and 0.001 s, respectively. As in the case study 1, the proposed method could predict the true value also in the case study 2. From this results, effectiveness of the true value prediction was confirmed.

Experimental Results of Spatio-temporal Interpolation

Fig. 4-29 shows the position tracking result. The contour following response with PD, CCC, and PD + DOB had a certain error. On the other hand, the contour following response with the proposed feed-forward control was almost equal to the command value. Also, in order to evaluate the errors, position

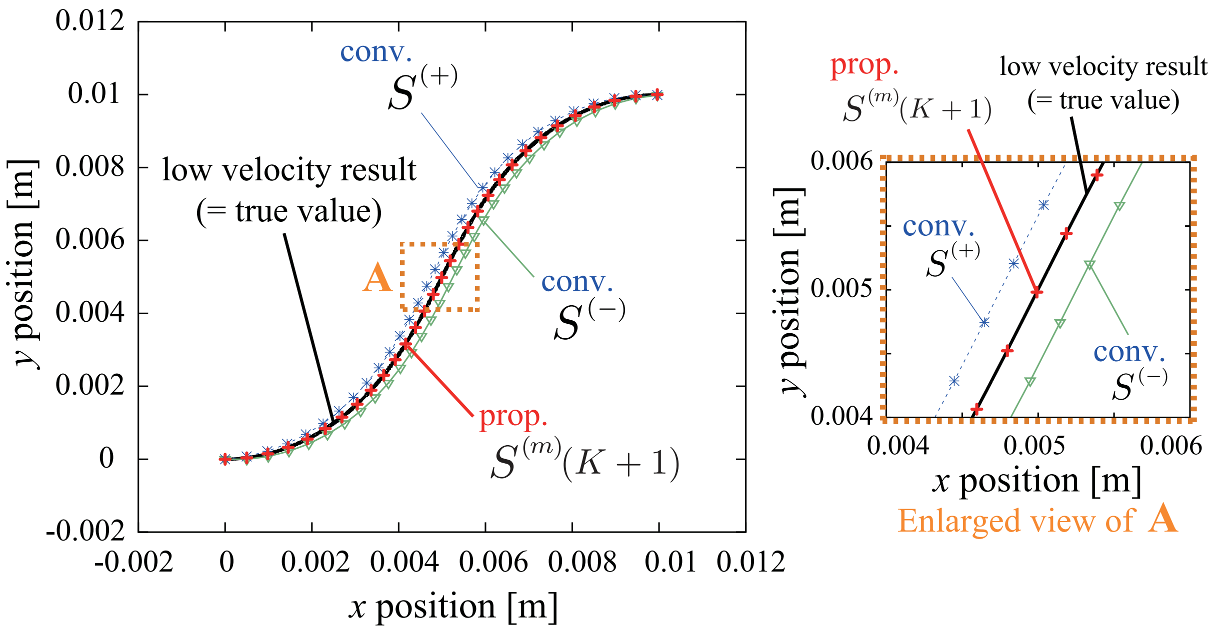

Fig. 4-27: Comparative verification of command values (constant velocity).

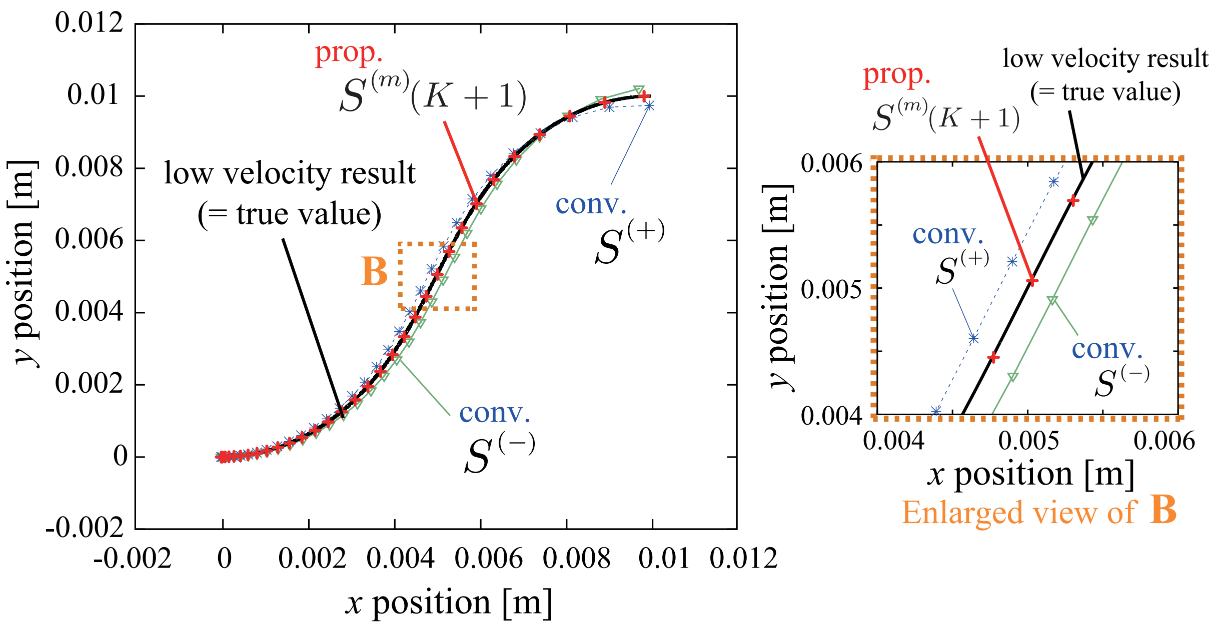

Fig. 4-28: Comparative verification of command values (constant acceleration).

errors of each axis were compared. Figs. 4-30 and 4-31 present the experimental results of the position response on each axis. These figures indicated that the proposed method had few errors. Meanwhile, the

Table 4.7: Experimental parameters of spatio-temporal interpolation.

Parameter	Description	Value
K_{p}	Position P gain for PD controller	10000 rad/s
K_{d}	Position D gain for PD controller	200 rad/s
C_{p}	Position gain for FF controller	10000 rad/s
C_{v}	Velocity gain for FF controller	200 rad/s
g_{dis}	Cut–off frequency of DOB	400 rad/s
g_{pd}	Cut–off frequency of pseudo derivative	5000 rad/s
g_{v}	Cut–off frequency of velocity calculation	10000 rad/s
$K_{\max}$	Series number of Aitken	10

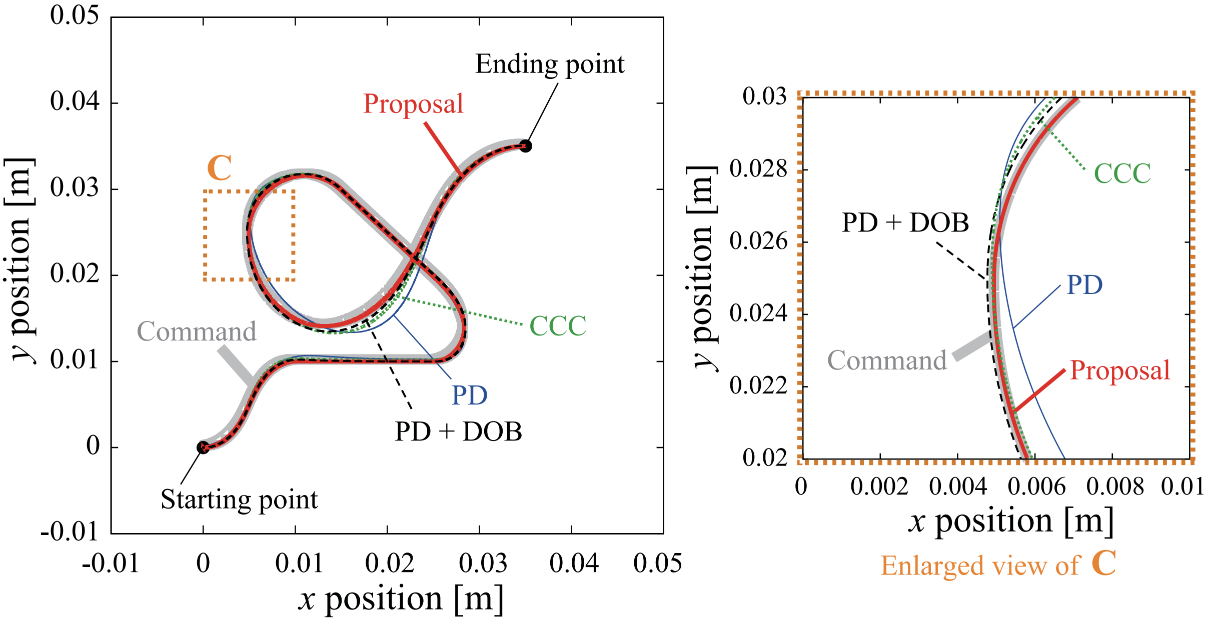

Fig. 4-29: Experimental results of trajectory tracking.

responses of PD, CCC, and PD + DOB had an error at the moments of acceleration and deceleration. Fig. 4-32 presents the tangential velocity response. Overshoots occurred at the moments of acceleration and deceleration in the case with the response of PD, CCC, and PD + DOB. Fig. 4-33 shows a comparison of velocity errors. The validity of the proposed method was confirmed because the proposal error was smaller than the PD, CCC, and PD + DOB.

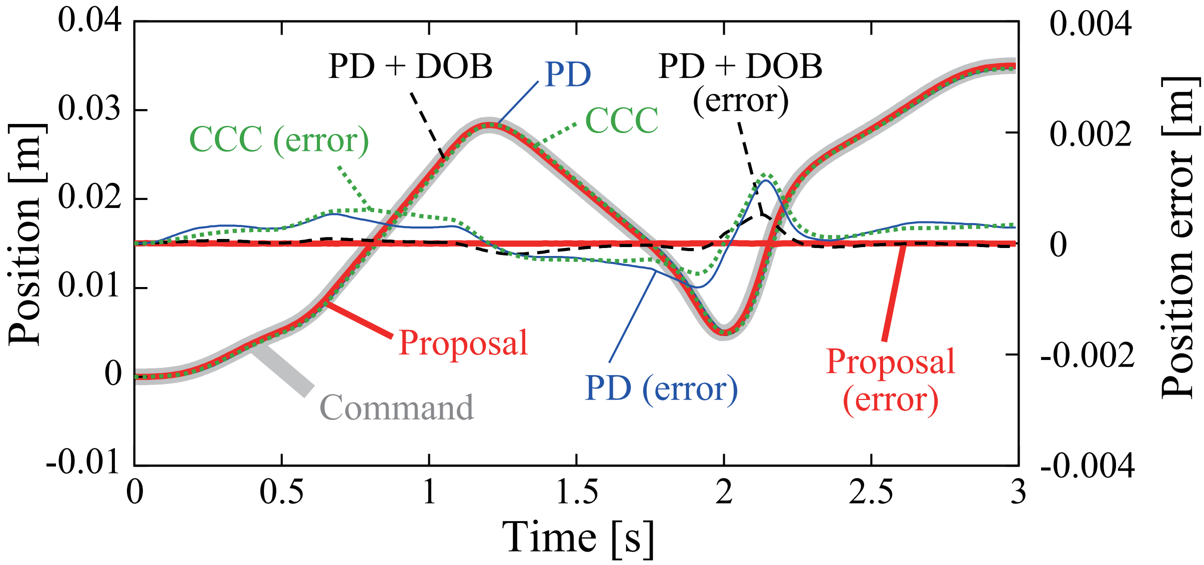

Fig. 4-30: Experimental results of x-axis position response.

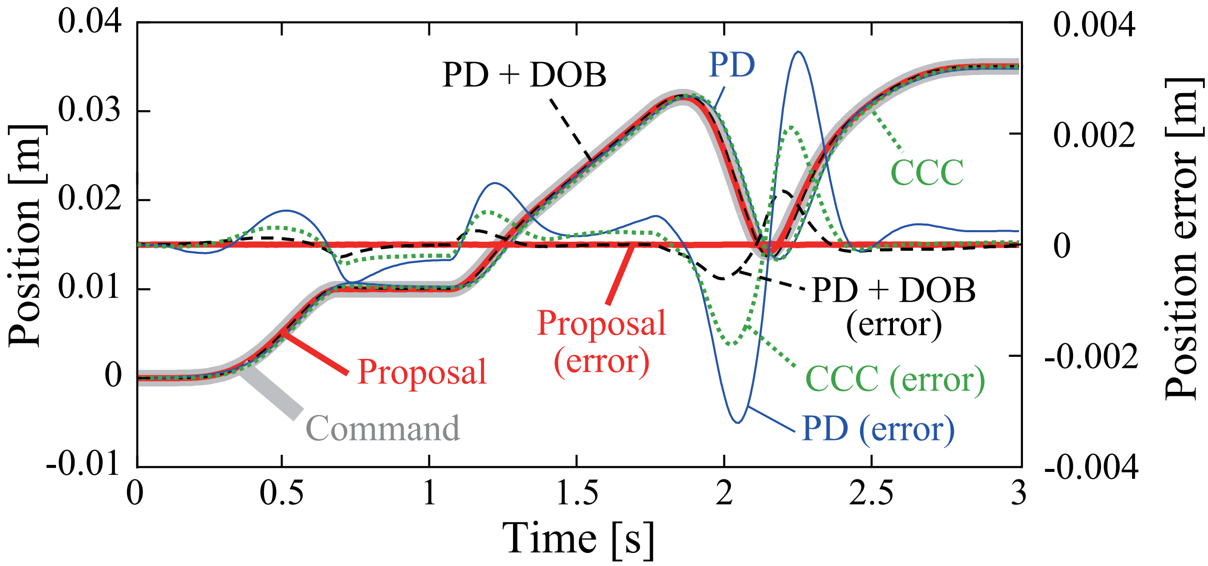

Fig. 4-31: Experimental results of y-axis position response.

4.3 Summary of Chapter 4

Chapter 4 proposed the command generation system of a servo system using the EDM and the clothoid curve. Firstly, the command generation method using the EDM was confirmed. By using the beam system as an example, the EDM can be applied to command value generation of servo systems. A command

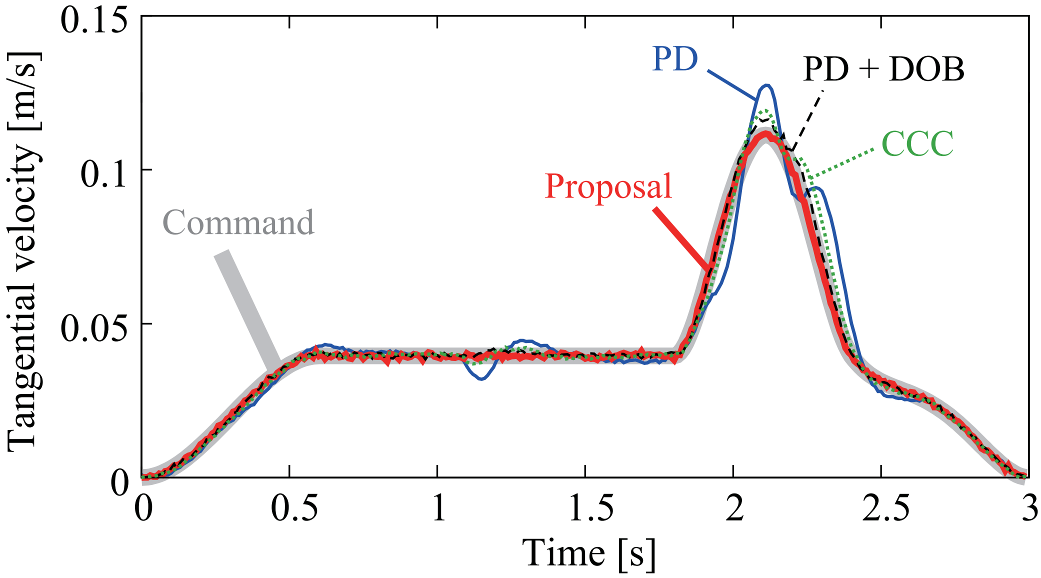

Fig. 4-32: Experimental results of tangential velocity.

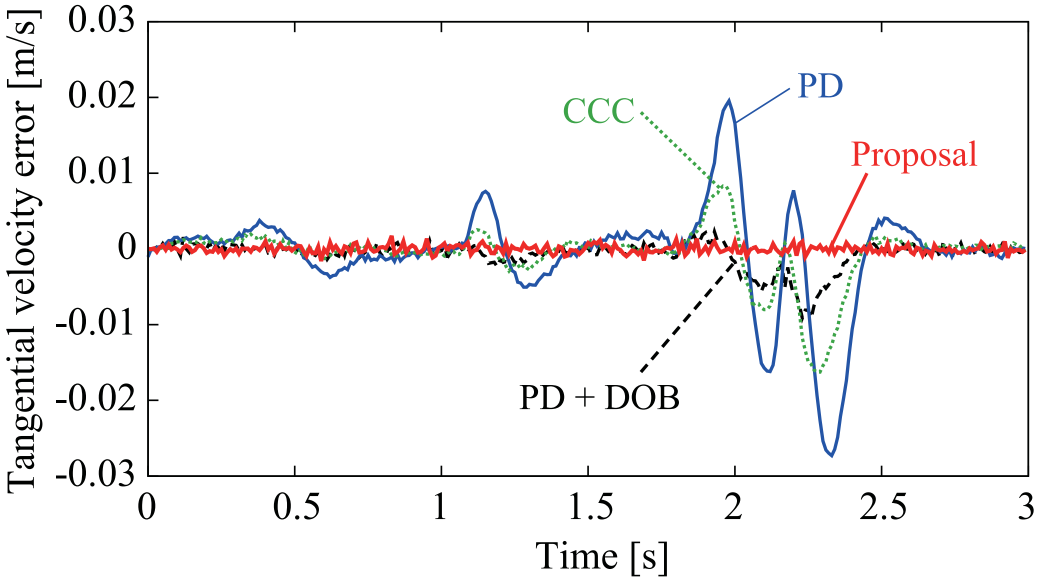

Fig. 4-33: Comparison of tangential velocity errors.

value to maximize the tip velocity of the beam system at the desired time was generated by the EDM. The proposed method can be used for various applications by designing the fitness function according to the target system. Also, this chapter proposed the high-accuracy interpolation method using clothoid curve considering the discretization error caused by the integration of the discrete-time function. Since the analytical solution of the clothoid curve can not be obtained, the method for predicting the true value is needed. The calculating resolution of the clothoid curve was determined by the tangential velocity and the sampling time. Hence, the discretization error of the numerical calculation must be considered. The discretization error was eliminated by the iterative true-value prediction. The proposed method can immediately estimate the true value of the clothoid curve by pinching integration and Aitken acceleration. In addition, the DOB and the feed-forward controller were implemented to follow the trajectory accurately. Consequently, the proposed method made it possible to move an arbitrary position trajectory at an arbitrary tangential velocity. In conclusion, the improvement in product quality in industrial applications can be expected when the proposed method is used.

Chapter 5

Skill Extraction Based on Motion-copying System

As shown in Fig. 1-3, not only the abstraction of knowledge but also the extraction of skills is necessary in order to achieve skilled machinery. In this chapter, a skill extraction method based on motion-copying system is described. One of the most effective methods that control contact force precisely is motion reproduction based on a motion-copying system [22, 23]. Since this approach does not require the model of an environment, there is no need to identify the environmental impedance like a model-based approach. Therefore, precise force control can be achieved for various environments. The time-adaptation control [30, 31] for motion reproduction is proposed for adapting to variations of environmental location and toward advanced manufacturing process. The proposed method has the highest priority on eliminating force error by lowering the priority on time correspondence, the reproducibility of contact motion is improved. Concretely speaking, the proposed method matches the force response value with its command under contact motion, by introducing a difference between save time and reproduction time. By using this method, even when the environmental location is changed, it is possible to reproduce the same reaching velocity at the moment of first contact. Then, the force error in the reproduced motion is suppressed immediately. In recent years, not only production speed, but also product quality must be ensured in a manufacturing site. In an actual manufacturing site, because materials are natural objects, properties, such as the size of an object, are different in different lots. Therefore, a control method that can adapt to variations of environmental location is effective for achieving high-quality manufacturing.

5.1 Introduction of Chapter 5

This section focuses on the use of position/force hybrid control. The position/force hybrid control is one of effective methods which can contact to an environment with high accuracy. The position/force hybrid control is composed of two phases: Bilateral control [19–21] and motion reproduction [24–30]. In the bilateral control, position and force are converted into acceleration so that those can be handled comprehensively. Bilateral control can save both position and force responses input by an operator. The position/force hybrid control follows these trajectories in the motion reproduction. Since the force information is included in the saved motion data and those can be reproduced, it is possible to conduct the contact motion which was difficult to be realized in a position control system.

However, in the conventional position/force hybrid control, it is difficult to execute the saved motion accurately when the environmental location of the motion reproduction is different from that in the bilateral control. For example, when the size of target object is deviated, equivalent location of contacting surface is changed and the error of the force control occurs in the contacting motion. Therefore, the objects should always be ensured to have constant size by the quality control. However, in many cases like natural feedstock, it is not always easy to maintain constant size. Thus, while maintaining high-speed movement enabled by method such as the conventional position control, the control with dexterity that can respond to the change in the object is needed. Therefore, several methods to address this problem have been proposed [24–30]. These methods can adapt to environmental location error. Tsunashima *et.al.* proposed a method based on acceleration information [24]. This method can adapt the changing of environment position because acceleration information does not depend on the initial position. Moreover, Tsunashima *et.al.* proposed a position-compensation method [26]. The compensation value of position calculated from force error information. Yajima *et.al.* proposed a method based on velocity information [27]. In this method, since differential mode is based on velocity information, the DC component of position response is ignored. Miyagi *et.al.* proposed a bandwidth-based method [28]. This method can divide motion data into free motion and contact motion by bandwidth information. These methods have the merit that motion reproduction time is same with saved motion. However, in these studies, velocity and force errors occur in the moment of first contact, because these methods have priority on the same finishing time of motion reproduction. In contact motion, reducing the force error is more important than correspondence of the finishing time between saved data and reproduced motion. Actually, accuracy is more required than production speed in production site. A method by time-scaling has also been

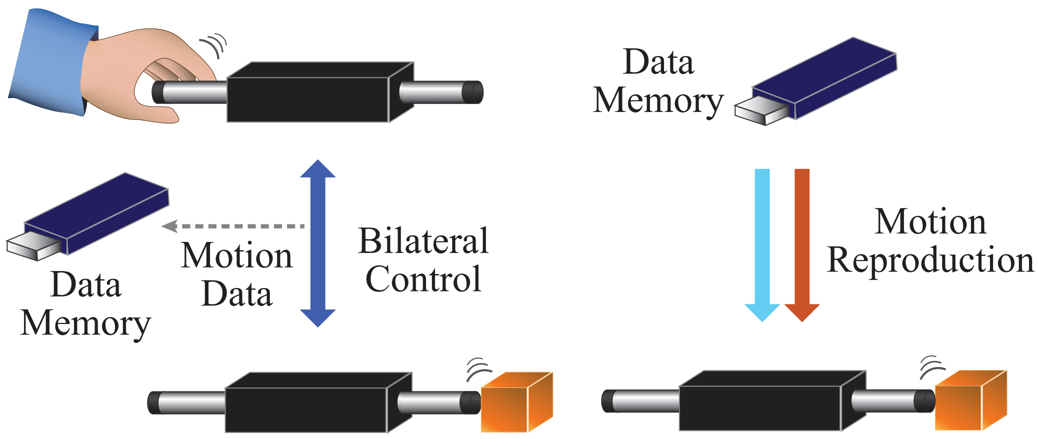

Fig. 5-1: Overview of the position/force hybrid control.

proposed [29]. This method can reduce force error by changing the speed of reproduction time. However, velocity and force errors still occur in the moment of first contact, because it is the method based on position information. Also, this method spends time before suppressing force error, because it changes the speed of reproduction time.

In this section, time-adaptation control is proposed for force error suppression. The method has the highest priority on eliminating force error; by lowering the priority on the time correspondence, the reproducibility of the contact motion is improved. By using this method, even when the location of the environment is changed, it is possible to reproduce the same reaching velocity at the moment of first contact. Then, force error in motion reproduction is suppressed immediately. The proposal in this dissertation will be expected to achieve dexterous motion for the production of high-quality products in the manufacturing site.

5.2 Position/Force Hybrid Control

In this section, the position/force hybrid control is introduced. Overview of the position/force hybrid control is shown in Fig. 5-1.

5.2.1 Bilateral Control

The control system is composed of two actuators and an acceleration-based bilateral control [19–21] is implemented. An actuator that contacts with human is called a master system, and another one

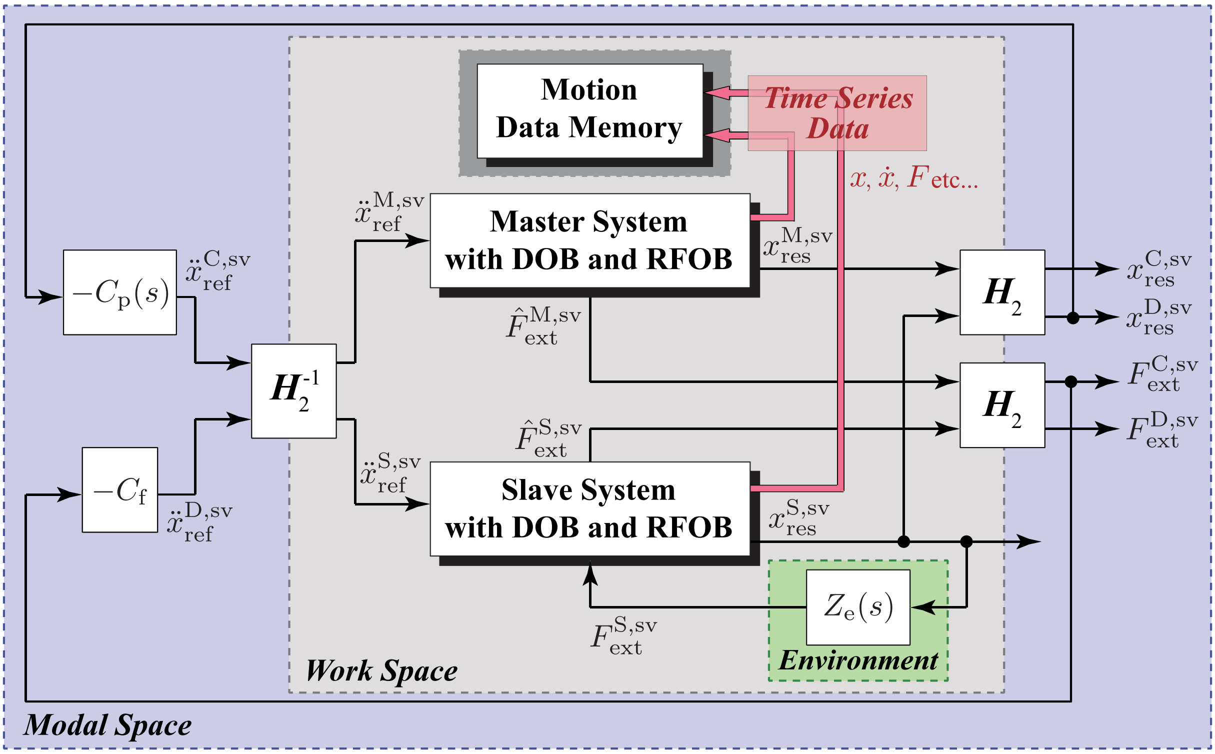

Fig. 5-2: Block diagram of the bilateral control.

that contacts with environment is called a slave system. In order to achieve acceleration control with robustness, the DOB is implemented in the master and slave systems. Also, the RFOB is implemented in each system. The external force can be estimated by the RFOB. The bilateral control has two control goals as follows:

$$x^{\mathrm{M}}_{\mathrm{res}} - x^{\mathrm{S}}_{\mathrm{res}} = 0, \tag{5.1}$$

$$F^{\mathrm{M}}_{\mathrm{ext}} + F^{\mathrm{S}}_{\mathrm{ext}} = 0. \tag{5.2}$$

The subscripts M and S represent the master system and the slave system, respectively. The (5.1) and (5.2) represent synchronization and reproduction of action-reaction law, respectively. In order to achieve the bilateral control, the systems are controlled in modal space. To transform values from real space to the modal one, the Hadamard matrix [102] is used as follows:

$$\boldsymbol{H}_2 = \frac{1}{2}\begin{bmatrix} 1 & 1 \\ 1 & -1 \end{bmatrix}. \tag{5.3}$$

By using the Hadamard matrix, the position and force information is transformed into the modal space as follows:

$$\begin{bmatrix} x_{\rm res}^{\rm C,sv} \\ x_{\rm res}^{\rm D,sv} \end{bmatrix} = \boldsymbol{H}_2 \begin{bmatrix} x_{\rm res}^{\rm M,sv} \\ x_{\rm res}^{\rm S,sv} \end{bmatrix}, \tag{5.4}$$

$$\begin{bmatrix} F_{\rm ext}^{\rm C,sv} \\ F_{\rm ext}^{\rm D,sv} \end{bmatrix} = \boldsymbol{H}_2 \begin{bmatrix} \hat{F}_{\rm ext}^{\rm M,sv} \\ \hat{F}_{\rm ext}^{\rm S,sv} \end{bmatrix}, \tag{5.5}$$

where the subscripts C, D and sv represent the common mode, differential mode and saved value in the bilateral control, respectively. In the modal space, position response in differential mode and force response in common mode are controlled. The former is controlled by position regulator to attain (5.1). The latter is controlled by force servoing to attain (5.2). These controllers are described as follows

$$\ddot{x}_{\rm ref}^{\rm C,sv} = -C_{\rm f} F_{\rm ext}^{\rm C,sv}, \tag{5.6}$$

$$\ddot{x}_{\rm ref}^{\rm D,sv} = -C_{\rm p}(s)\, x_{\rm res}^{\rm D,sv} = -\left(K_{\rm p} + \frac{s\, g_{\rm pd}}{s + g_{\rm pd}} K_{\rm d} \right) x_{\rm res}^{\rm D,sv}, \tag{5.7}$$

where $C_{\rm f}$, $g_{\rm pd}$, $K_{\rm p}$ and $K_{\rm d}$ denote the force gain, cut-off frequency of derivative controller, proportional gain and derivative gain of position regulator, respectively. The reference values of acceleration in real space is calculated by inverse Hadamard transformation as follows

$$\begin{bmatrix} \ddot{x}_{\rm ref}^{\rm M,sv} \\ \ddot{x}_{\rm ref}^{\rm S,sv} \end{bmatrix} = \boldsymbol{H}_2^{-1} \begin{bmatrix} \ddot{x}_{\rm ref}^{\rm C,sv} \\ \ddot{x}_{\rm ref}^{\rm D,sv} \end{bmatrix}. \tag{5.8}$$

Accordingly, bilateral control between the master and slave systems is conducted. Fig. 5-2 shows the block diagram of bilateral control. An environmental impedance is modeled by spring and damper as

$$Z_{\rm e}(s) = D_{\rm e} s + K_{\rm e}, \tag{5.9}$$

where $D_{\rm e}$ and $K_{\rm e}$ represent the damping coefficient and the stiffness, respectively. In bilateral control, time-series data of position, velocity and force responses are stored.

5.2.2 Motion Reproduction

In the motion reproduction, there is only one actuator in which acceleration control is implemented. The other actuator is replaced by the saved master data. Three control goals for the motion reproduction are expressed by

$$x_{\mathrm{res}}^{\mathrm{S,sv}}(t_{\mathrm{ld}}) - x_{\mathrm{res}}^{\mathrm{S,ld}}(t) = 0, \tag{5.10}$$

$$F_{\mathrm{ext}}^{\mathrm{S,sv}}(t_{\mathrm{ld}}) - \hat{F}_{\mathrm{ext}}^{\mathrm{S,ld}}(t) = 0, \tag{5.11}$$

$$t_{\mathrm{ld}} - t = 0, \tag{5.12}$$

where the subscript ld means the reproduced value. In order to achieve the perfect motion reproduction, these equations always must be established. Eqs. (5.10) and (5.11) mean the reproduction data of positions and force correspond to the saved one, respectively. Eq. (5.12) means the flow of time bilateral control and motion reproduction is same. t_{ld} denotes

$$t_{\mathrm{ld}} = t + t_{\mathrm{sf}}, \tag{5.13}$$

$$t_{\mathrm{ld}} \in [t_{\mathrm{ld}}^{\mathrm{str}}, t_{\mathrm{ld}}^{\mathrm{fin}}], \tag{5.14}$$

where the superscripts str and fin denote the starting time and finishing time of motion, respectively. The subscript sf stands for shifting time of motion reproduction. Moreover, t_{sf} should be constant for a period of the contact motion.

5.3 Time-adaptation Control in SDOF System

This section describes the proposed method of time-adaptation control. The conventional motion reproduction can reproduce the motion completely, when there is no change in the location of environment. Since the correspondence of both position and force at the same time is physically impossible, when the environmental location is changed, it is necessary to prioritize the control goal. In the case of contact motion, the most important factor is reducing the force error between saved data and loaded data. However, most of the previous researches have priority on the finishing time of motion reproduction whose objective is shown in (5.12). Therefore, velocity error and force error occur in starting time of contact.

5.3.1 Principle of Time-adaptation Control

The proposed method has the highest priority on eliminating force error. Since the approaching velocity to the object is the important factor for force in the moment of first contact, the objective shown in

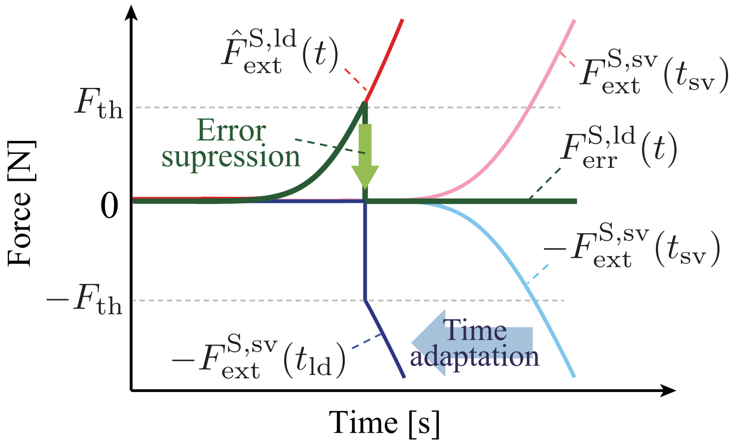

Fig. 5-3: Concept of time adaptation (shorten distance).

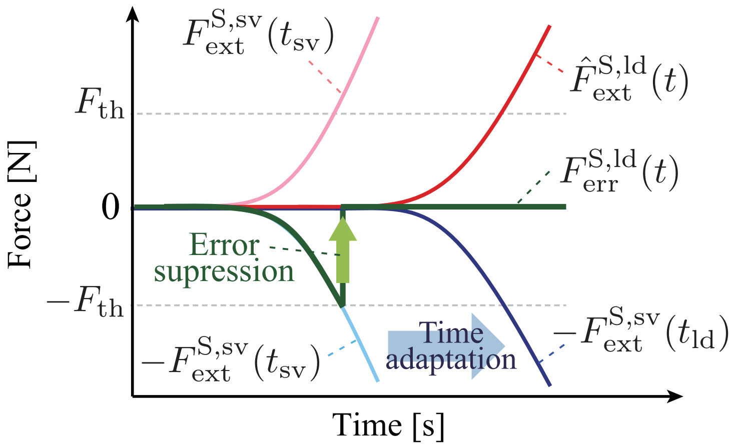

Fig. 5-4: Concept of time adaptation (lengthen distance).

(5.10) is modified as

$$v^{\mathrm{res}}_{\mathrm{S,sv}}(t_{\mathrm{ld}}) - v^{\mathrm{res}}_{\mathrm{S,ld}}(t) \quad = \quad 0, \tag{5.15}$$

where v expresses velocity. Overview of the proposed method is shown in Figs. 5-3 and 5-4. In Figs. 5-3 and 5-4, F_{th} denotes threshold value for time adaptation. Then, the superscript err stands for error value.

Fig. 5-3 shows the case when the distance between the actuator and environment is short. When the distance is short, reaction force appears faster than the time in saved data. Therefore, force error becomes positive when the saved action force applied by human $F^{\mathrm{ext}}_{\mathrm{S,sv}}$ is negative. When the force error exceeds F_{th}, a time-adaptation controller works to suppress the force error. Fig. 5-4 shows the case when the

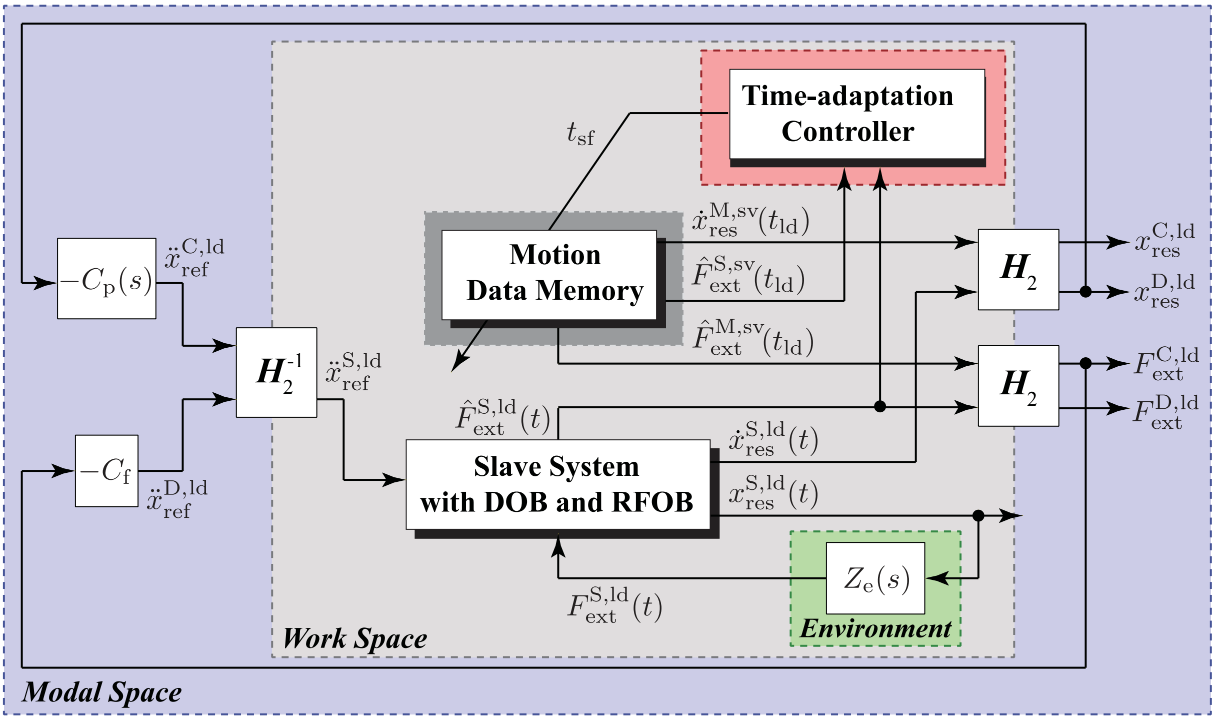

Fig. 5-5: Block diagram of the proposed motion reproduction in SDOF system.

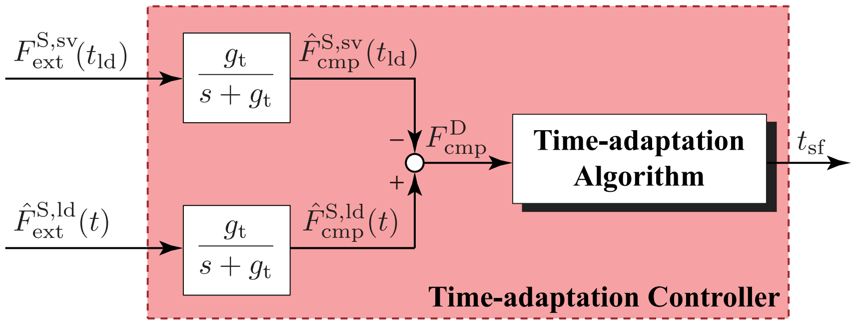

Fig. 5-6: Block diagram of the time-adaptation control in SDOF system.

distance is long. In this case, the force error becomes negative conversely. When the force error is less than $-F_{\mathrm{th}}$, a time-adaptation controller works to suppress the force error.

The block diagram of the time-adaptation control is shown in Fig. 5-5. Concretely speaking, the time-adaptation controller shifts the time of motion reproduction data according to the force error. Fig. 5-6 shows the structure of the time-adaptation. In Fig. 5-6, g_{t} means the cut-off frequency of the low-pass filters for time adaptation. A time-adaptation algorithm is shown in Fig. 5-7. In Fig. 5-7, a and t_{s} denote hysteresis coefficient and sampling time, respectively. This coefficient is set more than 0, less

$*$: Multiplier
$/$: Divider

If ($F^{\mathrm{D}}_{\mathrm{cmp}} < -F_{\mathrm{th}}$) Then
While ($F^{\mathrm{D}}_{\mathrm{cmp}} < -F_{\mathrm{th}} * a$)
$t_{\mathrm{sf}} = t_{\mathrm{sf}} - t_{\mathrm{s}}$
Loop **Time-delay loop**
ElseIf ($F^{\mathrm{D}}_{\mathrm{cmp}} > F_{\mathrm{th}}$) Then
While ($F^{\mathrm{D}}_{\mathrm{cmp}} > F_{\mathrm{th}} * a$)
$t_{\mathrm{sf}} = t_{\mathrm{sf}} + t_{\mathrm{s}}$
Loop **Time-lead loop**
End If

Time-adaptation Algorithm

Fig. 5-7: Structure of the time-adaptation algorithm.

Table 5.1: Parameter values used for simulations.

Parameters	Descriptions	Value
T_{s}	Sampling time	0.0001 s
K_{tn}	Nominal force coefficient	33.0 N/A
M_{n}	Nominal mass	0.5 kg
$K_{\mathrm{p}}^{\mathrm{hum}}$	Proportional gain of virtual human	1000
$K_{\mathrm{d}}^{\mathrm{hum}}$	Differential gain of virtual human	20
C_f	Force gain	5
g_{dis}	Cut-off frequency of the DOB	5000 rad/s
g_{reac}	Cut-off frequency of the RFOB	5000 rad/s
g_{t}	Cut-off frequency of time-adaptation	100 rad/s
F_{th}	Threshold of time-adaptation controller	0.1 N
K_{e}	Environmental stiffness	5000 N/m
D_{e}	Environmental damping coefficient	500 N・s/m

than 1. Therefore, the time-adaptation loop is continued until force error $|F^{\mathrm{ext}}_{\mathrm{C,ld}}|$ is suppressed less than $|F_{\mathrm{th}} \times a|$. By using this algorithm, force error is suppressed immediately.

In the time-adaptation control, the value of shifting time must converge in accordance with the changing length of environmental location. In the case of containing large impact force or large velocity noise, the shifting time may not converge to optimal value. In the former case, the impact force can be reduced by a low-pass filter in Fig. 5-6. The force information passed this filter $F^{\mathrm{cmp}}_{\mathrm{D}}$ is used only to shift loading-time. Therefore, it does not affect to sensitivity of position/force hybrid control. It only affects

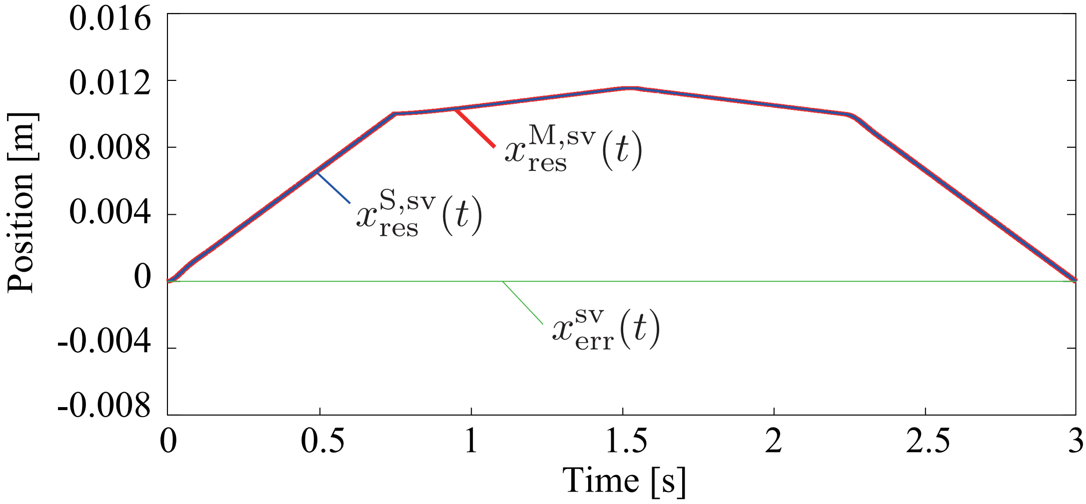

Fig. 5-8: Saved data of position (simulation) in SDOF system.

to the response of time shift to adapt environmental location change. In the latter case, the velocity error can be reduced by the pseudo-differentiator for velocity response calculation. The low-pass filter of the pseudo-differentiation can reduce the noise of velocity.

5.3.2 Simulations in SDOF System

Simulation Setup in SDOF System

In order to verify the validity of the proposed method, simulations are conducted. The simulation program is implemented by Visual Basic. In bilateral control phase, operational force by human is generated using an additional virtual motor connected to the master system. For the virtual motor, position PD controller is implemented, and following trajectory command x_{cmd} is applied

$$x_{\mathrm{cmd}} = \begin{cases} 0.02\,\dfrac{t}{1.5} & (0 \leq t < 1.5) \\[2ex] -0.02\,\dfrac{t-1.5}{1.5} + 0.02 & (1.5 \leq t \leq 3) \end{cases} . \tag{5.16}$$

Also, in the motion reproduction phase, the location of an environment is changed to three positions: same as the bilateral control phase, 3 mm nearer than the bilateral control phase, and 3 mm further than the bilateral control phase. Parameter values used for the simulations are shown in Table 5.1.

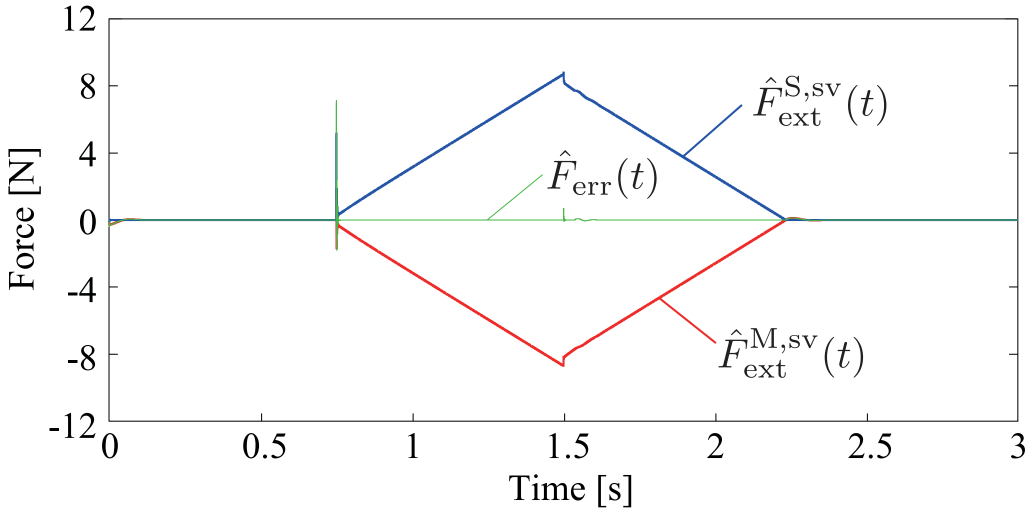

Fig. 5-9: Saved data of force (simulation) in SDOF system.

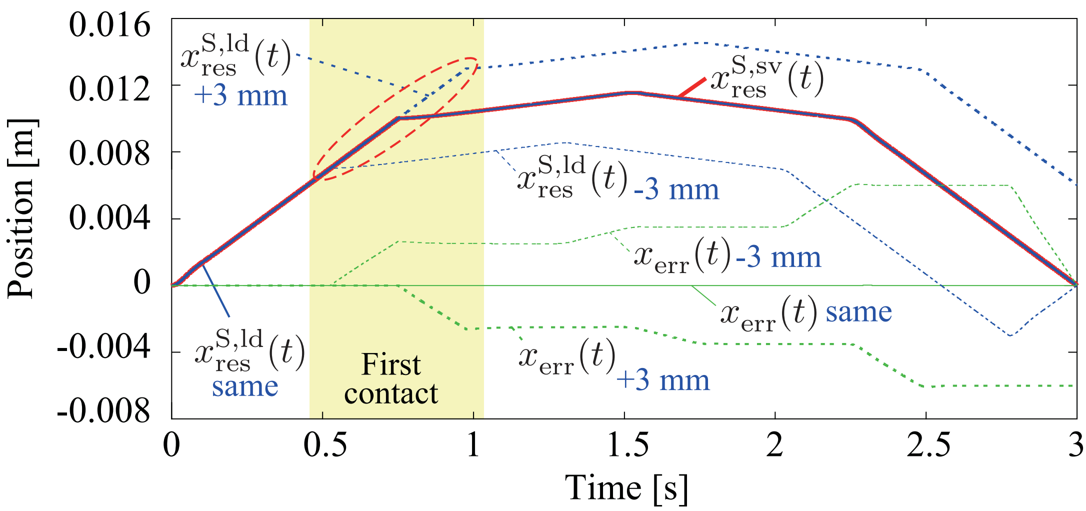

Fig. 5-10: Position response in reproduction (simulation) in SDOF system.

Simulation Results in SDOF System

The simulation results are shown in Figs. 5-8 to 5-11. Figs. 5-8 and 5-9 show the saved motion data. Figs. 5-10 and 5-11 show the motion reproduction results by using the proposed method. From Figs.5-9 and 5-11, since the waveform shapes of force responses are the same, motion reproduction is achieved perfectly. In the proposed method, the gradients of position variations are same for all cases, as shown in the circled area in Fig. 5-10. Therefore, in Fig. 5-11, impact forces are same even when the location of the environment is changed.

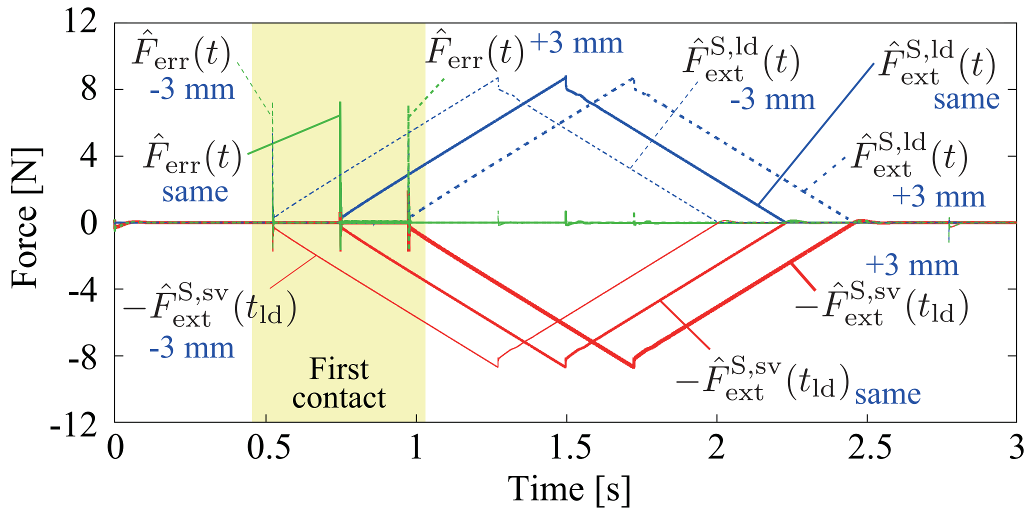

Fig. 5-11: Force response in reproduction (simulation) in SDOF system.

5.3.3 Experiments in SDOF System

In this section, the validity of the proposed method is confirmed by experiments. In this dissertation, the velocity-based method [27], time-scaling method [29] and the proposed method are compared.

Experimental Setup in SDOF System

Fig.5-12 shows the experimental setup in a SDOF system. There are two systems: the master system and slave system. Each system consists of a linear motor, a linear guide and a linear encoder. In bilateral control phase, a human operator manipulates the master system, and the slave system contacts with an environment. In the motion reproduction phase, only the slave system is used. The location of environment is changed to 5 mm further and 5 mm nearer than the bilateral control phase. Parameter values of the proposed method used for the experiments are shown in Table 5.2. Parameter values of the time-scaling method used for the experiments are shown in Table 5.3.

Experimental Results in SDOF System

Figs. 5-13 and 5-14 show the results that the environmental location is further and nearer, respectively. There are two contact motions. In the contact motion, it is most important to have the same force response with the saved data for the task achievement. The influence of the location change appears at the time of the first contact. The force error does not occur in any method at second contact, because the adaptation is completed in first contact.

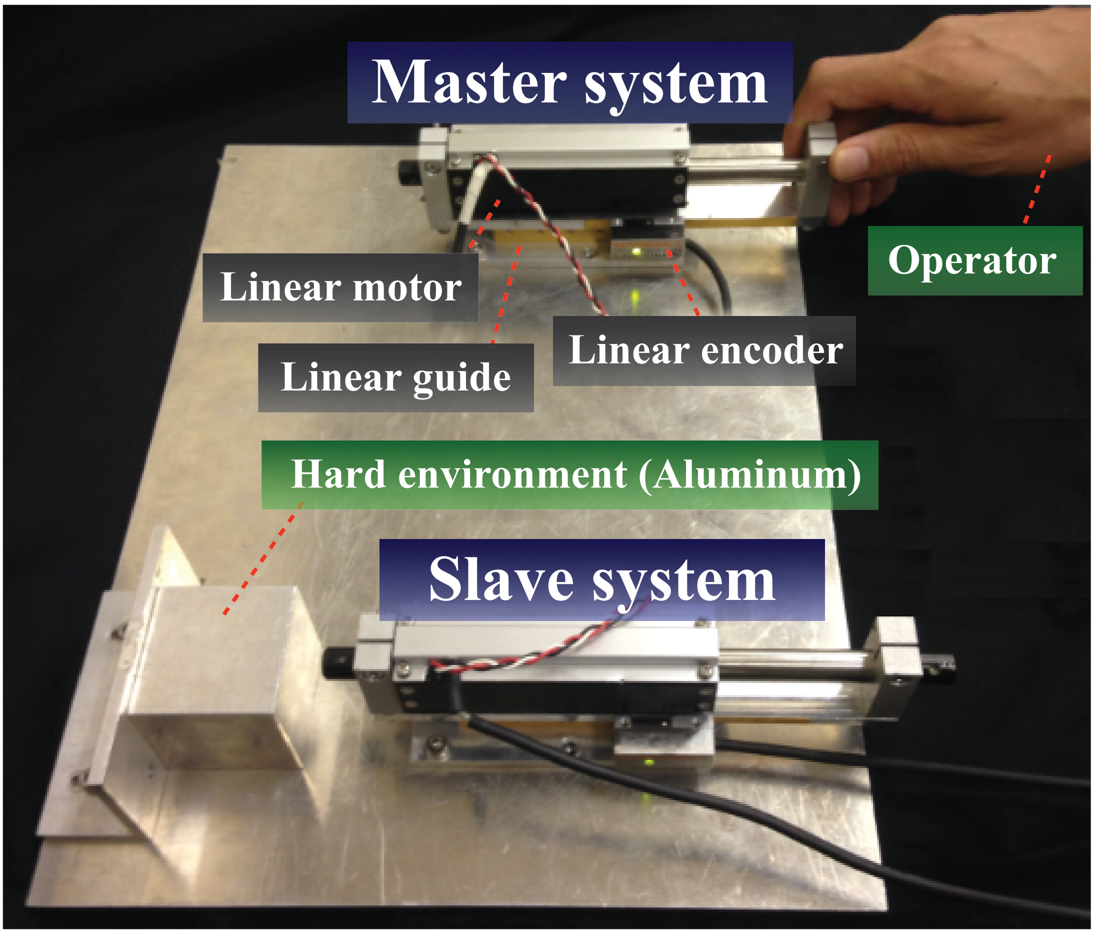

Fig. 5-12: Experimental setup of SDOF system.

Table 5.2: Parameters of the time-adaptation control in SDOF system.

Parameters	Descriptions	Value
$K_{\rm tn}$	Nominal torque coefficient	40 N/A
$M_{\rm n}$	Nominal mass	0.3 kg
$K_{\rm p}$	Proportional gain	10000
$K_{\rm d}$	Differential gain	200
$C_{\rm f}$	Force gain	5
$g_{\rm dis}$	Cut-off frequency of the DOB	1000 rad/s
$g_{\rm reac}$	Cut-off frequency of the RFOB	1000 rad/s
$g_{\rm v}$	Cut-off frequency of pseudo-differentiation for velocity calc.	1000 rad/s
$g_{\rm t}$	Cut-off frequency of time-adaptation	50 rad/s
$F_{\rm th}$	Threshold of time-adaptation controller	0.1 N
a	Hysteresis coefficient	0.5

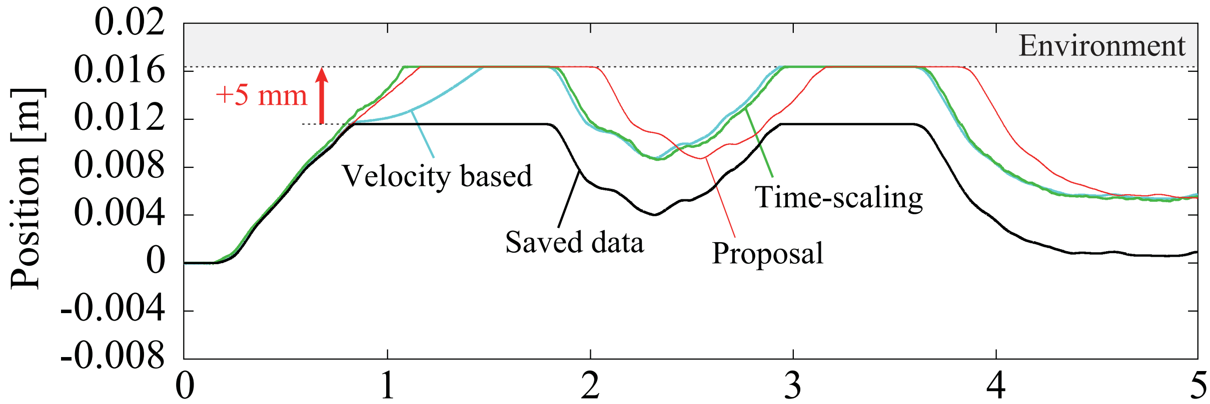

(a) Position responses

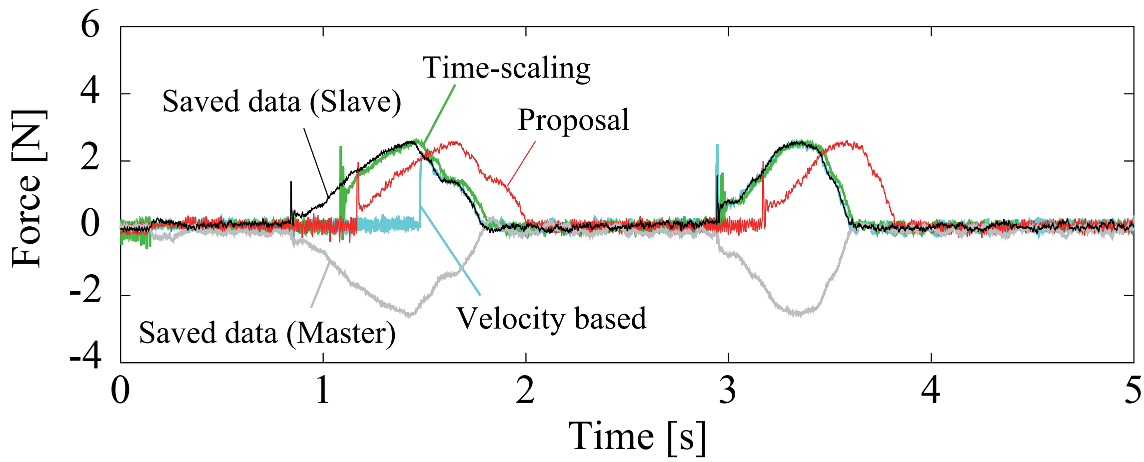

(b) Force responses

Fig. 5-13: Experimental results (environmental location +5 mm) in SDOF system.

The comparison of force responses at the moment of first contact is shown in Fig. 5-15. In Fig. 5-15, time axis is fitted to compare the waveforms of forces. From Fig. 5-15, it turns out that the waveform of reproduction force becomes the most similar with the saved data in the case of the proposed method. The conventional methods have force error at the moment of the first contact. Therefore, it is able to say that the accurate motion reproduction is achieved by the time-adaptation control and the validity of the proposed method is verified.

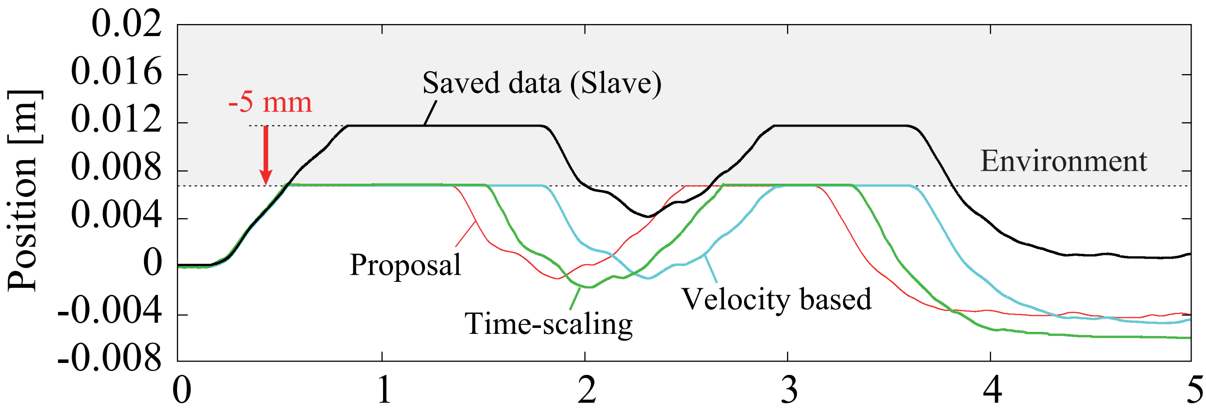

(a) Position responses

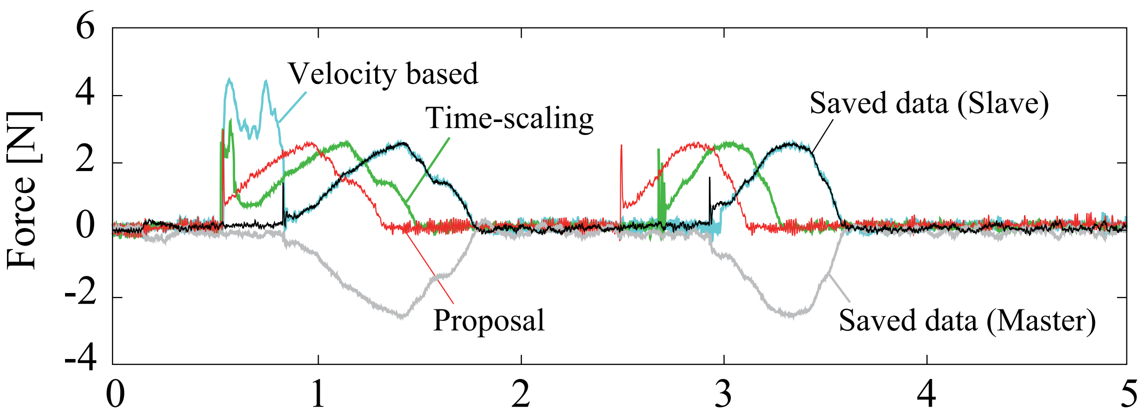

(b) Force responses

Fig. 5-14: Experimental results (environmental location -5 mm) in SDOF system.

Table 5.3: Parameters of the time-scaling method.

Parameters	Descriptions	Value
K_{tn}	Nominal torque coefficient	40 N/A
M_{n}	Nominal mass	0.3 kg
K_{p}	Proportional gain	10000
K_{d}	Differential gain	200
C_{f}	Force gain	5
g_{dis}	Cut-off frequency of the DOB	1000 rad/s
g_{reac}	Cut-off frequency of the RFOB	1000 rad/s
g_{hpf}	Cut-off frequency of position compensation	40 rad/s
k	Feedback gain of time-scaling	0.001 $\mathrm{m/s^2}$

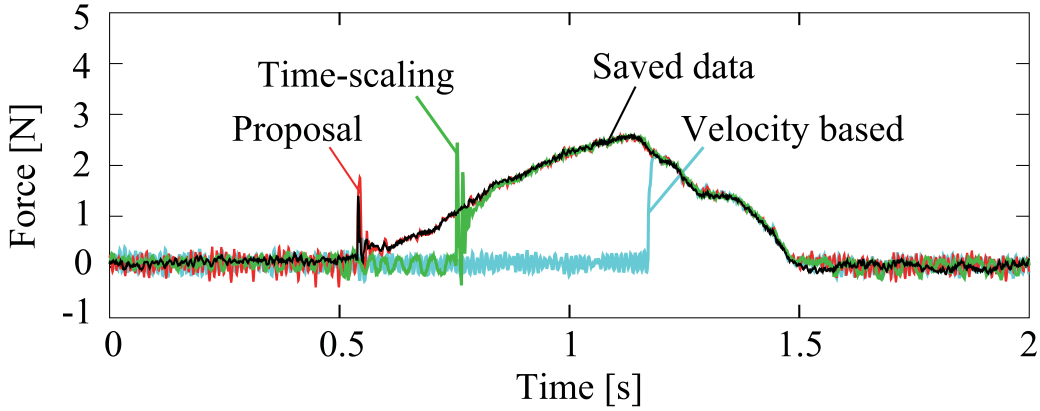

(a) The results of + 5 mm.

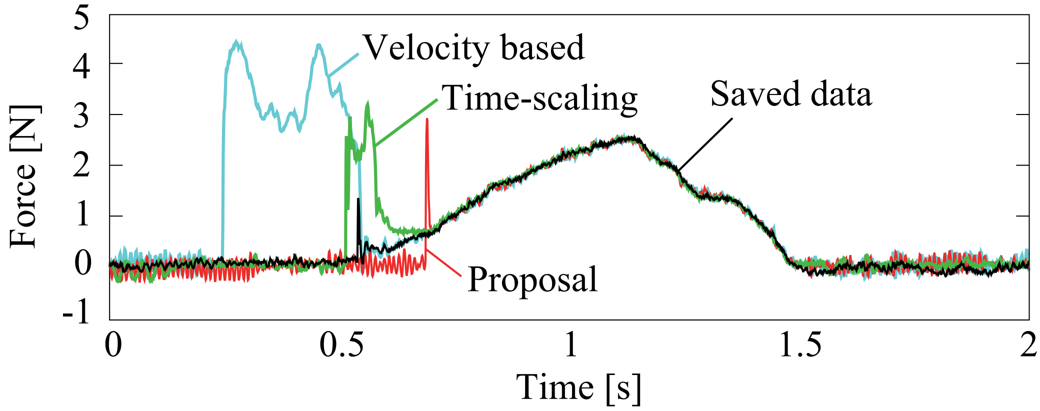

(b) The results of - 5mm.

Fig. 5-15: Comparison of force responses.

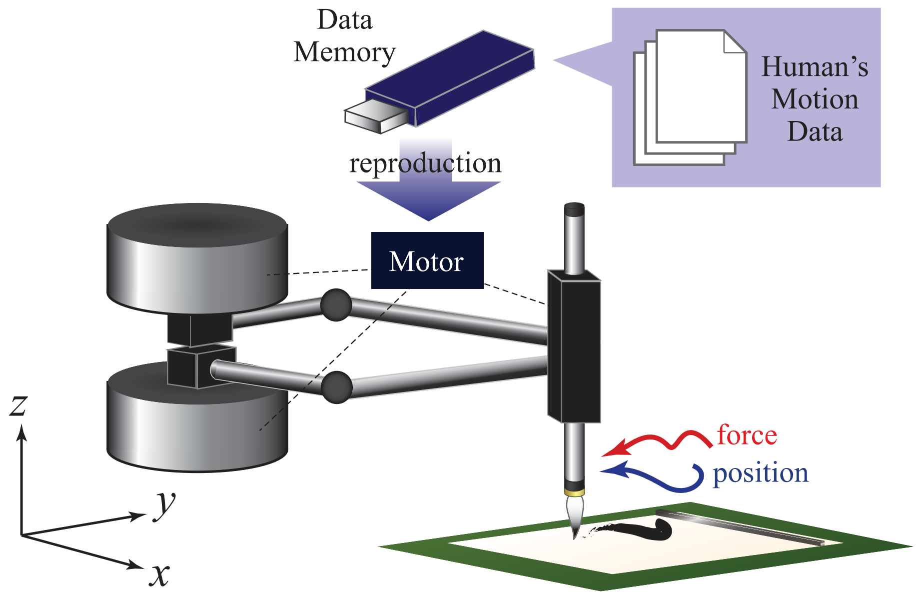

Fig. 5-16: Overview of motion loading in MDOF system.

5.4 Time-adaptation Control in MDOF System

In this section, the time-adaptation control in an MDOF system is introduced [31]. This method can contact to an environment by separately controlling force and position in the desired axes. The proposal can be achieved by hybrid-spatial value that mixed position and velocity information. Fig. 5-16 shows the overview of motion loading in an MDOF system. The motion-loading system is actuated based on human's saved motion data. The human's motion data are stored by the motion-saving system.

5.4.1 Motion-saving System in MDOF System

The motion-saving system is based on bilateral control [19–21]. In order to achieve bilateral control, acceleration control based on the DOB is constructed. Bilateral control can divide human action force and environment reaction force. These forces are estimated by the RFOB [59]. Here, control goals of motion-saving system are as follows:

$$\boldsymbol{x}^{\mathrm{M}}_{\mathrm{res}} - \boldsymbol{x}^{\mathrm{S}}_{\mathrm{res}} = 0, \tag{5.17}$$

$$\boldsymbol{f}^{\mathrm{M}}_{\mathrm{ext}} + \boldsymbol{f}^{\mathrm{S}}_{\mathrm{ext}} = 0, \tag{5.18}$$

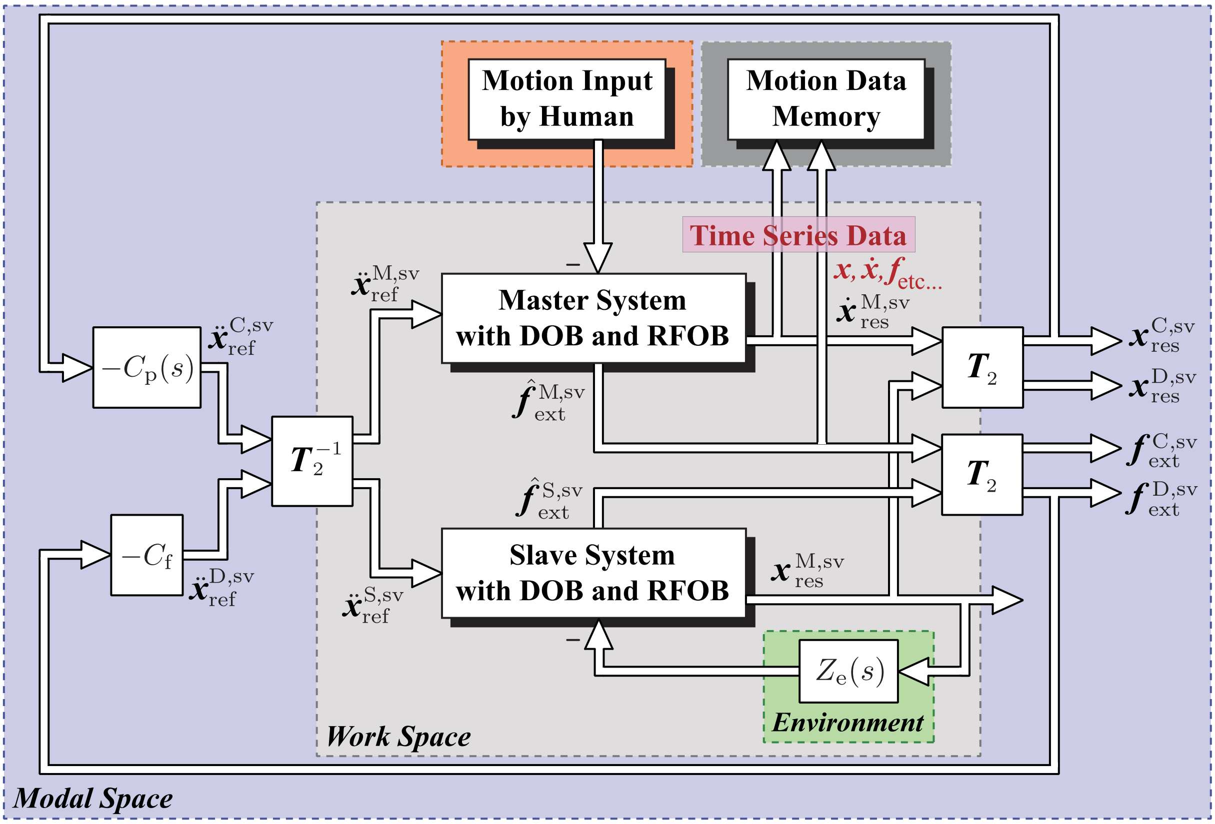

Fig. 5-17: Block diagram of motion-saving system.

where $\boldsymbol{x}$ and $\boldsymbol{F}$ denote the position vector and force vector on the Cartesian coordinate, respectively. This dissertation discusses about the motion in the work space. In order to achieve the control goals (5.17) and (5.18), the systems are controlled in the modal space. There are two modes in the modal space: common mode and differential mode. Transformation to the modal space from the work space is calculated by transformation matrix $\boldsymbol{T}$ as follows:

$$\boldsymbol{T}_2 = \frac{1}{2}\begin{bmatrix} \boldsymbol{I} & \boldsymbol{I} \\ \boldsymbol{I} & -\boldsymbol{I} \end{bmatrix}, \tag{5.19}$$

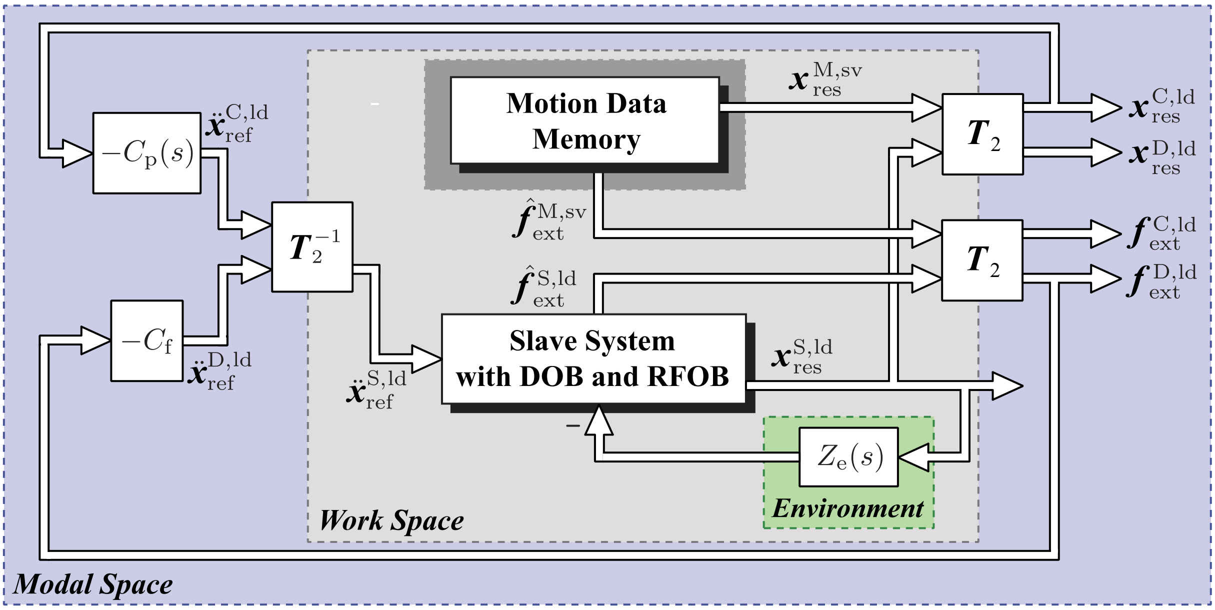

Fig. 5-18: Block diagram of motion-loading system.

where $\boldsymbol{I}$ is the unit matrix. By using the transformation matrix, the position and force information are transformed to modal space shown as:

$$\begin{bmatrix} \boldsymbol{x}_{\mathrm{res}}^{\mathrm{C,sv}} \\ \boldsymbol{x}_{\mathrm{res}}^{\mathrm{D,sv}} \end{bmatrix} = \boldsymbol{T}_2 \begin{bmatrix} \boldsymbol{x}_{\mathrm{res}}^{\mathrm{M,sv}} \\ \boldsymbol{x}_{\mathrm{res}}^{\mathrm{S,sv}} \end{bmatrix}, \tag{5.20}$$

$$\begin{bmatrix} \boldsymbol{f}_{\mathrm{ext}}^{\mathrm{C,sv}} \\ \boldsymbol{f}_{\mathrm{ext}}^{\mathrm{D,sv}} \end{bmatrix} = \boldsymbol{T}_2 \begin{bmatrix} \hat{\boldsymbol{f}}_{\mathrm{ext}}^{\mathrm{M,sv}} \\ \hat{\boldsymbol{f}}_{\mathrm{ext}}^{\mathrm{S,sv}} \end{bmatrix}. \tag{5.21}$$

The position value is controlled by position regulator. The force value is controlled by force servoing. These controllers are described as follows:

$$\ddot{\boldsymbol{x}}_{\mathrm{ref}}^{\mathrm{C,sv}} = C_f \boldsymbol{f}_{\mathrm{ext}}^{\mathrm{C,sv}}, \tag{5.22}$$

$$\ddot{\boldsymbol{x}}_{\mathrm{ref}}^{\mathrm{D,sv}} = \left(K_{\mathrm{p}} + \frac{s g_{\mathrm{pd}}}{s + g_{\mathrm{pd}}} K_{\mathrm{d}}\right) \boldsymbol{x}_{\mathrm{res}}^{\mathrm{D,sv}}, \tag{5.23}$$

where C_f, K_p, g_{pd} and K_d express the force gain, proportional gain, cut-off frequency of derivative and derivative gain of position regulator, respectively. The subscript ref represents reference value. By using these controllers, the acceleration reference values can be calculated in the modal space. The reference

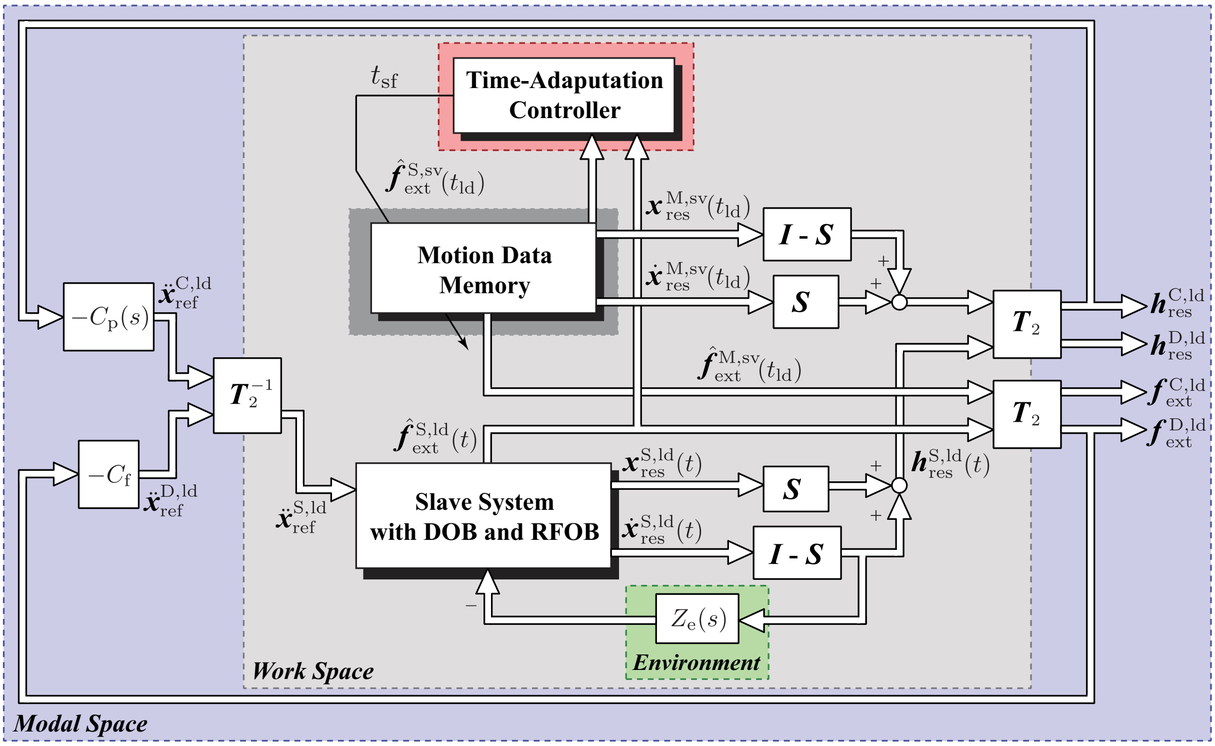

Fig. 5-19: Block diagram of motion-loading system with time adaptation.

values of acceleration in work space are calculated by the inverses transformation matrix as follows:

$$\begin{bmatrix} \ddot{\boldsymbol{x}}^{\mathrm{M,sv}}_{\mathrm{res}} \\ \ddot{\boldsymbol{x}}^{\mathrm{S,sv}}_{\mathrm{res}} \end{bmatrix} = \boldsymbol{T}_2^{-1} \begin{bmatrix} \ddot{\boldsymbol{x}}^{\mathrm{C,sv}}_{\mathrm{res}} \\ \ddot{\boldsymbol{x}}^{\mathrm{D,sv}}_{\mathrm{res}} \end{bmatrix}. \tag{5.24}$$

Accordingly, the bilateral control is achieved. The block diagram of the motion saving in an MDOF system is shown in Fig. 5-17. In Fig. 5-17, $Z_{\mathrm{e}}(s)$ stands for environmental impedance. In the motion-saving system, time-series data are stored as the human's motion data: such as position, velocity and force information.

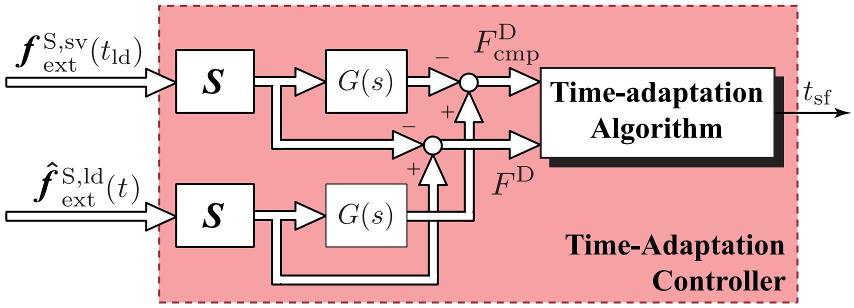

Fig. 5-20: Block diagram of time-adaptation control.

5.4.2 Motion Loading in MDOF System

In the motion-loading system, only the slave system is used. The master system is replaced by saved human's data. The control goals of the motion loading are expressed by

$$\boldsymbol{x}_{\rm res}^{\rm S,sv}(t_{\rm ld}) - \boldsymbol{x}_{\rm res}^{\rm S,ld}(t_{\rm ld}) = 0, \tag{5.25}$$

$$-\boldsymbol{f}_{\rm ext}^{\rm S,sv}(t_{\rm ld}) + \hat{\boldsymbol{f}}_{\rm ext}^{\rm S,ld}(t_{\rm ld}) = 0, \tag{5.26}$$

$$t_{\rm ld} - t = 0. \tag{5.27}$$

Here, $t_{\rm ld}$ denotes as (5.14). The block diagram of the motion loading in an MDOF system is shown in Fig. 5-18.

5.4.3 Time-adaptation Control in MDOF System

Then, the time-adaptation control in an MDOF system is proposed. The control goals of the time-adaptation control in an MDOF are as

$$\boldsymbol{S}\dot{\boldsymbol{x}}_{\rm res}^{\rm S,sv}(t_{ld}) - \boldsymbol{S}\dot{\boldsymbol{x}}_{\rm res}^{\rm S,ld}(t) = 0, \tag{5.28}$$

$$(\boldsymbol{I}-\boldsymbol{S})\boldsymbol{x}_{\rm res}^{\rm S,sv}(t_{ld}) - (\boldsymbol{I}-\boldsymbol{S})\boldsymbol{x}_{\rm res}^{\rm S,ld}(t) = 0, \tag{5.29}$$

$$-\boldsymbol{S}\boldsymbol{f}_{\rm ext}^{\rm S,sv}(t_{ld}) + \boldsymbol{S}\hat{\boldsymbol{f}}_{\rm ext}^{\rm S,ld}(t) = 0, \tag{5.30}$$

$$t_{\rm ld} - t = 0, \tag{5.31}$$

where $\boldsymbol{v}$ and $\boldsymbol{S}$ denote the velocity vector and selection matrix. When the environment location is changed from the saved one, the normal direction force on the environment contact surface is important. The selection matrix is designed as a diagonal matrix so that elements are more than zero less than

1. Because the importance is different by each axis, it is necessary to define this selection matrix. When an element is set to zero, this axis controls the position information. On the contrary, when a element is set to 1, this axis control the velocity information. Namely, this element stands for the axis that the force is important for contact task. Therefore, the force information on this axis is used for calculating the shift time. In the case of the calligraphy robot shown in Fig. 5-16, the most important thing is Z-axis force. Therefore, the selection matrix is designed as follows:

$$\boldsymbol{h} = \begin{bmatrix} h_x \\ h_y \\ h_z \end{bmatrix} = \boldsymbol{S} \begin{bmatrix} \dot{x}_x \\ \dot{x}_y \\ \dot{x}_z \end{bmatrix} + (\boldsymbol{I} - \boldsymbol{S}) \begin{bmatrix} x_x \\ x_y \\ x_z \end{bmatrix}, \tag{5.32}$$

$$\boldsymbol{S} = \begin{bmatrix} 0 & 0 & 0 \\ 0 & 0 & 0 \\ 0 & 0 & 1 \end{bmatrix}, \tag{5.33}$$

where $\boldsymbol{h}$ denotes the vector of spatial-hybrid value. The subscripts x, y and z express X-axis value, Y-axis value, and Z-axis value, respectively. By using the selection matrix $\boldsymbol{S}$, arbitrary time-adaptation control can be achieved in an MDOF system. The block diagram of the motion-loading system with time-adaptation in an MDOF system is shown in Fig. 5-19. The block diagram of time-adaptation controller in an MDOF system is shown in Fig. 5-20.

5.4.4 Experiments in MDOF System

In order to verify the validity of the proposed method, experiments are conducted. In the experiments, the hitting task was conducted. In the case of the hitting task, the force of Z-axis and the position of X-Y plane are important. Therefore, the selection matrix (5.33) can be designed same with the calligraphy task.

Experimental Setup in MDOF System

Fig. 5-21 shows the experimental setup in the MDOF system. Maseter and slave systems have three degrees of freedom. Z axis movement is achieved by a linear motor. X-Y plane movement is achieved by parallel-link mechanism and two direct-drive motors. The transformation from the joint plane to the work plane is calculated by direct kinematics and Jacobian matrix expressed by

$$\boldsymbol{x} = \boldsymbol{G}(\boldsymbol{q}), \tag{5.34}$$

$$\boldsymbol{f} = \boldsymbol{J}_{aco}^{-T} \boldsymbol{\tau}, \tag{5.35}$$

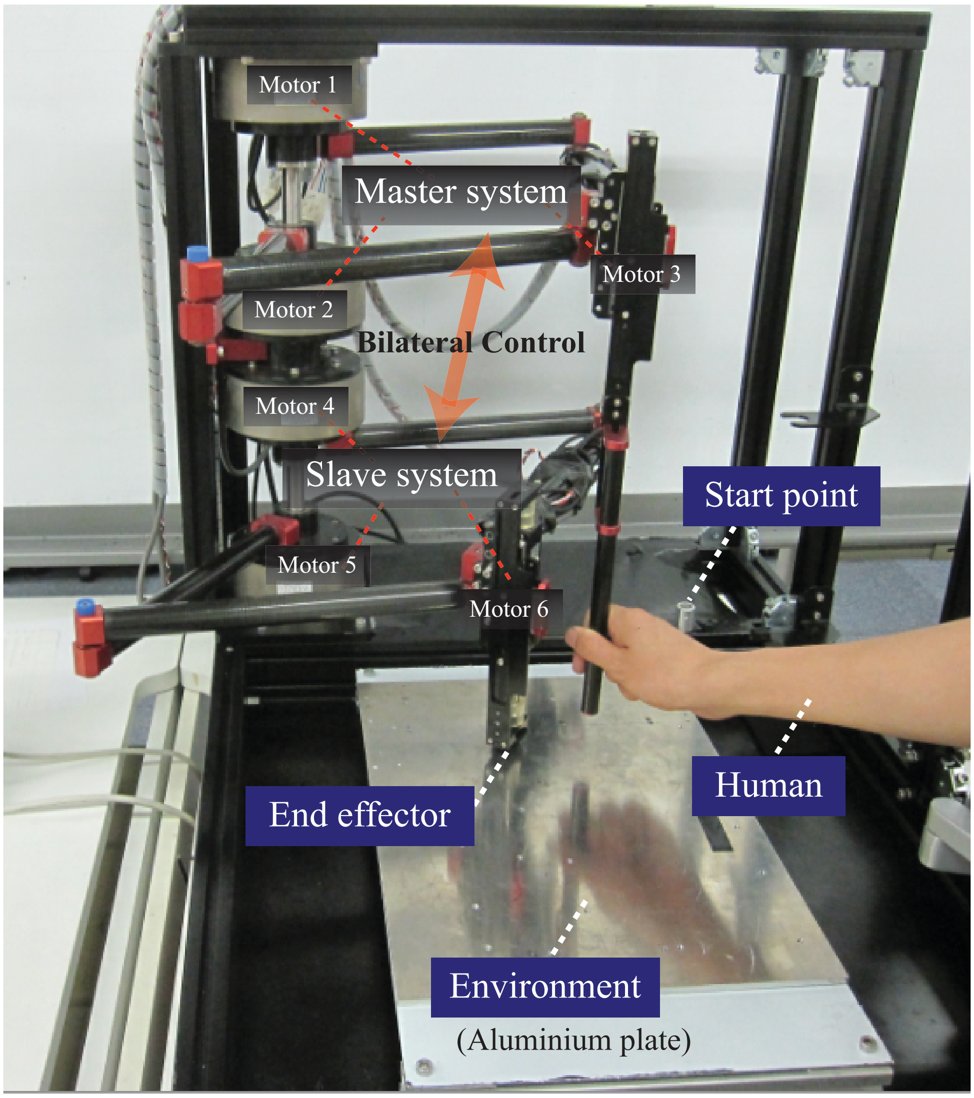

Fig. 5-21: Experimental setup of MDOF system.

where $\boldsymbol{q}$ and $\boldsymbol{\tau}$ denote the angle-information vector and torque vector, respectively. As the end effector, a rubber (Fig. 5-22) is set at the front end of the Z-axis on the slave system. In this experiment, contact motion is saved as shown in Fig. 5-23. During the experiments, the slave system contacts to the environment three times. At the first contact, soft pushing is saved. At the second, hard pushing is conducted. Finally, fluctuation contact is input. Parameters of the time-adaptation control in the MDOF system are shown in Table 5.4.

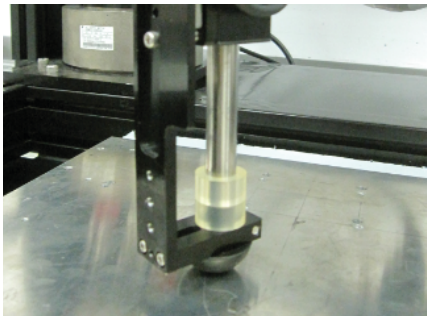

Fig. 5-22: End effector for experiment of MDOF system.

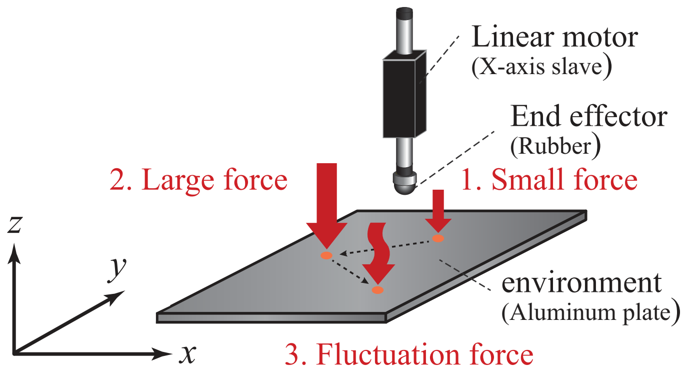

Fig. 5-23: Procedure of contact in MDOF system.

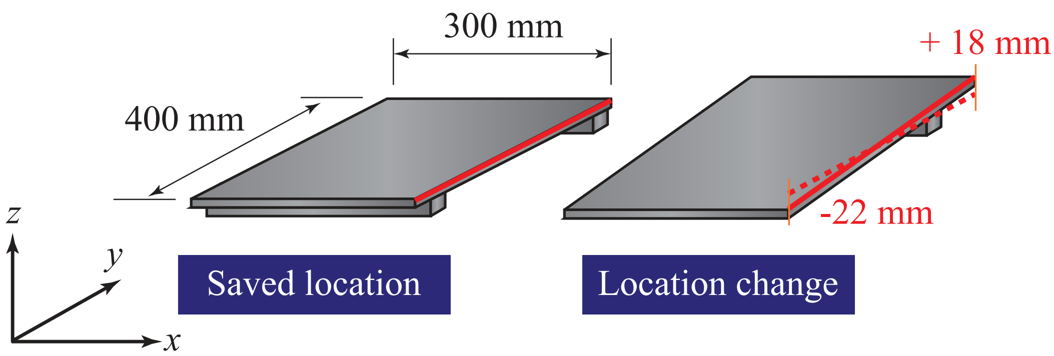

Fig. 5-24: Environmental location in experiments of MDOF system.

Experimental Results in MDOF System

The motion loading are conducted with the saved data that is described above. In these experiments, two situations are compared; one is that the environment is located at the same place as the saved phase,

Table 5.4: Parameters of the time-adaptation control in MDOF system.

Parameters	Descriptions	Value
K_{p}	Proportional gain	10000
K_{d}	Differential gain	200
C_{f}	Force gain	3.5
g_{dis}	Cut-off frequency of the DOB	100 rad/s
g_{reac}	Cut-off frequency of the RFOB	100 rad/s
g_{t}	Cut-off frequency of time-adaptation (Master)	5000 rad/s
F_{th}	Threshold of time-adaptation controller	0.4 N
a	Hysteresis coefficient	0.5

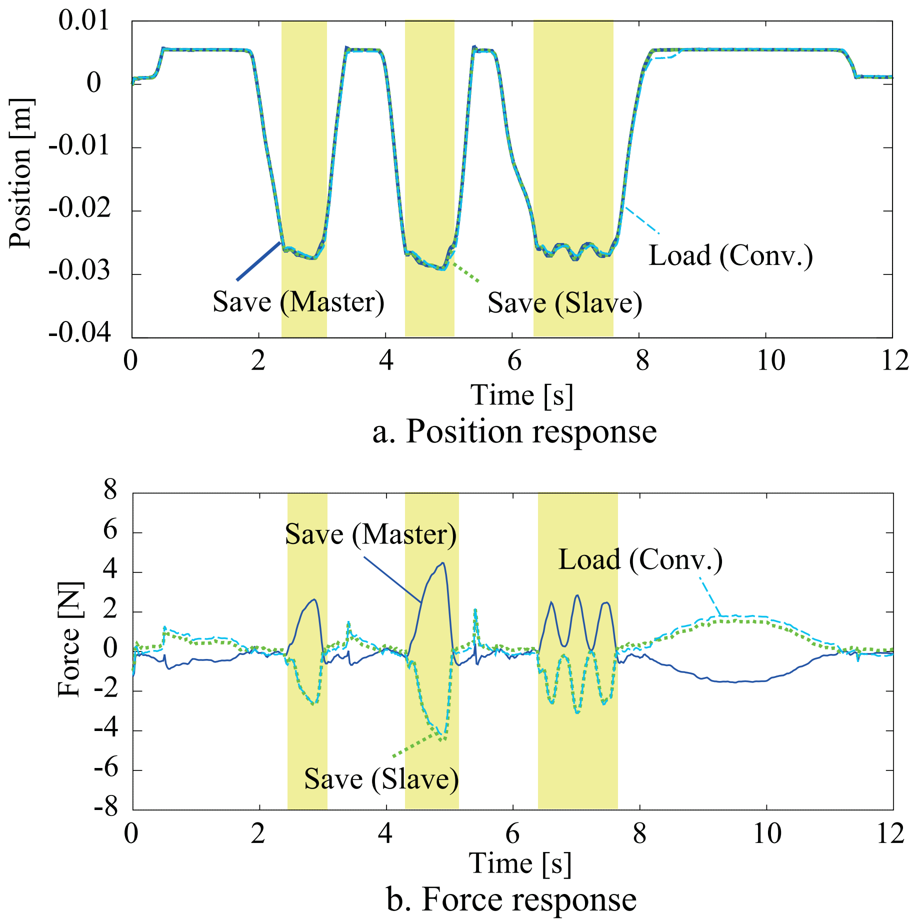

Fig. 5-25: Experimental results in same location with the conventional method.

and the other is the case where the location is inclined. These locations are shown in Fig. 5-24. Also, two control methods are compared; position-based motion loading as the conventional method and the

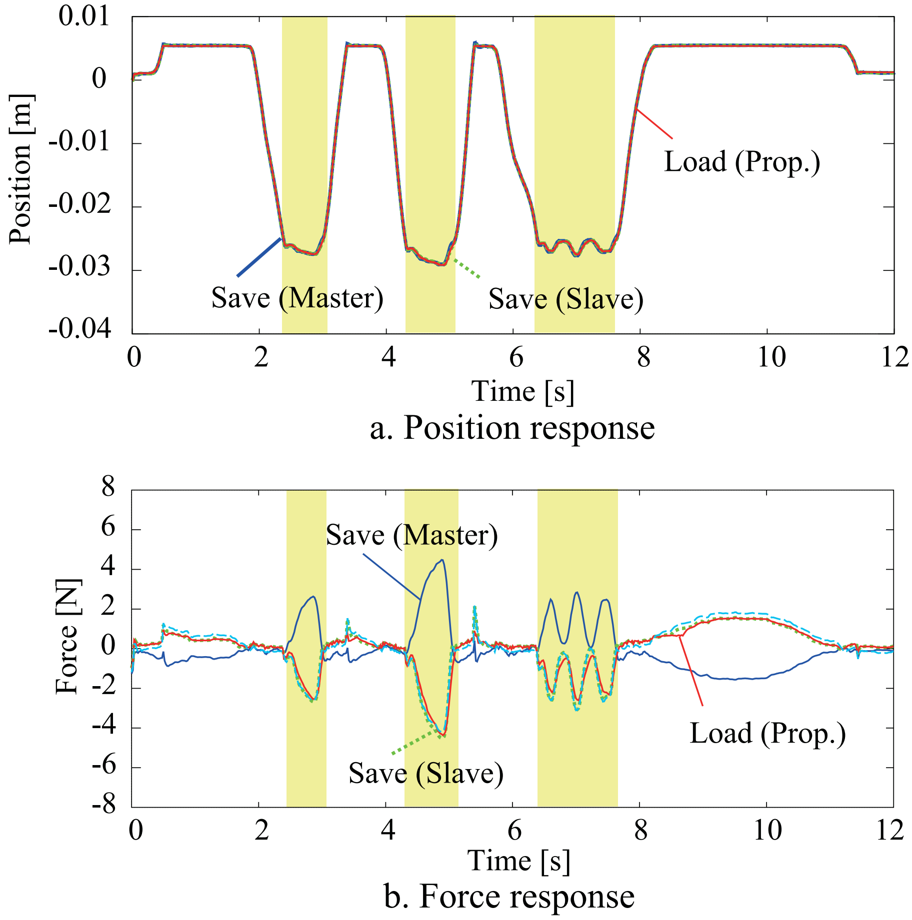

Fig. 5-26: Experimental results in same location with the proposed method.

proposed method. Figs. 5-25 to 5-28 show the experimental results. In the case of same location, position and force errors are very small, then precise tack can be reproduced. From this figure, it can be confirmed that good results can be obtained in any method. On the other hand, the result in the case of different location from saved mode is discussed in the following. In this case, it turns out that the conventional method has large force error. Fig. 5-30 shows the comparison of force waveform. At the first contact, large reaction force is generated from environment, because the actuator tries to push the environment even after contact. Conversely, the actuator cannot reach to the environment at the third contact, because the contact surface is further than the saved one. Fig. 5-29 shows the time-shift response. In the proposed method, force waveform is same as the saved shape, therefore it is confirmed that the accurate contact motion was achieved.

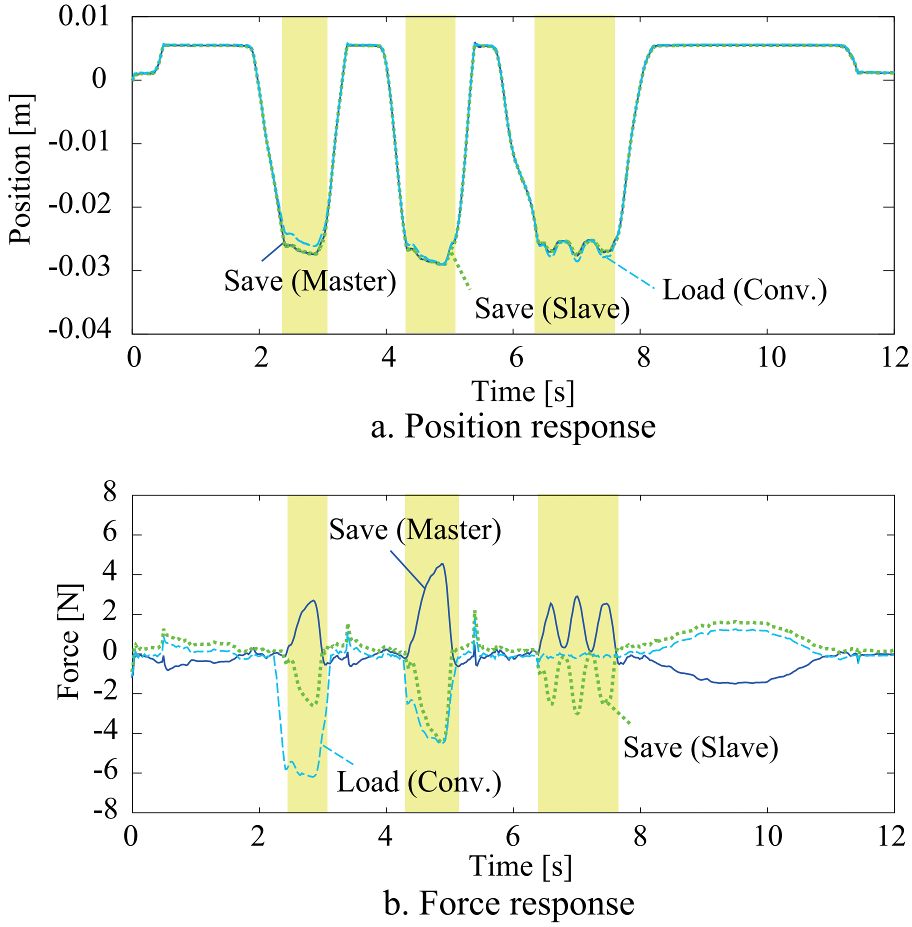

Fig. 5-27: Experimental results in different location with the conventional method.

5.5 Summary of Chapter 5

In Chapter 5, the time-adaptation control for motion reproduction was proposed for adapting to variations of environmental location. The proposed method has the highest priority on eliminating force error, and the reproducibility of the contact motion was improved. By using the propose method for manufacturing site, objects will be processed by the same force even when the location of environment is different. Thus, improvement of productivity is expected. Firstly, the validity of the proposed time-adaption control was confirmed in the SDOF system. Then, the time-adaption control was expanded to the MDOF system. In order to decide the most important information for target task, the select matrix was designed in the MDOF system.

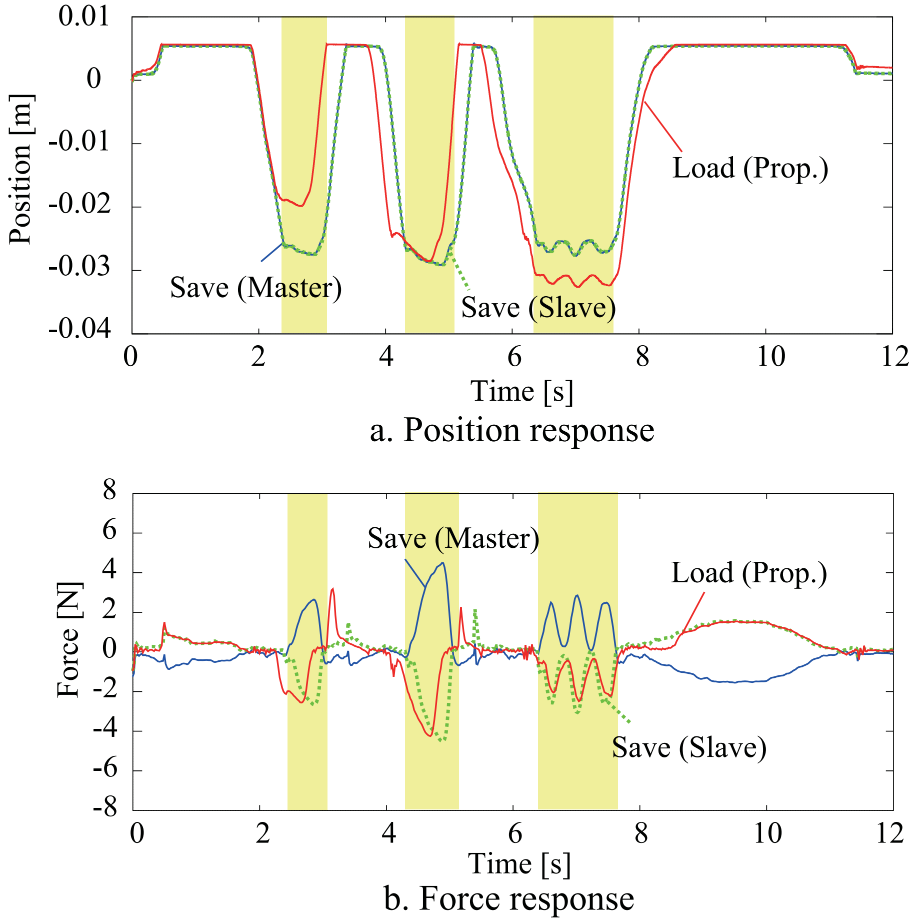

Fig. 5-28: Experimental results in different location with the proposed method.

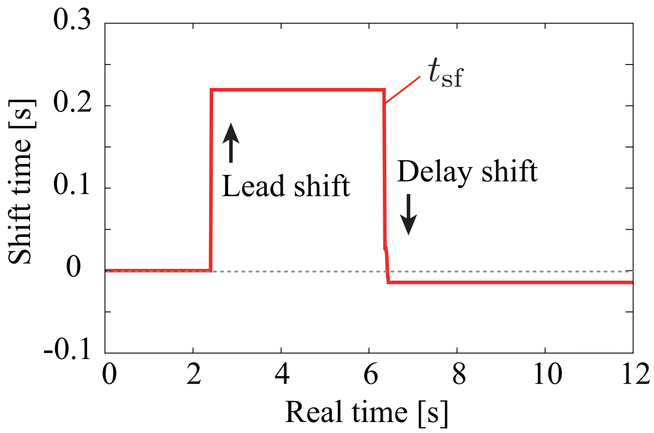

Fig. 5-29: Time-shift response.

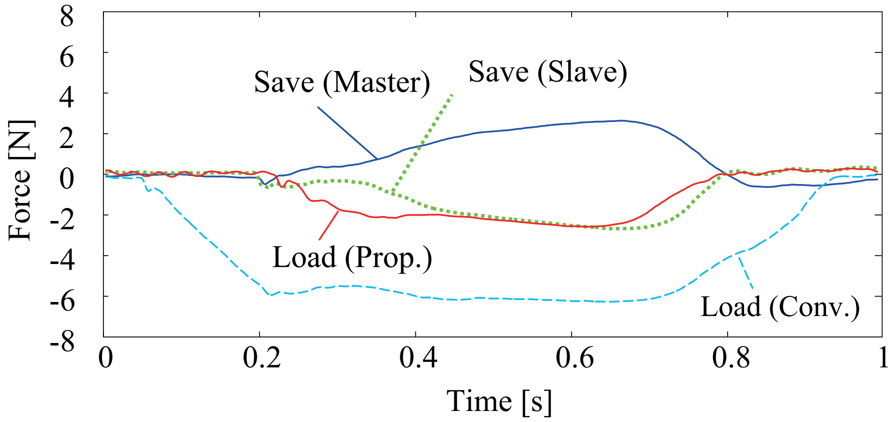

a. First contact

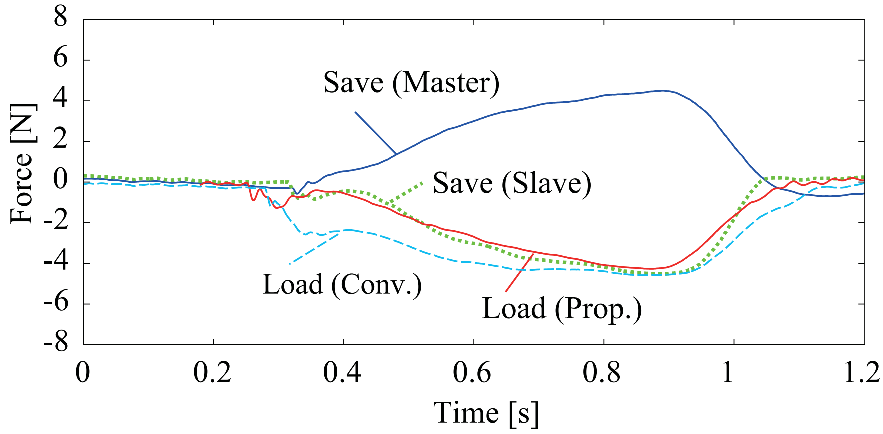

b. Second contact

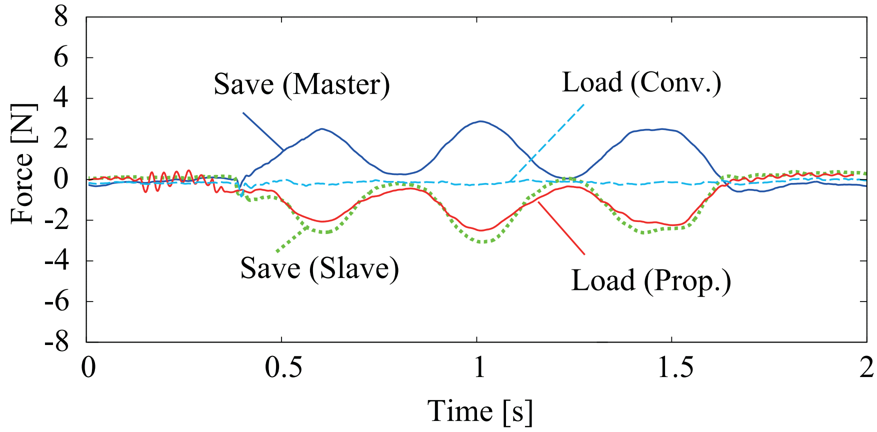

c. Third contact

Fig. 5-30: Comparison of force waveform.

Chapter 6

Knowledge Abstraction Based on Element Description Method

6.1 High-accuracy Powder Filling Control Based on the EDM

6.1.1 Powder Filling Machine

In our lives, a wide variety of powders are distributed in various fields such as foods, medicines and paints. “Filling technology” is required to fill a container with a predetermined amount of powder when flowing powder. In the food industry, when delivering powder, the content amount is specified in the package and it is necessary to fill the contents so that it is not less than the content amount. Inevitably, variations occur in the filling amount of the powder. Therefore, when filling is performed, the average filling amount is set to be larger by taking the variation into consideration. In recent years there has also been a background of rising raw material costs, etc. In order to reduce the overfilling amount, improvement of filling accuracy is strongly desired. Various powders are also used as raw materials for industrial products, and when the filling amount of powder varies at the time of manufacture, the quality of the product changes, and therefore high-precision powder filling technology is required. In this chapter, for the purpose of improving the filling accuracy in an auger-type powder filling machine, visualization of the powder physical properties and control based thereon were carried out.

Structure of Auger-type Powder Filling Machine

The structure of an auger-type powder filling machine is shown in Fig. 6-1. The auger-type filling machine is a device which encloses a spiral screw (auger) with a casing called funnel and discharges powder and granular material by rotational movement of the auger. The agitator is a device which agitates the powder in the hopper and promotes the entry of the powder into the auger while keeping the state of the powder as uniform as possible. The high-speed agitator rotates synchronously with the auger by the auger motor and the low-speed agitator is structured to be able to rotate independently by the low-speed agitator motor. In general, the charged amount of the powder is set by the rotation amount of the auger and is driven by position control in accordance with a predetermined angle, angular velocity, and angular acceleration designed in advance. However, with respect to powder, the physical properties of the powder change gradually due to various factors such as difference in such as changes in external environments, variations of physical properties of raw materials, and daily differences of manufacturing processes. Since the filling amount varies depending on the change, the sensory evaluation by a skilled worker and the fine adjustment of the machine parameters based on it are required at present. Although a method has been proposed in which the fluidity index and the floodability index are calculated from powder parameters such as angle of repose, angle of spatula, degree of agglomeration and degree of compression, and the state of powder is quantitatively grasped based on the index. Since it takes time to perform one measurement, it is difficult to grasp the powder physical properties that change from moment to moment, and the current situation is generally used for powder quality control and the like. In this dissertation, powder physical properties based on force information during powder filling is measured, and improved control of powder-filling accuracy by performing control based on it is proposed.

In general, the charged amount of the powder is set by the rotation amount of the auger and is driven by position control in accordance with angle, angular velocity, and angular acceleration designed in advance. This is the control based on the premise that the state of the powder is always constant. However, with respect to powder, the physical properties of the powder change gradually due to various factors such as difference in such as physical properties of raw materials, change in external environment, and variation in manufacturing process. Hence, the sensory evaluation by a skilled technician and the fine adjustment of the machine parameters based on it are required at present. There is also a method of feeding back the weight in real time, and by using this method, it is possible to fill the powder with high accuracy. However, since it takes time to perform one filling operation, the production speed becomes

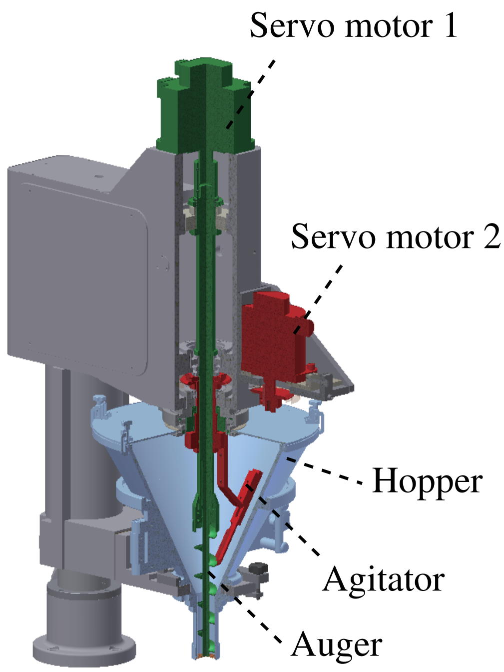

Fig. 6-1: Structure of auger-type powder filling machine.

slow. Therefore, in this dissertation, a new method to estimate the state of the powder and control the rotation amount of the motor is proposed. By using the proposed method, filling accuracy can be improved without decreasing production speed.

6.1.2 Visualization of Powder Loading

Detection of Powder Load Torque

When extracting the load of the powder with the auger-type powder filling machine, the sensing by the force sensor or the torque sensor increases the risk of contamination, which is undesirable. Therefore, in this research, the load torque estimation is performed by using the RFOB. Since the RFOB does not need to use an additional sensor, it is possible to extract the powder load information without increasing the risk of contamination. The external torque for the auger motor and the low-speed agitator motor is calculated as

$$\tau_{\mathrm{ext}} = \tau_{\mathrm{l}} + \tau_{\mathrm{fric}} + \tau_{\mathrm{v}}, \tag{6.1}$$

where $\tau_{\rm ext}$, $\tau_{\rm l}$, $\tau_{\rm fric}$, and $\tau_{\rm v}$ represent the external torque, load torque, friction torque, viscous torque, respectively. The auger-type powder filling machine is sealed to the shaft so as to prevent entry of powder into the motor section and mixing of grease in the motor section into the powder. Therefore, friction torque and viscous torque are generated, which affects the powder load torque estimation accuracy. In order to implement the RFOB with high accuracy, it is necessary to estimate the values of $\tau_{\rm l}$ and $\tau_{\rm v}$ with high accuracy. Therefore, the DOB was implemented on the auger-type powder filling machine, and the disturbance estimated value in free motion without powder in the hopper, the friction torque, viscous torque was identified by the following model

$$\hat{\tau}_{\rm fric} = A{\rm sgn}(\omega), \tag{6.2}$$

$$\hat{\tau}_{\rm v} = D_{\rm m}\omega. \tag{6.3}$$

Based on this identification result, it is possible to calculate the compensation value $\hat{\tau}_{\rm l}$ and $\hat{\tau}_{\rm v}$ of the RFOB. The block diagram of the RFOB is as shown in Fig. 2-28.

6.1.3 High Precision Filling Control Based on Powder Physical Properties

The amount of powder charged in the auger-type powder filling machine is expressed as

$$W_{\rm p} = \eta\rho\int_0^T \omega_{\rm res}dt \times \pi(D-d)^2(H-h), \tag{6.4}$$

where $W_{\rm p}$, η, ρ, ω, D, d, H, and h represent the filling amount g, filling efficiency, powder density ${\rm g/m^3}$, funnel inner diameter m, auger inner diameter m, auger pitch m, flight thickness m, respectively. Since D, d, and H are the fixed parameters, ω and T are the configuration parameters variations in filling amount are caused by the nominal errors of η and ρ. In other words, to improve the filling accuracy, it is found that it is a problem to design ω and T which estimates the nominal errors of η and ρ, and cancels them. Here, the product of η and ρ are defined as filling coefficient K.

$$K \triangleq \eta\rho. \tag{6.5}$$

Then, D, d, H, and h can be summarized as follows:

$$V \triangleq \pi(D-d)^2(H-h), \tag{6.6}$$

where $V\mathrm{m}^3$ refer to the output volume per auger revolution. From the above equations, (6.4) can be simplified using the filling coefficient K as follows:

$$W_{\mathrm{p}} = VK\int_0^T \omega_{\mathrm{res}}dt = VK\theta_n. \tag{6.7}$$

Since D, d, H, and h are the fixed machine parameters, ω and T are set parameters, V and θ_{n} rad are known parameters. In other words, it can be seen that the variation of the filling amount W occurs due to an error between the nominal value of K and the actual value as follows:

$$W_{\mathrm{p}} + \Delta W = V(K_{\mathrm{n}} + \Delta K)\theta_n, \tag{6.8}$$

where K_{n} and ΔK represent the nominal values and error value of the filling coefficient, respectively. Therefore, in order to improve the filling accuracy, it is necessary to estimate the error ΔK and calculate the corrected amount of rotation $\Delta\theta$ rad. The compensation calculation is expressed as

$$W_{\mathrm{p}} = V(K_{\mathrm{n}} + \Delta K)(\theta_n + \Delta\theta). \tag{6.9}$$

By modifying the equation (6.9), the corrected amount of rotation is derived as follows:

$$\Delta\theta = \frac{\Delta K}{K_{\mathrm{n}} + \Delta K}\theta_{\mathrm{n}}. \tag{6.10}$$

Therefore, filling control with high accuracy can be achieved by predicting the error of the filling coefficient.

6.1.4 High-precision Filling Control Based on Regression Analysis

Single regression analysis

Firstly, as a method of predicting the filling coefficient, a method based on a single regression analysis is explained. As an example, a single regression analysis using agitator torque information τ_{aji} is described here. The estimation formula of the filling coefficient K using the agitator torque τ_{aji} as an explanatory variable is shown as

$$\hat{K} = \hat{\beta}_1\tau_{\mathrm{aji}} + \hat{\beta}_0, \tag{6.11}$$

where β_1 and β_0 are the slope and DC component of the regression line, respectively. The regression line is calculated from the time series data of τ_{aji} and V by calculating the filling coefficient V_i from the auger rotation amount θ_i at the time of filling and the filling amount W_i. The regression coefficients are calculated as

$$\begin{aligned} \hat{\beta}_1 &= \frac{S_{xy}}{S_{xx}}, && (6.12) \\ S_{xy} &= \sum_{i=1}^{N}(x_i - \bar{x})(y_i - \bar{y}), && (6.13) \\ S_{xx} &= \sum_{i=1}^{N}(x_i - \bar{x})^2, && (6.14) \\ \hat{\beta}_0 &= \bar{y} - \hat{\beta}_1\bar{x}, && (6.15) \end{aligned}$$

where N, x, y, S_{xy}, and S_{xx} denote the number of data, an explanatory variable , the objective variable, the covariance of τ_{aji} and K, and the variance of τ_{aji}, respectively. In this case, x and y refer to τ_{aji} and V, respectively. By substituting $\Delta K = K_{\mathrm{n}} - \hat{K}$ into (6.10) expression, the corrected rotation amount is obtained.

Multiple Regression Analysis

By extending the above-mentioned method to multivariate and performing correction by multiple regression analysis, further improvement in filling accuracy is expected. Assuming that the number of parameters used for multiple regression analysis is p, the estimation of the filling coefficient K by multiple regression analysis is as follows:

$$\hat{K} = \sum_{j=1}^{p}\hat{\beta}_j x_j + \hat{\beta}_0. \tag{6.16}$$

Here, $\hat{\beta}_j$ and x_j represent the partial regression coefficients and explanatory variables, respectively. Firstly, the covariance matrix of each parameter is derived.

$$\boldsymbol{S} = \begin{pmatrix} S_{11} & S_{12} & \cdots & S_{1p} & S_{1y} \\ S_{21} & S_{22} & \cdots & S_{2p} & S_{2y} \\ \vdots & \vdots & \ddots & \vdots & \vdots \\ S_{p1} & S_{p2} & \cdots & S_{pp} & S_{py} \\ S_{y1} & S_{y2} & \cdots & S_{yn} & S_{yy} \end{pmatrix}, \tag{6.17}$$

$$S_{jj} = \sum (x_{ji} - \bar{x}_j)^2, \tag{6.18}$$

$$S_{jk} = S_{kj} = \sum (x_{ji} - \bar{x}_j)(x_{ki} - \bar{x}_k), \tag{6.19}$$

$$S_{yy} = \sum (y_i - \bar{y})^2, \tag{6.20}$$

$$S_{jy} = S_{yj} = \sum (x_{ji} - \bar{x}_j)(y_i - \bar{y}). \tag{6.21}$$

By using the inverse matrix of the covariance matrix, the partial regression coefficients are derived as follows:

$$\begin{pmatrix} \hat{\beta}_1 \\ \hat{\beta}_2 \\ \vdots \\ \hat{\beta}_p \end{pmatrix} = \boldsymbol{S}^{-1} \begin{pmatrix} S_{1y} \\ S_{2y} \\ \vdots \\ S_{py} \end{pmatrix}, \tag{6.22}$$

$$\hat{\beta}_0 = \bar{y} - \sum_{j=1}^{p} \hat{\beta}_{\mathrm{n}} \bar{x}_{\mathrm{n}}. \tag{6.23}$$

Here, variable selection is made to increase the reliability of the regression equation. The variable reduction method is used for variable selection. The residual sum of squares of the regression equation S_e, the coefficient of determination R^2, and the unbiased variance V_e are calculated as follows:

$$S_e = \sum_{i=1}^{N} (K_i - \hat{K}_i)^2, \tag{6.24}$$

$$R^2 = 1 - \frac{S_e}{S_{yy}}, \tag{6.25}$$

$$V_e = \frac{S_e}{n - p - 1}. \tag{6.26}$$

The standard deviation and t value of the partial regression coefficient are

$$SE_j = \sqrt{S_{jj}^{-1} V_e}, \tag{6.27}$$

$$t_j = \frac{\hat{\beta}_j}{SE_j}. \tag{6.28}$$

Then, exclude the explanatory variable that minimizes $|t_j|$ from the explanatory variable, and derive the regression equation again. Repeat this process and finally finish the regression analysis when all $|t_j|$ becomes 2 or more. Estimate the filling factor using the regression equation at that time, and calculate increase/decrease time $\Delta\theta$.

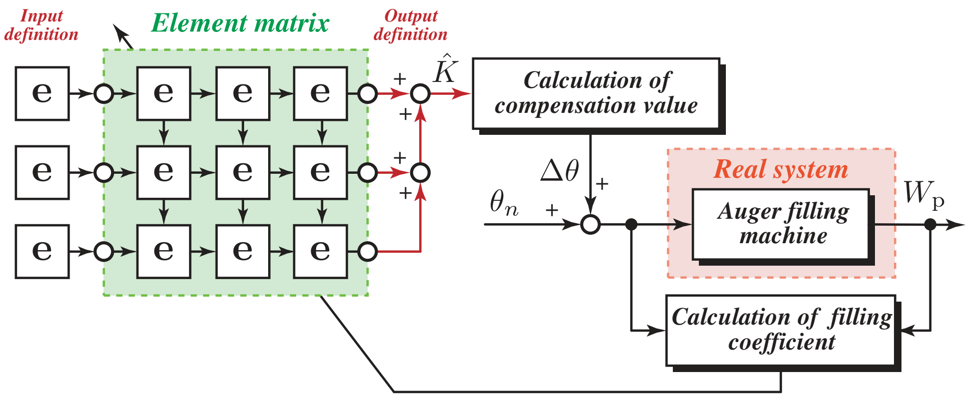

Fig. 6-2: Block diagram of high precision filling control based on the EDM.

6.1.5 High Precision Filling Control Based on the EDM

In this part, high precision powder filling based on the EDM is proposed. Fig. 6-2 depicts a block diagram of high precision filling control based on the EDM. In this control, time series data for each trial is handled. The input data to the element matrix are automatically selected from parameters related to powder filling. In this section, overall abstraction using multidirectional element matrix is applied. The sum of the outputs from the element matrix is treated as the estimated filling coefficient.

6.1.6 Experiments of Powder Filling

Experimental Machine

In order to confirm the validity of the proposed method, experiments are conducted. Fig. 6-4 shows the experimental setup. Soybean flour is used as a sample, and the target weight of filling is set 300 g. The method of extracting the state value used for predicting the filling coefficient will be described below. Parameters of the GA for powder filling system are shown in Table 6.1.

Load Torque of Powder

In order to extract load torque of the sample powder, the RFOB is implemented. Fig 6-3 shows the block diagram of the RFOB. $\hat{\tau}_{\mathrm{load}}$, $Q_2(s)$, D, and F_c refer to the load torque of powder, cut-off frequency of the low-pass filter for the RFOB, viscosity coefficient, and coulomb friction, respectively. Then, the maximum value of load torque $\tau_{\max}(N)$ and the mean value of load torque $\tau_{\mathrm{mean}}(N)$ are calculated as

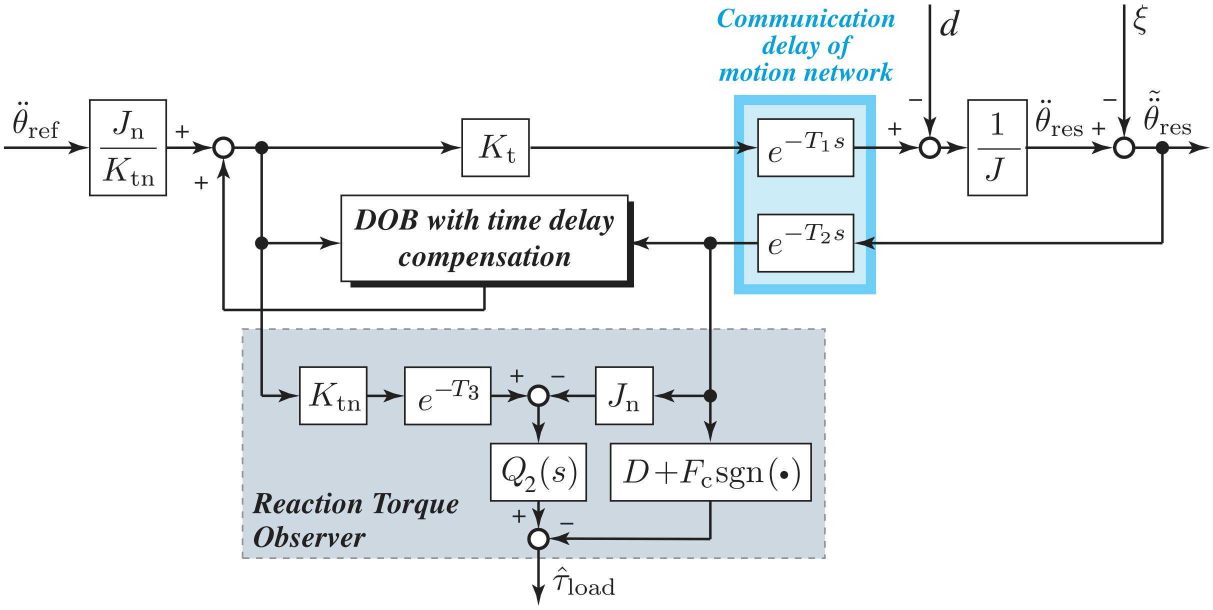

Fig. 6-3: Block diagram of the RFOB for powder filling machine.

follows:

$$N_{\mathrm{cyc}} \triangleq \frac{T_{\mathrm{cyc}}}{T_{\mathrm{s}}}, \tag{6.29}$$

$$\tau_{\max}(N) = \max_{N_{\mathrm{cyc}}N \leq n \leq N_{\mathrm{cyc}}(N+1)} \hat{\tau}_{\mathrm{load}}(T_{\mathrm{s}}n), \tag{6.30}$$

$$\tau_{\mathrm{mean}}(N) = \frac{1}{N_{\mathrm{cyc}}} \sum_{n=1}^{N_{\mathrm{cyc}}} \hat{\tau}_{\mathrm{load}}\{T_{\mathrm{s}}(N_{\mathrm{cyc}}N + n)\}, \tag{6.31}$$

where N_{cyc}, T_{cyc}, T_{s}, and N stand for the sampling number per one filling cycle, total time of one filling cycle, sampling time, and trial number of filling, respectively.

Viscosity and Equivalent Inertia of Powder

In this study, the viscous term and the inertia term of the powder is focused as powder physical properties that affect the filling accuracy. Based on the powder load torque estimated by the RFOB and the motor angle obtained from the encoder, the viscosity term and the inertia term of the powder were extracted using the recursive least squares method. The viscosity and equivalent inertia of powder are calculated using the angular velocity response and load torque. The relationship among the angular velocity, load torque, viscosity, and equivalent inertia are expressed as follows:

$$\tau_{\text{load}} = J_{\text{p}}\dot{\omega}_{\text{res}} + D_{\text{p}}\omega_{\text{res}}, \tag{6.32}$$

$$\boldsymbol{z} = [D_{\text{p}} \quad J_{\text{p}}]^T. \tag{6.33}$$

The recursive least square method was applied as follows to extract the above powder physical properties.

$$\boldsymbol{P}_{(k+1)} = \frac{1}{\mu}\left\{\boldsymbol{P}_{(k)} + \frac{\boldsymbol{P}_{(k)}\boldsymbol{m}_{(k+1)}\boldsymbol{m}^T_{(k+1)}\boldsymbol{P}_{(k)}}{\mu + m^T_{(k+1)}\boldsymbol{P}_{(k)}\boldsymbol{m}_{(k+1)}}\right\}, \tag{6.34}$$

$$\hat{\boldsymbol{z}}_{(k+1)} = \hat{\boldsymbol{z}}_{(k)} + \frac{\boldsymbol{P}_{(k)}\boldsymbol{m}_{(k+1)}}{\mu + m^T_{(k+1)}\boldsymbol{P}_{(k)}\boldsymbol{m}_{(k+1)}}\epsilon, \tag{6.35}$$

$$\epsilon = \tau_{\text{load(k+1)}} - \boldsymbol{m}^T_{(k+1)}\hat{\boldsymbol{z}}_{(k)}, \tag{6.36}$$

$$\boldsymbol{m}_{(k)} = [\omega_{\text{res(k)}} \quad \dot{\omega}_{\text{res(k)}}]^T, \tag{6.37}$$

where $\boldsymbol{P}$ and μ represent the coefficient matrix and forgetting factor, respectively. The recursive least squares method makes it possible to visualize successively varying powder physical properties, which was conventionally difficult. From time-series D_{p} and J_{p}, $D_{\text{max}}(N)$, $D_{\text{mean}}(N)$, $J_{\text{max}}(N)$, and $J_{\text{mean}}(N)$ are calculated using (6.30) and (6.31).

Start Angle and Rest Time

The start angle of auger and agitator in starting time is recorded. Also, break time from previous filling motion is saved. By the method described above, the following state variables are prepared.

$$\begin{aligned}\boldsymbol{x}^{\text{aug}}(N) = \Big[&\tau^{\text{aug}}_{\text{max}}(N)\ \tau^{\text{aug}}_{\text{mean}}(N)\ D^{\text{aug}}_{\text{max}}(N)\ D^{\text{aug}}_{\text{mean}}(N)\\ &J^{\text{aug}}_{\text{max}}(N)\ J^{\text{aug}}_{\text{mean}}(N)\ \theta^{\text{aug}}_{\text{ini}}(N)\ T^{\text{aug}}_{\text{rest}}(N)\Big]^T,\end{aligned} \tag{6.38}$$

$$\begin{aligned}\boldsymbol{x}^{\text{agi}}(N) = \Big[&\tau^{\text{agi}}_{\text{max}}(N)\ \tau^{\text{agi}}_{\text{mean}}(N)\ D^{\text{agi}}_{\text{max}}(N)\ D^{\text{agi}}_{\text{mean}}(N)\\ &J^{\text{agi}}_{\text{max}}(N)\ J^{\text{agi}}_{\text{mean}}(N)\ \theta^{\text{agi}}_{\text{ini}}(N)\Big]^T,\end{aligned} \tag{6.39}$$

where, $\boldsymbol{x}$, θ_{ini}, and T_{rest} express parameter vector, the start angle, and rest time, respectively. The super scripts aug and agi refer to the auger parameters and agitator parameters, respectively. The actual filling coefficient K is estimated from these parameters. In this study, constant rotation amount (13 rev.) as the conventional method 1, the filling coefficient prediction by multiple regression analysis (MRA) as the conventional method 2, and the filling coefficient prediction by the EDM as the proposed method are

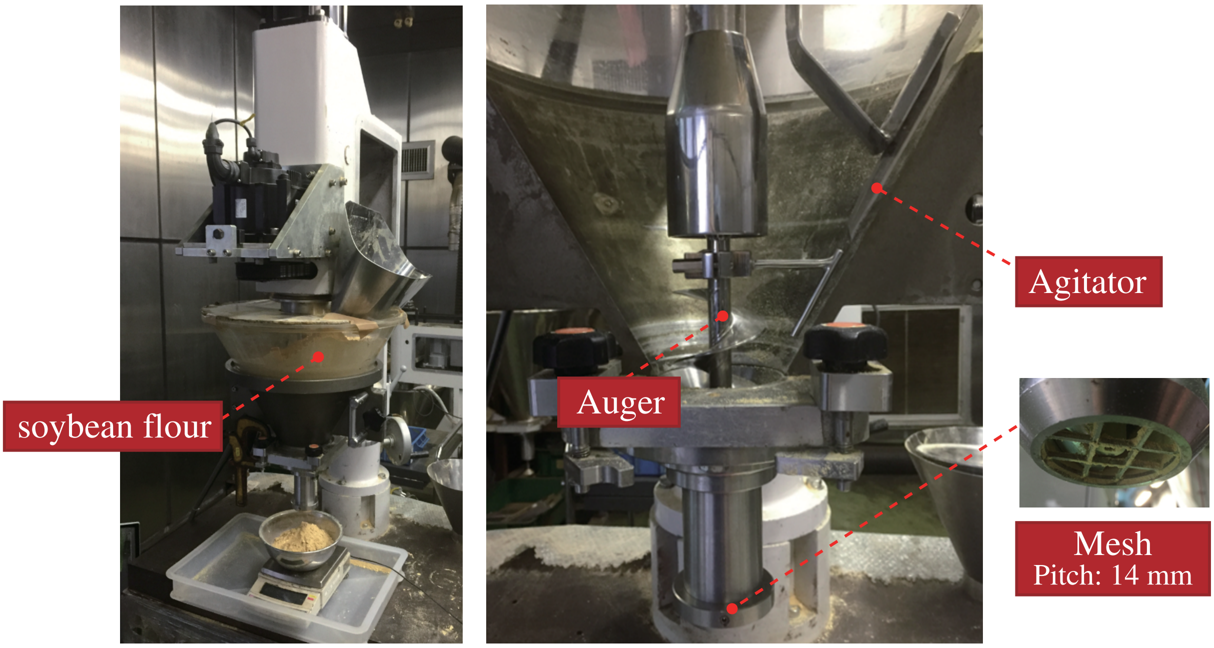

Fig. 6-4: Experimental machine.

Table 6.1: Parameters of the GA for powder-filling system.

Description	Value
Population size	8
Crossover rate	0.7
Mutation rate for element code	0.2
Mutation rate for element parameter	0.2

compared. The prediction equation is calculated using time-series data. Actual filling coefficient can be calculated after filling motion using revolution amount ans powder weight,

$$K(N) = \frac{W(N)}{\theta_{\mathrm{n}} V}. \tag{6.40}$$

6.1.7 Experimental Result of Powder Filling

The regression equation of the filling coefficient estimation by MRA was derived as follows:

$$\hat{K}(N) = 38.7\tau^{\mathrm{aug}}_{\mathrm{mean}}(N) - 0.002030\theta^{\mathrm{agi}}_{\mathrm{ini}}(N) + 20.0. \tag{6.41}$$

The explanatory variables were selected by Stepwise regression. Also, prediction equation of the filling coefficient by the EDM was estimated. The results of the optimization by the EDM is shown in Tables

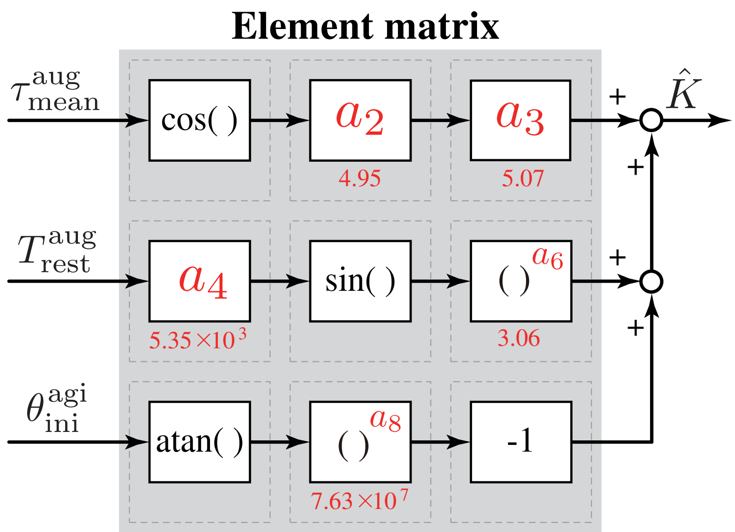

Fig. 6-5: Extracted model for powder filling machine by the EDM.

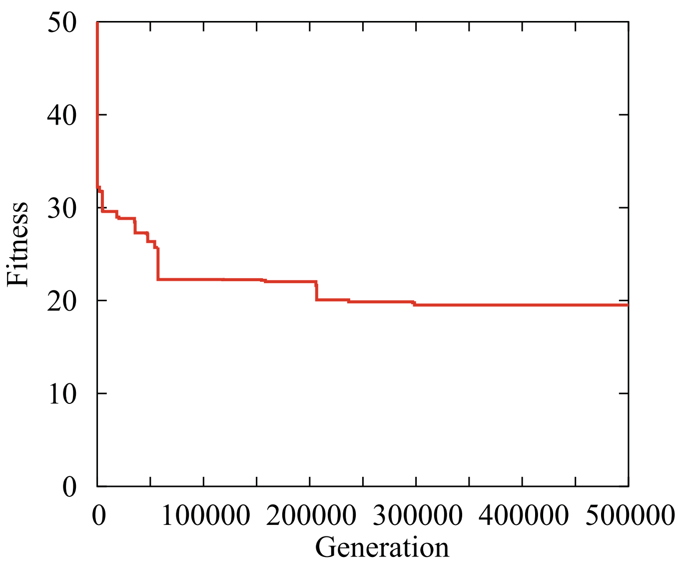

Fig. 6-6: Fitness response of the EDM for powder filling machine.

6.2. From these results, Fig. 6-5 is derived as prediction procedure. Fig. 6-6 shows fitness value response of the EDM. It can be seen that the fitness value decreases with the number of evolution.

Fig. 6-7 expresses comparison of filling weight. The mean value μ and the standard deviation σ are calculated from Fig. 6-7. Table 6.3 shows the comparison of filling accuracy estimation. From Table 6.3, it can be seen that standard deviation of the proposed method is the smallest in these methods. Therefore, the validity of the proposed method was confirmed.

Table 6.2: Abstraction results of powder filling system.

$\tau_{\mathrm{mean}}^{\mathrm{aug}}$ Mean torque (auger)	**COS** Cosine wave –	**P** Gain $a_2 = 4.95$	**P** Gain $a_3 = 5.07$
T_{rest} Rest time	**P** Gain $a_4 = 5.35 \times 10^3$	**SIN** Sine wave –	**POW** Power $a_6 = 3.06$
$\theta_{\mathrm{ini}}^{\mathrm{agi}}$ Initial angle (agitator)	**TANH** Hyperbolic tangent –	**POW** Power $a_8 = 7.63 \times 10^7$	**IN** Invert –

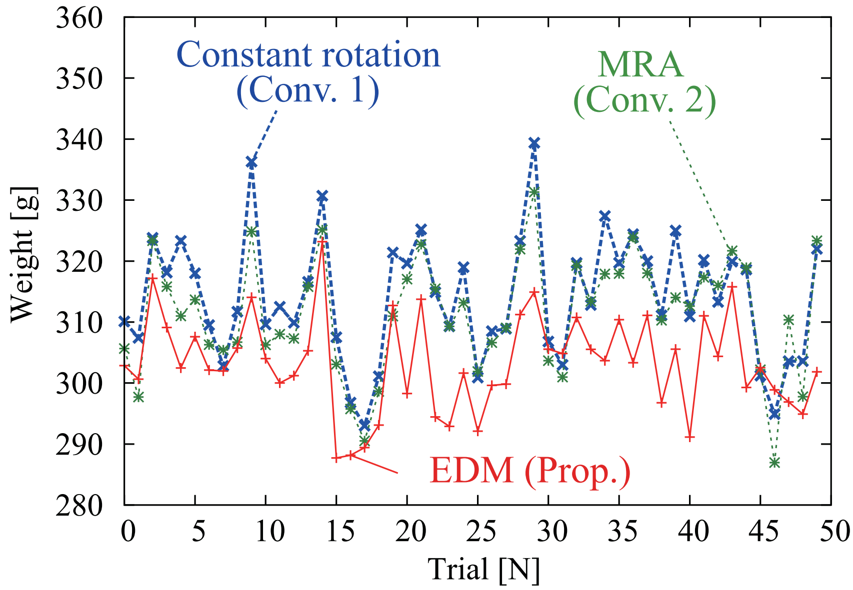

Fig. 6-7: Comparison of filling weight.

Table 6.3: Comparison of filling accuracy.

Method	μ [g]	σ [g]
conv. 1	314.14	10.12
conv. 2	311.33	9.47
prop.	303.23	7.90

6.2 Summary of Chapter 6

Chapter 6 introduced the high-precision powder filling method. The powder-filling machine was used as an example of machines that are being adjusted by skilled worker and knowledge of experts. The control was achieved by adaptation control based on filling coefficient prediction. The prediction equation was derived by the EDM. Since the EDM can deal with nonlinear function, it can also be applied to a system containing many nonlinear elements such as powder. Also, it becomes possible to extract skilled worker's knowledge by mathematical formula. The proposed method can give the abstracted intelligence as the initial value of the next learning even when the raw material and surrounding environment change or when the target powder changes. By using the proposed method, inheritance of intelligence in industrial machinery was achieved.

Chapter 7

Conclusions and Future Works

This dissertation proposed system abstraction based on the EDM. There are two general optimization methods; one is a model-based method and the other is a data-based method. Although the physical meaning of the model-based method is obvious, there is a problem that the result is restricted to a predetermined model. The data-based method is not limited to the model because there is no need to determine the model in advance; however, there is a problem that interpretation of the physical meaning is difficult. Since the proposed EDM does not need to determine a model in advance, it is not subject to model constraints, and it is also possible to interpret the physical meaning of the result obtained. Therefore, it is possible to extract an important governing equation in the target system, and the system is abstracted. This suggests the possibility to formalize knowledge, which was regarded as tacit knowledge of human. Furthermore, since the obtained result can be given as the initial value of the next optimization, it is possible to inherit sustainable knowledge. In addition, it is shown that interactive design is possible based on the characteristics that human intention can input and physical meaning of the result is understandable.

Chapter 2 described the basic principle of the EDM. The structure and parameters of the system can be optimized simultaneously. By including an input parameter in a gene, it is possible to extract only important parameters from a plurality of parameters. Also, it is possible to optimize the system including the plant by expressing the plant as a fixed gene. Since elements can be designed freely, nonlinear elements and time-varying elements can also be handled. Moreover, since input and output to the system can be arbitrarily designed, it can be applied to a system with multiple inputs and multiple outputs. Basically, the EDM was divided two ways; one is hierarchical abstraction using an unidirectional element matrix, the other is overall abstraction using a multidirectional element matrix. By hierarchical abstraction, it is possible to abstract from important mathematical expressions sequentially. This makes it possible to arbitrarily choose simplicity and accuracy. On the contrary, it is difficult to prove analytical optimality because it is a metaheuristic method based on the GA. The EDM was applied to automatic generation of the RFOB compensator in Chapter 2. In order to extract reaction force from environments, disturbance force excluding reaction force must be compensated. There are roughly two compensation methods to extract compensation force; one is model-based method, and the other is data-based method. Generally, model structure must be decided in previous when the model-based method is applied. Therefore, the compensator is constrained by the predetermined model structure, and it is difficult to apply to unknown system. Also, the EQ is introduces as data-based method. In the EQ, compensation force is derived by slave actuator. The EQ has merits that it is not necessary to determine model and identify parameters of the disturbance force. However, there are disadvantages that the installation space of the slave system is necessary and the cost of the machine raises. On the contrary, the EDM can apply to unknown system, and slave system is not needed. The validity was confirmed by experiments using a powder-filling machine and leak detector. The compensation accuracy of the EDM was better than LuGre model that is known as strict model of friction. Moreover, it was confirmed that it was possible to understand the physical meaning of the result, and the model was extracted in order from the most important one by the hierarchical abstraction. The performances of the hierarchical abstraction and the overall abstraction were compared experimentally using leak detector. It was confirmed that due to the restriction of the algorithm, overall abstraction with large matrix size tends to fall into local solution. On the contrary, it was shown that more optimal values can be derived from steady abstraction progressing step by step in the hierarchical abstraction.

In Chapter 3, the EDM was applied to automatic control designing. Firstly, the controller generates a multi-mass resonant system is attempted. EDM can give human intention to the machine such as initial individual, window function design, and type of individual to prepare. Furthermore, since it is possible to interpret the physical meaning of the answer led by the machine, it enables interactive design. By performing the hierarchical abstraction Interactively, controllers having the effect of stabilization, tracking performance, and overshoot reduction were independently extracted. In addition, it was confirmed that even if the inertia fluctuated, responsiveness was recovered by learning again. Also, the stability improvement by the EDM was applied in frequency domain. The characteristic of feedback compensator is evaluated based on gain characteristics of a loop transfer function and complementary sensitivity function. It was confirmed that frequency characteristics close to desired characteristics can be obtained by using a high-order feedback compensator. Furthermore, a feedback compensator which is very easy to implement was derived by dead time elements. From these results, it was shown that the sensitivity function/complementary sensitivity function can be brought close to arbitrary characteristics by automatically designing the feedback compensator using EDM. Furthermore, since the feedback compensator generated by EDM can interpret the physical meaning, it is easy to derive the inverse system, and it is also possible to design a feed-forward controller that improves the command tracking performance. Then, the acceleration control method via motion network was proposed. Since acceleration control is a fundamental part of various control structures, it can be said that it is one of the most important control techniques for automatic machines. In addition, since most of the actuators used in the automatic machines are controlled via the motion network, it is necessary to consider the delay of the motion network in the control design of the automatic machinery. In this dissertation, it was pointed out that the delay of the motion network adversely affects the acceleration control system, making the acceleration control system unstable. As a method to overcome this problem, an example of control design by compensation the DOB and Smith compensator was proposed. By the proposed method, it was possible to design control of various applications based on acceleration control even when delay of motion network exists. Then, the force control method based on impedance model of environment was described. The EDM is effective method for environment identification because it does not require pre-determined model and the result by the EDM is understandable.

Chapter 4 described an automatic command generation method using the EDM. Firstly, an automatic generation of command values to excite resonance of a beam was verified. Also, even when the constraint condition such as the movable range is changed, the command value corresponding to it was generated. This confirmed that EDM can be used for automatic generation of command values. Furthermore, a spatio-temporal interpolation method based on model-data synthesis was proposed. The interpolation was achieved by clothoid curve and minimum jerk model. Since the clothoid curve cannot solve analytically, numerical solution is used for interpolation. However, discretization error become larger when the resolution is low. To overcome this problem, the interpolation method using pinching integration and Aitken acceleration were proposed. By using the proposed method, the true value of the clothoid spline was calculated even if the tangential velocity is large. Also, tracking control is achieved precisely by the DOB and feed-forward controller. The validity of the proposed method was confirmed by experiments. Spatial interpolation and temporal interpolation were designed independently by the proposed method.

Therefore, easy and accurate interpolation could be achieved.

In Chapter 5, skill extraction based on a motion-copying system was proposed. In order to achieve a skilled machinery, not only knowledge abstraction, but also skill extraction of skilled worker is important. It is known that one of effectives methods to extract the skill is motion-copying system. By using the motion-copying system, human behavior can be preserved and reproduced. This saved data is the extracted human skill. However, there is a problem that it is difficult to reproduce with high precision when the environmental positions at the time of storage and reproduction are different. As a solution to this problem, the time adaptive control was proposed. With the time adaptive control, it can instantaneously adapt to environmental position fluctuations. The effectiveness of time adaptive control was confirmed by comparison with the conventional method in the experiment. In addition, time adaptive control has been extended to multiple degrees of freedom. When extending to multiple degrees of freedom, a selection matrix is needed to determine the value to be input to the time adaptation.

Knowledge abstraction based on the EDM was described in Chapter 6. As an application, powder-filling machine was used. The powder-filling machine has been adjusted based on skills and knowledge of experienced engineers for a long time. As described above, by using the proposed method, it became possible to achieve both abundant expressibility like neural network and readability of result like model based method. In addition, since the proposed method can perform learning hierarchically, it is possible to extract models in the order of dominant ones in the system. Therefore, by terminating learning at the time when a sufficient model is obtained, the system can be abstracted. The abstracted model can be succeeded also to the next abstraction so that maintenance and development of knowledge is possible. Furthermore, the proposed method can be applied not only to system abstraction but also to automatic design of controllers and automatic generation of command values. By using the proposed method, solving the lack of technical tradition and sustainable development of people and machinery can be expected.

In the future, the proposed EDM is a technology that can be expected to develop into various applications. In mechanical design, it is possible to develop automatic design of mechanisms such as cams and links to achieve a desired tip trajectory. When applied to the design of electronic circuits, there is a possibility that automatic circuit design can be realized by preparing the characteristics of parts as elements. If applied to the thermal system, it is considered that physical equations such as heat conduction and diffusion can be abstracted automatically. In control design of robots, it is possible to abstract Jacobian matrix of parallel-link robot and multi-degree-of-freedom robot which makes coordinate transformation complicated. It can be expected to be applied to process control like a large chemical plant. In this way, it can be applied to various systems according to the design of the evaluation function. Furthermore, since models and parameters can be abstracted at the same time, there is a possibility of obtaining new motion equations using big data. In actual manufacturing sites, abstract knowledge and skills of experienced technicians will be implemented. In the actual sites, there are very many cases where adjustment and judgment are made based on experience rules of experienced technicians. By achieving automatic machinery with knowledge and skills like experienced technicians by the EDM, sustainable symbiosis between human beings and machinery as well as labor savings at the manufacturing site will be expected.

References

[1] R. U. Ayres, “Future trends in factory automation,” IIASA, Laxenburg, Austria, IIASA Working Paper, Feb. 1987.

[2] I. Takeuchi, “Industry and real world haptics,” *The Journal of The Institute of Electrical Engineers of Japan*, Vol. 133, No. 5, pp. 286–289, May, 2013.

[3] Q. Zhang and M. Tseng, “Modelling and integration of customer flexibility in the order commitment process for high mix low volume production,” *International Journal of Production Research*, Vol. 47, No. 22, pp. 6397–6416, Aug. 2009.

[4] Y. P. Singh and D. Kohli, “Synthesis of cam-link mechanisms for exact path generation,” *Mechanism and Machine Theory*, Vol. 16, No. 4, pp. 447–457, Nov. 1981.

[5] H. J. V. de Straete and J. D. Schutter, “Hybrid cam mechanisms,” *IEEE/ASME Transactions on Mechatronics*, Vol. 1, No. 4, pp. 284–289, Dec. 1996.

[6] K. Ohishi, K. Ohnishi, and K. Miyachi, “Torque-speed regulation of dc motor based on load torque estimation method.” in *Proceedings of the IEEJ International Power Electronics Conference, IPEC*, Vol. 2, pp. 1209–1218. Inst of Electrical Engineers of Japan, Mar. 1983.

[7] K. Ohnishi, M. Shibata, and T. Murakami, “Motion control for advanced mechatronics,” *IEEE/ASME Transactions on Mechatronics*, Vol. 1, No. 1, pp. 56–67, Mar. 1996.

[8] M. Tomizuka, “Zero phase error tracking algorithm for digital control,” *Trans. of ASME, Journal of Dynamic Systems, Measurements and Control*, Mar. 1987.

[9] H. Fujimoto, Y. Hori, and A. Kawamura, “Perfect tracking control based on multirate feedforward control with generalized sampling periods,” *IEEE Transactions on Industrial Electronics*, Vol. 48, No. 3, pp. 636–644, Jun. 2001.

[10] S. Devasia, E. Eleftheriou, and S. O. R. Moheimani, “A survey of control issues in nanopositioning,” *IEEE Transactions on Control Systems Technology*, Vol. 15, No. 5, pp. 802–823, Sep. 2007.

[11] A. Albu-Schaffer, O. Eiberger, M. Grebenstein, S. Haddadin, C. Ott, T. Wimbock, S. Wolf, and G. Hirzinger, “Soft robotics,” *IEEE Robotics Automation Magazine*, Vol. 15, No. 3, pp. 20–30, Sep. 2008.

[12] S. Komada and K. Ohnishi, “Force feedback control of robot manipulator by the acceleration tracing orientation method,” *IEEE Transactions on Industrial Electronics*, Vol. 37, No. 1, pp. 6–12, Feb. 1990.

[13] S. Katsura, Y. Matsumoto, and K. Ohnishi, “Analysis and experimental validation of force bandwidth for force control,” *IEEE Transactions on Industrial Electronics*, Vol. 53, No. 3, pp. 922–928, Jun. 2006.

[14] T. Yoshikawa, “Dynamic hybrid position/force control of robot manipulators–description of hand constraints and calculation of joint driving force,” *IEEE Journal on Robotics and Automation*, Vol. 3, No. 5, pp. 386–392, Oct. 1987.

[15] H. Vallery, J. Veneman, E. van Asseldonk, R. Ekkelenkamp, M. Buss, and H. van Der Kooij, “Compliant actuation of rehabilitation robots,” *IEEE Robotics Automation Magazine*, Vol. 15, No. 3, pp. 60–69, Sep. 2008.

[16] N. Motoi, T. Shimono, R. Kubo, and A. Kawamura, “Task realization by a force-based variable compliance controller for flexible motion control systems,” *IEEE Transactions on Industrial Electronics*, Vol. 61, No. 2, pp. 1009–1021, Feb. 2014.

[17] N. Hogan, “Impedance control: An approach to manipulation,” in *Proceedings of the American Control Conference, ACC*, pp. 304–313, Jun. 1984.

[18] C. Ott, A. Albu-Schaffer, A. Kugi, and G. Hirzinger, “On the passivity-based impedance control of flexible joint robots,” *IEEE Transactions on Robotics*, Vol. 24, No. 2, pp. 416–429, Apr. 2008.

[19] R. J. Anderson and M. W. Spong, “Bilateral control of teleoperators with time delay,” *IEEE Transactions on Automatic Control*, Vol. 34, No. 5, pp. 494–501, May, 1989.

[20] D. A. Lawrence, “Stability and transparency in bilateral teleoperation,” *IEEE Transactions on Robotics and Automation*, Vol. 9, No. 5, pp. 624–637, Oct. 1993.

[21] W. Iida and K. Ohnishi, “Reproducibility and operationality in bilateral teleoperation,” in *Proceedings of the IEEE International Workshop on Advanced Motion Control, AMC*, pp. 217–222, Mar. 2004.

[22] Y. Yokokura, S. Katsura, and K. Ohishi, “Motion copying system based on real-world haptics,” in *Proceedings of the IEEE International Workshop on Advanced Motion Control, AMC*, pp. 613–618, Mar. 2008.

[23] Y. Yokokura, S. Katsura, and K. Ohishi, “Stability analysis and experimental validation of a motion-copying system,” *IEEE Transactions on Industrial Electronics*, Vol. 56, No. 10, pp. 3906–3913, Oct. 2009.

[24] N. Tsunashima and S. Katsura, “Reproduction of linear motion with adaptation for change in environmental position,” *IEEJ Transactions on Industry Applications*, Vol. 132, No. 5, Jan. 2012.

[25] D. Toyama, D. Yashiro, K. Yubai, and S. Komada, “Saving and loading of writing motion in three-dimensional work spaces with robustness against changes in paper position,” *IEEJ Transactions on Sensors and Micromachines*, Vol. 134, No. 3, pp. 308–316, Jan. 2014.

[26] N. Tsunashima and S. Katsura, “Reproduction of human motion using motion-copying system based on coordinate modification,” in *Proceedings of the Annual Conference of IEEE Industrial Electronics Society, IECON*, pp. 1609–1614, Nov. 2010.

[27] S. Yajima and S. Katsura, “Motion-copying system based on velocity information for motion reproduction,” in *Proceedings of the Annual Conference of IEEE Industrial Electronics Society, IECON*, pp. 221–226, Nov. 2011.

[28] T. Miyagi and S. Katsura, “Motion reproduction system considering control bandwidth in force transmission,” in *Proceedings of the IEEE International Workshop on Advanced Motion Control, AMC*, pp. 452–457, 2014.

[29] T. Nozaki, T. Mizoguchi, and K. Ohnishi, “Motion reproduction using time-scaling for adaptation to difference in environmental location,” in *Proceedings of the IEEE International Conference on Industrial Technology, ICIT*, pp. 45–50, Sep. 2014.

[30] I. Takeuchi and S. Katsura, “Motion reproduction with time-adaptation control for dealing with variations of environmental location,” *IEEJ Journal of Industry Applications*, Vol. 5, No. 3, pp. 221–227, Sep. 2016.

[31] I. Takeuchi and S. Katsura, “Motion reproduction based on time-adaptation in multi-degree-of-freedom system for contact task,” in *Proceedings of the Annual Conference of IEEE Industrial Electronics Society, IECON*, pp. 3786–3791, Nov. 2015.

[32] A. Mandloi, “Bigdata, iot and ubiquitous nature of data and software,” in *Proceedings of the IEEE International Conference on ICT in Business Industry Government, ICTBIG*, pp. 1–1, Nov. 2016.

[33] M. Hermann, T. Pentek, and B. Otto, “Design principles for industrie 4.0 scenarios,” in *Proceedings of the IEEE Hawaii International Conference on System Sciences, HICSS*, pp. 3928–3937, Jan. 2016.

[34] F. Pasqualetti, F. Dorfler, and F. Bullo, “Attack detection and identification in cyber-physical systems,” *IEEE Transactions on Automatic Control*, Vol. 58, No. 11, pp. 2715–2729, Nov. 2013.

[35] K. Kaur, S. Garg, G. S. Aujla, N. Kumar, J. J. P. C. Rodrigues, and M. Guizani, “Edge computing in the industrial internet of things environment: Software-defined-networks-based edge-cloud interplay,” *IEEE Communications Magazine*, Vol. 56, No. 2, pp. 44–51, Feb. 2018.

[36] M. H. U. Rehman, E. Ahmed, I. Yaqoob, I. A. T. Hashem, M. Imran, and S. Ahmad, “Big data analytics in industrial iot using a concentric computing model,” *IEEE Communications Magazine*, Vol. 56, No. 2, pp. 37–43, Feb. 2018.

[37] J. Jiang and R. Doraiswami, “Convergence analysis of least-squares identification algorithm for unstable systems,” *IEE Proceedings D - Control Theory and Applications*, Vol. 134, No. 5, pp. 301–308, Sep. 1987.

[38] W. X. Zhao, H. F. Chen, and W. X. Zheng, “Recursive identification for nonlinear arx systems based on stochastic approximation algorithm,” *IEEE Transactions on Automatic Control*, Vol. 55, No. 6, pp. 1287–1299, Jun. 2010.

[39] R. Johansson, “Identification of continuous-time models,” *IEEE Transactions on Signal Processing*, Vol. 42, No. 4, pp. 887–897, Apr. 1994.

[40] B. Wahlberg, “System identification using laguerre models,” *IEEE Transactions on Automatic Control*, Vol. 36, No. 5, pp. 551–562, May, 1991.

[41] J. Oaki, “Stable force controller design based on frequency response identification,” in *Proceedings of the IEEE/RSJ International Conference on Intelligent Robots and Systems, IROS*, pp. 1116–1121 vol.2, Nov. 1991.

[42] M. Tarokh and S. Bailey, “Force tracking with unknown environment parameters using adaptive fuzzy controllers,” in *Proceedings of the IEEE International Conference on Robotics and Automation, ICRA*, Vol. 1, pp. 270–275, Apr. 1996.

[43] S. Jung and T. C. Hsia, “Robust neural force control scheme under uncertainties in robot dynamics and unknown environment,” *IEEE Transactions on Industrial Electronics*, Vol. 47, No. 2, pp. 403–412, Apr. 2000.

[44] V. Mallapragada, D. Erol, and N. Sarkar, "A new method of force control for unknown environments," in *Proceedings of the IEEE/RSJ International Conference on Intelligent Robots and Systems, IROS*, pp. 4509–4514, Oct. 2006.

[45] I. Arel, D. C. Rose, and T. P. Karnowski, "Deep machine learning - a new frontier in artificial intelligence research [research frontier]," *IEEE Computational Intelligence Magazine*, Vol. 5, No. 4, pp. 13–18, Nov. 2010.

[46] H. C. Shin, H. R. Roth, M. Gao, L. Lu, Z. Xu, I. Nogues, J. Yao, D. Mollura, and R. M. Summers, "Deep convolutional neural networks for computer-aided detection: CNN architectures, dataset characteristics and transfer learning," *IEEE Transactions on Medical Imaging*, Vol. 35, No. 5, pp. 1285–1298, May, 2016.

[47] I. Takeuchi and S. Katsura, "Model generation and parameter identification of unknown environment using element description method," in *Proceedings of the IEEE International Conference on Mechatronics, ICM*, pp. 330–335, Feb. 2017.

[48] K. S. Tang, K. F. Man, S. Kwong, and Q. He, "Genetic algorithms and their applications," *IEEE Signal Processing Magazine*, Vol. 13, No. 6, pp. 22–37, Nov. 1996.

[49] K. Ito, M. Iwasaki, and N. Matsui, "GA-based practical compensator design for a motion control system," *IEEE/ASME Transactions on Mechatronics*, Vol. 6, No. 2, pp. 143–148, Jun. 2001.

[50] R. Zhang and J. Tao, "A nonlinear fuzzy neural network modeling approach using an improved genetic algorithm," *IEEE Transactions on Industrial Electronics*, Vol. 65, No. 7, pp. 5882–5892, Jul. 2018.

[51] F. Almeida, D. Gimenez, J. J. Lopez-Espin, and M. Perez-Perez, "Parameterized schemes of metaheuristics: Basic ideas and applications with genetic algorithms, scatter search, and grasp," *IEEE Transactions on Systems, Man, and Cybernetics: Systems*, Vol. 43, No. 3, pp. 570–586, May, 2013.

[52] M. H. Tayarani-N., X. Yao, and H. Xu, "Meta-heuristic algorithms in car engine design: A literature survey," *IEEE Transactions on Evolutionary Computation*, Vol. 19, No. 5, pp. 609–629, Oct. 2015.

[53] P. G. Espejo, S. Ventura, and F. Herrera, "A survey on the application of genetic programming to classification," *IEEE Transactions on Systems, Man, and Cybernetics, Part C (Applications and Reviews)*, Vol. 40, No. 2, pp. 121–144, Mar. 2010.

[54] J. R. Koza, F. H. Bennett, D. Andre, M. A. Keane, and F. Dunlap, "Automated synthesis of analog electrical circuits by means of genetic programming," *IEEE Transactions on Evolutionary Computation*, Vol. 1, No. 2, pp. 109–128, Jul. 1997.

[55] J. R. Koza, M. A. Keane, and M. J. Streeter, "What's AI done for me lately? genetic programming's human-competitive results," *IEEE Intelligent Systems*, Vol. 18, No. 3, pp. 25–31, May, 2003.

[56] J. R. Koza, "Survey of genetic algorithms and genetic programming," in *Proceedings of the IEEE Conference record. 'Microelectronics Communications Technology Producing Quality Products Mobile and Portable Power Emerging Technologies', WESCON*, pp. 589–594, Nov. 1995.

[57] W. Banzhaf, J. R. Koza, C. Ryan, L. Spector, and C. Jacob, "Genetic programming," *IEEE Intelligent Systems and their Applications*, Vol. 15, No. 3, pp. 74–84, May, 2000.

[58] I. Takeuchi, "Packaging machinery and precision servo technology," *The Journal of The Institute of Electrical Engineers of Japan*, Vol. 137, No. 1, pp. 27–30, Jan. 2017.

[59] T. Murakami, F. Yu, and K. Ohnishi, "Torque sensorless control in multidegree-of-freedom manipulator," *IEEE Transactions on Industrial Electronics*, Vol. 40, No. 2, pp. 259–265, Apr. 1993.

[60] I. Takeuchi, N. Suzuki, A. Matsui, Y. Mizutani, and S. Katsura, "Development of a packing-leak tester by high-accuracy force detection," *Journal of the Japan Society for Precision Engineering*, Vol. 81, No. 3, pp. 242–246, Mar. 2015.

[61] I. Takeuchi and S. Katsura, "A study of acceleration control system via industrial motion network," in *Proceedings of the IEEE International Conference on Industrial Technology, ICIT*, pp. 29–34, Feb. 2018.

[62] I. Takeuchi and S. Katsura, "Interpolation of a clothoid curve based on iterative true-value prediction considering discretization error," *IEEE Transactions on Industrial Informatics (Early Access)*, 2018.

[63] K. Hoshino, Y. Nishimura, Y. Yamashita, and D. Tsubakino, "Global asymptotic stabilization of nonlinear deterministic systems using wiener processes," *IEEE Transactions on Automatic Control*, Vol. 61, No. 8, pp. 2318–2323, Aug 2016.

[64] K. V. Nielsen, M. Blanke, and L. Eriksson, "Adaptive observer for nonlinearly parameterized hammerstein system with sensor delay – applied to ship emissions reduction," *IEEE Transactions on Control Systems Technology*, Vol. 26, No. 4, pp. 1508–1515, Jul. 2018.

[65] L. Wang, R. Jiao, Q. Li, Y. Yin, and Q. Zheng, "Active disturbance rejection control in stribeck friction dynamic compensation for high-accuracy servo systems," in *Proceedings of the Chinese Control Conference, CCC*, pp. 4771–4775, Jul. 2016.

[66] I. Nilkhamhang and A. Sano, "Adaptive friction compensation using the gms model with polynomial stribeck function," in *Proceedings of the IEEE International Conference on Control Applications, CCA*, pp. 1085–1090, Oct. 2006.

[67] C. C. de Wit, H. Olsson, K. J. Astrom, and P. Lischinsky, "A new model for control of systems with friction," *IEEE Transactions on Automatic Control*, Vol. 40, No. 3, pp. 419–425, Mar. 1995.

[68] L. Freidovich, A. Robertsson, A. Shiriaev, and R. Johansson, "Lugre-model-based friction compensation," *IEEE Transactions on Control Systems Technology*, Vol. 18, No. 1, pp. 194–200, Jan. 2010.

[69] S. Katsura, Y. Matsumoto, and K. Ohnishi, "Quarry of environmental information based on twin robot system environment quarrier," in *Proceedings of the IEEE International Workshop on Advanced Motion Control, AMC*, pp. 243–248, Mar. 2004.

[70] S. Katsura, K. Ohnishi, and K. Ohishi, "Transmission of force sensation by environment quarrier based on multilateral control," *IEEE Transactions on Industrial Electronics*, Vol. 54, No. 2, pp. 898–906, Apr. 2007.

[71] S. Kumagai, K. Ohishi, N. Shimada, and T. Miyazaki, "High-performance robot motion control based on zero-phase notch filter for industrial robot," in *Proceedings of the IEEE International Workshop on Advanced Motion Control, AMC*, pp. 626–630, Mar. 2010.

[72] S. Katsura and K. Ohnishi, "Absolute stabilization of multi-mass resonant system by phase-lead compensator based on disturbance observer," in *Proceedings of the IEEE International Workshop on Advanced Motion Control, AMC*, pp. 194–199, Mar. 2006.

[73] K. Yuki, T. Murakami, and K. Ohnishi, "Vibration control of 2 mass resonant system by resonance ratio control," in *Proceedings of the Annual Conference of IEEE Industrial Electronics Society, IECON*, Vol. 3, pp. 2009–2014, Nov. 1993.

[74] E. Saito and S. Katsura, "Vibration suppression of resonant system by using wave compensator," in *Proceedings of the Annual Conference of IEEE Industrial Electronics Society, IECON*, pp. 4250–4255, Nov. 2011.

[75] R. J. M. Masey, J. O. Gray, T. J. Dodd, and D. G. Caldwell, "Elliptical point to point trajectory planning using electronic cam motion profiles for high speed industrial pick and place robots," in

Proceedings of the IEEE International Conference on Emerging Technologies Factory Automation, ETFA, pp. 1–8, Sep. 2009.

[76] A. Suzumura and Y. Fujimoto, “Generalized design of position-based bilateral control parameterized by complementary sensitivity function,” *IEEE Transactions on Industrial Electronics (Early Access)*, 2018.

[77] G. Cena, I. C. Bertolotti, S. Scanzio, A. Valenzano, and C. Zunino, “Evaluation of ethercat distributed clock performance,” *IEEE Transactions on Industrial Informatics*, Vol. 8, No. 1, pp. 20–29, Feb. 2012.

[78] H. Xu, Y. Gao, K. Liu, B. Zhu, and C. Zhang, “Research on cross-communication based on real-time ethernet powerlink,” in *Proceedings of the Chinese Control and Decision Conference, CCDC*, pp. 2577–2581, May, 2014.

[79] N. Taki, T. Satou, and H. Ikeda, “Mechatrolink technology for high-speed and precise control in factory automation,” in *Proceedings of the SICE Annual Conference*, pp. 1060–1065, Jul. 2015.

[80] O. J. M. Smith, “Posicast control of damped oscillatory systems,” *Proceedings of the IRE*, Vol. 45, No. 9, pp. 1249–1255, Sep. 1957.

[81] K. Natori, R. Oboe, and K. Ohnishi, “Stability analysis and practical design procedure of time delayed control systems with communication disturbance observer,” *IEEE Transactions on Industrial Informatics*, Vol. 4, No. 3, pp. 185–197, Aug. 2008.

[82] T. Murakami and K. Ohnishi, “Observer-based adaptive force control of multi-degrees-of-freedom manipulator,” in *Proceedings of the Annual Conference of IEEE Industrial Electronics Society, IECON*, pp. 1500–1505 vol.3, Nov. 1992.

[83] S. Komada, K. Nomura, M. Ishida, and T. Hori, “Robust force control based on compensation for parameter variations of dynamic environment,” *IEEE Transactions on Industrial Electronics*, Vol. 40, No. 1, pp. 89–95, Feb. 1993.

[84] E. Saito and S. Katsura, “Wave-based load disturbance observer for robust enhancement of reflected wave rejection-based vibration control,” in *Proceedings of the IEEE International Conference on Advanced Intelligent Mechatronics, AIM*, pp. 1114–1119, Jul. 2015.

[85] A. Ferrolho and M. Crisostomo, “Intelligent control and integration software for flexible manufacturing cells,” *IEEE Transactions on Industrial Informatics*, Vol. 3, No. 1, pp. 3–11, Feb. 2007.

[86] Z. Yang, L.-Y. Shen, C.-M. Yuan, and X.-S. Gao, “Curve fitting and optimal interpolation for cnc machining under confined error using quadratic b-splines,” *Computer-Aided Design*, Vol. 66, pp. 62–72, Sep. 2015.

[87] S. Tulsyan and Y. Altintas, “Local toolpath smoothing for five-axis machine tools,” *International Journal of Machine Tools and Manufacture*, Vol. 96, pp. 15–26, Sep. 2015.

[88] S.-H. Nam and M.-Y. Yang, “A study on a generalized parametric interpolator with real-time jerk-limited acceleration,” *Computer-Aided Design*, Vol. 36, No. 1, pp. 27–36, Jan. 2004.

[89] R. Nozawa, H. Kawamura, and M. Miyata, “Numerical control method,” U. S. Patent 4 591 968, May 27, 1986.

[90] X. Han, B. Wang, and W. Wang, “The research of open cnc system circular interpolation track based on kinetics and kinematics,” in *Proceedings of the IEEE International Conference on Measuring Technology and Mechatronics Automation, ICMTMA*, pp. 1216–1218, Jan. 2013.

[91] T. Yamazaki, K. Ohnishi, N. Miyagawa, and T. Inoue, “Numerically controlled method,” U. S. Patent 6 922 607 B2, Jul. 26, 2005.

[92] F. Kimura, H. Makino, and Y. Matsuo, “Design method for industrial product using clothoid curve, industrial products designed by the design method, and method and device for numerical control using the clothoid curve,” U. S. Patent 7 860 592 B2, Dec. 28, 2010.

[93] M. Brezak and I. Petrovic, “Real-time approximation of clothoids with bounded error for path planning applications,” *IEEE Transactions on Robotics*, Vol. 30, No. 2, pp. 507–515, Apr. 2014.

[94] Q. Zhang, L. Lapierre, and X. Xiang, “Distributed control of coordinated path tracking for networked nonholonomic mobile vehicles,” *IEEE Transactions on Industrial Informatics*, Vol. 9, No. 1, pp. 472–484, Feb. 2013.

[95] M. Abramowitz, “Handbook of mathematical functions, with formulas, graphs, and mathematical tables,.” Dover Publications, Incorporated, 1974.

[96] L. Guiqing, L. Xianmin, and L. Hua, “3D discrete clothoid splines,” in *Proceedings of the International Conference on Computer Graphics*, Ser. CGI ’01, pp. 321–324. Washington, DC, USA: IEEE Computer Society, 2001.

[97] X. Zhang, Y. Fang, and N. Sun, “Minimum-time trajectory planning for underactuated overhead crane systems with state and control constraints,” *IEEE Transactions on Industrial Electronics*, Vol. 61, No. 12, pp. 6915–6925, Dec. 2014.

[98] A. Piazzi and A. Visioli, “Global minimum-jerk trajectory planning of robot manipulators,” *IEEE Transactions on Industrial Electronics*, Vol. 47, No. 1, pp. 140–149, Feb. 2000.

[99] A. C. Aitken, “On bernoulli’ s numerical solution of algebraic equations,” in *Proceedings of the Royal Society of Edinburgh, RSE*, Vol. 46, pp. 289–305, 1926.

[100] K. Umezawa, Y. Kakinuma, S. Katsura, K. Ohnishi, T. Aoyama, and K. Yokoi, “Interaction mode control for the machine tool table with three linear servo motors,” *Journal of Advanced Mechanical Design, Systems, and Manufacturing*, Vol. 2, No. 4, pp. 482–492, Jul. 2008.

[101] S.-S. Yeh and P.-L. Hsu, “Estimation of the contouring error vector for the cross-coupled control design,” *IEEE/ASME Transactions on Mechatronics*, Vol. 7, No. 1, pp. 44–51, Mar. 2002.

[102] D. A. Bell, “Walsh functions and hadamard matrixes,” *Electronics Letters*, Vol. 2, No. 9, pp. 340–341, Sep. 1966.

List of Achievements

Journals (As a first author)

[1] Issei Takeuchi, Nozomi Suzuki, Ayaka Matsui, Yosuke Mizutani, and Seiichiro Katsura, "Development of a packing-leak tester by high-accuracy force detection [in Japanese]," *Journal of the Japan Society for Precision Engineering*, Vol. 81, No. 3, pp. 242–246, Mar. 2015.

[2] Issei Takeuchi and Seiichiro Katsura, "Motion reproduction with time-adaptation control for dealing with variations of environmental location," *IEEJ Journal of Industry Applications*, Vol. 5, No. 3, pp. 221–227, Sep. 2016.

[3] Issei Takeuchi and Seiichiro Katsura, "Interpolation of a clothoid curve based on iterative true-value prediction considering discretization error," *IEEE Transactions on Industrial Informatics (accepted)*.

Articles (As a first author)

[1] Issei Takeuchi, "Industry and real world haptics [in Japanese]," *The Journal of The Institute of Electrical Engineers of Japan*, Vol. 133, No. 5, pp. 286–289, May, 2013.

[2] Issei Takeuchi, "Packaging machinery and precision servo technology[in Japanese]," *The Journal of The Institute of Electrical Engineers of Japan*, Vol. 137, No. 1, pp. 27–30, Jan. 2017.

International Conference (As a first author)

[1] Issei Takeuchi and Seiichiro Katsura, "Motion-loading system with time adaptation toward advanced manufacturing process," *Proceedings of the 1st International Workshop on Sensing, Actuation, Motion Control, SAMCON*, TT3-2-4, Mar. 2015.

[2] Issei Takeuchi and Seiichiro Katsura, “Motion reproduction based on time-adaptation in multi-degree-of-freedom system for contact task,” *Proceedings of the 41st Annual Conference of IEEE Industrial Electronics Society, IECON*, pp. 3786–3791, Nov. 2015.

[3] Issei Takeuchi and Seiichiro Katsura, “Model generation and parameter identification of unknown environment using element description method,” *2017 IEEE International Conference on Mechatronics, ICM*, pp. 330–335, Feb. 2017.

[4] Issei Takeuchi and Seiichiro Katsura, “Instantaneous identification of environment considering rotation center of impedance plane for adaptive force control,” *Proceedings of the 1st International Symposium on Applied Abstraction and Integrated Design, AAID*, RS2-6, Mar. 2017.

[5] Issei Takeuchi and Seiichiro Katsura, “A study of acceleration control system via industrial motion network,” *2018 IEEE International Conference on Industrial Technology, ICIT*, pp. 29–34, Feb. 2018.

Domestic Conference (As a first author)

[1] Issei Takeuhci and Seiichiro Katsura, “Future of automatic machinery and haptic technology,” *Proceedings of the 2015 Annual Conference of IEEJ Industry Applications Society, Oita*, 2-S9-2, pp. Sep. 2015.

[2] Issei Takeuchi, Yukiko Osawa, Akihito Beppu, Hisayoshi Muramatsu, and Seiichiro Katsura, “Visualization and control technology of force for next-generation food packaging,” *Proceedings of the 2017 Annual Meeting of the Institute of Electrical Engineers of Japan, Toyama*, 4-S11-6, pp. Mar. 2017.